Polar Geomagnetism: Developing models of high-latitude geomagnetic fields

Thesis submitted in accordance with the requirements of
the University of Liverpool for the degree of Doctor in Philosophy
by

Gemma Samantha Kelly

March 2013

UNIVERSITY OF
LIVERPOOL

Abstract

The availability of high-quality data during the past decade has allowed the development of geomagnetic field models which reproduce well the observed field at low to mid latitudes. However, the complexity of un-modelled processes and interactions in the polar ionosphere and magnetosphere causes significant residuals between data and models at high latitudes. Signatures of high latitude currents are clearly visible in the residuals for several recent models in both amplitude and direction, and so are not easily interpretable as field-aligned currents.

Motivated by this we identify new techniques to allow more, and better quality, data to be selected for use in field modelling at high latitudes. We also look to include more vector data to improve data uniformity and distribution whilst still avoiding the un-modelled sources of the field, in particular within the auroral oval. We investigate both the use of additional indices in the selection process and a method of locating the highly variable external currents to identify the region where vector data are not selected.

By introducing additional criteria we extended the local-time window allowing data density to have greater uniformity in time. We also include vector data at higher latitudes, only using scalar data where we believe external field sources are introducing noise to the data.

When using our data selection criteria in the generation of a relatively simply parameterised geomagnetic model we get results that are close to more complex models. For example, we are able to reproduce features of the field seen in CHAOS-4, MF7 and EMAG3, despite only using CHAMP data for a single year. This makes us optimistic for future developments using longer time series.

Acknowledgements

First and foremost this thesis would not have been possible without the help, guidance and support of my supervisors Richard Holme and Alan Thomson.

I also owe a huge thank you to Brian Hamilton at BGS for having the patience to keep running the modelling code for the endless 'final' versions of my data selection.

I am indebted to Adam who spent hours whilst bored at work amusing himself by listening to my tired ranting about computers, and providing useful (sometimes) programming advice. I would also like to thank the lovely post-graduates in Liverpool for providing a brilliant academic and social environment. In particular I would like express my gratitude to Natasha, Gemma, Victoria and Kirsty for keeping me (mostly) sane and for making the trials and tribulations of PhD writing much more bearable.

I am also eternally grateful to Rob who greeted every crisis and moment of panic with his unflappable practical outlook, and knew exactly when a cup of tea, a bar of chocolate or hug could solve any problem.

Finally I owe the biggest thank you to mum. Without her suggestion to study geology at A-level I might never have stumbled into geophysics.

Contents

List of Figures

List of Tables

Chapter 1

Introduction

The Earth has a spatially and temporally complex magnetic field, with contributions from many sources (e.g., *Lesur et al.*, 2005). At, or near the surface of the Earth we measure a superposition of all these sources, which can be separated into four groups (*Lesur et al.*, 2005), as illustrated in Figure 1.1: (1) the geodynamo, which produces the core field, (2) sources in the magnetosphere and the ionosphere (including coupling currents between them), (3) sources induced in the Earth by these time-varying external fields and (4) magnetisation of rocks in the lithosphere.

The complex nature of the field allows it to be used to probe many diverse regions of the Earth (e.g., *Whaler*, 2007). The core field, and particularly the secular variation, are among the few means available for studying the outer core, along with disciplines such as seismology and mineral physics. Geomagnetic data are used in many geophysical studies, including core-mantle coupling and interactions (e.g., *Aurnou et al.*, 1996), the conductivity of the mantle (e.g., *Constable*, 1993), the structure and thermo-mechanical properties of the crust and decadal scale changes in the length of day (*Holme and de Viron*, 2005). The geomagnetic field is also used for directional drilling in the petroleum industry (e.g., *Reay et al.*, 2005), as well as in space and ground navigation systems (e.g., *Thomson*, 2007).

To make use of the information the geomagnetic field can provide, the field sources need to be separated and modelled individually, based on their distinguishing characteristics. In principle internal and external sources contribute at all time scales, however, separation of these signals is possible based on assumptions about their different time behaviour (*Olsen et al.*, 2002). In general higher frequency variations (periods of shorter than one year) are attributed to external sources located in the magnetosphere and ionosphere, and the induced fields these sources generate. Variations with time scales longer than about four years are usually attributed to the internal field as the electrical conductivity of the mantle causes shorter fluctuations of the core field to be heavily attenuated (*Olsen et al.*, 2002).

Unfortunately, at intermediate time scales both internal and external sources contribute making such a distinction more difficult. For example, there are external

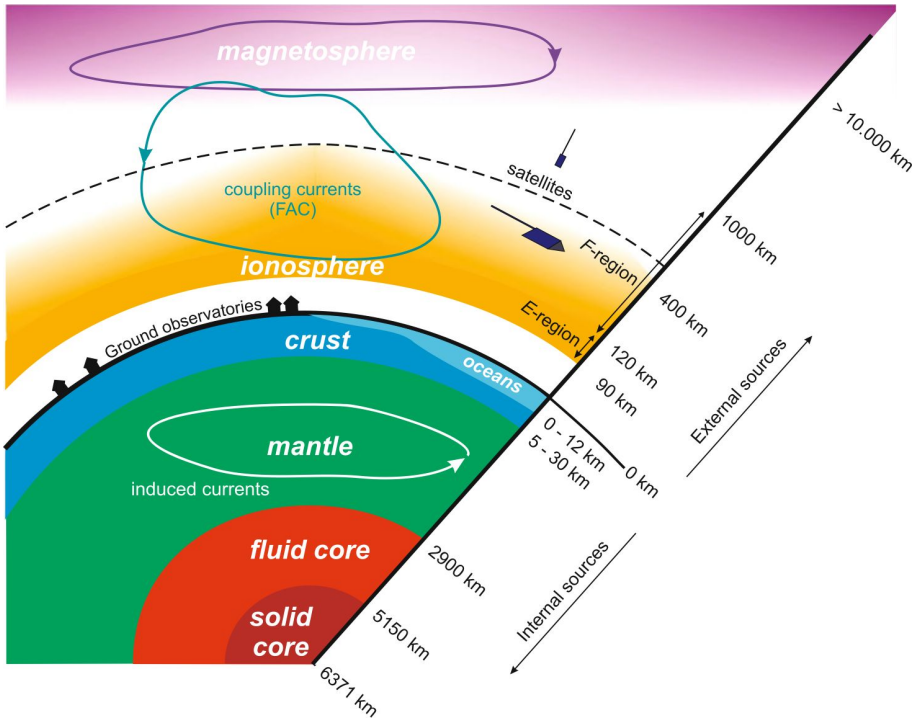

Figure 1.1: Schematic of current sources contributing to the near-Earth magnetic field (from *Olsen et al.*, 2010a).

variations associated with the solar cycle which produce a clear 11-year geomagnetic variation which can be misinterpreted as secular variation of the core field (*Olsen et al.*, 2002); there are also sudden changes in the trend of secular variation, called geomagnetic jerks, which occur within 1-2 years (*Bloxham et al.*, 2002).

Current geomagnetic models perform well, providing the best ever estimates of the main field and its temporal variation. High quality satellite data, which have become available over the last decade, have allowed great advancements in the study of small scale features and describing spatial variations of the field. However, the complex processes and interactions in the polar regions still remain problematic. The plot in Figure 1.2 shows an example of the residuals (measured - modelled) between the CHAMP satellite data and the CHAOS-2 model (*Olsen et al.*, 2009). It is clear in this plot that the model performs well (residuals close to zero) over most of the globe, but leaves large residuals at high latitudes. This is a problem, especially when modelling the core or crustal field in these regions. These residuals are undoubtedly related to the highly variable external field sources, but they will leak into internal field models, creating spurious features at high latitudes and leading to misinterpretation of flow features at the core-mantle boundary. It will be difficult to resolve either polar flow, or high latitude crustal fields until the problem of leakage from external fields is resolved.

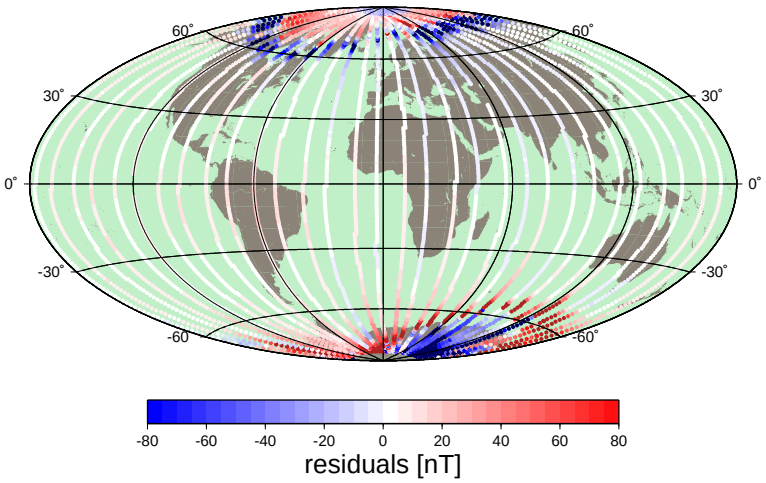

Figure 1.2: Residuals (CHAMP minus CHAOS-2) for the longitudinal, ϕ, component (see Appendix A.1 for a descritpion of coordinate systems) of the field for magnetically quiet ($K_p < 2$o), data between 18:00-06:00 UT from 10^{th} - 11^{th} December 2001.

1.1 Motivation

The aim of this thesis is to improve global geomagnetic field models by addressing the problem of high latitude sources of external field noise. To do this we investigate new data selection criteria and techniques, and methods of modelling the high latitude ionospheric field. We also aim to introduce more vector data at high latitudes to provide more angular information and better data uniformity across the whole dataset.

Improving global field models is important for the many applications which make use of magnetic field models. For example: Geophysical exploration (e.g., location of ore bodies and directional drilling), space weather applications (e.g., hazard to power grids), and understanding deep Earth properties, such as core flow. By removing unwanted high latitude signals from global field models leakage from external field sources into internal field models is reduced. This should in turn enable calculation of improved core flow models, with a higher level of confidence that features at high latitude are genuine.

In the future the Swarm satellite (see Section 2.5.2) will provide the best ever survey of the Earth's magnetic field. By understanding how the many different sources contribute to measurements of the magnetic field at high latitude we will be better placed to make full use of these new high quality data as soon as they become available.

1.2 Thesis Outline

Chapter 2 explores the background to, and theories of, the geomagnetic field as well as information on the indices, satellites and models used in this thesis.

Chapter 3 provides a short proof of concept using Green's functions to assess how much additional information can be gained by successfully using 'noise-free' vector data at high latitudes. The rest of this chapter is then dedicated to investigating the residuals to existing models to find the major problem areas.

Chapters 4 and 5 explore the possibilities for new data selection techniques and criteria.

In Chapter 6 we assess the benefits of our chosen data selection using the BGS Global Geomagnetic Model (BGGM, *Hamilton et al.*, 2010) and comparing the results to CHAOS-4 (*Olsen et al.*, 2010b).

Finally, in Chapter 7 we review the main conclusions of this work and look forward to work that is still required.

Chapter 2

The Earth's Magnetic Field

2.1 Internal Fields in the Core and Crust

2.1.1 The main field

A large proportion of the geomagnetic field (on the order of 97% of the field observed at the Earth's surface at quiet times) is attributed to a self-sustaining dynamo within the outer core (e.g., *Dormy and Le Mouël*, 2008; *Jonkers*, 2007). Convection in the Earth's outer core, driven by solidification of the inner core, is vigorous enough to maintain electrical currents, and a magnetic field (*Olsen et al.*, 2010c). Ohmic losses should dissipate the magnetic field in about 10^5 years (*Buffett and Glatzmaier*, 2000), however, the electrical currents (and therefore the magnetic field) are maintained by electromotive forces, induced by the convective motion of the conducting fluid in a magnetic field (*Olsen et al.*, 2010c). This process is known as the geodynamo and the field it produces is referred to as the core or 'main' field.

The main field is approximately dipolar, with the dipole axis tilted by about 11° from the Earth's rotational axis at the present time. At the Earth's surface the core field ranges in intensity from about 30,000nT near the equator to about 60,000nT at the poles (*Love*, 2008; *Sabaka et al.*, 2002).

The main field changes over time periods of years to millenia (*Bloxham et al.*, 1989) and its first time derivative is known as secular variation (SV). Secular variation originates in the Earth's core and directly reflects fluid flow in the outermost core (*Olsen et al.*, 2002). Maps of secular variation show a clear westward movement of features in the field. It was originally believed that a large part of secular variation could be explained by 'westward drift' of the field (*Halley*, 1692). However, westward drift is more evident in some parts of the world (Europe and North America) than others (Asia and the Pacific hemisphere), and some features of the field drift northwards rather than westwards. It is now known that the concept of westward drift is an oversimplification of secular variation, although it can still be useful in the interpretation of the historical field (*Holme*, 2007).

There are also abrupt changes in the second time derivative (secular acceleration) of the Earth's magnetic field termed 'geomagnetic jerks' (*Courtillot et al.*, 1978; *Malin and Hodder*, 1982; *Courtillot and Le Mouël*, 1984). These jerks are believed to be of internal origin (e.g., *Malin and Hodder*, 1982; *Le Huy et al.*, 1998; *Dormy and Mandea*, 2005) and it is thought that they are due to a change in fluid flow at the surface of the core (*Bloxham et al.*, 2002). They have important implications for a range of core related studies including the understanding of fluid motions in the core, lower mantle conductivity (e.g., *Mandea Alexandrescu et al.*, 1999; *Nagao et al.*, 2003), changes in angular momentum in the core, and variations in length of day (*Holme and de Viron*, 2005).

The magnetic field has important implications for studying the deep Earth, as the core field and particularly the secular variation are among the few means available for probing the properties of the outer core (Olsen et al., 2002). The secular variation has been used to study core-mantle interactions and to constrain flow in the core and the possible dynamo processes responsible for generating the field (*Holme and Olsen*, 2006).

2.1.2 The crustal field

Magnetisation of the crust is responsible for the second largest contribution to the magnetic field of the solid earth measured at the Earth's surface (*Mandea and Purucker*, 2005). Permanent magnetisation of crustal rocks (as they cool below the Curie temperature), and an additional magnetisation proportional to the amibent magnetic field (induced magnetisation), produces a magnetic field that is strong enough to be mapped by low Earth orbiting satellites (*Maus et al.*, 2006a; *Olsen et al.*, 2007).

Ship and airborne surveys provide good local maps of crustal magnetisation, however, stitching together such near surface surveys is not a reliable method for determining magnetic anomalies with wavelengths of more than 500km (*Maus et al.*, 2002). Satellites provide good quality, uniform, global data coverage for crustal magnetic anomalies with wavelengths larger than 400km (*Hemant et al.*, 2007). Unfortunately, in global surveys the longest wavelength crustal fields, with scale lengths in excess of several thousand km (*Mandea and Purucker*, 2005), cannot be distinguished from the features associated with the core field (*Rajaram*, 1993). Short wavelength crustal anomalies are attenuated with altitude (*Maus et al.*, 2006a) and can be easily masked by external contributions to the magnetic field. The situation is further complicated in the polar regions by auroral external fields and by the complex behaviour of the core field near the geomagnetic poles (*Kim et al.*, 2005).

Some crustal anomalies extend over large continental areas with amplitudes reaching thousands of nT, such as Kursk in the Ukraine and Bangui in the Central African Republic (*Mandea and Purucker*, 2005). In the oceans there are magnetic

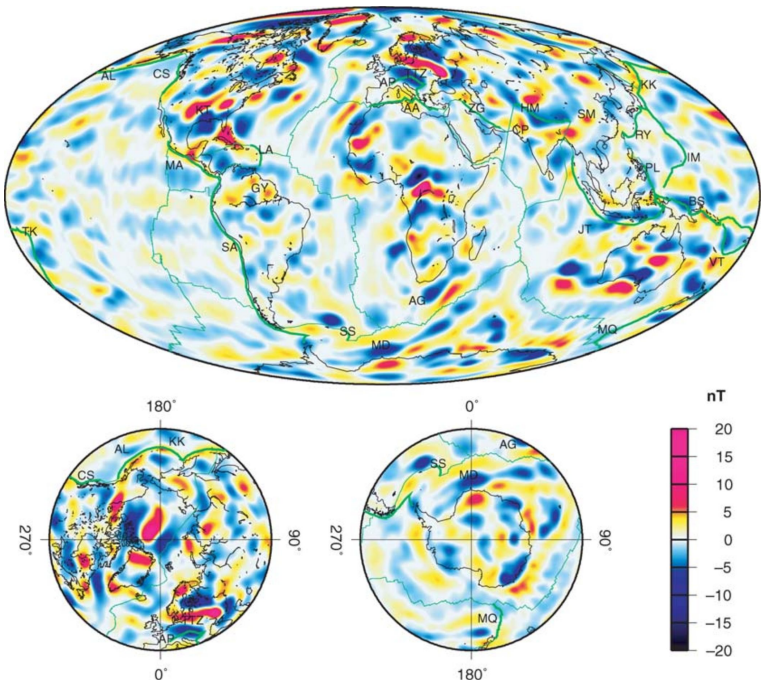

Figure 2.1: Vertical component of the lithospheric magnetic field at a satellite altitude of 400 km above the mean Earth radius, as given by MF4. Plate boundaries are indicated as thin, dark green lines, subduction zones as thick, light green lines (from *Maus et al.*, 2006a)

stripe anomalies associated with sea-floor spreading which can be correlated with magnetic dipole reversals (e.g., *Vine and Matthews*, 1963).

High resolution magnetic field models based on data from the three most recent satellite missions (Ørsted, CHAMP and SAC-C) are helping to improve the global lithospheric models and several models have been produced by teams at, for example, the British Geological Survey, the Danish Technical University, the Geological Survey of Finland, GSFC-NASA, GeoForschungsZentrum (GFZ), National Geophysical Data Center (NGDC) and University of Leeds. An example of a lithospheric field model, MF4 (GFZ), can be seen in Figure 2.1. The major continental magnetic anomalies are clearly identifiable, for example, in West Africa, the Gulf of Mexico and South Australia. Recently NGDC have created a model of the magnetic field to degree and order 720 (*Maus*, 2010), making use of ellipsoidal harmonics to map the lithospheric field down to wavelengths of approximately 56km.

The World Digital Magnetic Anomaly Map (WDMAM) (*Hemant et al.*, 2007) is a global compilation of crustal magnetic field anomaly data from airborne surveys, shipborne surveys and satellites, at an altitude of 5km above the geoid. Because WDMAM includes the aeromagnetic and marine data, it can resolve much smaller scale features of the field than models produced using satellite data alone.

2.2 External Fields in the Ionosphere and Magnetosphere

The Sun's magnetic field dominates interplanetary space, and interacts with the Earth's magnetic field to generate 'external' magnetic fields. The sources of the external magnetic field can be roughly separated into three classes (*Maus and Lühr*, 2005): magnetospheric currents, ionospheric currents and field aligned currents connecting the two regions. These fields also induce currents in the Earth's subsurface (*Love*, 2008).

The Sun's outer atmosphere (the corona) is a plasma; the temperature is sufficiently high to allow the plasma to escape the Sun's gravitational field and stream off into interplanetary space as the solar wind (*Schwenn*, 2006). The field from the Sun, also called the Interplanetary Magnetic Field, or IMF, is 'frozen' in to the solar wind (i.e. moves with it) because of the very high conductivity of the solar wind; this magnetic field has a strength on the order of 5-10nT near the Earth's orbit (*Baumjohann and Nakamura*, 2007). The interaction of the solar wind with the Earth's magnetic field defines the Earth's magnetic environment. When the solar wind encounters the Earth's magnetic field a bow shock wave is generated where the plasma is slowed down; a large proportion of the particles' kinetic energy is converted into thermal energy creating a region of dense, hot plasma behind the bow shock called the magnetosheath (*Baumjohann and Nakamura*, 2007). The cavity generated by the terrestrial magnetic field is called the magnetosphere, and the boundary between the two regions is termed the magnetopause (*Langel et al.*, 1996).

The magnetosphere is an elongated structure which has an interface with the solar wind at approximately 10 Earth radii (R_E) on the sunward side (*Pulkkinen*, 2007); in the anti-sunward direction the magnetic field lines from the Earth are stretched into the magnetotail which extends beyond the orbit of the moon to at least $60R_E$ (*Langel et al.*, 1996). The magnetosphere is highly variable with a strong dependence on the orientation of the IMF and solar wind properties (*Menvielle and Marchaudon*, 2007). The solar wind and the terrestrial magnetic field establish an equilibrium, such that when the solar wind is stronger the magnetosphere shrinks and when it abates, the magnetosphere expands (*Kivelson and Russel*, 1995).

Figure 2.2 shows the complicated system of currents that exist within the magnetosphere; these currents help to dissipate the energy which is transferred to the magnetosphere from the solar wind. In general the strongest currents in the magnetosphere occur in the boundary layers. Within the tail there is a current sheet, called the neutral sheet, which is a region of high plasma density; the neutral sheet flows between the northern and southern lobes of the tail where the magnetic field lines are in opposing directions (*Langel et al.*, 1996). The magnetopause, or Chapman-Ferraro, current flows at the magnetopause boundary and is a result of interaction

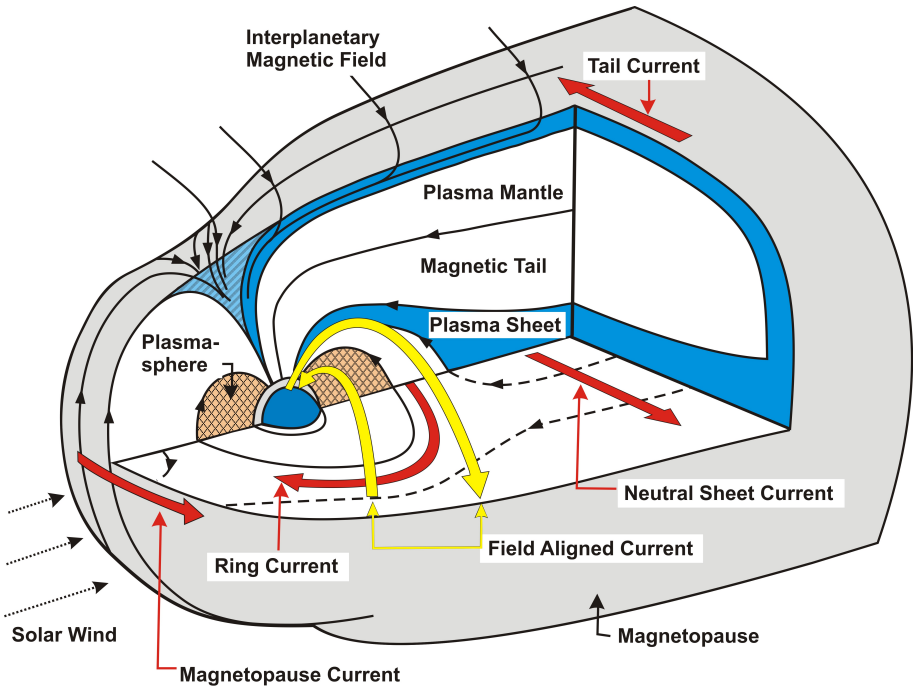

Figure 2.2: Currents and plasma populations within the magnetosphere, after *Kivelson and Russel* (1995)

between the solar wind and magnetosphere plasmas (*Menvielle and Marchaudon*, 2007). The magnetosphere and ionosphere are linked via field-aligned, or Birkeland, currents, which flow along magnetic field lines and are associated with aurorae. The neutral sheet currents also interact with the radiation belts near the Earth, producing a ring current which partially encircles the Earth (*Olsen et al.*, 2010c).

Close to the Earth the ring current is the main source of the magnetospheric field (*Lesur et al.*, 2005), flowing between 4 and 6 R_E (*Baumjohann and Nakamura*, 2007). The direction of current flow of the ring current depends upon the local plasma pressure gradient but is mainly westward (*Langel et al.*, 1996). The current strength varies with local time, especially during magnetically active periods, with the highest intensity near the dipole equatorial plane (*Langel et al.*, 1996). The ring-current achieves closure into and out of the ionosphere via the field-aligned currents (FACs) (*Sabaka et al.*, 2002).

The ionosphere is the electrically conducting part of the upper atmosphere where solar radiation (X-ray and UV) maintains partial ionisation (*Love*, 2008; *Kivelson and Russel*, 1995). It extends from approximately 90km to 1000km and is one of the main sinks of energy transmitted from the solar wind into the magnetosphere (*Lester et al.*, 2006). The dayside ionosphere is also heated by the sun; heating of the ionosphere drives tides in the atmosphere. These tidal winds in the 'ionospheric dynamo region' generate currents which peak between 100-150km altitude (*Stening*, 2003). These currents take the form of two circulating systems (shown in Figure 2.3),

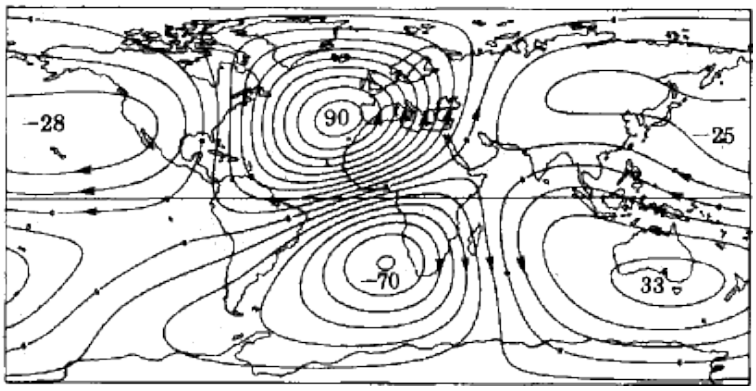

Figure 2.3: Equivalent external ionospheric current system for annual average Sq at midnight UT, 1964−1965. Contour interval and extrema are in kiloamperes, from *Winch* (1981)

with an anti-clockwise vortex in the Northern hemisphere and a clockwise vortex in the Southern Hemisphere (*Kuvshinov*, 2008). The current vortices are fixed with respect to the sun. As observatories rotate under this system they measure a distinct diurnal variation termed the solar-quiet, or S_q, magnetic field variation.

At the geomagnetic equator there is a narrow zone (∼500km) where the magnetic field lines are near parallel to the Earth's surface. Within this band the horizontal conductivity of the ionosphere is enhanced, and the vertical conductivity reduced. This gives rise to a strong eastward Hall current, called the equatorial electrojet (EEJ). On the Earth's surface, near the dipole equator, the EEJ causes a threefold increase in the daily variations of the horizontal component of the magnetic field (*Kuvshinov*, 2008).

Geomagnetic activity within the magnetosphere is controlled by coupling between the solar wind and the magnetosphere, which is, in turn, dominated by magnetic reconnection (*Lester et al.*, 2006). For a southward directed IMF, interplanetary magnetic field lines can merge with a closed terrestrial magnetic field line, creating newly opened field lines which are attached to the Earth at one end and the IMF at the other. The solar wind will then transport this field line across the polar cap towards the nightside. In the tail the two open field lines will eventually reconnect, then return earthward due to magnetic tension. This process is called the Dungey cycle (*Dungey*, 1961) and is depicted in Figure 2.4. The process for northward IMF is much more complicated, with reconnection at much higher latitudes (*Lester et al.*, 2006).

The Dungey cycle drives magnetospheric convection, which in turn drives high latitude ionospheric convection. This takes the form of a two cell convection pattern in the polar ionosphere (shown in Figure 2.5), generating three types of current (*Baumjohann and Nakamura*, 2007):

- FACs flowing parallel to the magnetic field lines

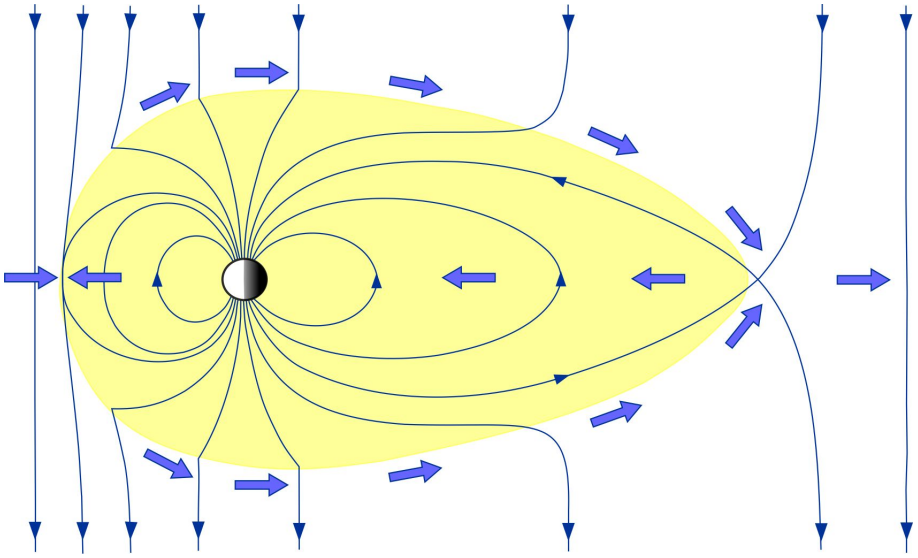

Figure 2.4: Reconnection and convection cycle in the magnetosphere, from *Baumjohann and Treumann* (1996). The small arrows indicate the direction of the magnetic field lines, the large arrows depict the motion of field lines.

- Pedersen currents flowing perpendicular to magnetic field lines and parallel to ionospheric electric fields
- Hall currents flowing perpendicular to both magnetic and electric fields.

These high latitude currents are discussed in Section 2.3.

2.2.1 Induced fields

The highly time-variable external fields induce secondary currents in the Earth's electrically conductive interior and oceans. Further secondary currents are produced by motional induction, caused by electrically conductive seawater moving (e.g., via tides) through the Earth's main magnetic field (*Olsen et al.*, 2010c). Hence, the disturbance field measured at the Earth's surface is a sum of the external field sources and their induced counterparts.

The size and amplitude of the induced field vary greatly, with a dependence on the strength, period and scale of the inducing field, and the conductivity structure of the Earth. In an ideal conductor the secondary and inducing fields would be exactly in phase, but for the real Earth there is a phase lag (*Maus and Weidelt*, 2004).

2.3 The High Latitude Field

The polar regions are home to the most intense current systems in the ionosphere. Measurements of the magnetic field at high latitudes exhibit large perturbations,

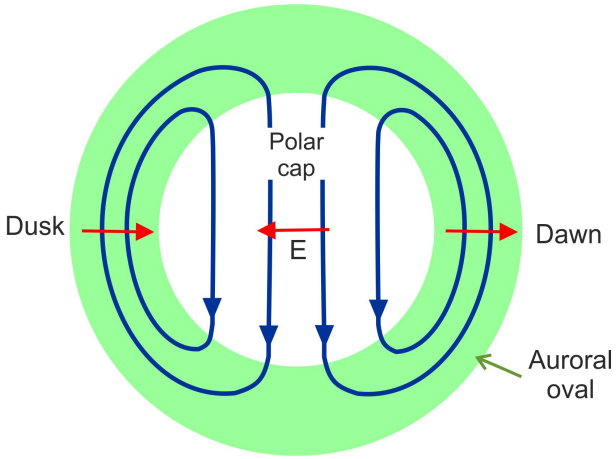

Figure 2.5: Convection (blue) and electric field (red) in the polar ionosphere, adapted from *Baumjohann and Treumann* (1996)

which are superimposed on the field of internal origin. These variations are attributed to ionospheric Hall, Pedersen and field-aligned currents (*Ritter et al.*, 2004a; *Vennerstrøm et al.*, 1991). Measurements made aboard satellites contain contributions from all three types of current, whilst ground-based measurements only contain a signature from Hall currents, as the field-aligned and Pedersen currents can be shown to cancel each other out below the ionopshere (*Fukushima*, 1976).

The high latitude current system is primarily driven by interaction between the solar wind and the magnetosphere. Field-aligned currents (FACs) couple the high latitude ionosphere to processes occurring at the magnetopause and in the magnetotail (*Ritter and Lühr*, 2006). As mentioned previously, magnetic activity is highly dependent on the orientation of the Interplanetary Magnetic Field (IMF). When the IMF develops a southward component (negative B_z) the influence of the solar wind increases, increasing the magnetic activity within the magnetosphere. This close association to the solar wind-magnetosphere interaction makes the high latitude currents an important space weather parameter (*Moretto et al.*, 2002). High latitude currents cause effects such as geomagnetically induced currents, disruption to communications systems, and increased drag on spacecraft due to atmospheric (Joule) heating.

Iijima and Potemra (1976a,b) demonstrated that the large scale FACs are concentrated in two regions encircling the geomagnetic pole, as can be seen in Figure 2.6; the region 1 FACs are located in the poleward portion, and region 2 in the equatorward portion (*Iijima and Potemra*, 1978). In the morning sector, around 2300-1100 MLT (evening sector, around 1300-2300 MLT), FACs flow into (away from) region 1 and away from (into) region 2.

Field-aligned currents vary in intensity and location with geomagnetic activity, and the region 2 currents are much more variable than those in region 1. In disturbed

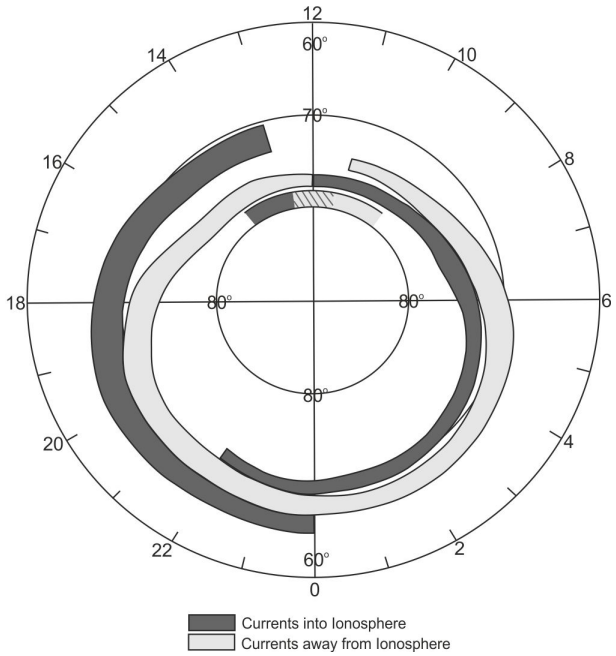

Figure 2.6: A summary of the distribution and flow directions of large-scale field-aligned currents, in magnetic local time (azimuthal variable) and dipole latitude (radial variable), during weakly disturbed conditions (modified from *Iijima and Potemra* (1976b)). The hatched area in the polar cusp region indicates that the current flow directions are often confused.

conditions the field aligned current belt expands both poleward and equatorward (*Chen et al.*, 2003). At non-disturbed times the fields from FACs have magnitudes on the order of 20-100nT, which can increase to several thousand nT during substorms (*Olsen et al.*, 2010a). The current pattern in the polar regions, and in particular the electrojets, strongly depends upon the distribution of FACs and ionospheric conductivity (*Kamide and Matsushita*, 1979a,b).

The auroral ovals in the Northern and Southern Hemispheres are located between $65° - 70°$ dipole latitude and roughly centred on the geomagnetic poles. The conductivity of the auroral oval is much higher than that of the polar cap, due to significant ionization from particle precipitation (*Baumjohann and Nakamura*, 2007). This leads to a concentration of current within the auroral oval forming Hall currents, called electrojets. The auroral electrojets are the most intense currents in the ionosphere (*Moretto et al.*, 2002; *Olsen et al.*, 2002), carrying a total current of around one million Amperes (*Baumjohann and Nakamura*, 2007).

The eastward electrojet flows in the dusk side of the oval, and the westward auroral electrojet in the dawn side; the most intense currents are found in the westward electrojet (*Moretto et al.*, 2002). The electrojets give rise to magnetic field variations which occur on timescales from a few minutes to a few hours, causing ground magnetic perturbations from a few nT to around 2000nT (*Lyons*, 2000). The size of the oval is controlled by the amount of open flux in the Earth's magnetic

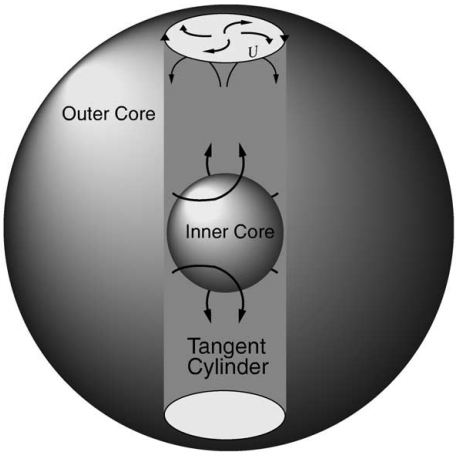

Figure 2.7: Illustration of the tangent cylinder from *Aurnou et al.* (2003).

field. *Milan* (2009) showed this is determined by both the dayside reconnection rate and the intensity of the ring current.

It is generally assumed that the aurorae in the two hemispheres are approximately symmetric; however, it has been argued that there may be inter-hemispheric differences (e.g., *Cowley et al.*, 1991; *Holzworth and Meng*, 1984), and recent investigations have shown this to be the case. For example, *Laundal and Østgaard* (2009) observed asymmetric auroral intensity in the two hemispheres, which they interpret as inter-hemispheric currents related to the seasons. *Stubbs et al.* (2005) used simultaneous observations of the entire ovals from both hemispheres, and found interhemispheric asymmetries caused by an effective partial penetration of IMF.

At mid-latitudes, the quiet time variations of the ionospheric field are described by the S_q current system (as discussed previously in section 2.2). At high latitudes there is an additional field, the S_q^p, field which has been introduced as part of the global S_q system (*Sillanpää et al.*, 2004; *De Michelis et al.*, 2009). The S_q^p field is generated by two current vortices, which are confined to the polar cap and believed to be driven by external forces (*De Michelis et al.*, 2009). In general the S_q^p system can only be observed when the field is very quiet (*Sillanpää et al.*, 2004).

The high latitude field is further complicated by the complex nature of the core field near the poles, where core flow is believed to behave differently. Within the core there are two distinct regions of convection, inside and outside of the 'tangent cylinder' (*Sreenivasan and Jones*, 2006). The tangent cylinder is the notional cylinder that is tangential to the inner core at the equator; it cuts the core mantle boundary at approximately 70° latitude, as illustrated in Figure 2.7. Convection outside the tangent cylinder has a different structure and occurs much more readily than inside (*Holme*, 2007).

Associated with the tangent cylinder are the so-called 'polar vortices', first identified in the Northern hemisphere by *Olson et al.* (1999), as a rotation of field features

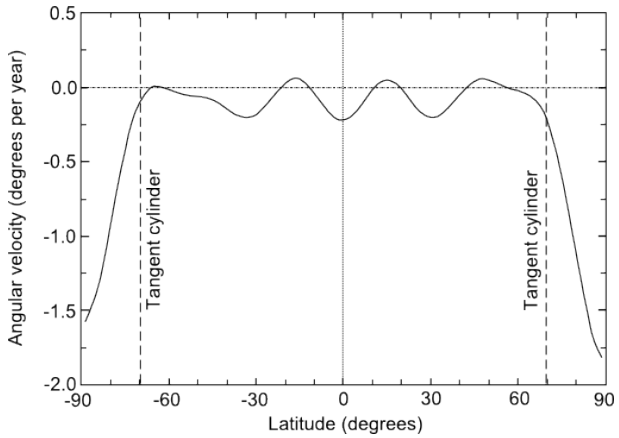

Figure 2.8: Axisymmetric component of flow at the core surface from the model of *Hulot et al.* (2002) suggesting evidence for polar vortices in both the North and South Hemispheres. Flow velocity is positive for eastward with respect to the mantle, negative for westward flow.

with time. *Hulot et al.* (2002) identified vortices in both the Northern and Southern Hemispheres. Figure 2.8 shows their calculated axially averaged flow, for a model based on the difference in field between 1980 and 2000, which indicates strong westward flows within the tangent cylinder, whilst the rest of the profile remains uniform. The flow within the tangent cylinder may reflect inner core rotation, although at the present time nonuniqueness of the flow determination makes it difficult to draw robust conclusions about polar vortices.

2.4 Magnetic Indices

Measurements of the magnetic field made at ground based observatories are used to derive geomagnetic indices. Indices describe irregular variations in the field which originate in the magnetosphere and ionosphere (*Mayaud*, 1980; *Verbanac et al.*, 2010; *Love and Remick*, 2007). When defining magnetic indices there are two main purposes. The first is to estimate global magnetic field characteristics; the second is to fully describe the field variations associated with an isolated physical effect, for example, the D_{st} index is specifically designed for monitoring the ring current.

Magnetic indices are often used to identify quiet data, for example, for core field modelling, or for direct studies of solar-terrestrial physics. When modelling the geomagnetic field the K_p and D_{st} indices are typically used for data selection (for more on data selection see section 2.6.2) and D_{st} is commonly used for external field parametrization (*Olsen et al.*, 2007).

Table 2.1 presents a list of some of the more commonly used indices with a brief summary of the observatories and time intervals used for their calculation. Each of these indices is also described in more detail below.

Index	Number of Observatories	Time interval	Available from
Kp	13 midlatitude observatories	3-hour	1932
Dst	4 near-equatorial observatories	1-hour	1957
AE	12 observatories underneath the Northern auroral oval	1-min	1957
PC	1 North, 1 South polar observatory	1 and 15-min	1975

Table 2.1: Some commonly used magnetic indices

Range, nT	K-values
0-5	0
5-10	1
10-20	2
20-40	3
40-70	4
70-120	5
120-200	6
200-330	7
330-500	8
500+	9

Table 2.2: Limits of classes of K indices at Niemegk observatory, from *Menvielle and Berthelier* (1991)

2.4.1 K_p

Bartels et al. (1939) introduced the observatory K-index to measure the range of local irregular magnetic activity at a given place, i.e. after accounting for S_q. For each 3-hour interval the range of magnetic variations is calculated and attributed to one of ten classes, between 0 and 9. Table 2.2 displays the ten classes of ranges defined by Bartels for Niemegk observatory. The scale is quasi-logarithmic to allow for the separation of both the higher and lower levels of activity. There is a latitudinal variation to magnetic activity which requires that the K-index is calculated separately for each observatory in order to make comparisons of K indices from different observatories meaningful. Therefore, each observatory has its own scale that is proportional to that of Niemegk (*Menvielle and Berthelier*, 1991; *Love and Remick*, 2007). The K-indices are the most widely used geomagnetic indices, both for characterising the activity at a single station and for computing planetary indices, which include: K_p, A_m, K_m, A_n, A_s and aa. Only K_p will be discussed here, for a full description of K-derived indices see *Menvielle and Berthelier* (1991).

The K_p index, introduced by *Bartels* (1949), is a measure of planetary geomagnetic disturbances derived from the K-indices at the 13 observatories shown in Figure 2.9 and Table 2.3. The subauroral latitudes (between $\sim 35^\circ - 60^\circ$) are sensitive to

perturbations from both high- and low-latitude regions without being dominated by one current system; as such, a global characterisation of the energy input from the magnetosphere can be inferred from indices at these latitudes (*Menvielle and Berthelier*, 1991).

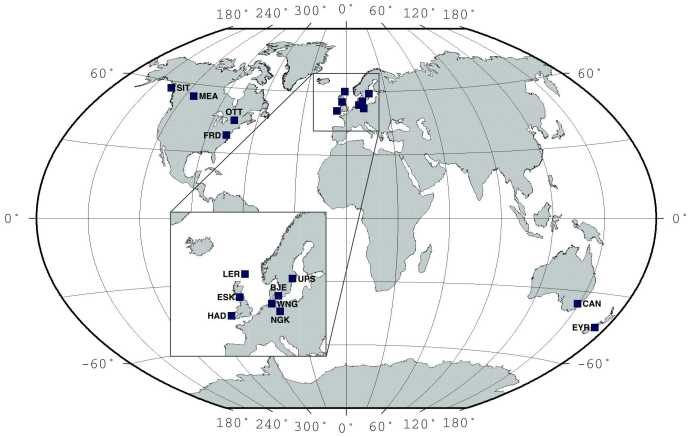

Figure 2.9: Locations of the Kp observatories

The K_p network has very little input from the Southern Hemisphere, and even in the Northern hemisphere has a highly non-uniform distribution. Despite this geographical bias the K_p index is very useful in geomagnetic studies. After being officially accepted by the Internation Association of Geomagnetism and Aeronomy (IAGA) in 1951 the series for K_p was extended back to 1932. This long timescale makes K_p particularly valuable for studies of long-term effects, such as solar cycle variations in magnetic activity. Other examples of studies using the K_p index include: studies of auroral boundary size (e.g., *Carbary*, 2005; *Milan et al.*, 2010), solar wind velocity (*Snyder and Neugebauer*, 1963) and interplanetary magnetic field parameters (e.g., *Barkhatov et al.*, 2008). The K_p index is one of the most commonly used indices in the selection of 'quiet' data (see Section 2.6.2 for more on data selection).

The K_p index is available from the International Service of Geomagnetic Indices[1], GeoForschungsZentrum (GFZ), the German Research Centre for Geosciences[2], and the World Data Centre for Geomagnetism (Edinburgh)[3].

2.4.2 D_{st}

Moos (1910) discovered the existence of a general depression of the horizontal magnetic field, recorded in magnetometer data at near-equatorial observatories. This signature is characteristic of a magnetic storm associated with the ring current, an

[1]ISGI: http://isgi.latmos.ipsl.fr/lesdonne.htm
[2]GFZ: http://www-app3.gfz-potsdam.de/kp_index/index.html
[3]BGS: http://www.wdc.bgs.ac.uk

Observatory	Code	Latitude	Longitude	Active
Northern Hemisphere				
Abinger	ABN	51.11°	359.37°	1932-1957
Hartland	HAD	51.00°	353.50°	1957-now
Agincourt	AGN	43.47°	280.44°	1932-1969
Ottawa	OTT	45.26°	284.27°	1969-now
Cheltenham	CLH	38.42°	283.12°	1932-1957
Fredericksburg	FRD	38.20°	282.60°	1957-now
Eskdalemuir	ESK	55.30°	356.80°	1932-now
Lerwick	LER	60.10°	358.80°	1932-now
Lovö	LOV	59.34°	17.82°	1954-2004
Uppsala	UPS	59.19°	17.21°	2004-now
Meanook	MEA	54.62°	246.65°	1932-now
Rude Skov	RSV	55.51°	12.27°	1932-1984
Brorfelde	BJE	55.60°	11.70°	1984-now
Sitka	SIT	57.06°	224.67°	1932-now
Wingst	WNG	53.80°	9.10°	1938-now
Witteveen	WIT	52.49°	6.40°	1932-1988
Niemegk	NGK	52.04°	12.41°	1988-now
Southern Hemisphere				
Amberley	AML	-43.09°	172.43°	1932-1978
Eyrewell	EYR	-43.42°	172.35°	1978-now
Toolangi	TOO	-37.32°	145.28°	1972-1981
Canberra	CAN	-35.18°	149.00°	1981-now

Table 2.3: The K_p network observatories

intensified current in the magnetosphere which circles the equatorial region (*Mendes Jr. et al.*, 2006). *Chapman* (1919) first used the name 'D_{st}' for this average storm-time signature of field disturbance, identifiable after the removal of a baseline and the regular daily variations. The D_{st} procedure was standardised by *Sugiura* (1964) using the 4 low-latitude observatories shown in Figure 2.10 and Table 2.4. D_{st} was officially adopted by IAGA as a standard activity index in 1969 (Resolution 2, p.123, in IAGA Bulletin 27, Madrid, 1969).

Unlike K_p, which is an index of mid-latitude activity, D_{st} is specifically aimed at monitoring the axi-symmetric part of magnetospheric currents in the horizontal component (*Menvielle and Marchaudon*, 2007). The disturbance field quantified by the D_{st} index is actually the sum of the external source field and its induced counterpart; D_{st} can therefore be separated into two indices representing the external, E_{st}, and induced, I_{st}, contributions (*Maus and Weidelt*, 2004).

Although D_{st} is assumed to represent the ring-current it has been proven that there are many current processes which contribute (*Campbell*, 1996). Additional contributions come from the dayside magnetopause current, the tail current, field-aligned currents and currents induced in the ground (*Burton et al.*, 1975; *Kamide*

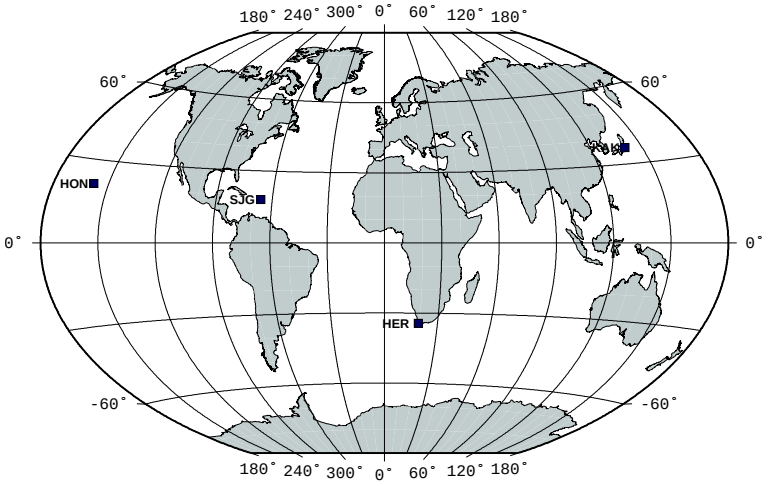

Figure 2.10: Locations of the D_{st} observatories

Observatory	Code	Latitude	Longitude
Hermanus	HER	-34.40°	19.22°
Kakioka	KAK	36.23°	140.18°
Honolulu	HON	21.32°	201.98°
San Juan	SJG	18.11°	293.85°

Table 2.4: Locations of the D_{st} observatories

et al., 1998; *Karinen and Mursula*, 2005). Despite this D_{st} is still a reliable indicator of the magnitude of magnetospheric activity at mid- to low-latitudes where the ring current dominates (*Mendes Jr. et al.*, 2006), and is one of the most widely used indices in research on the magnetosphere (*Love and Remick*, 2007). For example, D_{st} is particularly important for providing information on the development of magnetic storms and is also useful as a long term indicator of magnetospheric activity, having been calculated for dates from 1957. The D_{st} index has also been used in studies of solar wind parameters (*Murayama*, 1982) and investigations of the ring current (e.g., *Akasofu and Chapman*, 1961; *Davis and Sugiura*, 1966; *Kamide et al.*, 1998).

The D_{st} index is available from both the International Service of Geomagnetic Indices[4], and the World Data Center (WDC) for geomagnetism at Kyoto University, Kyoto, Japan[5].

2.4.3 Auroral Electrojet indices

Davis and Sugiura (1966) introduced the Auroral Electrojet (AE) indices as a measure of global electrojet activity in the auroral zone. Originally the AE indices were derived from transient variations in the horizontal (H) component observed at 7 stations, but are now based on data at the 12 observatories shown in Figure 2.11 and Table 2.5. The observatories are located at $61.7° - 70°$ geomagnetic latitude

[4]ISGI: http://www.wdc.bgs.ac.uk/catalog/master.html
[5]WDC Kyoto: http://wdc.kugi.kyoto-u.ac.jp/ae_realtime/index.html

and form a network distributed in longitude over the auroral oval (*Menvielle and Marchaudon*, 2007). The AE observatories are all in the Northern hemisphere due to the limited landmass in the auroral zone in the Southern Hemisphere; therefore, there will be times when the AE index does not provide a true representation of the auroral activity in the Southern Hemisphere and as such caution should be employed when using AE in global studies, and particularly in studies of the Southern Hemisphere (*Weygand and Zesta*, 2008).

To calculate AE, a base value is calculated at each observatory by averaging all the data for the 5 international quietest days in each month (*Tomita et al.*, 2011). This base value is then subtracted from each one-minute value for that month. The highest value (or the upper envelope) from the various observatories at each minute is the AU value, and AL the lowest (or lower envelope). AE is defined as the range of the data, AE = AU - AL and, for completeness, AO = (AU + AL)/2 (*Love and Remick*, 2007).

The AE index provides a measure of the overall activity of the electrojets, whilst the AU and AL indices are intended to represent the maximum intensity of the eastward and westward electrojets, respectively (*Tomita et al.*, 2011; *Menvielle and Marchaudon*, 2007). During periods of intense activity the auroral oval moves equatorwards; at such times the AE indices may fail to fully capture the signature of auroral phenomena, as the auroral electrojet observatories are all at standard auroral latitudes (*Menvielle and Marchaudon*, 2007).

The AE indices have been used to study many phenomena, for example: magnetic storms (e.g., *Nikolaeva et al.*, 2011), solar wind parameters (e.g., *Murayama*, 1982, and references therein), aurora X-ray total intensity (*Zhao and Tu*, 2005), the total energy dissipation in the Northern hemisphere (*Østgaard et al.*, 2002; *Spiro et al.*, 1982) and the characteristics of substorms (e.g., *Gjerloev et al.*, 2004; *Kullen et al.*, 2009). Efforts have also been made to calculate an equivalent AE index for the Southern Hemisphere, to extend the usefulness of the AE indices (*Weygand and Zesta*, 2008, and references therein).

The AE index is available from the World Data Center (WDC) for geomagnetism at Kyoto University, Kyoto, Japan[6].

2.4.4 Polar Cap index

The Polar Cap (PC) index provides a way to monitor geomagnetic activity over the polar caps, generated by the solar wind coupling with the magnetosphere. *Troshichev et al.* (1988) suggested the index following studies by *Troshichev et al.* (1979) and *Troshichev and Andrezen* (1985) and a review of polar magnetic disturbances and field aligned currents (*Troshichev*, 1982). Since then there have been further contributions to the PC index (e.g., *Vennerstrøm et al.*, 1991; *Stauning et al.*, 2006;

[6]http://wdc.kugi.kyoto-u.ac.jp/ae_realtime/index.html

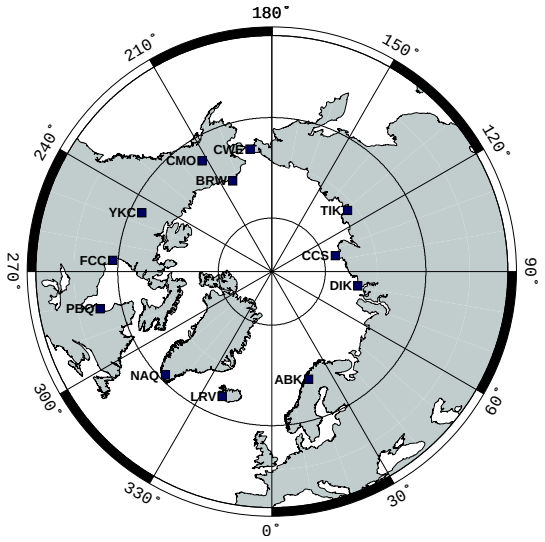

Figure 2.11: Locations of the AE observatories

McCreadie and Menvielle, 2010) but, as yet, PC has not successfully been endorsed as an official IAGA index.

PC is a dimensionless index, parameterised by season, UT and hemisphere, and is proportional to the intensity of the polar cap magnetic disturbance and calibrated for the merging interplanetary electric field E_m. There are two versions of the index, one for the Northern hemisphere and one for the Southern Hemisphere.

The Polar Cap North (PCN) index is derived from the near pole observatory Qaanaaq (Thule) in Greenland (12.53° colatitude). It is calculated at the Danish Meteorological Institute (DMI) and is available from their website[7]. The Polar Cap South (PCS) index is created using the Vostok observatory in Antarctica (at 168.45° colatitude). PCS is calculated at the Arctic Antarctic Research Institute (AARI) and is available on request[8].

Recently there have been efforts at creating a 'unified' PC index such that the derivation procedures for the two indices are consistent. Two papers have been published with regards to this: *Troshichev et al.* (2006) and *Stauning et al.* (2006). However, is has been shown by *McCreadie and Menvielle* (2010) that the PC index is still not unified and it remains a controversial topic within the IAGA scientific community.

There are many geophysical parameters which have a high degree of correlation with the PC index, including: auroral electrojet intensity (e.g., *Vennerstrøm et al.*, 1991), the cross polar cap voltage and polar cap diameter (*Troshichev et al.*, 1996; *Ridley and Kihn*, 2004), the ionospheric electric field in the near-pole region (*Troshichev et al.*, 2000; *Ridley and Kihn*, 2004), and the D_{st} index (*Stepanova et al.*,

[7]http://web.dmi.dk/fsweb/projects/wdcc1/pcn/pcn.html
[8]http://geophys.aari.ru/registration_pc/login.html

Observatory	Code	Latitude	Longitude
Abisko	ABK	68.36°	18.82°
Dixon Island	DIK	73.55°	80.57°
Cape Chelyskin	CCS	77.72°	104.28°
Tixie Bay	TIK	71.58°	129.00°
Cape Wellen	CWE	66.17°	190.17°
Barrow	BRW	71.30°	203.25°
College	CMO	64.87°	212.17°
Yellowknife	YKC	62.40°	245.60°
Fort Churchill	FCC	58.80°	265.90°
Poste de la Baleine	PBQ	55.27°	282.22°
Narssarssuaq	NAQ	61.20°	314.16°
Leirvogur	LRV	64.18°	338.30°

Table 2.5: The AE network observatories

2005; *Troshichev et al.*, 2011).

2.5 Measuring the Field

Early records of direct measurements of the magnetic field come mainly from ships' logs. These charted declination, and later, inclination for navigation purposes. There were also land based measurements in, for example, Paris and London, dating back to 1600 (*Kono*, 2007). Calculation of the vector field was made possible in the mid-19^{th} century with Gauss' development of a method for measuring absolute intensities (*Jackson et al.*, 2000). Gauss then went on to establish the first permanent magnetic observatories (*Whaler*, 2007).

Since those initial measurements the global observatory network has grown substantially. However, the distribution of observatories remains highly uneven which considerably hampers the determination of the global pattern of the geomagnetic field. The introduction of magnetic satellite data in the latter half of the 20^{th} century produced a more global and homogeneous coverage of data. Satellite data can also provide much more information on the magnetospheric field.

The launching of satellite magnetic surveys altered the role of observatories. Now, observatory data, typically with long and stable time series, can be combined with satellite data (when available), to provide good spatial and temporal coverage.

2.5.1 Observatories

Ground based magnetic observatories have been accurately monitoring the full vector magnetic field since the end of the 19^{th} century. There are approximately 200 observatories currently in operation (*Mandea*, 2006), with data available for around 300 (including those that have ceased operations) from the world data centre for geomagnetism in Edinburgh[9].

Observatory data reveal variations in the magnetic field on a wide range of time scales, from seconds to centuries, with the longest available time scale defined by the length of time an observatory remains in operation (*Love*, 2008). Some observatories operate for only a few years, whilst others have been recording measurements of the magnetic field for well over a century. Carefully combining nearby sites can also provide long time series, for example, the present site measurements at Hartland (1957-now) can be combined with Abinger (1924-1957) and Greenwich (1836-1926) to provide more than 170 years of data for the UK.

The position of magnetic observatories is largely determined by factors such as the availability of land, funding, local expertise and energy supply (*Macmillan*, 2007a). This leads to a highly uneven global distribution of magnetic observatories (shown in Figure 2.12), with dense coverage in some areas (e.g., Europe), and very few observatories in other regions (e.g., the oceans and Asia). To maintain accuracy in recording magnetic measurements it is important to avoid sources of

[9]WDC Edinburgh: www.wdc.bgs.ac.uk

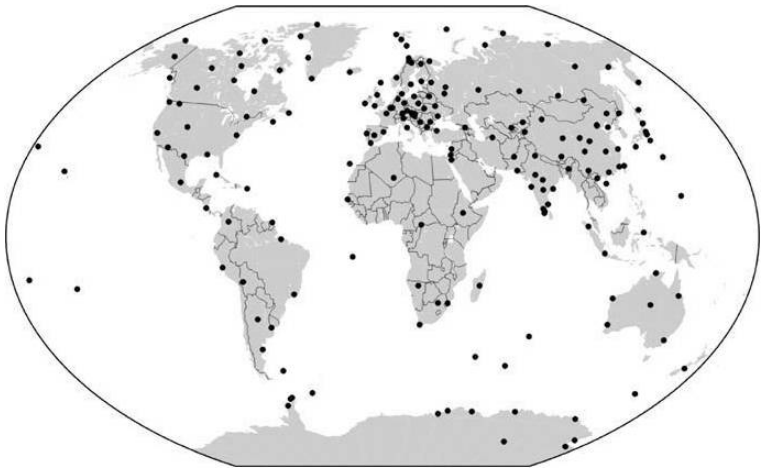

Figure 2.12: Locations of currently operating magnetic observatories, from (*Macmillan*, 2007a)

anthropogenic noise, so many observatories are in relatively remote locations, and many have had to move (with careful consideration for the continuity of the data) due to encroaching urbanisation (*Macmillan*, 2007a; *Love*, 2008).

Observatories typically use fluxgate magnetometers to make measurements of the three-component field variations with one-minute sampling or faster. These instruments are known as variometers because they measure the variation of the field whilst temperature, sources in the instrument and the stability of the mounting cause instrument drift (*Mandea and Purucker*, 2005). The variation of the field components, is measured continuously and corrected using baseline values. These baselines are established using absolute measurements of the field which are performed regularly by an observer (*Rasson*, 2007a; *Mandea*, 2006). The final, 'definitive', data are produced after this baseline, and any other required processing (for example, instrument effects like scaling factors, offsets, temperature responses and timing errors) have been applied; these data have an absolute accuracy of better than 5nT (*Love*, 2008; *Macmillan*, 2007a).

Originally, observatory data were provided as annual means, however, over the course of the last century the number of observatories providing hourly means increased markedly. A rapid increase in both the number of observatories and the number offering hourly means was prompted by The International Geophysical Year in 1957-58, as can be seen in Figure 2.13. In recent years improvements in instrument technology has enabled the production of one-minute data to increase significantly, and one-minute data are now a standard observatory product (*Olsen et al.*, 2007; *Love*, 2008). Some observatories even produce measurements of one-second data, for example, the Kakioka Magnetic Observatory in Japan has produced one-second data since 1983 (*Love*, 2008), and UK observatories have produced one second data

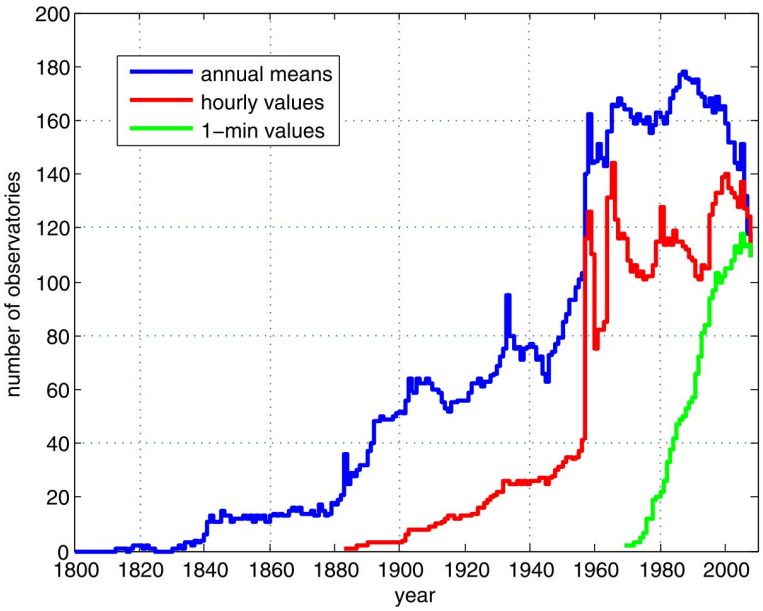

Figure 2.13: Number of geomagnetic observatories at 2008 providing annual means, hourly means and 1min values, from 1800 to 2008 from *Matzka et al.* (2010). The small drop in availability towards 2008 is in part due to the characteristic delay in producing definitive magnetic observatory data.

since 2000.

Hourly, daily, monthly and annual means are calculated from the one-minute data. Hourly, monthly and annual means are used in the determination of secular variation originating in the Earth's core, whilst one-minute data are important for studying the external magnetic field, particularly the daily variation and magnetic storms (*Mandea*, 2006; *Mandea and Purucker*, 2005). The quality of secular variation estimates depends upon both the quality of absolute measurements, and the distribution of global measurements. The uneven distribution of observatories leads to large uncertainties in the calculation of secular variation in some regions; for example, in the Pacific the uncertainty is on the order of hundreds of nT/year (*Mandea et al.*, 2000; *Mandea and Purucker*, 2005).

In 1987 the global network of digital observatories, INTERMAGNET[10], was founded, it currently has around 120 participating observatories in 43 countries. INTERMAGNET (*Inte*rnational *R*eal-time *Mag*netic Observatory *Net*work) exists to facilitate efficient data exchange between a network of observatories, by setting standard specifications for measuring, recording and distributing data. There are five Geomagnetic Information Nodes (GINs) in N America, Europe and Japan, which serve as data collection centres for real-time data (*Kerridge*, 2001). Before an observatory is accepted as an INTERMAGNET magnetic observatory (IMO), it has to demonstrate the compliance of its data with the standards set by INTERMAGNET.

[10]www.intermagnet.org

The definitive data and overall performance of an observatory are then continually reviewed by a committee of experts. INTERMAGNET extends technical support for both maintaining existing, and establishing new, observatories (*Rasson*, 2007b).

In addition to observatory data there are also ground-based variometer networks and magnetic repeat stations. At magnetic repeat stations observations of the Earth's magnetic field vector are made for a few hours (occasionally up to a few days) every few years (*Macmillan*, 2007b). They offer better spatial resolution than observatory data, although their distribution is still far from uniform (see Figure 2.14); repeat station locations are, in general, chosen on the basis of local need for mapping, rather than global coverage (*Matzka et al.*, 2010). Repeat stations are mainly used to track secular variation and can provide a cost-effective method of adding to observatory data for secular variation modelling (*Macmillan*, 2007b).

Variometer networks typically operate for a few years for space-physics research, and are generally maintained by universities and national government programs (*Love*, 2008). For example, SAMNET, the UK Sub-Auroral Magnetometer NETwork[11], is run by the Space Plasma Environment and Radio Science (SPEARS) group at the University of Lancaster, to gain information about the interactions within the Solar wind-magnetosphere-ionosphere system. Magnetometer networks can be used to provide indices describing the activity over the region they cover, for example, the IMAGE[12] electrojet indices IE, IL and IU based on the 31 magnetometers in the IMAGE (International Monitor for Auroral Geomagnetic Effects) network.

The SuperMAG initiative[13] is a collaboration of magnetometer networks, containing over 300 magnetometers. This collaborative approach allows global investigations of the ionosphere-magnetosphere system with standardised temporal resolution, coordinate systems and baseline subtraction (*Gjerloev*, 2009). This approach minimises possible errors (e.g., from confusing or even unknown coordinate systems) and makes it much easier to obtain global magnetic data. The SuperMAG collaboration also allows additional data products to be provided, for example, polar plots of ground magnetic perturbations and new magnetic indices.

2.5.2 Satellites

Satellites provide an opportunity to collect data with global coverage at a uniform precision and accuracy. The POGO satellite missions (1965-71) provided the first global survey measuring the intensity of the magnetic field (*Olsen et al.*, 2002). *Backus* (1970) soon realised that intensity measurements alone are insufficient to recover robust global geomagnetic field models, and the resulting model is formally

[11]SAMNET: http://spears.lancs.ac.uk/samnet/
[12]IMAGE: http://www.ava.fmi.fi/image/
[13]SuperMAG: http://supermag.jhuapl.edu/index.html

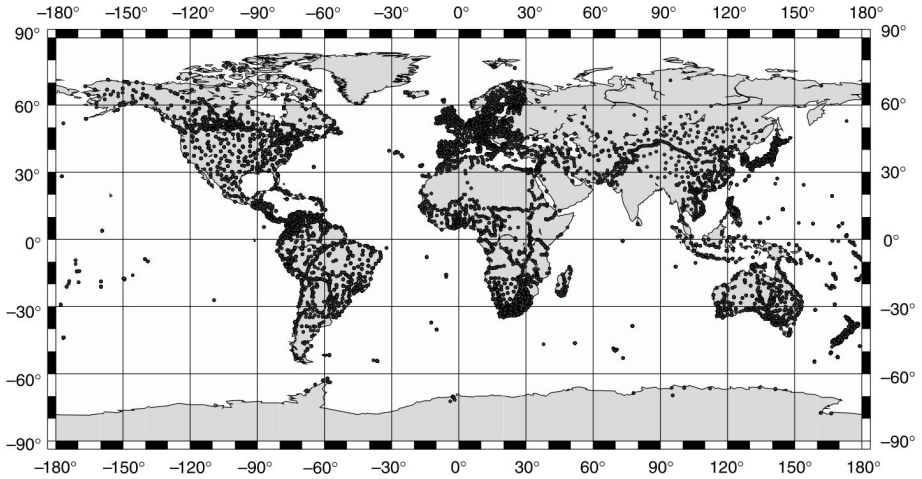

Figure 2.14: Global distribution of magnetic repeat stations since 1900, from (*Matzka et al.*, 2010)

non-unique. To derive models which do not suffer from this so-called 'Backus effect', at least some oriented (vector) data are required (*Olsen et al.*, 2002).

MAGSAT (Magnetic Field Satellite) was the first dedicated magnetic satellite to collect absolute vector data (*Rajaram*, 1993). Magsat operated for 6 months between 1979 and 1980, with a near polar, dawn-dusk orbit which allowed good spatial coverage. Not only did Magsat data provide the much needed vector data for main field modelling, it also provided new information about the ionosphere (*Purucker*, 2007).

The launch of Ørsted in 1999 marked the start of 'The Decade of Geopotential Field Research', an international effort to promote continuous gravity and geomagnetic field modelling in the near-Earth environment (*Friis-Christensen et al.*, 2008). During this time there were two additional geomagnetic mapping missions: CHAMP, and the Ørsted-2 experiment on board the SAC-C satellite. Table 2.6 contains a summary of information about these satellites, along with information on the upcoming Swarm 3-satellite mission.

The instrumentation used on Ørsted, which was an improvement upon the technology used on Magsat, has provided a model for the satellites that followed (*Olsen et al.*, 2007). Star cameras are used to determine the orientation of a triaxial fluxgate sensor and an absolute intensity instrument is used for calibration (*Mandea*, 2006). Both Ørsted and CHAMP measured the vector field to an accuracy of a few nT (*Mandea and Purucker*, 2005).

Ørsted is in an orbit with a perigee at 650km and apogee at 860km, inclined at 98° allowing mapping of almost the entire globe (*Mandea*, 2006). The local time of the orbit changes by 0.9min day^{-1}, so over the duration of the mission all local times have been sampled; the local time evolution of the Ørsted orbit is shown in

Satellite	Launch	Lifetime	Altitude (Km)	Inclination	Data type
MAGSAT	1979	1980	352-561	96.76°	Vector Scalar
Ørsted	1999	Still in Operation	630-880	98°	Vector Scalar
CHAMP	2000	2010	350-450	87.3°	Vector Scalar
SAC-C	2000	2005	700	98.2	Scalar
Swarm A+B	2013	-	450	87.4°	Vector Scalar
Swarm C	2013	-	530	88°	Vector Scalar

Table 2.6: Dedicated magnetic satellite missions

Figure 2.15 (top). Attitude data are essential for providing meaningful vector data, so at times when the star cameras provide no data (e.g., due to thermal problems, or blinding of the instrument by the sun, moon or Earth) there are no vector data. Figure 2.15 (bottom) shows the availability of the different types of data for the duration of the mission. Ørsted is currently still in operation, although since 2005 only measurements of field intensity are available. Ørsted data are accessible through the Ørsted Science Data Centre[14] and on the DTU Space ftp site[15].

CHAMP (Challenging Minisatellite Payload) was launched in 2000 to provide high precision gravity and magnetic field measurements. CHAMP's orbit, which was almost circular and inclined at 87.3° from the equator, allowed homogeneous, global data coverage of the Earth (*Mandea*, 2006). CHAMP moved much more rapidly through local time, compared to Ørsted, at 5.45min day^{-1}. Initially CHAMP was at 454km altitude, by May 2010 this had decreased to 290km and in September 2010 CHAMP re-entered the Earth's atmosphere (*Matzka et al.*, 2010).

A copy of the Ørsted package (but with a different absolute instrument), called Ørsted-2, was also launched in 2000, aboard the Argentinian SAC-C (Satellite Argentino de Observacion de la Tierra) satellite. SAC-C had a circular, Sun-synchronous orbit at 702km. It was fixed in local time and crossed the equator at 10:24 and 22:24 local time. Unfortunately a cabling problem prevented the measurement of any attitude data; therefore, no vector data are available from the SAC-C satellite (*Olsen and Kotsiaros*, 2011).

Satellite measurements of the magnetic field naturally filter out signals from local heterogeneities, so that only long wavelength regional anomalies are observed (*Rajaram*, 1993). Because the satellite is not at a fixed location it is very difficult to

[14]Ørsted Science data centre: http://www.dmi.dk/projects/oersted/SDC
[15]DTU Space: ftp://ftp.spacecenter.dk/data/magnetic-satellites/

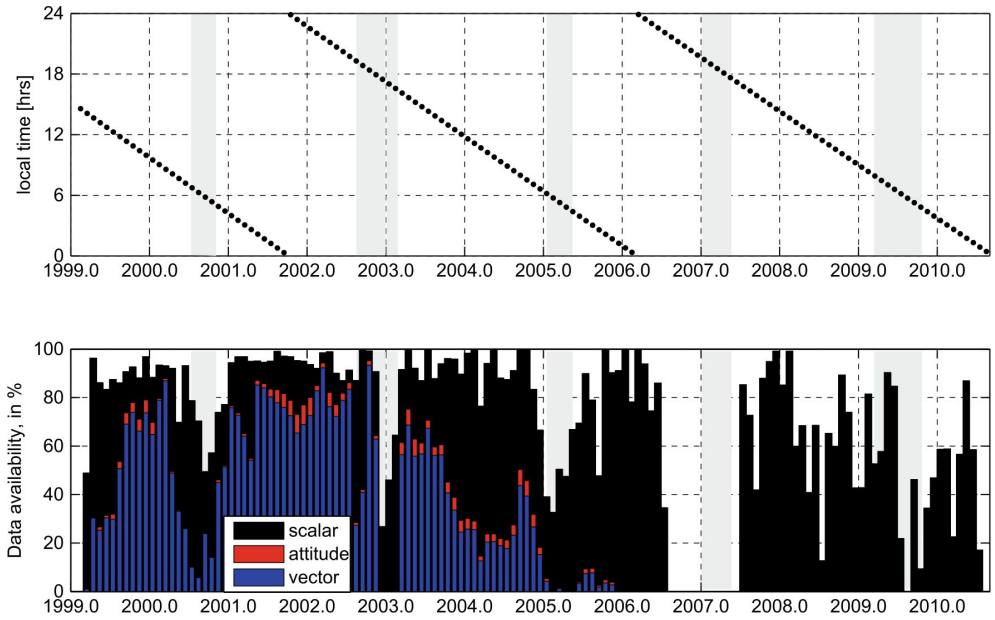

Figure 2.15: Local time evolution of the Ørsted orbit ascending node (top) and data availability as of September 2010, from *Olsen and Kotsiaros* (2011)

separate spatial from temporal variations (*Olsen et al.*, 2007). Contributions from external currents, which vary rapidly in both space and time, present the biggest challenge to the accuracy of present geomagnetic field models. One solution to this problem is to use multiple satellites to measure the field simultaneously over different regions of Earth (*Friis-Christensen et al.*, 2008).

The upcoming Swarm constellation mission (due for launch in 2013) will comprise of three satellites to provide the best ever survey of the geomagnetic field and its temporal evolution (*Olsen et al.*, 2007; *Friis-Christensen et al.*, 2008). Two satellites will fly side-by-side, at an initial altitude of 450km to measure the East-West gradient of the field. The third satellite will be at a higher altitude of 530km in a different local time to the lower pair (*Olsen et al.*, 2007). Over time the orbital planes of the upper and lower satellites will drift apart to allow a better recovery of the high-degree secular variation and mantle conductivity (*Mandea and Purucker*, 2005).

The Swarm mission aims to improve our understanding of the Earth's interior and the Geospce environment. The primary research objectives are:

- studies of core dynamics, geodynamo processes, and core-mantle interaction,
- mapping of the lithosphere magnetisation and its geological interpretation,
- determination of the 3-D electrical conductivity of the mantle,
- investigation of electric currents flowing in the magnetosphere and ionosphere.

The Swarm data will provide opportunities to improve existing, and create new,

models of the near-Earth magnetic field with higher resolution and better separation of sources, compared to single satellite missions (*Friis-Christensen et al.*, 2008).

2.6 Models and Modelling Techniques

Models of the geomagnetic field are highly important for studies for the core, lithosphere, mantle conductivity, space weather hazard and much more. However, the problem of extracting high quality data for creating geomagnetic field models is highly challenging. Measurements of the field contain a superposition of fields produced by many sources, including: the core field, the lithospheric field and field sources caused by currents in the magnetosphere and ionosphere, as well as currents induced by these fields (*Olsen et al.*, 2002). Separating these sources is not straightforward, and the issue is made more complicated by contributions from ionospheric sources peaking around 110km altitude, which behave like an internal field when measured from a higher satellite altitude (*Olsen et al.*, 2010a).

Ionospheric and magnetospheric fields are highly time variable, whilst the field of internal origin varies on much longer time scales, and the crustal field can be assumed to be constant (*Olsen et al.*, 2007). These different behaviours can, in principle, be exploited to separate them from internal (core and crustal) fields; measurements at different altitudes (i.e. ground observatories and satellites) should also distinguish between sources. However, when measured from a single, fast-moving satellite, it is difficult to distinguish between rapid temporal and rapid spatial variations (*Whaler*, 2007).

Models of the internal field are designed with different purposes in mind. For example, some models aim to provide a snapshot of the field at a specific time (e.g., *Olsen et al.*, 2000), whilst others aim to model the field over time (e.g., *Sabaka et al.*, 2004). Some models focus on the main field only (e.g., *Maus et al.*, 2010), whilst others aim to represent the crustal field (e.g., *Maus et al.*, 2007a). Whatever the purpose of the model it is essential it remains as uncontaminated as possible, with no input from external or unmodelled fields.

The most commonly used technique for representing the geomagnetic field is spherical harmonic analysis (e.g., *Olsen et al.*, 2007; *Mandea and Purucker*, 2005). In a source free region (where curl $\mathbf{B} = 0$) the magnetic field, $\mathbf{B}$, can be expressed in spherical coordinates (r, θ, ϕ) (see Appendix A.1 for information on coordinate systems) as

$$\mathbf{B}\left(r, \theta, \phi\right) = -\nabla V\left(r, \theta, \phi\right) \tag{2.1}$$

where V is a scalar potential. At the surface of the Earth $V = V_i + V_e$, where V_i and V_e represent the internal and external potential respectively. V can be expanded in spherical harmonics (*Mandea and Purucker*, 2005) to give:

$$V_i(r,\theta,\phi) = a\sum_{n=1}^{N_i^{max}}\left(\frac{a}{r}\right)^{n+1}\sum_{m=0}^{n}\left(g_n^m\cos(m\phi)+h_n^m\sin(m\phi)\right)P_n^m(\cos\theta) \quad (2.2)$$

$$V_e(r,\theta,\phi) = a\sum_{n=1}^{N_e^{max}}\left(\frac{r}{a}\right)^{n}\sum_{m=0}^{n}\left(q_n^m\cos(m\phi)+s_n^m\sin(m\phi)\right)P_n^m(\cos\theta) \quad (2.3)$$

where a is the radius of the Earth and r denotes the radial distance of the observation from the centre of the Earth. $P_n^m(\cos\theta)$ are the Schmidt-normalised, associated Legendre equations and (g_n^m, h_n^m) and (q_n^m, s_n^m) are the Gauss coefficients describing the internal and external sources for degree n and order m.

The Gauss coefficients (g_n^m, h_n^m) describe the field of internal origin, with sources in both the core and lithosphere. We note that these two sources cannot formally be separated further with potential theory. *Mauersberger* (1956) and *Lowes* (1966) demonstrated that the total mean square value, R, of the field can be broken up into the sum of individual contributions from each spherical harmonic degree, n, given by

$$R_n = (n+1)\left(\frac{R_e}{r}\right)^{2n+4}\sum_{m=0}^{n}\left[(g_n^m)^2+(h_n^m)^2\right] \quad (2.4)$$

for any value of $r \geq R_e$. As first demonstrated by *Langel and Estes* (1982), plotting this Mauersberger-Lowes spectrum indicates a 'knee' in the curve at degree 13-15 which separates the main field at low degrees from the crustal field at high degrees. An example of a power spectrum for a recent model can be seen in Figure 2.16. The longest wavelength (low degree) crustal fields remain undetermined because the core dominates at these wavelengths, and similarly the shortest wavelength (high degree) core fields are also undetermined.

When modelling with both observatory and satellite data, external fields must be taken into account; to do this there are two main modelling approaches. The first is the 'Comprehensive approach' (e.g., *Sabaka et al.*, 2002, 2004), where the major contributions to the field are parametrised and solved for simultaneously (see Section 2.6.1 for more on the comprehensive models). The second is to filter or average the data before modelling the field, in order to minimise the influence of un-modelled external fields on the model (e.g., *Maus et al.*, 2007a). In both approaches the data are generally selected to be from times which are as magnetically quiet as possible to reduce the relative magnitude of highly variable external field sources (*Whaler*, 2007), see Section 2.6.2 for more on criteria used in data selection.

The long term variation (secular variation) of the geomagnetic field can be computed with either observatory data alone or observatory data in combination with

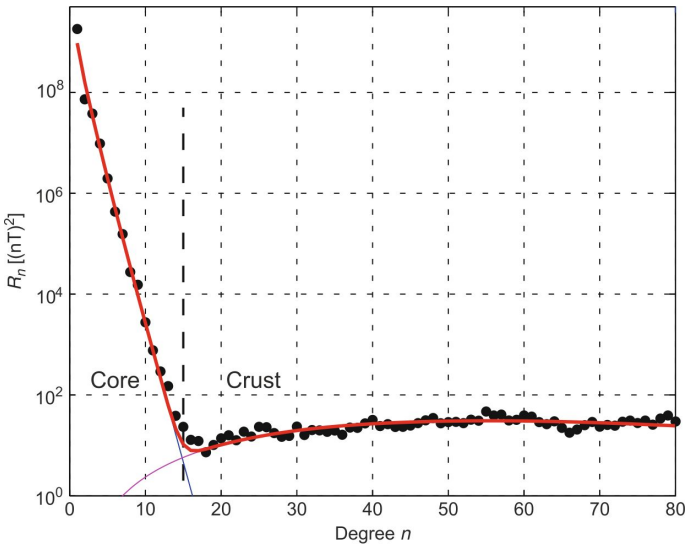

Figure 2.16: Spatial power spectrum of the geomagnetic field at the Earth's surface. Black dots represent the spectrum of a recent field model (Olsen et al. 2009; Maus et al. 2008) Also shown are theoretical power spectra (Voorhies et al., 2002) for the core (blue) and crustal (magenta) parts of the field, as well as their superposition (red curve), from *Olsen et al.* (2010c)

satellite data (*Olsen et al.*, 2002). Observatory monthly or annual means are the average of all data at a station, and so will contain contributions from the external field; however, it can be argued that the external signal will average out over time (*Wardinski and Holme*, 2006). This is not the case for satellite data, as satellites rarely return to exactly the same position (*Wardinski and Holme*, 2006). The long time series provided by observatory data is highly important for studies of secular variation, although unfortunately the signal will contain short wavelength crustal field and the global distribution of observatories is poor (*Wardinski and Holme*, 2006); satellite data are used, in addition to ground based measurements, to improve the global coverage.

2.6.1 Existing models

There are many geomagnetic field models, which exist for a range of purposes. This study uses CM4, CHAOS-2 and T01 described below. However, the most widely used model (both scientifically and in applications) is the IGRF, a relatively simple, predictive model of the magnetic field. Also described below are some other recent geomagnetic models of note.

IGRF

The International Geomagnetic Reference Field (IGRF) is published at 5 year intervals by IAGA, the International Association of Geomagntism and Aeronomy. It

is the product of a collaboration between many field modellers and data collection institutes. The IGRF is used for many purposes, both by scientists and commercial organisations. Initially one of the main uses of the IGRF was in regional magnetic surveys; by subtracting an internationally agreed global model from measurements it became much easier to combine adjacent surveys (*Macmillan and Finlay*, 2011). The IGRF is also used extensively in studies of the external magnetic field, with many ionospheric and magnetospheric models (e.g., *Tsyganenko*, 2002a) using the IGRF to describe the internal field. Calculations of geomagnetic coordinate systems now almost exclusively use the IGRF, using the centred dipole in particular (*Macmillan and Finlay*, 2011).

The IGRF model is designed to predict the field of internal origin both for an instantaneous epoch and the following 5 year interval. It was first computed in 1965, with all constituent main field models up to and including 1995.0, extending to maximum spherical harmonic degree n=10. After 1995 this limit is increased to n=13 due to the addition of high quality data from Ørsted and CHAMP (*Maus et al.*, 2005a; *Macmillan and Finlay*, 2011). The IGRF now extends back to 1^{st} January 1900 and provides a series of snapshots of the field at 5 year intervals. Between the models the magnetic field is assumed to vary linearly with time, hence the magnetic field for the interim periods can be derived using linear interpolation (*Olsen et al.*, 2007).

'Candidate models' are produced several months prior to the creation of the next IGRF, and submitted to IAGA. These models are then assessed by IAGA Working Group V-MOD (formerly working group V-8), and their evaluations are widely documented (for example, the 11^{th} Generation candidate models are described in Earth Planets Space, v62, issue 10, 2010). The coefficients of the IGRF are then derived by taking (weighted) means of the coefficients of selected candidate models (*Olsen et al.*, 2007; *Macmillan and Finlay*, 2011). All available data for the few years preceding the model are considered, including observatory data, satellite measurements and repeat stations, and even ship and aircraft surveys have sometimes been used (*Olsen et al.*, 2007).

The field of internal origin can be predicted 5 years into the future using the secular variation model (the $\left(\dot{g}_n^m, \dot{h}_n^m\right)$coefficients), which is published alongside the fixed-epoch model. Again candidate models of the average temporal variation of the field, in the few years preceding the model, are averaged and extrapolated to predict the field for the next 5 years (*Olsen et al.*, 2007).

When each model is released the previous IGRF is reassessed. Additional data that may have become available are considered, and if no new data are considered likely to emerge, the new definition of the model is called a Definitive Geomagnetic Reference Field (DGRF).

The most recent version is the 11^{th} Generation IGRF, which was finalised in

December 2009. It has a definitive main field model for epoch 2005.0, a main field model for epoch 2010.0, and a linear predictive secular variation model for 2010.0-2015.0 (*Finlay et al.*, 2010). The IGRF model coefficients are available from IAGA[16] and the World Data Centres.

The Comprehensive Model

The 'Comprehensive approach' uses a joint inversion of ground-based and satellite magnetic field measurements to co-estimate models of the internal, magnetospheric and ionospheric fields, along with their associated Earth-induced signals. Theoretically, this analysis of surface and satellite measurements together, allows parametrisation of all sources, provided the parameter set is treated consistently (*Mandea and Purucker*, 2005).

CM4, created by *Sabaka et al.* (2004), utilizes the comprehensive approach to produce a model of the fields associated with the major current sources in the near-Earth regime. CM4 is based on only quiet-time data (for more on data selection see section 2.6.2) to minimise the fast changing signals of external origin, associated mostly with disturbed times. This selection allows the remaining highly variable field to be described as an essentially dipolar magnetospheric field. This field can then be parametrized using the D_{st} index, and any remaining quiet-time magnetospheric and ionopsheric fields are then Sun-synchronous, producing regular temporal periodicities (*Olsen et al.*, 2007).

CM4 makes full use of observatory data, along with CHAMP scalar data and Ørsted scalar and vector data. It uses a degree and order 65 spherical harmonic expansion to estimate the core and lithospheric fields; the secular variation is represented by cubic B-splines through degree and order 13 (see *Sabaka et al.*, 1997). Figure 2.17 shows an example of how the different component fields add together in the comprehensive approach.

CHAOS

The CHAOS series of models (*Olsen et al.*, 2006; *Olsen and Mandea*, 2008; *Olsen et al.*, 2009, 2010a), are based on Ørsted, CHAMP and SAC-C satellite data. The original version of CHAOS determined the field up to spherical harmonic degree n=50 but subsequent versions go up to n=60, and CHAOS-4 now extends to n=100. The time dependence of the core field is expressed by spherical harmonic expansion coefficients up to n=20 (n=18 for CHAOS).

The near Earth magnetospheric sources (e.g., the ring current) are described in SM coordinates, whilst far magnetospheric sources (e.g., tail current) are described in GSM coordinates (for a description of coordinate systems see Appendix A.1), and the degree-1 external fields are co-estimated separately for every 12 hour interval. To

[16]IAGA IGRF: http://www.ngdc.noaa.gov/IAGA/vmod/igrf.html

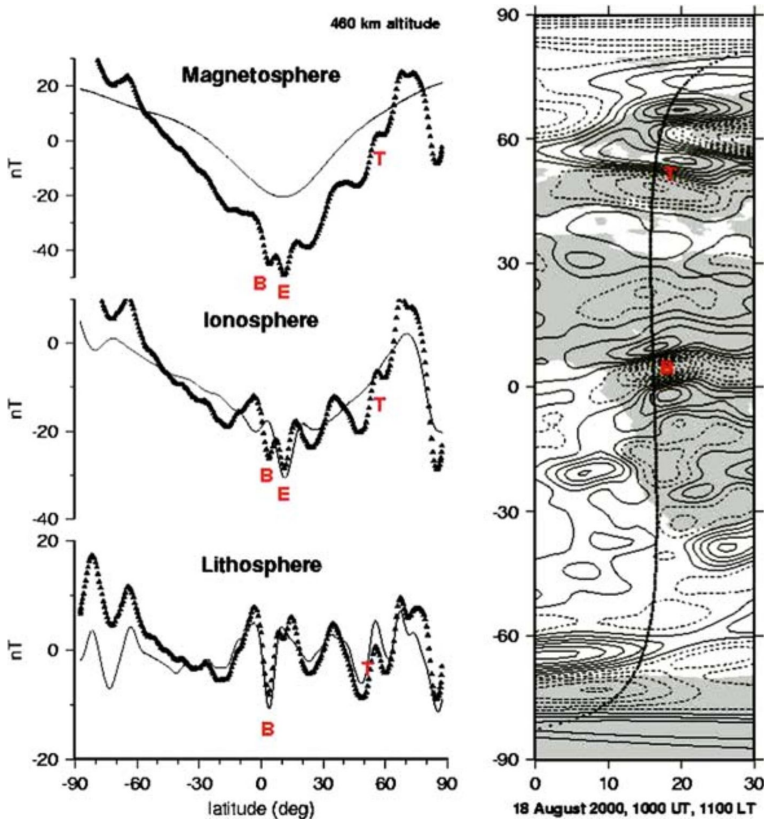

Figure 2.17: Residual progression after magnetic fields from the three main source regions are removed with the Comprehensive Model. This profile is for a pass on 18 August 2000 during magnetically quiet conditions. In each panel the black dots represent residuals to the main field (up to degree 13) plus all fields labelled in the panels above. The plot on the right is a contour map of the scalar field originating in the lithosphere (2nT contour intervals, dashed lines represent negative values). The letters on the plots represent the position of major anomalies, e.g., Bangui. See *Mandea and Purucker* (2005) for a full explanation of this figure.

avoid the inconsistency of using vector data that have been aligned using a different field model, the Euler angles describing the transformation from the magnetometer frame to the star-imager frame are co-estimated.

Tsyganenko

The Tsyganenko models (*Tsyganenko*, 1989, 1995, 1996, 2002a) have an entirely different focus to the models discussed above. Rather than aiming at describing the quiet-time, internal field, they are designed to represent the configuration of the magnetosphere, generally during active magnetic conditions.

The model used in this study, T01 (*Tsyganenko*, 2002a), is constructed using mathematical representations of a number of current systems in the magnetosphere. This includes realistic representations of the cross-tail current, the ring current, magnetopause current, region 1 and 2 field-aligned currents and the interplanetary

magnetic field penetration. The magnetopause shape (defined by the model of *Shue et al.*, 1998) is controlled by the solar wind pressure and ensures that all fields are confined within the magnetosphere. As the T01 model only represents the magnetospheric contribution to the magnetic field, the IGRF is used to represent the internal field.

MF

The MF series of models (e.g., *Maus et al.*, 2006b, 2007a, 2008) are aimed primarily at modelling the lithospheric magnetic field to high spherical harmonic degrees using CHAMP satellite data.

Early versions provided spherical harmonic coefficients up up to degree 80, which has been increased in subsequent versions; the latest version, MF7[17], models the lithospheric field to spherical harmonic degree 133 using CHAMP data between May 2007 and April 2010. With the resolution provided by this high degree representation the oceanic magnetic lineations are visible on a global scale (*Maus et al.*, 2008).

POMME

The POMME (POtsdam Magnetic Model of the Earth) series of models include a parametrisation of the main, crustal, magnetospheric and induced fields (*Maus et al.*, 2005b, 2006c, 2010). The static and time-varying magnetospheric fields are parametrised in Geocentric Solar-Magnetospheric (GSM) and Solar-Magnetic (SM) coordinates and include contributions from the Est/Ist indices and the Y component of the Interplanetary Magnetic field (IMF-By) (*Maus et al.*, 2006a).

The most recent version, POMME-7[18], extends to spherical harmonic degree 133 and is produced from CHAMP satellite vector magnetic measurements from July 2000 to September 2010, and Ørsted satellite total field measurements from January 2010 to October 2011.

GRIMM

The GRIMM (GFZ Reference Internal Magnetic Model) models are focused on describing the core magnetic field with better temporal resolution (*Lesur et al.*, 2008). GRIMM-2 is built using CHAMP vector data and observatory data from 2001.0 to 2009.5 (*Lesur et al.*, 2010). To allow separation between the fields generated by the ionosphere and field aligned currents, and between the fields generated by the Earth's core and lithosphere, full vector satellite data are used at all local times at high latitudes. This avoids data gaps during the polar summers, allowing the modelling of the core field with an unprecedented time resolution (*Lesur et al.*, 2010).

[17] http://geomag.org/models/MF7.html
[18] http://geomag.org/models/pomme7.html

BGS/G/L/0706

BGS/G/L/0706 is a global internal field model for spherical harmonic degree 60 derived from quiet-time Ørsted and CHAMP satellite data sampled between 2001.0 and 2005.0 (*Thomson and Lesur*, 2007). It describes the field to spherical harmonic degree 60 and includes a degree 15 core and piecewise-linear secular variation model. The main aim of the BGS/G/L/0706 model was to examine the value of new and old data selection algorithms for satellite data. This model also includes a new parametrisation of the large scale symmetric external field by replacing D_{st} with a new index called 'Vector Magnetic Disturbance' (VMD).

2.6.2 Data selection in modelling

When modelling the internal magnetic field, ideally only quiet magnetic data are wanted, to reduce the influence of fast changing external fields. It is particularly important to minimise the effect of ionospheric sources, which appear to be internal when measured at satellite altitude. Not only does selection limit noise in the data (by minimising the contributions from unmodelled fields), it also reduces the volume of data required; this can often result in over 90% of available data being discarded (*Whaler*, 2007). However, it is important not to be too restrictive with data selection criteria as the dataset needs to be large enough to allow the robust derivation of high degree and order spherical harmonic models.

As solar activity is the main factor affecting external magnetic fields, it is standard to use only night-time data (dawn-side data for MAGSAT), limiting contributions from ionospheric currents. It is also common to identify 'magnetically quiet' periods using magnetic indices (see Section 2.4 for a descritption of magnetic indices), and their rate of change. By selecting data using local time (LT) and geomagnetic indices the remaining temporally variable field can be parametrized with the D_{st} index. The quiet-time ionspheric fields and the remaining magnetospheric fields are then approximately fixed with respect to the sun, producing regular temporal periodicities (*Olsen et al.*, 2007).

At high latitudes there will still be contributions from ionospheric and magnetospheric field sources, even during magnetically quiet periods. In the polar regions, FACs, flowing between the ionosphere and magnetosphere, and the auroral electrojets, in the ionosphere, produce large contributions to the measured magnetic field. Field variations associated with these currents are seen predominantly in the vector components perpendicular to the main field. As such, the data are usually restricted to scalar only measurements at high latitude (*Olsen et al.*, 2002), where the magnetic field is approximately radial. In general models specify a cut-off value (usually either $\pm 50^\circ$ or $\pm 60^\circ$ dipole latitude), polewards of which only scalar data are used to minimise the effects of FACs (*Mandea and Purucker*, 2005). However, the auroral electrojets are not field-aligned so not all the unwanted signal will be

removed with this approach.

The K_p index is one of the most used criteria for identifying quiet magnetic data. Typically data will be required to have a K_p value $\leq 2o$ (or less) and also to have $K_p \leq 2o$ for the preceding three hour interval. The D_{st} index is also used for selecting data at times when the large scale magnetospheric field is quiet. A typical selection might use $|D_{st}| \leq 20nT$ and the rate of change of D_{st}, $|d(D_{st})/dt| \leq 2nT/hr$ (see Table 2.7). However, at high latitudes, it has been shown that K_p and D_{st} are not well suited for selecting quiet periods (*Ritter et al.*, 2004b). *Thomson and Lesur* (2007) found that their 'Vector Magnetic Disturbance' index, along with the longitude sector A indices, the IMAGE auroral zone index IE (*Viljanen and Hakkinen*, 1997) and the polar cap index PC proved much better at removing rapidly varying external field signals than K_p and D_{st}.

The Interplanetary Magnetic Field (IMF) is also an important data selection parameter, as the interaction of the IMF with the Earth's magnetic field influences magnetic disturbances in the external magnetic field. Some models simply require IMF-Bz to be positive (e.g., *Lesur et al.*, 2008), whilst others have constraints on both IMF-Bz and IMF-By (e.g., *Maus et al.*, 2010).

Table 2.7 shows examples of typical selection criteria for some recent models: CM4 (*Sabaka et al.*, 2004), CHAOS (*Olsen et al.*, 2006), MF5 (*Maus et al.*, 2007a) and POMME-6 (*Maus et al.*, 2010). It is intended to show the most common criteria; all the models have other data selection criteria in addition to those indicated. For example, CM4 excludes data if the magnitude of the X,Y,Z or F residual is greater than 100, 100, 50 or 40nT respectively, whilst CHAOS requires that, at polar latitudes, (polewards of 60°) the merging electric field, E_m, at the magnetopause is $< 0.8mVm^{-1}$.

As well as careful data selection, some modelling methods also remove remaining measurements made during active conditions by pre-filtering the data. This may include, for example, averaging surface measurements under quiet conditions to remove external magnetic fields, or filtering satellite data along-track to remove contributions from magnetospheric currents. Sometimes models of unwanted source fields are subtracted from the data before modelling (e.g., *Maus et al.*, 2006a, 2007a); there is, however, an inherent risk with this approach, as some of the wanted signal may be removed, whilst signals from other unmodelled sources may remain in the data (*Thomson and Lesur*, 2007).

In some cases data weighting is also applied, for example in the MEME model (*Thomson et al.*, 2010). This allows additional data to be included in the modelling process, improving geographical and temporal distribution, whilst keeping the noise level to a minimum.

Model	Vector limit	Kp	Dst	Sampling interval	LT
CM4	All latitudes used	Magsat: $\leq 1o$ C,Ø: $\leq 1+$ All:(t-3) $\leq 2o$	±20nT	60s	?
CHAOS	±60°	$\leq 2o$	$\frac{d(Dst)}{dt} < 2nT/hr$	60s	sun 10° below horizon
MF5	±55°	$\leq 2o$	no D_{st} selection	1s	20:00-05:00
POMME v6	±60°	no K_p selection	±30nT $\lvert\frac{d(Dst)}{dt}\rvert < 2nT/hr$ $< 5nT/hr$ at hl	20s	C 22:00-05:00 Ø 20:00-05:00 all LT at hl

Table 2.7: Data criteria for several recent models. This is not an exhaustive list of all the criteria used for each of the models but aims to represent the most commonly used criteria. C = CHAMP only, Ø= Ørsted only, hl = high latitude, and (t-3) indicates the preceding three hour interval.

Chapter 3

Testing Existing Models

As discussed in the previous chapter, the high latitude regions are most problematic for geomagnetic field modelling, particularly for internal field modelling. Here we investigate existing models with the aim of identifying their strengths and weaknesses, in terms of how well they resolve the field. We also study signals and patterns in the residuals (measured minus model) which provide information about the sources of 'noise', i.e. the unmodelled signals; understanding these sources will allow better selection of quiet data and should allow better recovery of the internal field.

3.1 Why are High Latitude Vector Data Valuable?

Currently, many geomagnetic field models only use intensity data in the high latitude regions rather than the full vector data. Here we use Green's functions to investigate how much more information could be gained from using vector data at high latitudes, particularly for measurements taken at satellite altitude.

The magnetic potential, V, in the mantle can be determined using the radial component of the magnetic field at the core mantle boundary (*Gubbins and Roberts*, 1983). Using a spherical coordinate system with its origin at the centre of the Earth, the magnetic potential, $V(r, \theta, \phi)$, can be calculated by forming the spherical harmonic expansion of Ω from B_r, assuming internal sources. We require the solution in the form

$$V(r, \theta, \phi) = \int_0^{2\pi} \int_0^{\pi} B_r(c, \theta', \phi') N(\mu) \sin\theta' d\theta' d\phi' \tag{3.1}$$

where $\alpha = \cos^{-1}\mu$ is the angle between the points (θ, ϕ) and (θ', ϕ'), the core surface is at $r = c$ and N is the Green's function for the Neumann problem:

$$N(\mu) = \frac{c}{4\pi}\left\{ln\left[\frac{f + x - \mu}{1 - \mu}\right] - \frac{2x}{f}\right\} \tag{3.2}$$

where $x = c/r$ and $f = (1 - 2x\mu + x^2)^{1/2}$,

A measurement of the field at the Earth's surface is a weighted average of the

value of the field at the core mantle boundary (CMB). The Green's functions describe how the field component samples the CMB, and therefore what information is given by the observation. The Green's function in Equation 3.2 can be separated into the Green's functions for the vertical and horizontal components (see *Gubbins and Roberts* (1983) for the full derivation). The function N_z describes how the measurements of the vertical component sample the core boundary:

$$N_z = \left(\frac{dN}{dr}\right)_{r=a} = \frac{b^2}{4\pi}\frac{(1-b^2)}{f^3} \tag{3.3}$$

where $b = c/a$, and $r = a$ at the Earth's surface.

For the horizontal components:

$$N_h(\mu) = \left(\frac{1}{r}\frac{\partial N}{\partial \mu}\right)_{r=a}\left(1-\mu^2\right)^{1/2} \tag{3.4}$$

where

$$\frac{1}{r}\frac{\partial N}{\partial \mu} = -\frac{x}{4\pi}\left[\frac{1-2x\mu+3x^2}{f^3} + \frac{\mu}{f\,(f+x-\mu)} - \frac{1}{(1-\mu)}\right] \tag{3.5}$$

N_z and N_h are plotted as a function of α in Figure 3.1. For N_z the maximum is immediately beneath the site and the minimum is at the antipodal point. N_h reaches a maximum at about 23° from the site. The radial field is dominated by the point directly below the measurement, but the highest contribution to the horizontal component is from the field 23° away. Therefore the horizontal observation provides information about the radial field some distance away, and therefore could provide information about the polar field for measurements made at high latitudes.

To investigate how important the horizontal components of satellite measurements are to geomagnetic field modelling, we have used the above formulae to test how the field at the Earth's surface is sampled at satellite altitude. Figure 3.2 shows the Green's functions for CHAMP (a) and Ørsted (b) altitudes. Again, N_z is a maximum directly beneath the measurement site, whilst N_h reaches its maximum at around 3° for CHAMP and 4° for Ørsted. For both satellites there is a crossover where the N_h component becomes larger than N_z; this occurs at around 5° for CHAMP and 7° for Ørsted.

This crossover is significant as it suggests the horizontal component is providing additional information about the field, that is not gained from the vertical component alone. Near the poles the magnetic field is approximately vertical with respect to the surface of the Earth. At high latitudes, models can therefore only gain information provided by the vertical component, when using only scalar data. Including more vector data at high latitudes would facilitate the inclusion of the horizontal components which are more sensitive to the field at approximately 5° (or 7° for Ørsted) away from the measurement point.

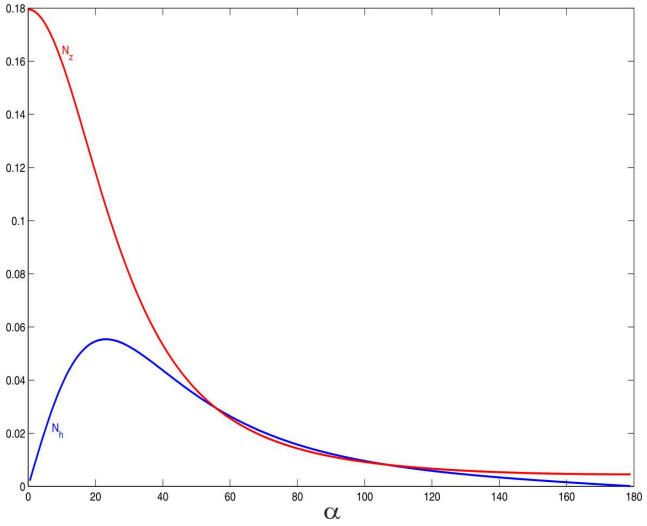

Figure 3.1: How components of the magnetic field measured at the surface sample the Earth's core field. Green's functions for vertical (N_z, red) and horizontal (N_h, blue) components plotted as a function of α. $\alpha = 0$ corresponds to the point on the core immediately below the site, $\alpha = 180$ that 180° away.

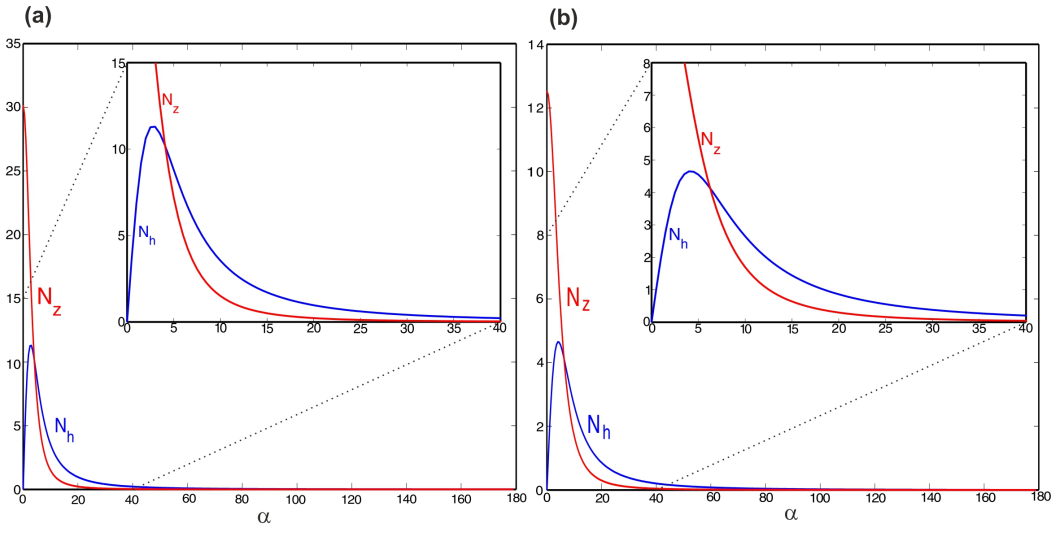

Figure 3.2: How measurements at satellite altitude sample the field at the Earth's surface. Green's functions for vertical (N_z, red) and horizontal (N_h, blue) components plotted against α where $\alpha = 0$ corresponds to a point on the core directly beneath the measurement site. For **(a)** CHAMP altitude (455km) and **(b)** Ørsted altitude (700km).

3.2 Data and Models Used in this Thesis

For the purposes of this investigation we use data from two satellites: Ørsted and CHAMP (see section 2.5.2 for more information about satellites), and three models: CHAOS-2 (*Olsen et al.*, 2009), CM4 (*Sabaka et al.*, 2004) and T01 (*Tsyganenko*, 2002a,b), which are described briefly in section 2.6.1. CM4 and CHAOS-2 are chosen because they are both quiet-time models, which model the all the sources of the near-Earth magnetic field, and so should have small residuals to quiet-time data. T01 is aimed at modelling the magnetosphere and is included here to investigate how well a model with such a different approach fits the data.

All the data used are night-side only, between 18:00 and 06:00hrs local time, to reduce ionospheric effects. However, there will clearly be some noise during local summer, when the polar regions are sunlit for most of the day. We have chosen four datasets from International Quiet Days[1], all with $K_p < 2$o, which are termed the 'quiet' datasets. These are for the following dates:

- 15th-16th March 2001
- 28th-29th June 2001
- 8th-9th September 2001
- 10th-11th December 2001

We also use four datasets from more disturbed times with K_p values up to 7o, in order to investigate how well the models perform at more disturbed times. These sets are termed the 'disturbed' datasets and are for the following dates:

- 20th-21st March 2001
- 9th-10th June 2001
- 29th-30th September 2001
- 30th-31st December 2001

3.3 Orbit by Orbit Analysis

3.3.1 Residuals to existing models

As an initial stage in testing the models the residuals (data minus model) for the quiet data are reviewed. Small residuals indicate that the models are performing well; where residuals are large the models are failing to fully represent the data.

[1]The International Quiet Days are classified as the five quietest days in each month based on three criteria: The sum of the eight Kp values, the sum of squares of the eight Kp values and the maximum of the eight Kp values. They are calculted by GFZ-Potsdam and available at http://www-app3.gfz-potsdam.de/kp_index/index.html

Figure 3.3 shows an example of the residuals for the night-side Ørsted orbits of the September dataset for the three magnetic field components, r, θ and ϕ in geographic coordinates (see Appendix A.1 for more information about coordinate systems). This figure clearly shows that at high latitudes ($\theta < 40°$ and $\theta > 140°$) there is a poor fit to the data, particularly for the θ and ϕ components. This is consistent with field-aligned currents (FACs) being responsible for most of the noise, as these components are approximately perpendicular to the field at high latitude.

There is some indication in these plots that there are a few orbits, even at high latitudes, which have small residuals. These orbits have the potential to provide 'quiet' vector data at high latitudes for use in modelling.

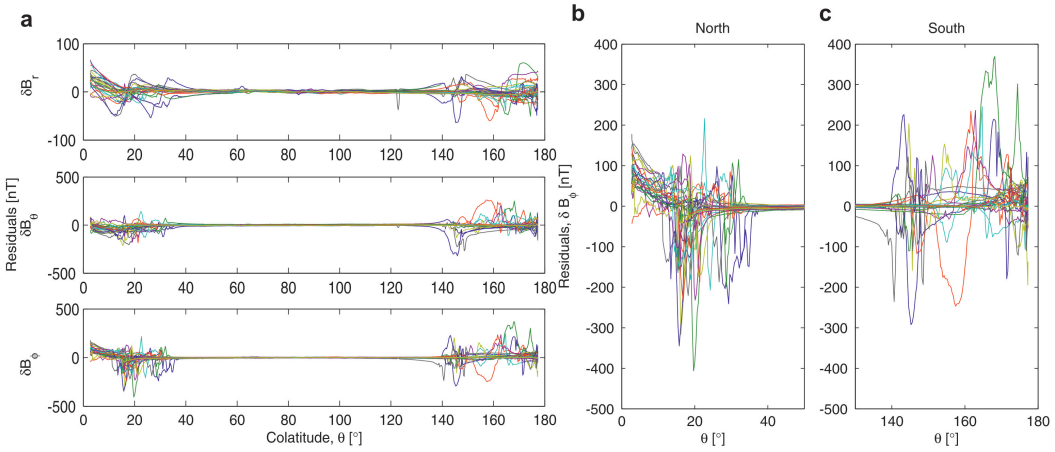

Figure 3.3: Residuals between Ørsted and CHAOS-2 for night-side orbits during 8^{th}-9^{th} September 2001. **(a)** all colatitudes in $\delta B\,(r, \theta, \phi)$, **(b and c)** δB_ϕ for the Northern and Southern polar regions respectively.

Averages of the residuals (for the T01 model) in 1° bins of colatitude, are shown for each of the four quiet datasets in Figure 3.4. These averages clearly show increased residuals near the poles which must contain un-modelled signal, rather than random noise, as they do not average out to zero.

3.3.2 Dealing with correlated errors

The attitude accuracy of the Ørsted star imager (SIM) is anisotropic causing correlated errors between the orthogonal components traditionally used for modelling. With this in mind we have projected the residuals into a new coordinate system defined by the magnetic field vector, $\mathbf{B}$, and the vector of SIM bore-sight, $\hat{\mathbf{n}}$. The magnetic residual vector $\delta\mathbf{B} = (\delta B_B, \delta B_\perp, \delta B_3)$ is constructed with δB_B in the direction of $\mathbf{B}$, $\delta B_\perp$ in the direction $(\hat{\mathbf{n}} \times \mathbf{B})$ and δB_3 in the direction $\mathbf{B} \times (\hat{\mathbf{n}} \times \mathbf{B})$ (see *Olsen et al.*, 2000, for more details). For the CHAMP data the $\hat{\mathbf{y}}$ vector is used in place of $\hat{\mathbf{n}}$. In this coordinate system most of the noise is in the perpendicular ($\delta B_\perp$) direction.

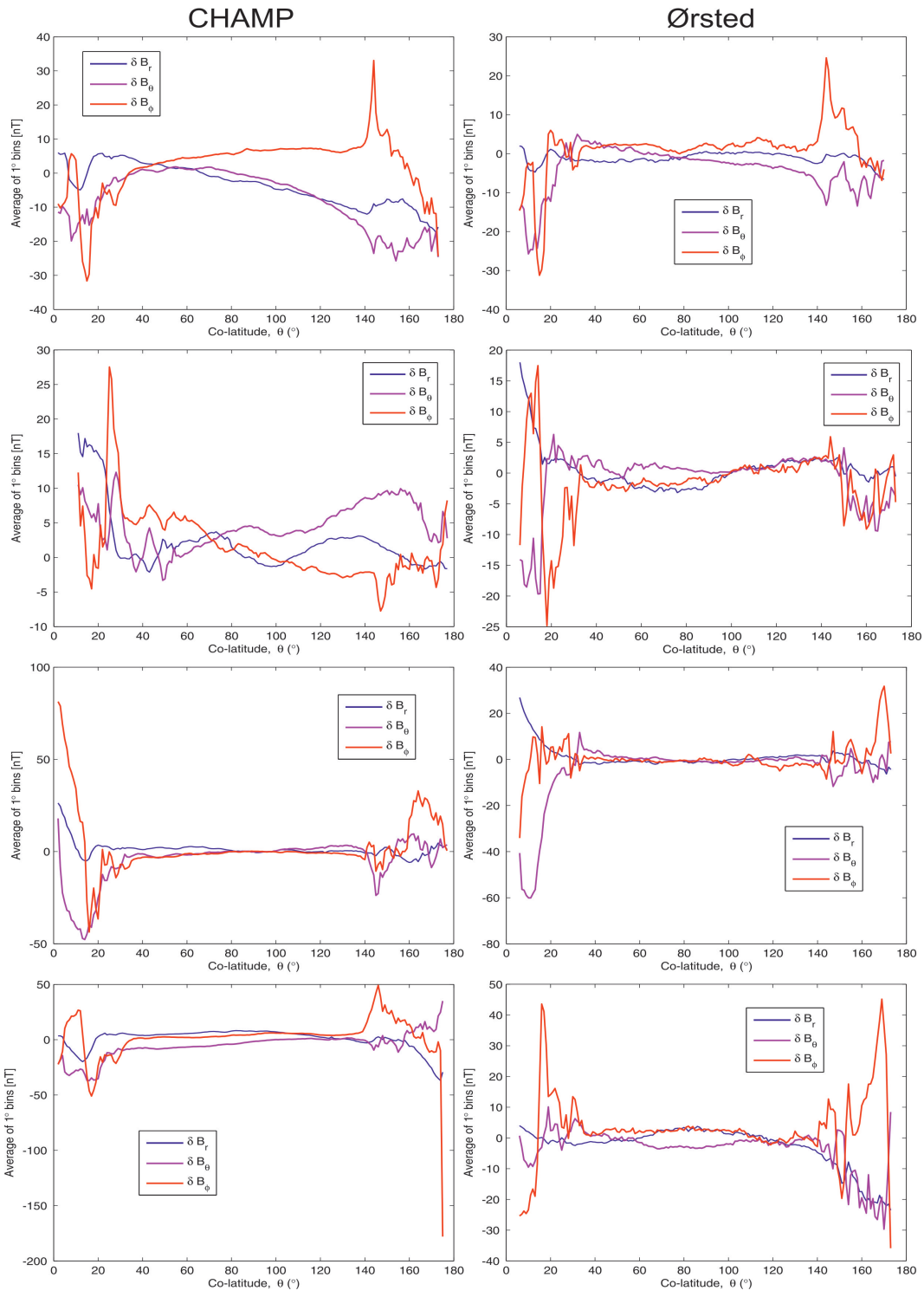

Figure 3.4: Residuals, averaged in 1° bins of colatitude, for the four quiet datasets in March (top row), June, September and December (bottom row) 2001. The left and right columns show the residuals between CHAMP and CHAOS-2 and Ørsted and CHAOS-2 respectively.

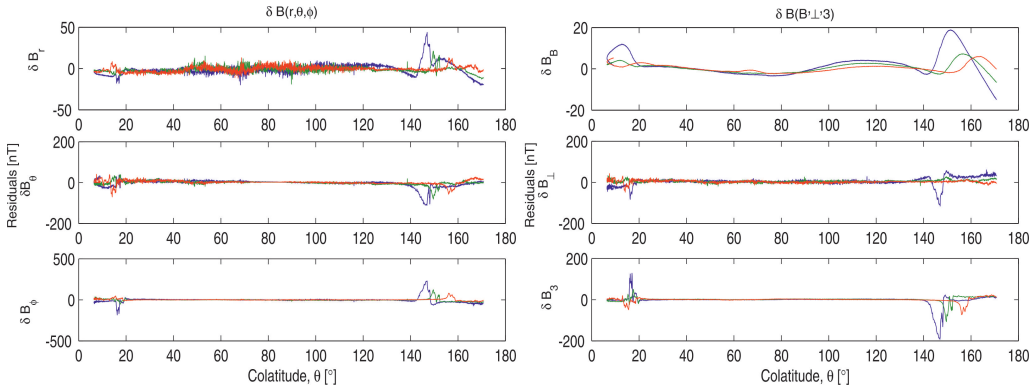

Figure 3.5: Residuals between Ørsted and CHAOS-2 for three consecutive orbits on the 15^{th} March 2001 in **(a)** $\delta B\,(r, \theta, \phi)$ and **(b)** $\delta B\,(B, \perp, 3)$

Figure 3.5 shows an example of the residuals for three consecutive orbits plotted in both $\delta B\,(r, \theta, \phi)$ and $\delta B\,(B, \perp, 3)$. The **B** direction is much smoother than the other directions and contains much less noise (note the different scale on the y axis).

Field aligned currents are aligned with the magnetic field and so the magnetic perturbations they cause are perpendicular to the field. Therefore, FAC signatures will not appear in δB_B so any signal in the residuals in this direction will have some other source. Many of the features we see are concentrated in the $\delta B_\perp$ and δB_3 and are most likely caused by FACs. However, there are some features which can be seen in all three directions, which may indicate a signal from auroral currents.

The residuals in this coordinate system have also been averaged in 1° bins of colatitude, over each of the two day datasets, and are shown in Figure 3.6. As for the residuals in (r, θ, ϕ), the regions close to the poles clearly have the largest residuals, even in the δB_B component.

3.4 Spatial Patterns

In order to investigate the spatial distribution we have averaged the data for each two-day period in bins of 1° longitude by 1° latitude. As discussed above, field-aligned currents cause magnetic perturbations in the directions perpendicular to the magnetic field. At high latitudes the radial component is approximately in the direction of **B** and as such is relatively unaffected by FACs; the θ and ϕ components are approximately perpendicular to the field and contain more FAC signal.

3.4.1 Geographical plots of the quiet datasets

In all months there is an enhancement of residuals in an oval centred on the geomagnetic pole, for both the Northern and Southern Hemispheres. This is most evident in the ϕ direction, with some indication also in the θ and radial directions. An example of this for CHAMP-CHAOS-2 residuals is shown in Figure 3.7. In this figure

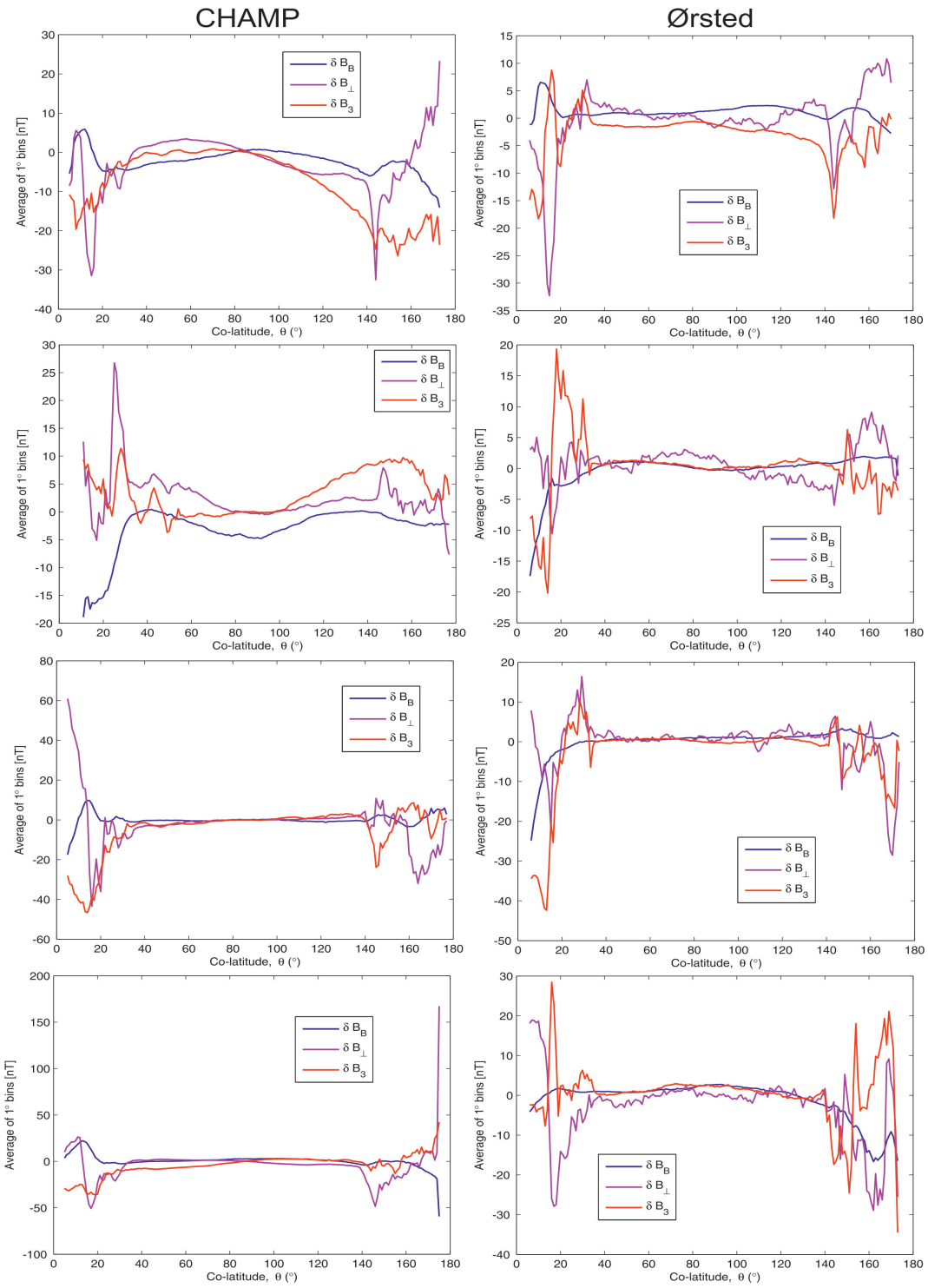

Figure 3.6: Residuals in the $\mathbf{B}\,(B, \perp, 3)$ coordinate system, averaged in 1° bins of colatitude, for the four quiet datasets in March (top row), June, September and December (bottom row) 2001. The left and right columns show the residuals between CHAMP and CHAOS-2 and Ørsted and CHAOS-2 respectively.

the oval is indicated by large negative (blue) residuals in the ϕ component in the Northern Hemisphere and large positive (red) residuals in the Southern Hemisphere. The other quiet datasets all show a very similar pattern, although the sign of the residuals is not always the same, and there are minor differences to the shape and size of the oval. We believe that the oval we see identified in the residuals is directly related to the auroral oval (see Section 2.3).

The residuals to CM4 look very similar to CHAOS-2 but are not shown here for brevity; the residuals to T01 show a similar size and shape oval, but a more complicated pattern of positive and negative residuals within the oval. The residuals to Ørsted show the same overall shape as for CHAMP for all three models, however, there is more variability in the size of the oval and the sign of the residuals.

There are also some seasonal differences between the two hemispheres; for the December dataset, when the Northern Hemisphere is in winter, the residuals are smaller overall in the North than the South. This is not surprising as at this time of year the Southern polar region will be sunlit almost all the time, so an increase in activity is to be expected. In June the reverse is true, the residuals in the Southern Hemisphere are smaller overall than in the Northern Hemisphere.

3.4.2 Geographical plots of the disturbed datasets

An example of these averaged residuals for a more disturbed dataset (K_p up to 7o) can be seen in Figure 3.8. In general the plots for the more disturbed datasets have larger residuals than the quiet data (as is to be expected), but still give an indication of the oval, along with enhanced residuals over the polar cap. The oval is still most evident in the ϕ component, although the θ and radial components now also show this auroral signature more clearly. The plots for the other months all show very similar patterns with the largest residuals within the oval.

The oval is again centred on the geomagnetic pole, but is now wider, with the outer boundary closer to the equator than for that of the quiet plots. This is to be expected as the auroral oval is known to expand as activity increases (e.g., *Holzworth and Meng*, 1975). The fact that most of the large residuals are still confined to the oval is encouraging, as it indicates that the models are still valid to some extent even at more disturbed times.

3.4.3 Full field residuals

As discussed previously (see Section 2.6.2), at high latitudes only scalar values are included in the modelling process. This is to avoid the highly variable magnetic contributions from FACs; as such, the residuals for the field intensity would be expected to be small. However, as can be seen in Figure 3.9 we do see enhanced residuals near the poles and in the auroral oval, particularly for the CHAMP satellite. These residuals are caused by the auroral electrojets which are not field-aligned, and

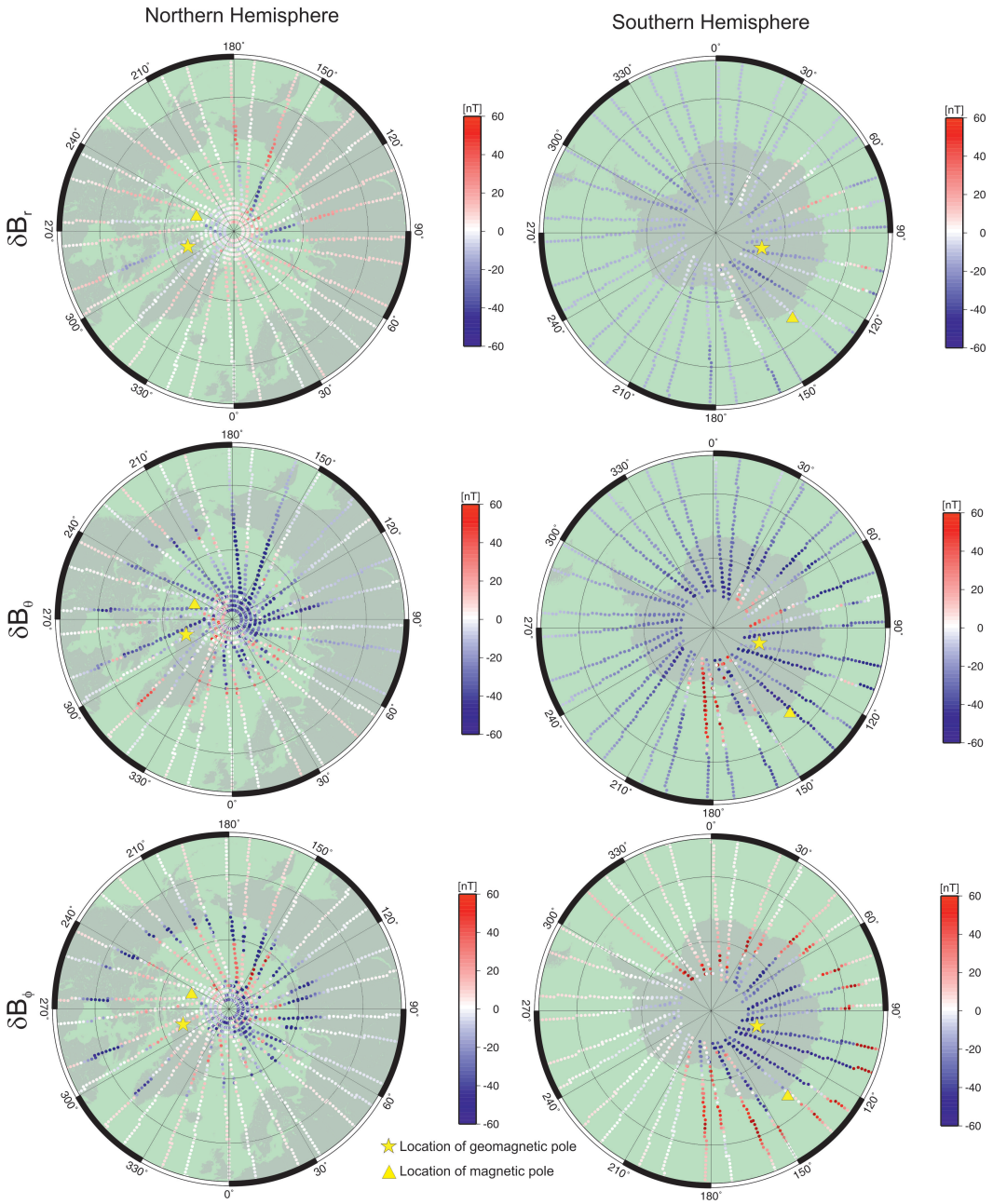

Figure 3.7: CHAMP-CHAOS-2 residuals averaged in bins of1 ° latitude by 1° longitude for $10^{th} - 11^{th}$ December 2001. Plots are centred on the geographic North (left) and South (right) poles, with lines of latitude 15° apart. The positions of the geomagnetic (star) and magnetic (triangle) poles in 2001 are shown in yellow (see Appendix A.2 for definitions of poles).

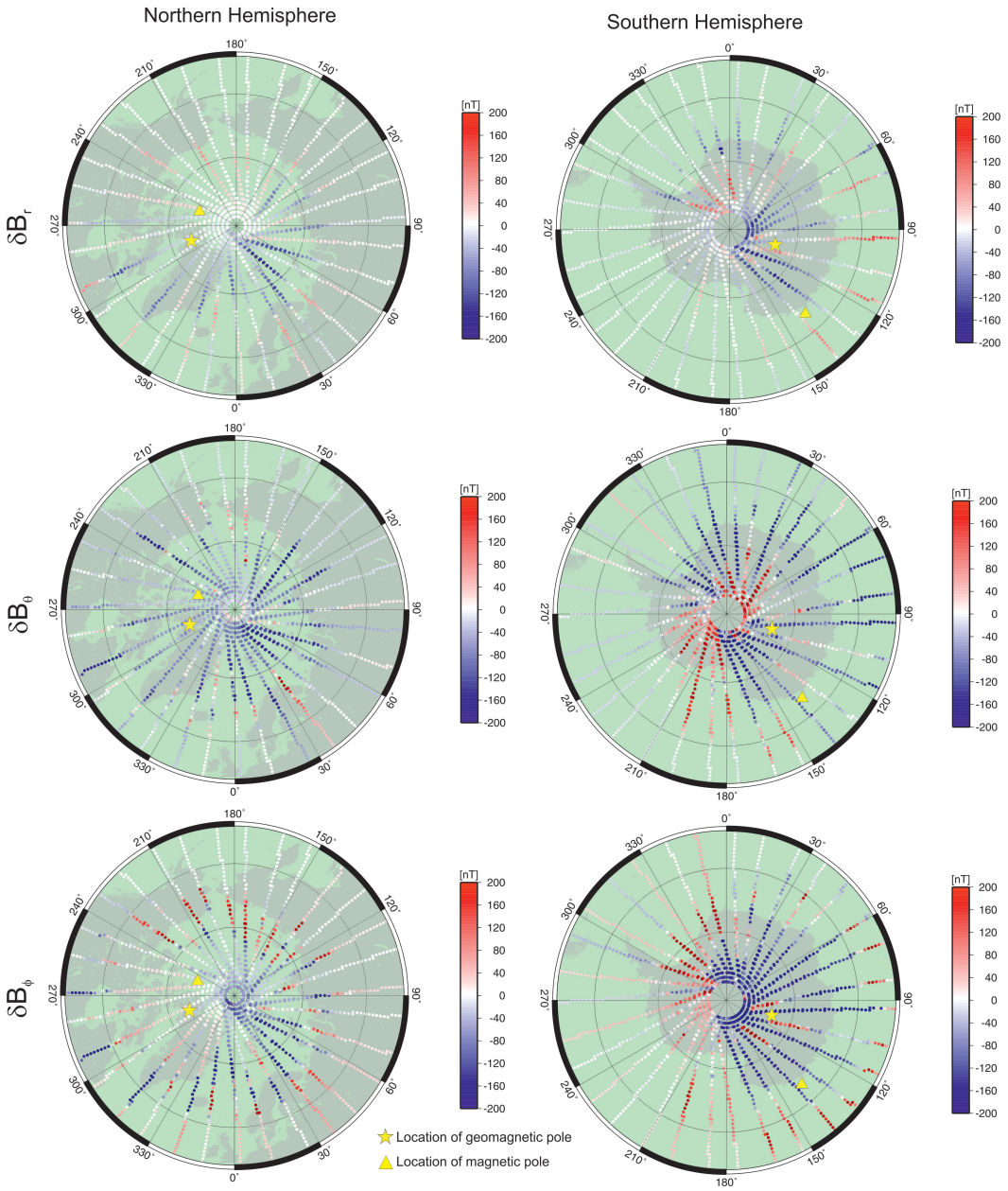

Figure 3.8: CHAMP-CHAOS-2 residuals averaged in bins of 1° latitude by 1° longitude for the disturbed dataset, $30^{th} - 31^{st}$ December 2001. Plots are centred on the geographic North (left) and South (right) poles, with lines of latitude 15° apart. The positions of the geomagnetic (star) and magnetic (triangle) poles in 2001 are shown in yellow.

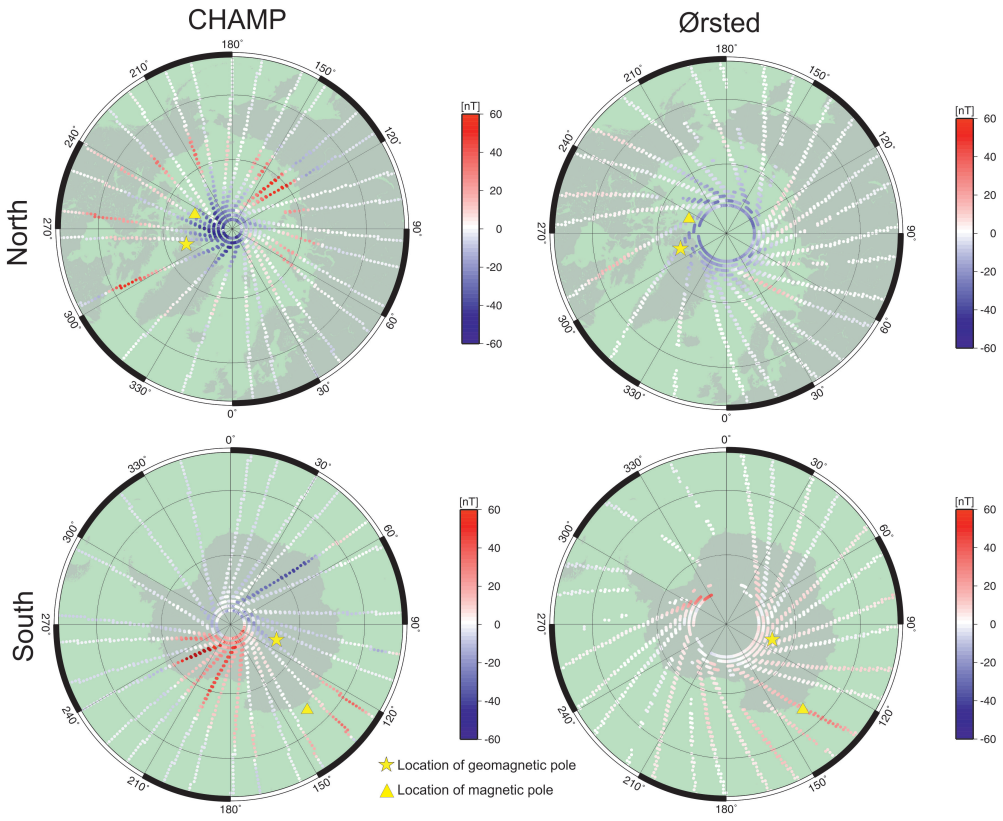

Figure 3.9: Scalar residuals averaged in bins of 1° latitude by 1° longitude for CHAMP minus CHAOS-2 (left) and Ørsted minus CHAOS-2 (right) for the 8^{th} – 9^{th} September 2001. Lines of latitude are at 15° spacing. The positions of the geomagnetic (star) and magnetic (triangle) poles in 2001 are shown in yellow.

will therefore have some signature in the scalar data. For Ørsted the field intensity residuals are smaller and much more localised to the geographic pole. As Ørsted is at a higher altitude than CHAMP the amplitude of the auroral oval signature is likely to have reduced sufficiently that it is no longer visible in the residuals.

At more disturbed times the residuals in the F field are much larger, and the Ørsted residuals now also show a more widespread distribution, as can be seen in Figure 3.10. The enhanced residuals are still predominantly confined to the oval and polar cap.

3.5 Standard Deviations

Signals from external sources are highly time variable, so we would expect the residuals associated with these sources to also be highly variable. To investigate this we have calculated the standard deviations of the residuals for the same 1° bins of latitude and longitude as for the averages discussed previously.

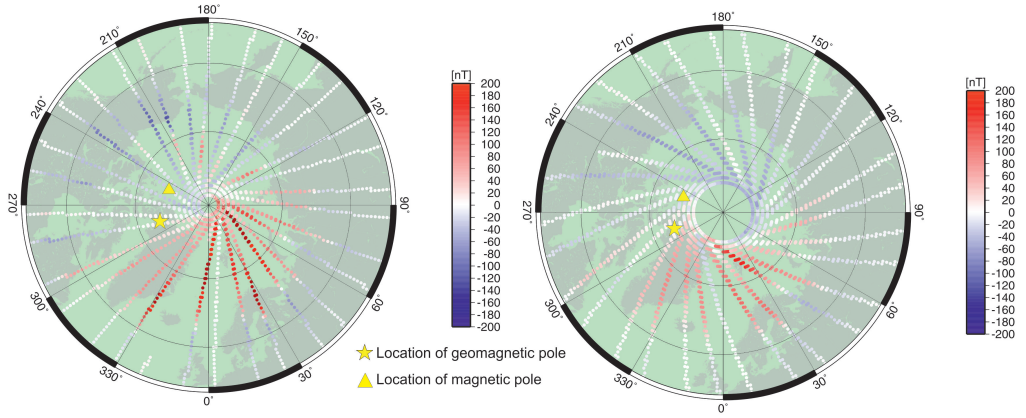

Figure 3.10: Scalar residuals averaged in bins of 1° latitude by 1° longitude for CHAMP minus CHAOS-2 (left) and Ørsted minus CHAOS-2 (right) for the 29^{th} – 30^{th} September 2001. Lines of latitude are at 15° spacing. The positions of the geomagnetic (star) and magnetic (triangle) poles in 2001 are shown in yellow.

3.5.1 Standard deviation of the quiet datasets

For the CHAMP residuals the oval is picked out quite clearly as enhanced standard deviation values, as can be seen in the example in the left hand column of Figure 3.11. As for the averages, the oval is most evident in the ϕ direction, with a clear oval signature also seen in both the θ and radial directions. The Ørsted plots show much more variability across the pole as a whole and the auroral oval is much less well defined than for CHAMP. In the Ørsted plots in Figure 3.11 there are also increased standard deviation values very close to the pole which are not seen in the CHAMP plots. This example is representative of all the datasets investigated; the oval is identifiable in the standard deviation plots for all months.

3.5.2 Standard deviation of the disturbed datasets

The disturbed data, Figure 3.12, show a similar pattern of standard deviation to the quiet residuals. However, the standard deviation values are larger and the oval signature has increased in size. The auroral oval is more obvious in the Ørsted residuals for the disturbed data, however, it is still not as clearly defined as for CHAMP. The auroral oval does appear more clearly if the scale of the Ørsted plot is increased (not shown here), however, there is still more variability over the whole polar cap in the Ørsted data.

3.6 Model Comparison

All three geomagnetic field models in this study show similar residuals, even though they are constructed using different methods. We would expect T01 in particular to perform very differently as it is designed primarily to describe the large scale

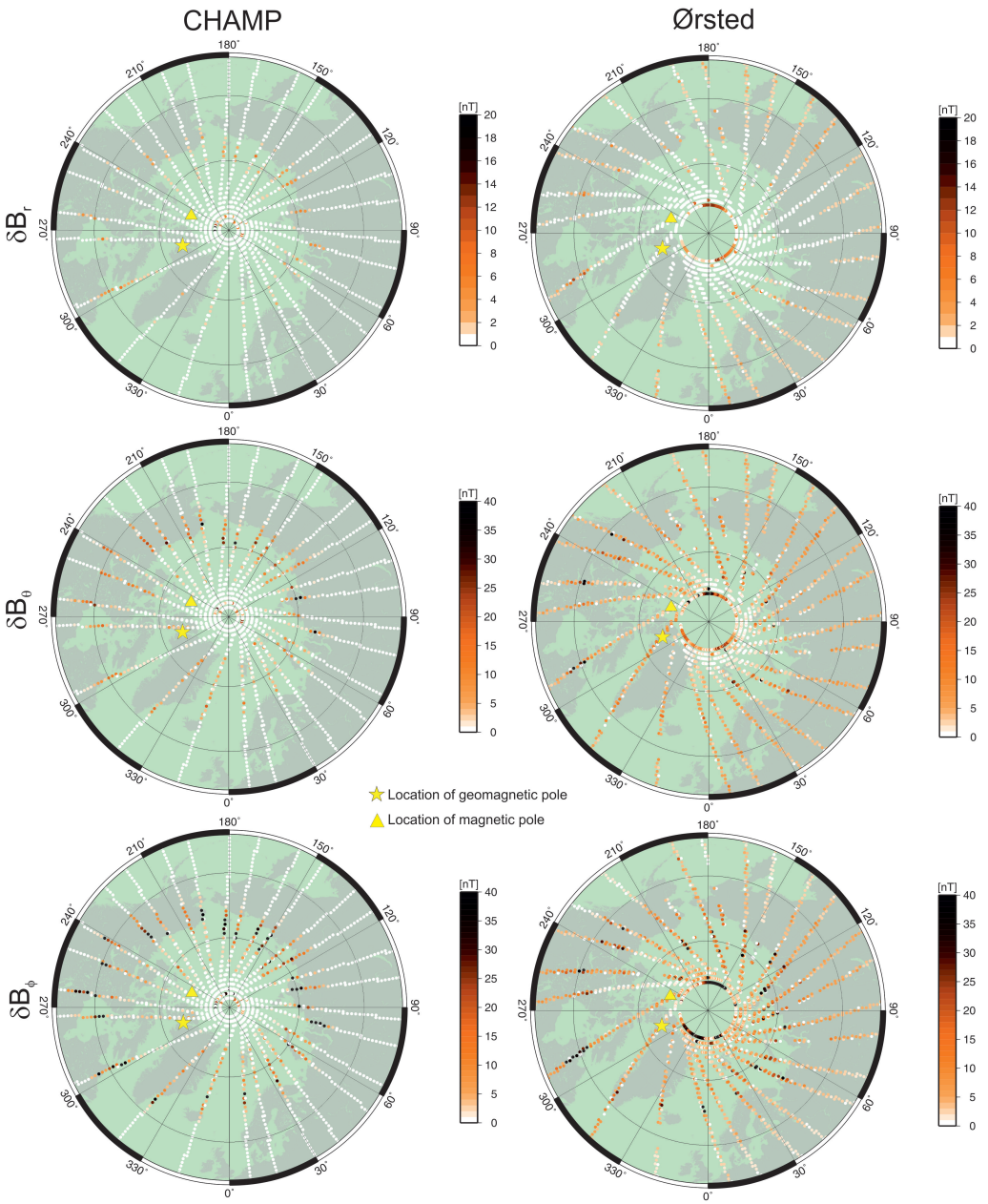

Figure 3.11: Standard deviations of the residuals, CHAMP (left) and Ørsted (right) minus CHAOS-2, of bins of 1° latitude by 1° longitude on $8^{th} - 9^{th}$ September 2001. Plots are centred on the North pole, with lines of latitude at 15° spacing. The scale is saturated (black dots indicate standard deviation >40nT) to allow smaller scale detail to be seen.

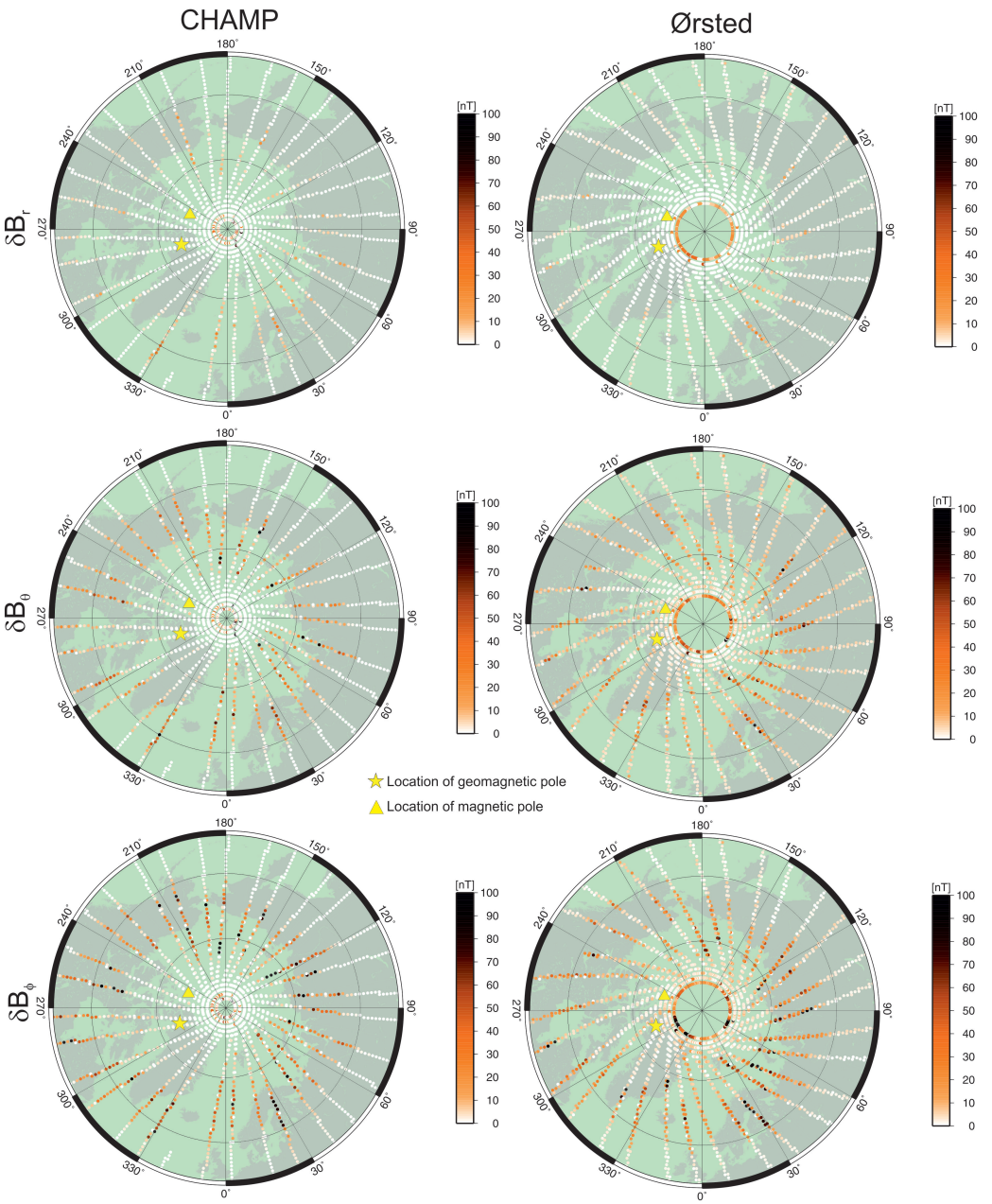

Figure 3.12: Standard deviations of the residuals, CHAMP (left) and Ørsted (right) minus CHAOS-2, of bins of 1° latitude by 1° longitude on $29^{th} - 30^{th}$ September 2001. Plots are centred on the North pole, with lines of latitude at 15° spacing. The scale is saturated (black dots indicate standard deviation >100nT) to allow smaller scale detail to be seen.

magnetosphere and is not a 'quiet-time' model like the CHAOS and CM4 models. Here we investigate whether one model performs 'better' than the others, or if there are deficiencies which are common to all the models.

3.6.1 Orbit by orbit

Figure 3.13 shows the residuals, for a representative orbit, between CHAMP and the three models, for both coordinate systems. There are two versions of T01 included which use different models (CHAOS-2 and IGRF) to describe the internal field. There is a lot of similarity between the models, particularly CHAOS-2 and CM4, although the residuals with respect to T01 often have a larger magnitude than the other models.

For most components the two versions of T01 plot almost on top of one another at this scale; however, in the radial and **B** directions the version of T01 with the CHAOS-2 internal model plots much closer to CM4 and CHAOS-2 than the standard T01 model (IGRF internal). This indicates that the internal model (i.e. IGRF) is not as detailed as CHAOS-2; it also shows that the external model in T01 is a poorer overall fit to the data as the residuals are still consistently larger than CHAOS-2 and CM4, even with a more sophisticated internal field model.

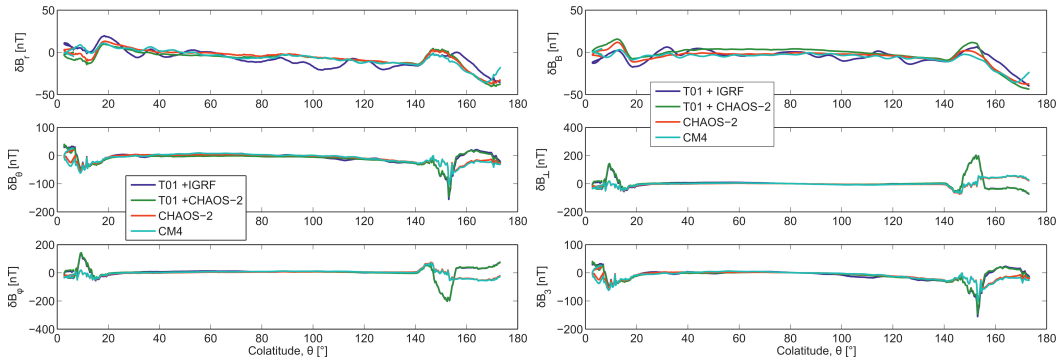

Figure 3.13: Comparison of the residuals between CHAMP data and four different models for an individual orbit in the geographic (r, θ, ϕ), left, and $(B, \perp, 3)$ coordinates, right. T01+IGRF (blue) and T01+CHAOS-2 (green) are the residuals for the T01 model where the IGRF or CHAOS-2, respectively, represents the internal field.

3.6.2 Rms misfit

To test for a 'best' model the rms misfit of each orbit is taken for all the models. Figure 3.14 is a plot of rms against orbit number of the March dataset, for the residuals between CHAMP and each of the models. The figures for other months and for Ørsted are not included here but show a similar result. The T01 model clearly has the worst overall fit to the data; however, it is harder to draw a clear distinction between CHAOS-2 and CM4.

To investigate the rms values further, the orbits were separated into three sections: North pole ($\theta < 50°$), low-latitudes ($50° < \theta < 130°$) and South pole ($\theta > 130°$), which can be seen in Figure 3.15. The low-latitudes have consistently low rms values for the θ and ϕ components. In the radial component, r, the low latitudes do not always have the lowest rms values, although the rms values for all three latitude sectors are smaller for r than the other components. In this example the southern segment is noticeably poorer in r; however, the northern and southern segments are relatively evenly matched in θ and ϕ, with the northern segment performing marginally better in θ.

In the March and September datasets, the rms values for the north and south segments are comparable for all three models and both satellites; in September the northern section is marginally better in the ϕ component. In December, when the Southern Hemisphere has its summer, the southern segment has higher rms values in general than the north. In June during northern summer the reverse is true, with the rms values clearly worse for the north. All the models show these trends, with no model noticeably performing better for either pole. This suggests that all the models are missing at least some physics in the polar regions.

3.6.3 Spatial model comparison

For a more direct comparison of the models we have taken differences between the field estimates for each of the three models for 15th-16th March; Figure 3.16 shows the differences between CHAOS-2 and T01 (left column) and CHAOS-2 and CM4 (right column). T01 again shows the most difference to the other models, and the difference plots give some indication of the auroral oval, particularly in the ϕ direction. The difference between CHAOS-2 and CM4 is much smaller and shows no obvious pattern.

At more disturbed times (not shown) the differences between the models become larger, and extend further from the pole. The differences are again mostly associated with the auroral oval and polar cap, and the difference between CHAOS-2 and CM4 is still smaller than the difference between CHAOS-2 and T01.

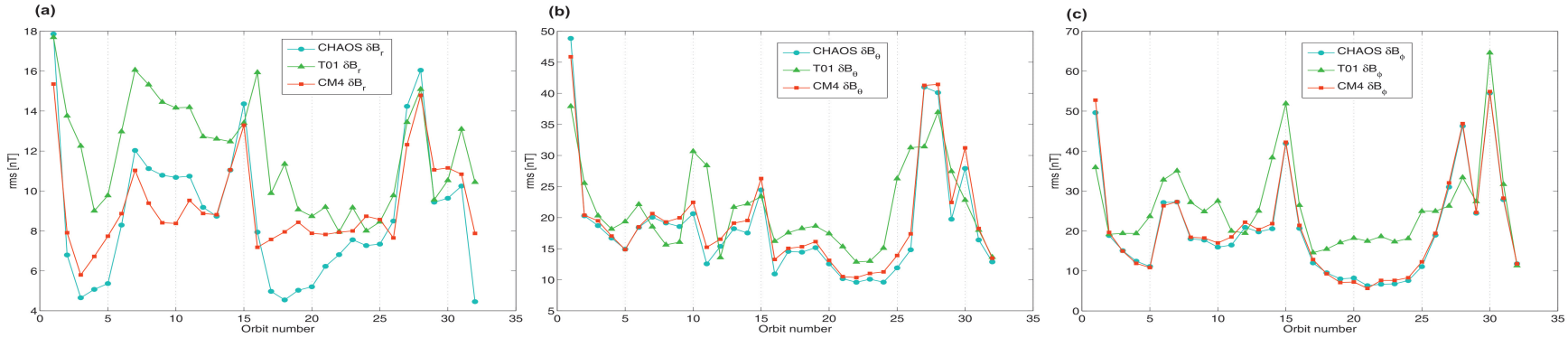

Figure 3.14: Rms values, per orbit, for the residuals between CHAMP and each of the models for 15th-16th March 2001.

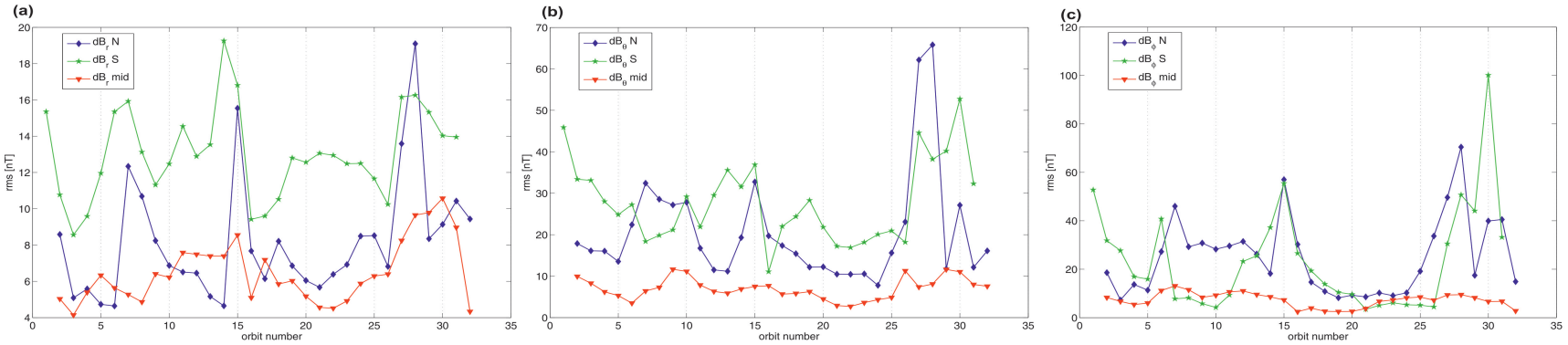

Figure 3.15: Rms values, per orbit segment, of the residuals between CHAMP and CM4 for 15th-16th March 2001. Each orbit is split into three segments, North ($\theta < 50°$, blue), South ($\theta > 130°$, green) and low-latitudes ($50° < \theta < 130°$, red)

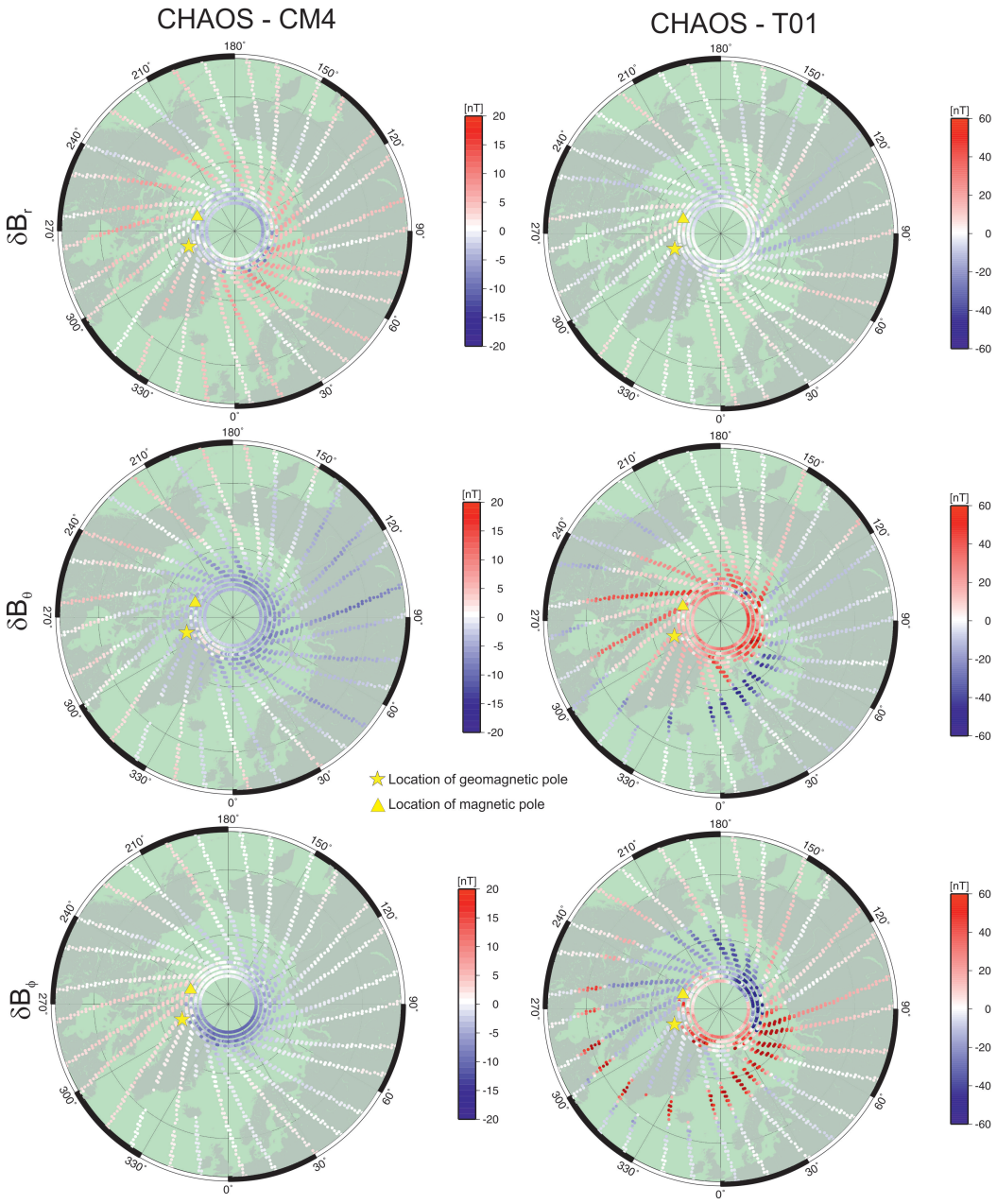

Figure 3.16: Differences between the model predictions on 15th-16th March for each of the three components. Note the change in scale between the plots for CHAOS-2 minus CM4 (left) and CHAOS-2 minus T01 (right)

3.7 Comparing CHAMP and Ørsted

For the March dataset CHAMP and Ørsted are at very similar local times (see Figure 3.17b), so it is reasonable to compare them directly. This is useful because they are at different altitudes, and will give different views of current systems; unfortunately their orbit tracks do not coincide completely, due to their different inclinations. In Figure 3.17a we show the residuals for CHAMP minus CHAOS-2 (blue) and Ørsted minus CHAOS-2 (red) for orbits which are at approximately the same universal time. The residuals do show similar features, particularly near the South pole (180° colatitude), which is where the two satellites are closest to being in the same geographical location (Figure 3.17c), and are therefore only separated by their different altitudes. These features are also seen when CHAOS-2 is replaced by either CM4 or T01. Ørsted appears to be more variable in this plot as we have used Ørsted data at 1 second sampling and CHAMP data at 5 second sampling.

In Figure 3.17a there are some data spikes in the Ørsted dataset. The spike in box 2 is associated with a data gap and therefore is unlikely to be real. However, the cause of spike in box 1 is less obvious, as there is no gap in data. It may be due to an instrument fault or it could be related to a short-lived localised source near the satellite. In geomagnetic field modelling it is important to remove such spikes through careful data selection.

The orbits for the disturbed data (Figure 3.18) cross over in a slightly different colatitude, coinciding spatially close to the South pole, but closer in UT near the North pole. Again the residuals show similarities for the two satellites, particularly in the radial direction, although there are larger differences between the two models than for the quiet data.

The residuals for the two satellites can also be compared spatially. In Figure 3.19 residuals for the ϕ component with a magnitude over 30nT are plotted in bright colours for CHAMP in blue and Ørsted in red. The large residuals for the two satellites plot in very similar locations, in the auroral oval in particular.

This comparison allows us to investigate how field-aligned current density changes with altitude. If FAC density decreased with altitude we would expect to see a decrease in the size of the Ørsted residuals, this is not obviously the case here. Also, in an approximately dipolar field the field lines in the polar regions will diverge with altitude. In Figure 3.17 there is a small offset in colatitude of the main peak in the residuals in the South pole, however, this is not so obvious in Figure 3.19; this may be an artefact of the threshold chosen for identifying the largest residuals.

3.8 Extending to a Larger Dataset

So far, all the data used in this study are for two-day periods. Here we investigate the effect on the averaged residuals of extending to longer datasets.

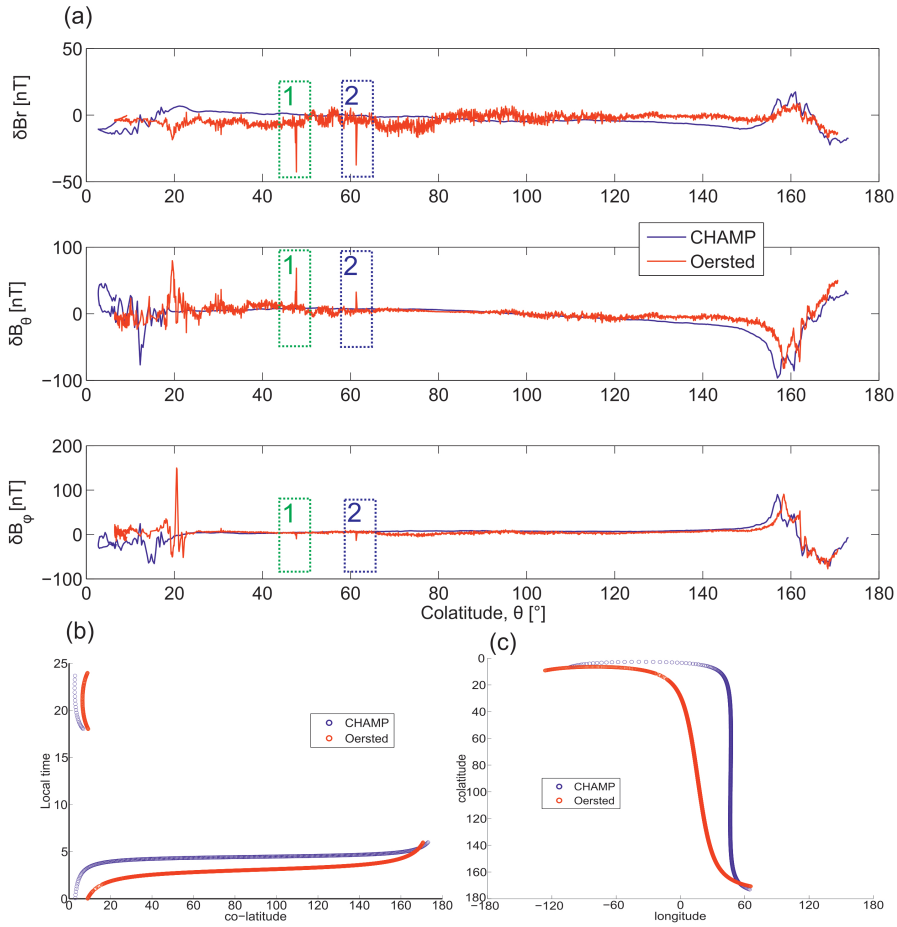

Figure 3.17: (a) The residuals for CHAMP (blue) and Ørsted (red) minus CHAOS-2 for a single orbit on 15th March 2001. (b) Local time vs colatitude for the two satellites and (c) the position of the satellite tracks in colatitude and longitude. The dashed rectangular boxes indicate the locations of data spikes discussed in the text.

Figure 3.20 contains plots of the residuals averaged in 1° bins of colatitude for four quiet (selected with $K_p < 2o$) datasets ranging in length from two days (16th-17th September 2001) to 20 days (5th - 25th September 2001). As the size of dataset increases the overall magnitude of the residuals does decrease, however, the shape remains consistent. For the averages in bins of 1° latitude by 1° longitude, shown in Figure 3.21, the overall pattern of the auroral oval is again persistent.

The fact that the plots are so consistent over differing time ranges suggests that either:

1. large residuals for a few days dominate the data
2. there are limited data with $K_p < 2o$ on most days
3. features seen in these plots are consistent over time

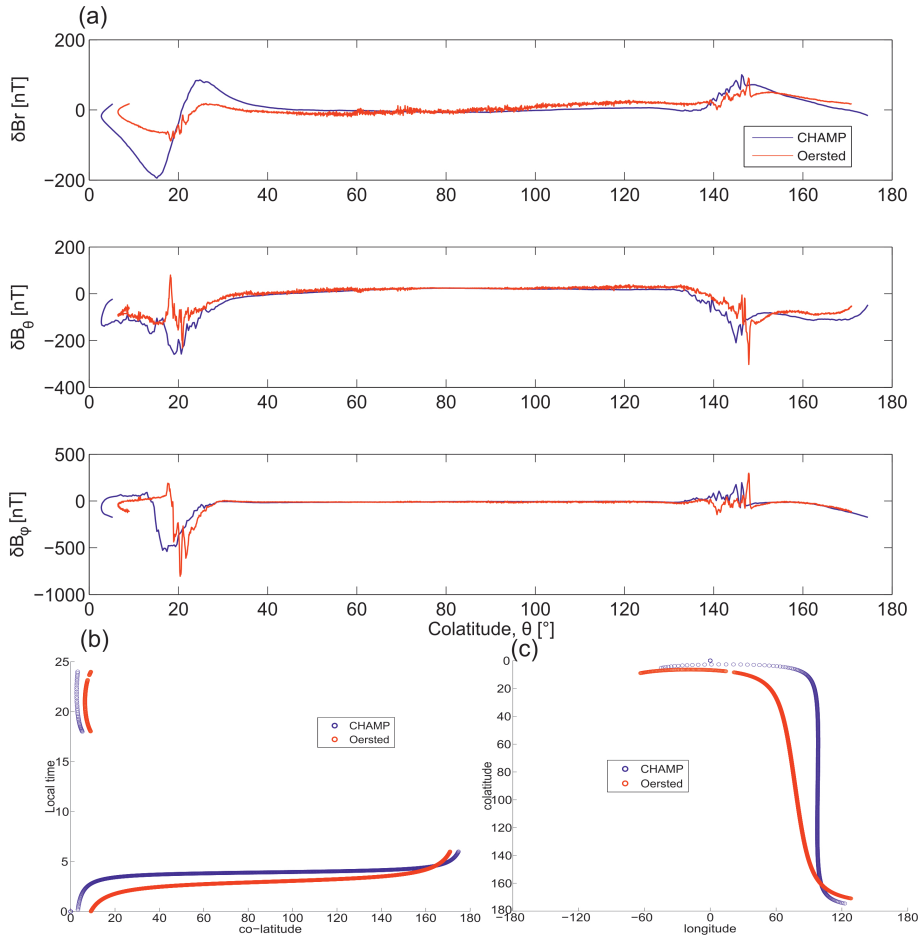

Figure 3.18: An example of an orbit for the disturbed March dataset (20^{th} to 21^{st}) for CHAMP (blue) and Ørsted (red) minus CHAOS-2. (b) the local times covered by the satellite orbit and (c) shows the geographical position of the two satellites

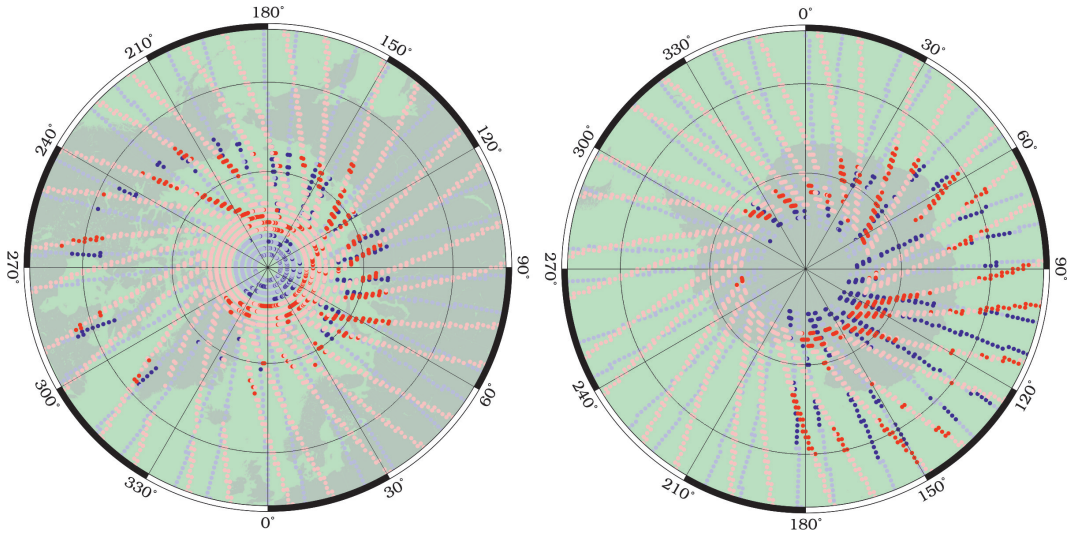

Figure 3.19: Comparison of CHAMP (blue) and Ørsted (red) residuals for the ϕ component of the CHAOS-2 model at the North (left) and South (right) poles on the 15th-16th March 2001. Strong colours represent residuals with a magnitude larger than 30nT, light coloured residuals are smaller than 30nT

For a selection including more disturbed data (K_p up to 7o)[2], as shown in Figure 3.22 the residuals are in general larger. However there is again consistency in the shape of the plots, when averaged in 1° bins of colatitude. When averaged in bins of 1° latitude by 1° longitude, plots of the disturbed residuals (Figure 3.23) show a similar trend to the quiet averages (Figure 3.21); the magnitude of the residuals increases with the length of the dataset, but the overall shape and size of the oval remains uniform.

3.8.1 Standard deviation

Figure 3.24 contains plots of the standard deviation of the residuals (CHAMP-CHAOS-2) in the northern polar region for the four different length quiet datasets. In all three components the standard deviation of the bins increases as data for additional days are included. The location and shape of the outside boundary remains consistent between the plots, but there is much more variability within this boundary for the longer datasets. The disturbed data (K_p up to 7o, not shown here) also show an increase in variability as the length of the dataset increases, again with the outer boundary staying the same size and shape.

The increase in variability over the polar cap is likely to be due to short-lived sources of signal which increase the size of the residuals for particular days, thus increasing the range of values in any particular bin as more days are added. The consistency in the location and size of the oval indicates that this is a persistent feature of the field.

[2]between 40-50% of the data in each of the four data sets have $K_p > 2$o

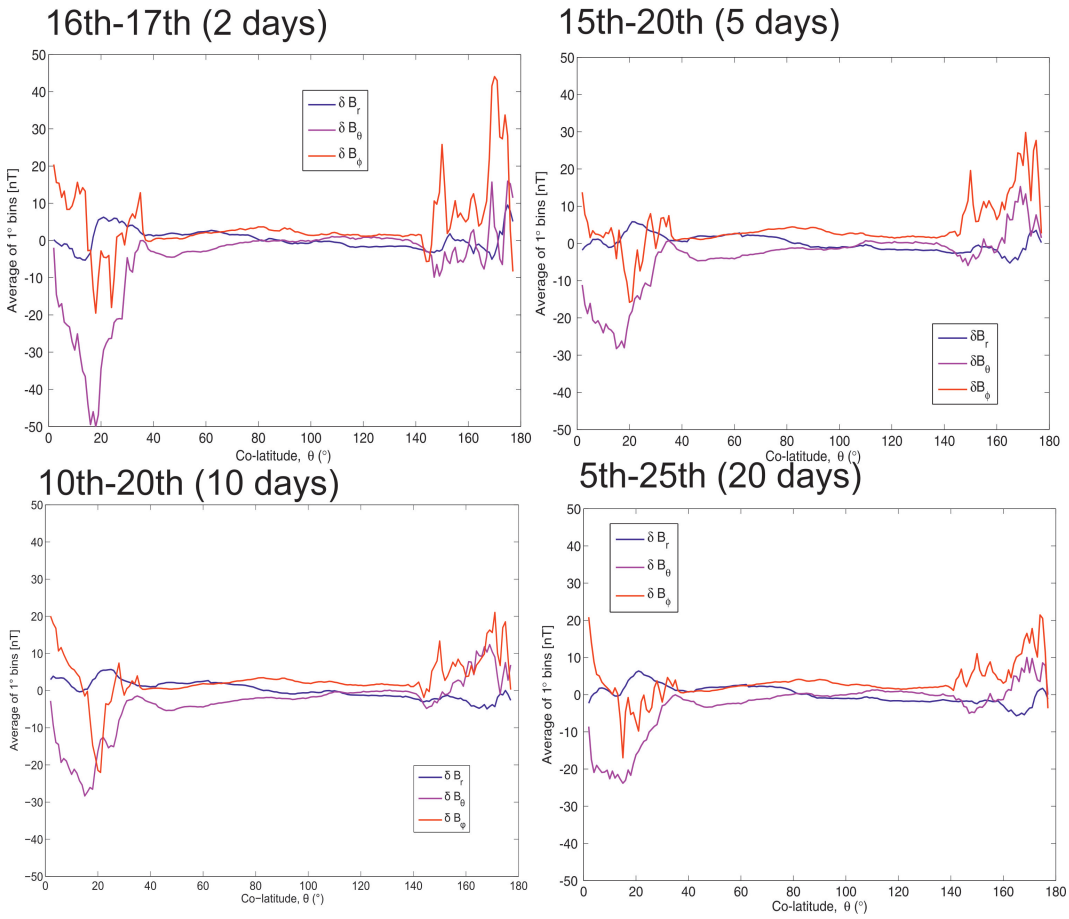

Figure 3.20: Residuals (CHAMP-CHAOS-2) averaged in bins of 1° colatitude for four datasets of increasing size in September 2001, with $K_p < 2o$.

3.8.2 Outlier rejection

To identify whether the morphology of the plots for the different length datasets (e.g., Figure 3.20) is genuinely consistent or due to one or two days' data dominating the signal, we have removed the largest residuals in each dataset. To do this the standard deviation of the whole dataset is calculated and any data which lies over either one or two standard deviations from the mean is excluded. For example, Figure 3.25 is a plot of the residuals for the largest dataset (5th-25th September for K_p <2o) with the 1σ and 2σ values labelled. Any residuals which appear outside of these lines were not included in the averages. The percentage of data removed in this process is shown in Table 3.1; less than 7% is removed from any of the datasets.

When we do this either for a limit of 1σ or 2σ (see Figure 3.26) there are still features which are consistent between the three different length datasets. They are often smaller in magnitude for the longest dataset but the curves do still have a very similar shape.

The same process was then followed for more disturbed data to see if there is still consistent signal even at more active times. We take the same time periods and

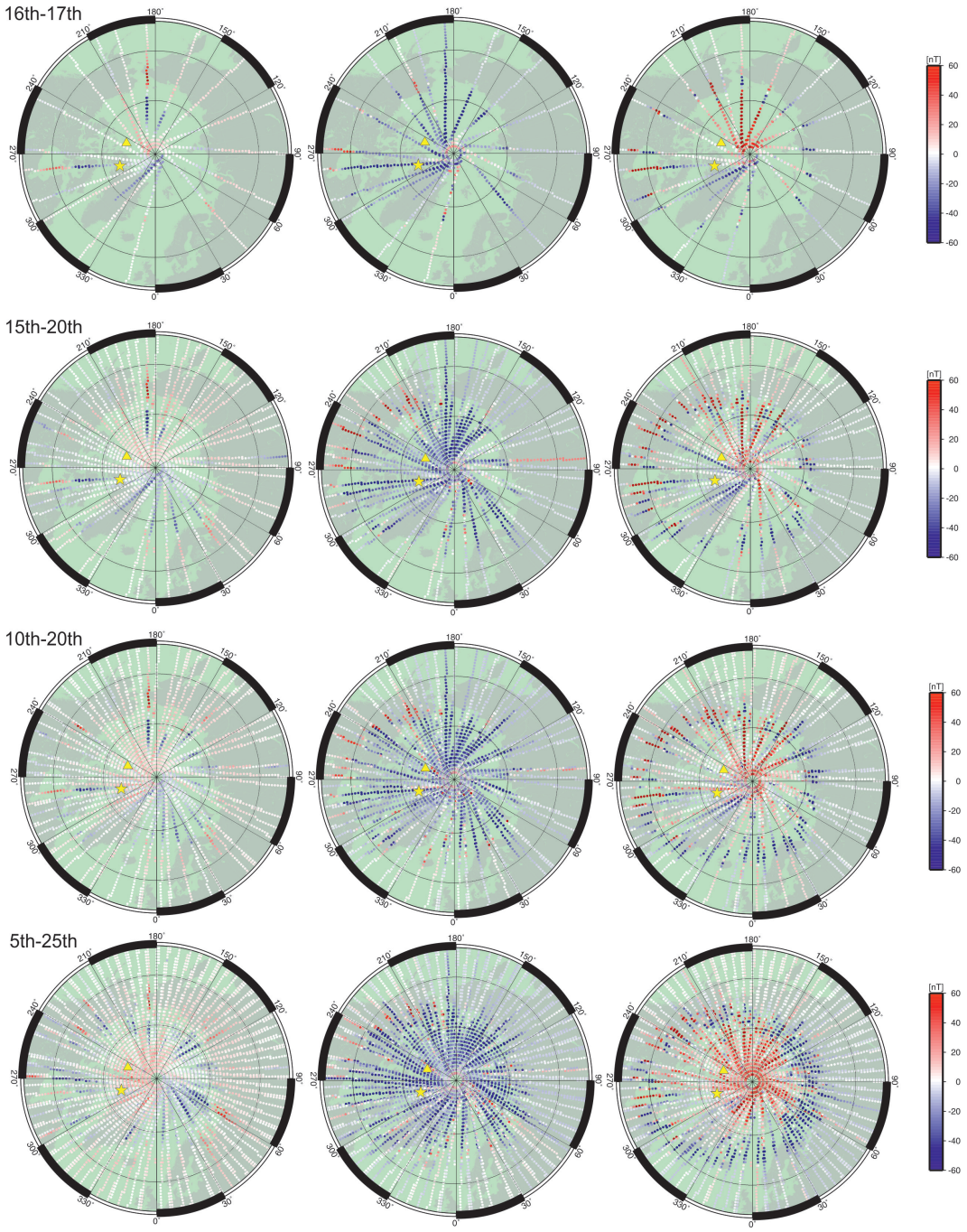

Figure 3.21: Residuals (CHAMP-CHAOS-2) averaged in bins of 1° latitude by 1° longitude, for four datasets of increasing size in September 2001, with $K_p < 2$o. The locations of the magnetic and geomagnetic poles in 2001 are marked in yellow.

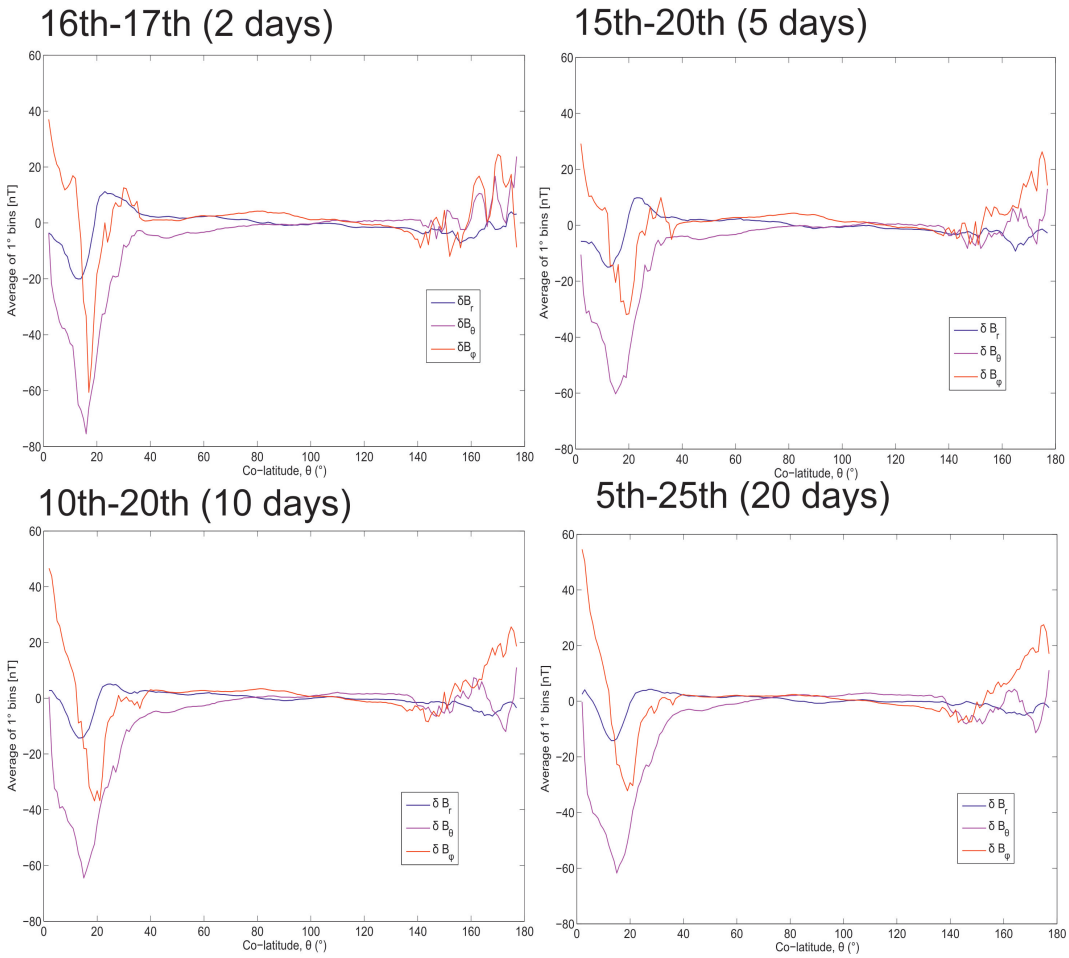

Figure 3.22: Residuals (CHAMP-CHAOS-2) averaged in bins of 1° colatitude for four datasets of increasing size in September 2001, with K_p up to 7o.

only include data with 2o $< K_p <$ 7o and recalculate the averages. The percentage of data excluded with this process are shown in Table 3.2. Data with $K_p <$ 2o are not included so that we can be sure that the quiet time data are not contributing to the shape of the curve. We find that, as for the quiet data, there are features which are clearly consistent between the different length sets.

3.9 Testing Summary

Residuals to existing models clearly show that the high latitude regions are the hardest to model adequately. There is a signal (or signals) associated with the auroral oval and field-aligned currents, even during quiet periods (see e.g., Figure 3.7). Plots of the standard deviation (Figure 3.11) show that the large residuals correspond to highly variable regions, which would be expected for residuals related to these highly variable external sources.

We also see some signature of the external field leaking into the total intensity

Dates	1σ			2σ		
	Br	$B\theta$	$B\phi$	Br	$B\theta$	$B\phi$
16-17	5.4	2.8	6.8	2.9	1.1	3.5
15-20	6.1	4.2	5.8	2.8	1.9	2.9
10-20	6.6	4.3	5.3	2.5	1.9	2.5
5-25	6.2	4.1	6.2	2.8	1.9	2.9

Table 3.1: Percentages of data that were excluded from the averages for being further than 1σ or 2σ from the mean

Dates	1σ			2σ		
	Br	$B\theta$	$B\phi$	Br	$B\theta$	$B\phi$
16-17	4.4	4.5	5.4	1.5	2.5	2.6
15-20	4.0	2.8	5.1	1.4	1.2	2.5
10-20	4.9	2.5	6.3	1.9	1.2	2.6
5-25	4.8	2.7	6.9	1.9	1.1	2.6

Table 3.2: Percentages of data that were excluded from the averages for being further than 1σ or 2σ from the mean for data with $2\text{o} < K_p < 7\text{o}$

field at high latitude (Figure 3.9), particularly in the CHAMP data and close to the pole. Although the features seen are small, this confirms that the use of scalar data at high latitudes does not fully remove the signal associated with ionospheric currents. This is not surprising as the auroral electrojets are not field-aligned so some auroral signal will remain in the intensity data. This shows how important it is to carefully consider the high latitude data.

When comparing the different models we find that T01 produces larger residuals (Figure 3.13) and higher rms values (Figure 3.14) than both CHAOS-2 and CM4. There is much more similarity between CHAOS-2 and CM4 with CHAOS-2 perhaps performing marginally better. The comparison between CHAMP and Ørsted (Figures 3.17, 3.18 and 3.19) indicates that high latitude features maintain their amplitude and approximate location with altitude.

Although most of the testing in this chapter was performed on two-day datasets, we extended this to see how the time span affects the residuals. We find that there are features that remain consistent over time (e.g., Figure 3.20) related to the auroral oval. Other months also show this consistency; however, the pattern and sign of the residuals in the auroral oval vary between the months tested here, suggesting at least a seasonal variability. Given more time and computing power we could continue this study to test just how consistent the shape and size of the auroral oval signature is over the course of a year. In the future this could potentially provide a method for approximating an average oval; this average oval can then be used for selecting data which is not affected by the auroral oval.

We can see that the inclusion of vector data at high latitudes could be very important for providing additional information about the field in the polar regions.

This provides the motivation for finding methods of selecting quiet, high latitude vector data in the following chapters. In studying the standard deviation of residuals to existing models we see that the auroral oval and associated FACs cause the field to be highly variable. This could provide a means for identifying, and therefore avoiding data from this region, and is investigated in more detail in the next chapter.

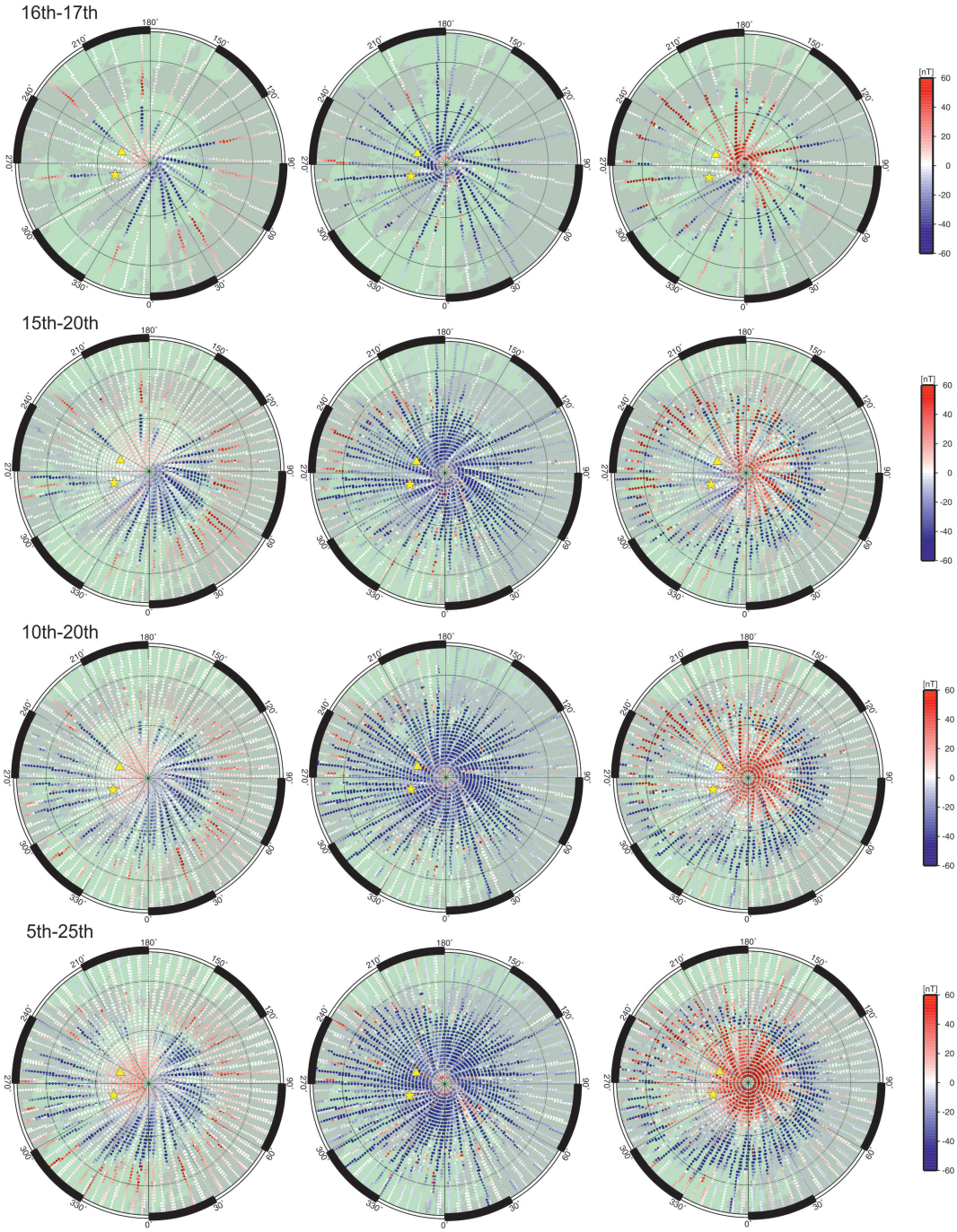

Figure 3.23: Residuals (CHAMP-CHAOS-2) averaged in bins of 1° latitude by 1° longitude, for four datasets of increasing size in September 2001, with K_p up to 7o.

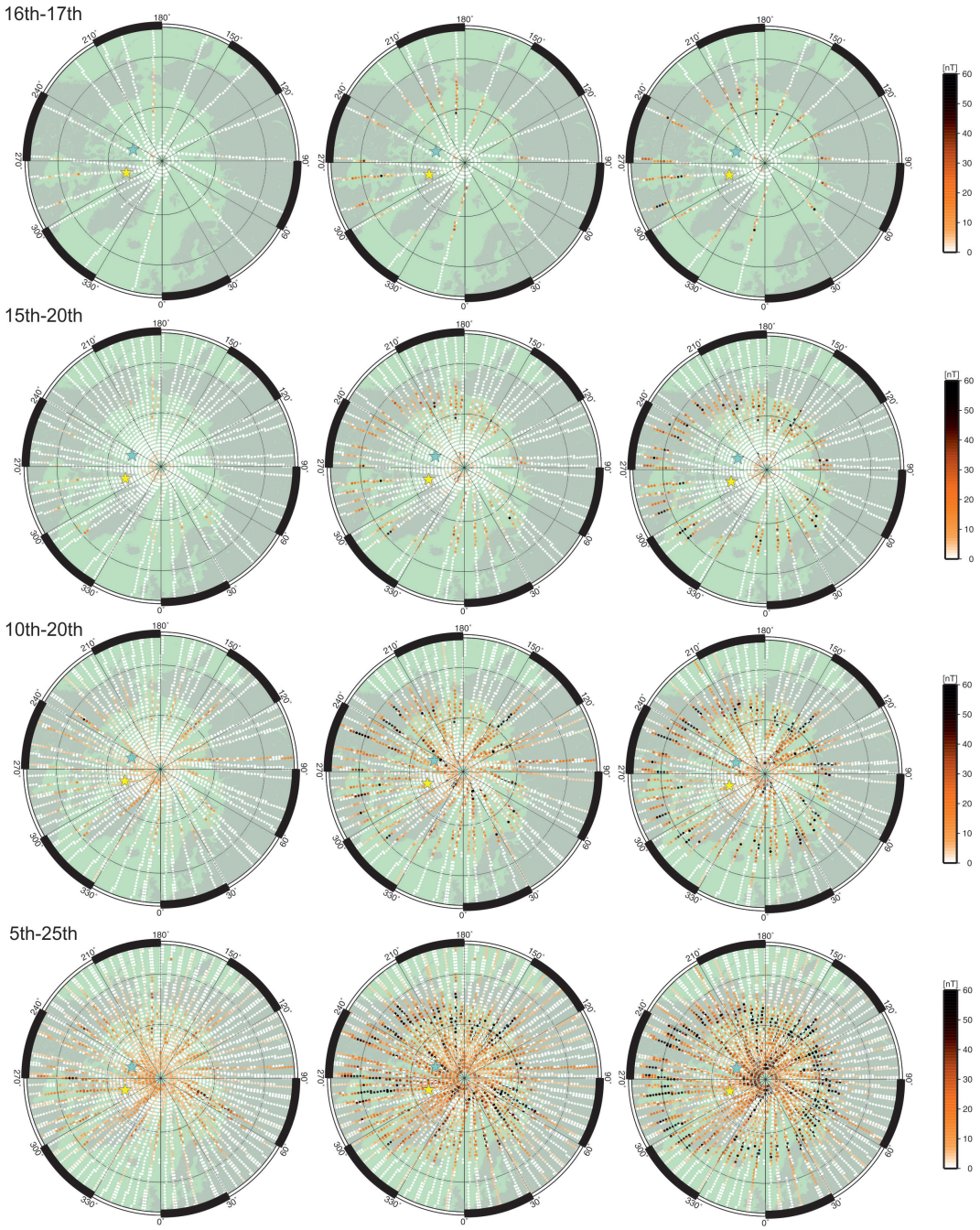

Figure 3.24: Standard deviations of the residuals (CHAMP-CHAOS-2) for bins of 1° latitude by 1° longitude for four datasets in September 2001 with $K_p < 2o$, increasing in length from top to bottom. The scale is saturated (black dots indicate standard deviation >60nT) to allow smaller scale detail to be seen.

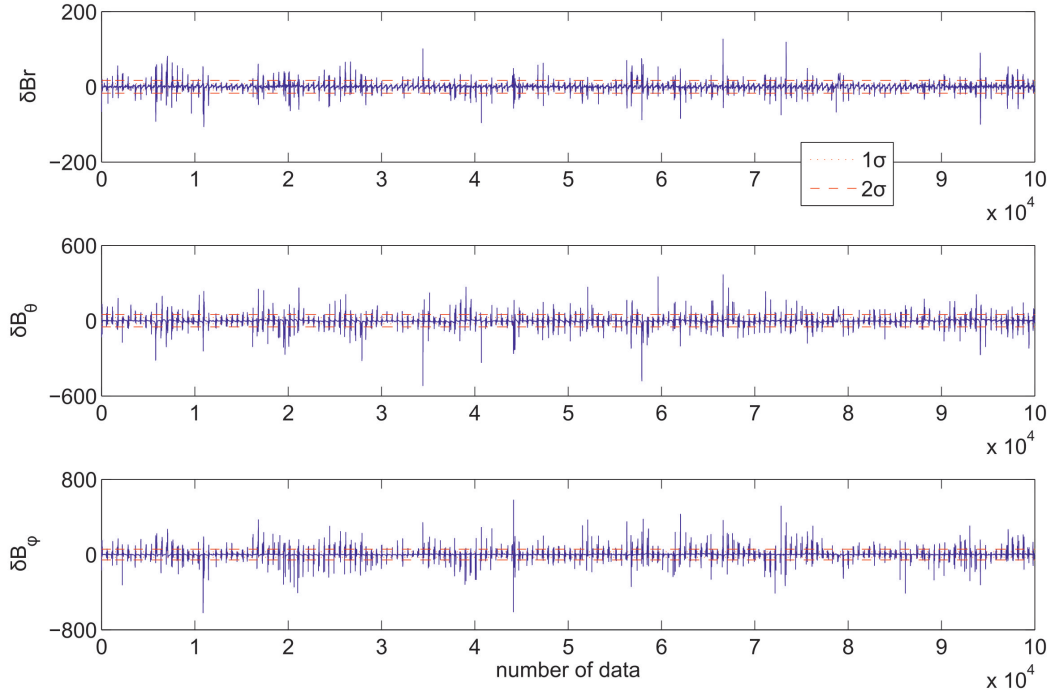

Figure 3.25: Residuals for the 5-25th September ($K_p < 2o$) with 1σ and 2σ limits shown in red. Data points outside of these ranges were considered outliers

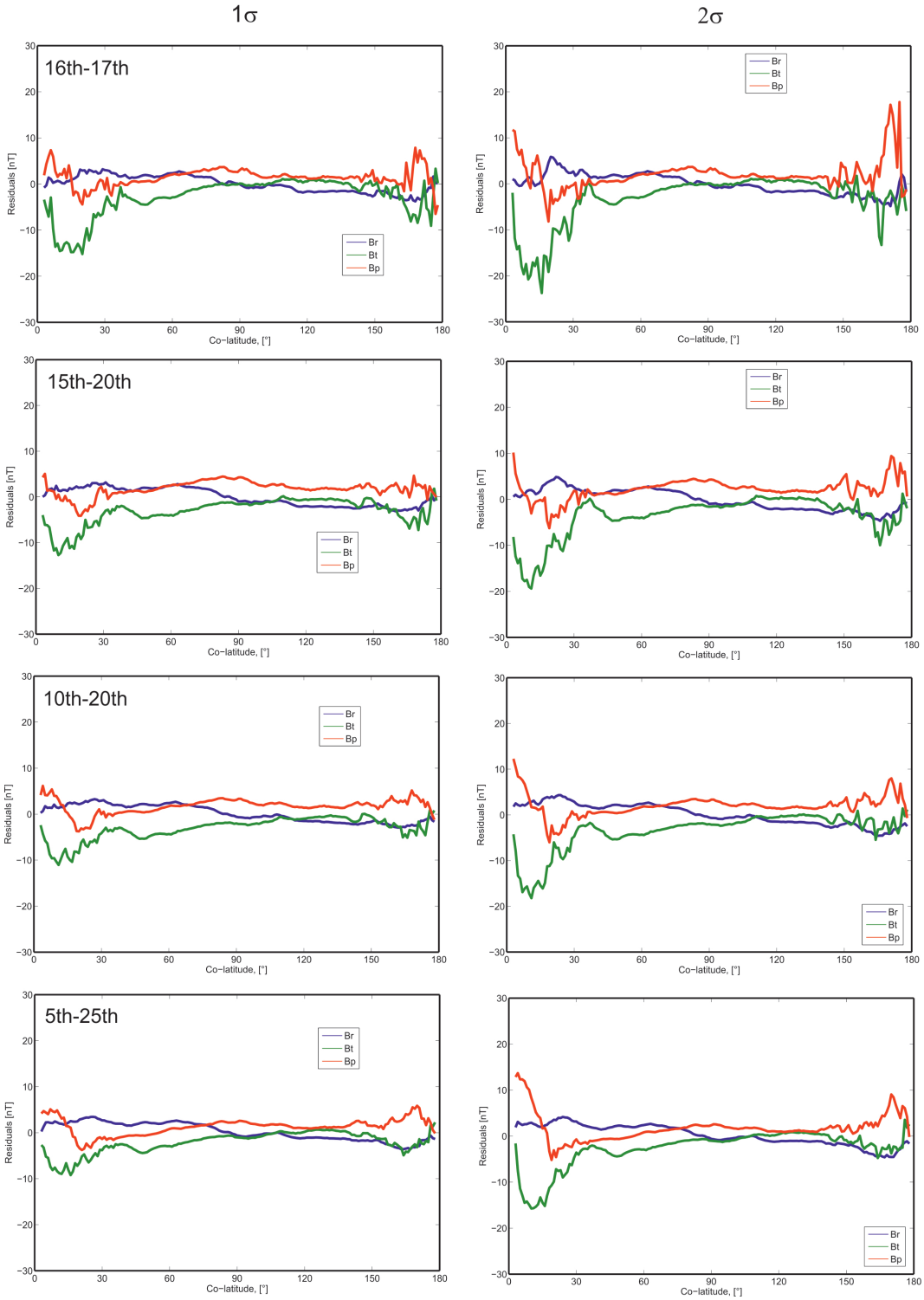

Figure 3.26: Averages of residuals with $K_p < 2o$ in 1° bins of colatitude, excluding data further than 1σ (left column) or 2σ (right column) from the mean.

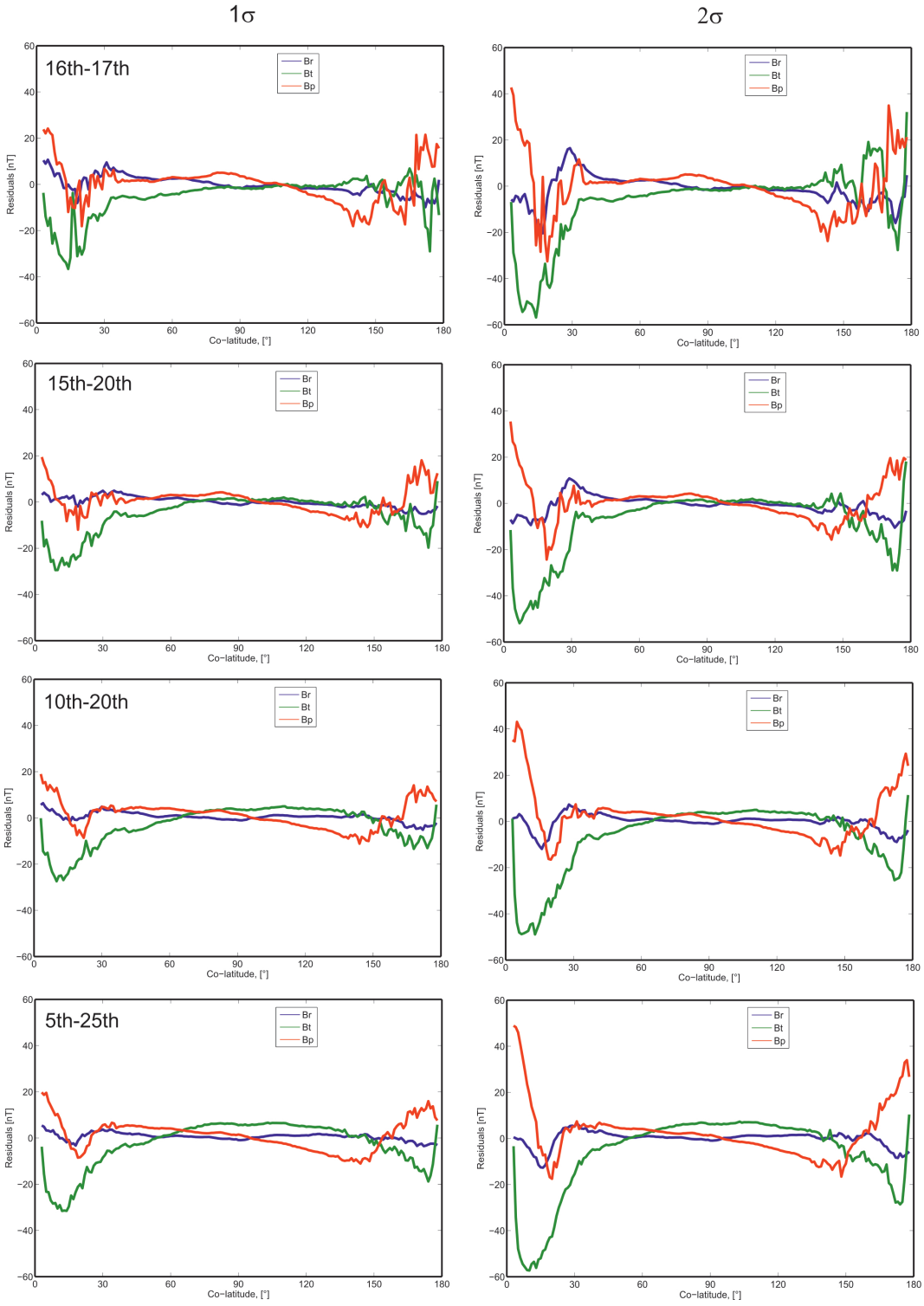

Figure 3.27: Averages of residuals with $2o < K_p < 7o$ in 1° bins of colatitude, excluding data further than 1σ (left column) or 2σ (right column) from the mean.

Chapter 4

Identifying the Auroral Oval

The intense currents in the auroral oval, and the field-aligned currents which couple the auroral ionosphere to the magnetosphere, cause large variations in the magnetic field. In chapter 3 it was evident that most of the residual signal (between satellite data and existing models) was directly related to the auroral oval. In most models vector data are not used at high latitudes (e.g., above a limit of either $\pm 50^\circ$ or 60° geomagnetic latitude), to minimise the effect of field-aligned currents (e.g., *Olsen et al.*, 2007). At times this limit means that there are quiet vector data near the poles that are not exploited; there are also times when the oval, or parts of the oval, may extend equatorward beyond this limit, and therefore highly variable data from external sources are allowed into the selection.

To produce models of the geomagnetic field which have even accuracy and resolution over the whole globe it is important to have consistency in the quality, type and distribution of data. By excluding all high latitude vector data this is clearly no longer the case and we saw in Section 3.1 that vector data can provide important additional information. The aim is to maximise the number and quality of data, whilst retaining a certain smoothness of data. Although the high latitudes contain more unwanted signal, and therefore more of these data are excluded, the geometry of polar satellite orbits means there is much higher data density in these regions. This should allow more data to be discarded at high latitude whilst retaining a similar data density to the rest of the globe.

We believe that the location of the oval itself could be used to better define the limit at which vector data are discarded. This would allow additional vector data to be used when the auroral oval is quiet (and therefore small), but would also increase confidence that selections made at lower latitudes do not contain auroral signatures.

There have been many efforts to formulate a method to locate the boundaries of the auroral oval (e.g., *Gussenhoven et al.*, 1981; *Starkov*, 1994; *Sotirelis et al.*, 1998). Originally the locations were defined using photographs of the aurorae for differing geomagnetic activity levels (*Feldstein and Starkov*, 1967); nowadays there are many sources of data for describing the oval, including dedicated satellite missions, like

the NOAA Polar-orbiting Operational Environment Satellite (POES)[1]. Here we use the OVATION model which makes use of several different data sources.

4.1 OVATION Auroral Model

OVATION (Oval Variation, Assessment, Tracking, Intensity and Online Nowcasting) is a collaborative effort to define the location and intensity of the auroral oval. Multiple datasets are used in OVATION, including global images from Polar UVI[2], SuperDARN[3] boundaries, and meridian scanning photometer images[4], which are all cross-calibrated with the DMSP[5] particle dataset (*Newell et al.*, 2002). The DMSP satellites are used for the standard as they have operated since the 1980s and cover both hemispheres. OVATION is particularly useful for this study as it identifies the locations of the oval boundaries, and is independent of the data used in geomagnetic field models. OVATION has the advantage of being available in both geomagnetic and geographic coordinates at regular intervals, and is available for the time period covering the datasets we have already investigated.

For the poleward boundary OVATION determines the open-closed boundary (OCB). The OCB is the interface between the closed magnetic field lines of the auroral zone and the open field lines of the polar cap, and is widely recognised (e.g., *Boakes et al.*, 2008; *Laundal et al.*, 2010; *Longden et al.*, 2010) as a proxy for the poleward boundary of the auroral oval. The definition of the equatorward boundary is less obvious; OVATION uses the low energy electron boundary (e.g., *Gussenhoven et al.*, 1981), determined from the DMSP satellite, which has been used successfully in several studies (e.g., *Gussenhoven et al.*, 1983).

Figure 4.1 contains two examples of OVATION estimates of the location of the auroral oval in the Southern Hemisphere for two orbits in December 2001 (far left). Also plotted are the residuals (CHAMP-CM4), in the radial, θ and ϕ components (columns 2,3 and 4 respectively), for an hour before and after the time at which the OVATION estimates are made; the OVATION boundaries are superimposed for reference. The equatorward boundary does delineate the outer limit of the largest residuals, particularly for the θ and ϕ components, consistent with the auroral oval being the main source of disturbance. The polar boundaries do not appear to correlate as well with the residuals, which suggests that activity in the polar cap also has some influence. The OVATION boundaries also match the region of largest residuals in the Northern Hemisphere and for the other datasets (not shown here).

[1] http://www.swpc.noaa.gov/pmap/

[2] Ultraviolet Imager onboard the Polar satellite, http://tideuvira.nsstc.nasa.gov/uvi/

[3] Super Dual Auroral Radar Network, http://superdarn.jhuapl.edu/index.html

[4] University of Alaska, Fairbanks MSP

[5] Defense Meterological Satellite Program archive maintained by the Earth Observation Group at NGDC, http://www.ngdc.noaa.gov/dmsp/index.html

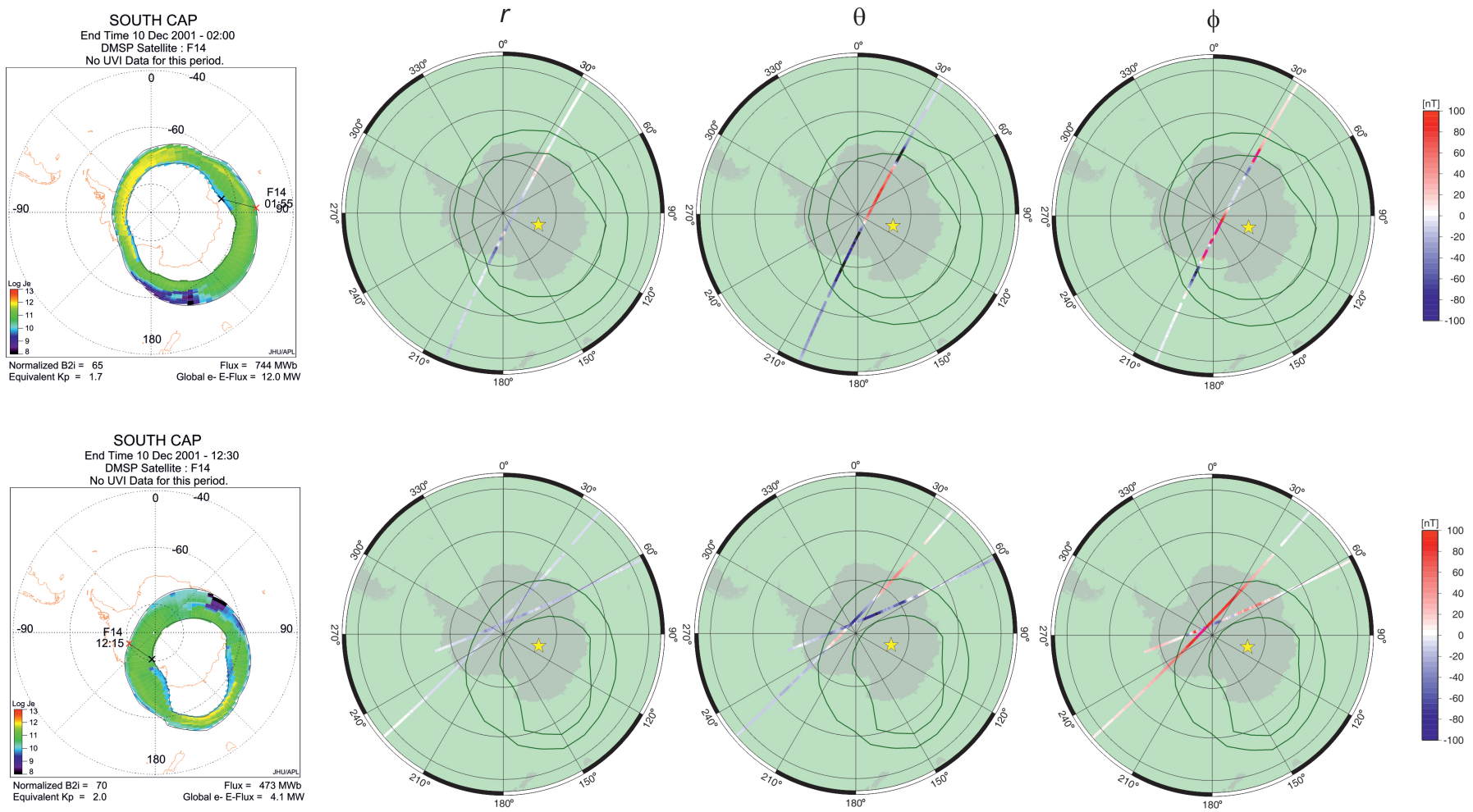

Figure 4.1: OVATION boundaries in the Southern Hemisphere (far left) on 10th December 2001. Alongside each OVATION plot are the residuals (CHAMP-CM4) for the r, θ and ϕ components for an hour either side of the time at which the boundaries are estimated.

4.1.1 Using OVATION to select data

Using the OVATION boundaries it is possible to identify the noisiest part of an orbit and exclude it from the selection. Figure 4.2 shows the residuals (CHAMP-CHAOS-2) for a single orbit of quiet data in September 2001. In grey are the residuals for the whole orbit, the thick green line is the data that would be selected using the OVATION boundaries. Near the South geomagnetic pole the orbit appears to loop back on itself (in terms of latitude); this is due to the geometry of converting from geographic to geomagnetic latitude. For this example the OVATION boundaries were estimated for a time approximately in the middle of the orbit.

To ensure that all noise associated with the auroral oval is avoided we add a safety margin of 5° colatitude either side of the oval. Figure 4.3 shows some examples of other safety margins tested; it is clear that the having no margin (Figure 4.3a) would allow the selection of data which are clearly affected by sources in the auroral oval. A margin of 3° latitude also allows the selection of data which have larger residuals to the model (again suggesting an influence from auroral currents). In the example shown, the loss of data with 7° and 10° (Figures 4.3c and d) is not obviously worse than the 5° used in Figure 4.2; however, testing across the other datasets from 2001 (listed in Section 3.2) suggests that a 5° margin provides the optimum balance of excluding data affected by the auroral oval whilst maintaining an adequate coverage of high latitude data.

The largest residuals are avoided with this selection, particularly for the low- to mid- latitude section between the equatorward boundaries. The OVATION method does identify some quiet data, however, there are evidently signatures from the polar cap which would leak into the data near the poles. Even without the poleward data (i.e., only selecting data between the equatorward boundaries), there is still an improvement upon using a fixed limit in geomagnetic latitude; in the example shown there are clearly additional data that would not be selected if a limit of ±50° were employed. The example shown is representative of all the orbits investigated, with slightly more data selected (in terms of latitude) for some orbits and less for others. The main differences occur for the poleward selection, where some orbits indicate that the OVATION method selects only very quiet data, whilst for others this selection would introduce lots of data over the polar cap which is clearly affected by external sources.

4.1.2 Problems with the use of OVATION

Unfortunately there are several drawbacks to using OVATION to determine the auroral oval. The OVATION boundaries are estimated at 110km altitude, whilst magnetic satellite measurements are made above 400km. This means that the OVATION boundary locations will not directly translate to satellite altitude. The oval will be wider in latitude at higher altitudes, as the Earth's magnetic field lines

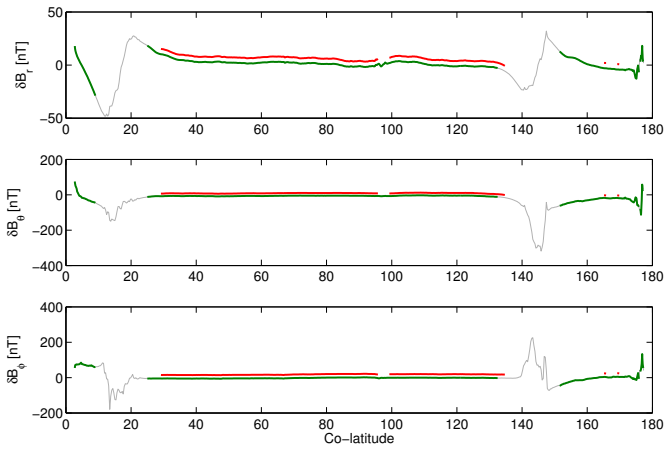

Figure 4.2: An example of data selection using the auroral oval boundaries estimated with OVATION, for a single orbit in September 2001. The grey line shows the residuals (CHAMP-CHAOS-2) for the entire orbit, the green line is the data that are selected using the OVATION boundary locations.

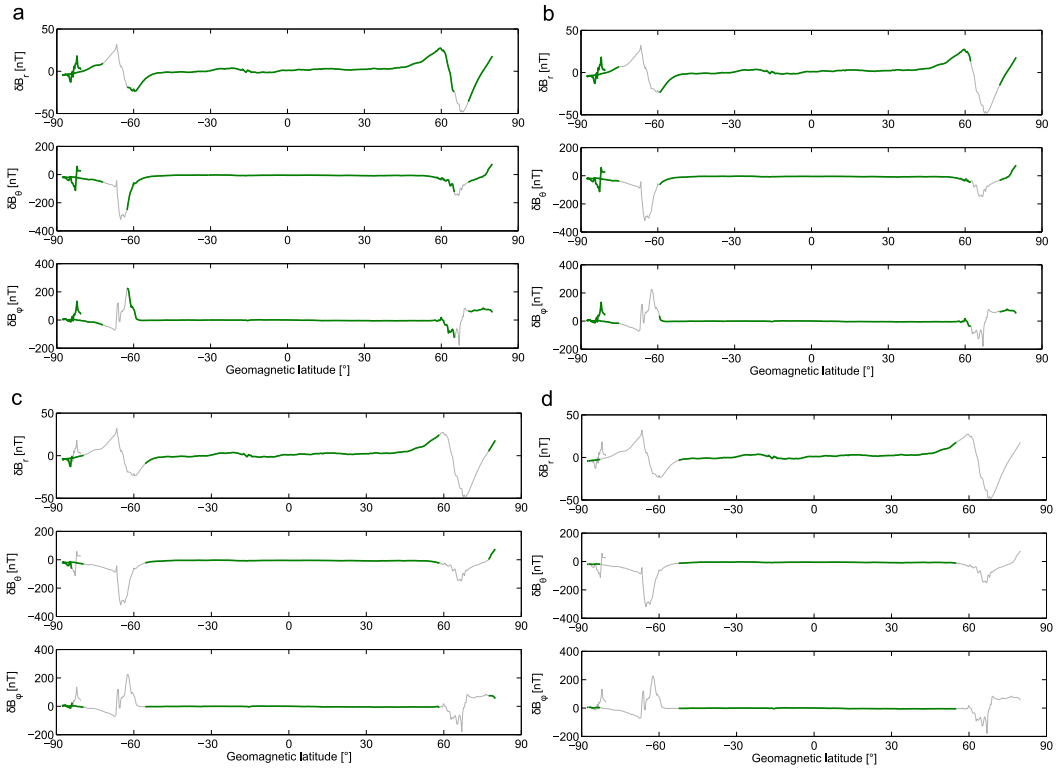

Figure 4.3: Testing the size of the safety margin required in a selection using OVATION for four different margins: (a) 0°, (b) 3°, (c) 7° and (d) 10° latitude.

diverge; hence the safety margin is suggested.

Also, OVATION can only provide snapshots of the boundary locations (estimated every two hours); the highly variable nature of the auroral oval means it is unclear exactly how long each boundary estimate is valid for. Using this information as part of the data selection process would require continuous searching for the boundary estimate closest in time to the data. Where there are gaps in the OVATION predictions the satellite magnetic data would all need to be discarded or downweighted. Each set of boundary coordinates also requires interpolation so the whole process would be computer intensive.

With enough background work and better computer capabilities it could be viable to use OVATION or a similar model in data selection; however, it is not, at present, readily adaptable to processing large quantities of satellite data. For the purposes of this study we look for other simpler methods for selecting vector data outside of the auroral oval.

4.2 An Alternative Method for Defining Oval Location

Figure 4.4 contains plots of the standard deviation (left) and averages (right) of the residuals between CHAMP and CHAOS-2, calculated for 1° bins of latitude for 15th-16th March 2001. 1° bins provide a large enough sample to be confident that the averages are representative of the activity for each degree, in the example shown the average number of points per bin was 84.5, with the smallest bin having 78 and the largest 137 points.

The polar regions clearly contain the largest, and most variable residuals, which are likely to be a direct result of highly variable sources within the auroral oval. It is also evident that the radial direction is the quietest and ϕ the most affected by activity; hence why scalar (approximately radial) data are currently used in models at high latitudes.

At high latitudes the magnetic field is approximately radial, so the radial component should be the least affected by field-aligned currents. We see, in Figure 4.5, that there are orbits in the radial component which have very low standard deviation along their whole length, with a standard deviation less than 0.3nT for most of the orbit and remaining below 1.5nT even near the poles (only 5 % of the orbits tested have standard deviation below 1.5nT along their whole length).

In the θ and ϕ components it is, unsurprisingly, much harder to identify an orbit with such low standard deviation values for an entire orbit. However, there are sections of orbits, even close to the poles, which do have low standard deviation values. For example, Figure 4.6 shows the standard deviations in θ and ϕ for two consecutive orbits in March which both have sections of very low standard deviation (< 1nT) polewards of the auroral oval.

This fairly simple method of calculating standard deviation values does well at identifying the data which are most affected by the auroral oval. In the following sections we investigate how this method can be employed in the data selection process.

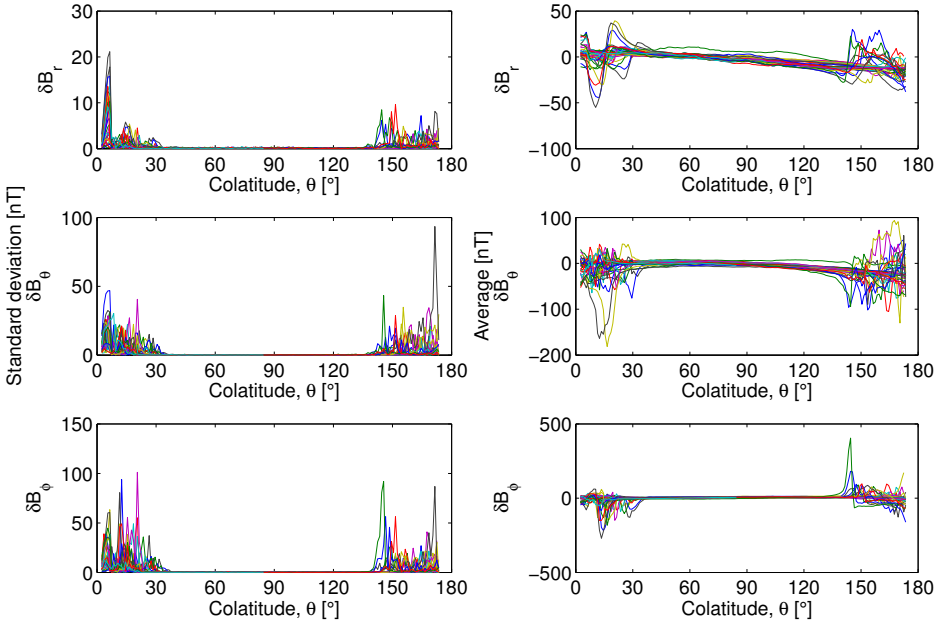

Figure 4.4: Standard deviations (left) and averages (right) of the residuals (CHAMP-CHAOS-2) in 1° bins of geographic colatitude on 15th March 2001

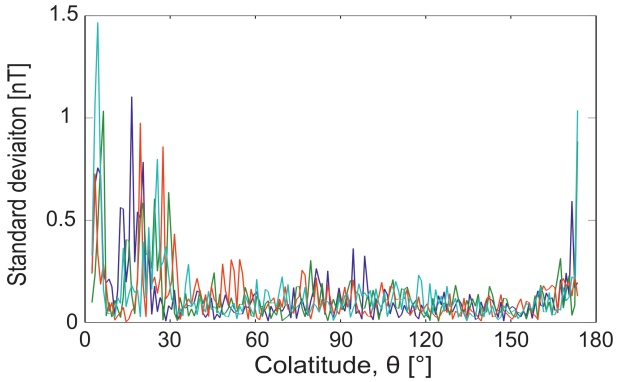

Figure 4.5: Examples of orbits in the radial direction for the March dataset which have very low standard deviation values (CHAMP-CHAOS2)

4.2.1 Geomagnetic field models

The standard deviation of the residuals to a geomagnetic field model (e.g., CHAOS-2 or CM4) are calculated in 1° bins of colatitude. Data with a standard deviation

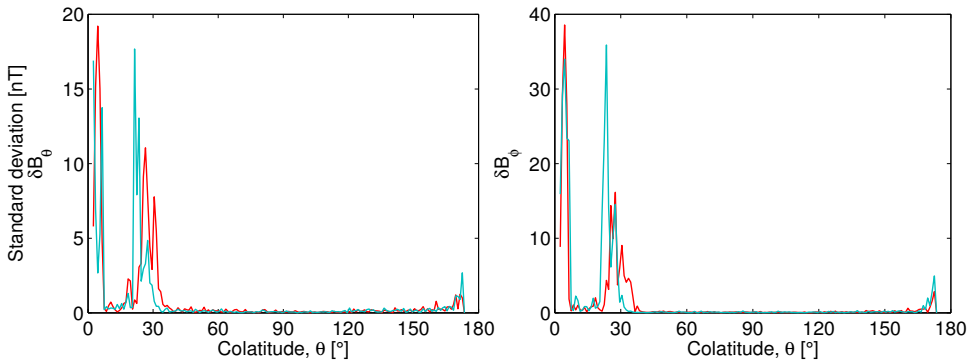

Figure 4.6: Orbits in the θ (left) and ϕ (right) direction for the March dataset (CHAMP-CHAOS2) which have low standard deviation values near the poles

below a set threshold in all three components are then selected. Figure 4.7 provides a comparison between the residuals (CHAMP minus CHAOS-2) for one orbit (grey line), the residuals after a selection using OVATION with a 5° margin (green), and the residuals for a selection based on a standard deviation value less than 0.5nT (red). The standard deviation selection is offset from the other lines for illustrative purposes. The threshold of 0.5nT was chosen after testing a few different values and finding the optimum balance between selecting only the quietest data, and maintaining adequate data density.

This method of selection does provide a similar selection to using the equatorward OVATION boundaries. For the example orbit shown in Figure 4.7 the standard deviation selection picks out the quietest residuals, avoiding the noisy polar regions. This selection also excludes some smaller sections at lower latitudes, for example at approximately $-15°$. These sections could be related to unmodelled ring current or phenomena such as equatorial plasma bubbles (plasma density depletion) and plasma blobs (regions of abrupt density enhancements) which occur in the low latitude ionosphere (e.g., *Park et al.*, 2010; *Stolle et al.*, 2006). Such features have been reported to cause localised fluctuations in magnetic field strength as well as deflections in the perpendicular magnetic field components (*Park et al.*, 2008; *Stolle et al.*, 2006). This suggests that this method is useful for identifying small scale sources of noise at all latitudes.

This example also shows that the limits of the quiet data are less than $\pm 60°$, so some noise would leak into the modelling process if a simple limit of $\pm 60°$ geomagnetic latitude is used. However, there are also additional quiet data that would be gained compared to using a limit of $\pm 50°$. To the right of the Figure 4.7 the residuals for this selection for all the orbits on the 8th-9th September are shown. Here we can see there are also data above $\pm 60°$ geomagnetic latitude which would be selected for some orbits, although there is still some noise in these high latitude selections which needs to be addressed.

When applied to other orbits this method generally selects a similar amount of data to that selected when using the equatorward boundaries provided by OVATION. In some examples this method selects more data than OVATION, particularly when the residuals are small to higher latitudes, allowing more quiet data to be utilised. In the polar regions this method consistently selects fewer data than using the poleward boundaries of OVATION, but what is selected generally has smaller residuals.

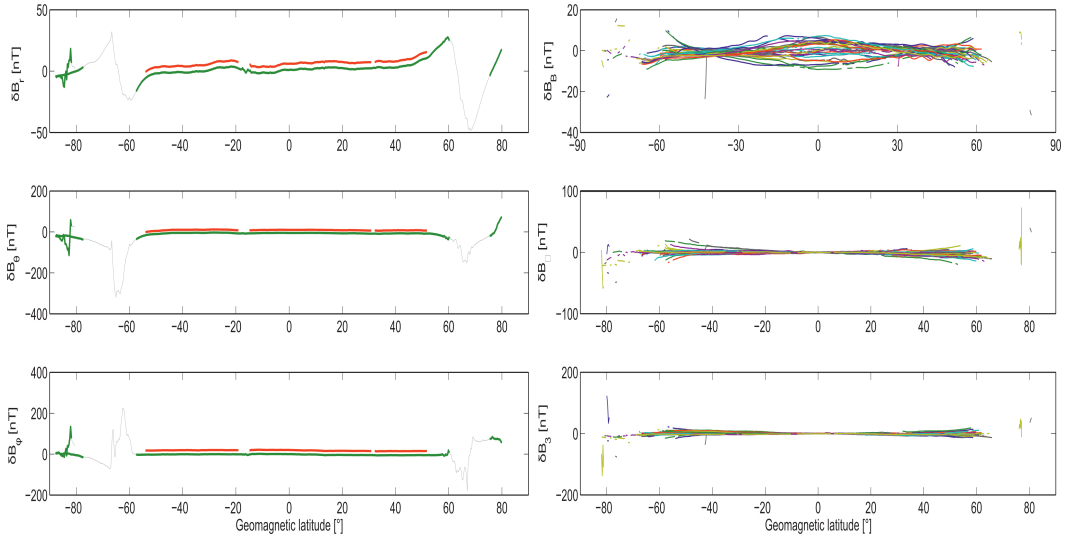

Figure 4.7: Selection using standard deviation values (for 1° bins of geographic colatitude) of < 0.5nT. Left - a comparison with OVATION (green) and residuals for the whole orbit (grey). The selection based on standard deviation (red) is plotted with an offset (5, 15 and 20nT in r, θ, ϕ respectively) to make the comparison clearer. Right - Standard deviation selection for all the orbits in the September dataset.

This method is still not ideal, due to the use of a pre-existing model to make the selection. This makes the selection highly dependent on the parameters used in the original model, rather than being led by the data.

IGRF

To reduce the influence of the chosen external field parameters on our selection we have also tested the IGRF. Although this still causes a dependence on a model, the IGRF (described in Section 2.6.1) is a much simpler model aimed primarily at modelling the core field.

We again calculate the standard deviation of the residuals in 1° bins of colatitude and select data which for which the standard deviation is below a threshold in all three components. If we use 0.5nT as this threshold, as before, this method excludes far more data than the OVATION boundaries. Instead we use 1.0nT for the limit and this provides a more reasonable selection, with data selected at similar latitudes, and similar sizes of residuals as the methods described previously. However, there

are clearly problems with using the IGRF. The example in Figure 4.8 (left) is the same orbit shown in Figure 4.7. There are more low latitude gaps with this selection and data with large residuals remain in the selection, for example the red orbit in 4.8 (right) which has large residuals at around $-65°$ in all three components.

The geomagnetic field models used in the previous section (e.g., CHAOS-2) are designed to parametrize the external field sources as well as the core field; however, the IGRF is designed only to describe the core field. Therefore, the IGRF would not be expected to fit the data as closely, so the standard deviation values are also likely to be larger (which is the case). In the example shown, a limit of 0.5nT selects around 47% of the original data compared to around 68% selected when using CHAOS-2. Losing around half of the data is not ideal, particularly as the original data used for this example are already for a magnetically quiet day. When the standard deviation limit is increased to 1nT the percentage of data selected increases to approximately 70%, similar to that using CHAOS-2.

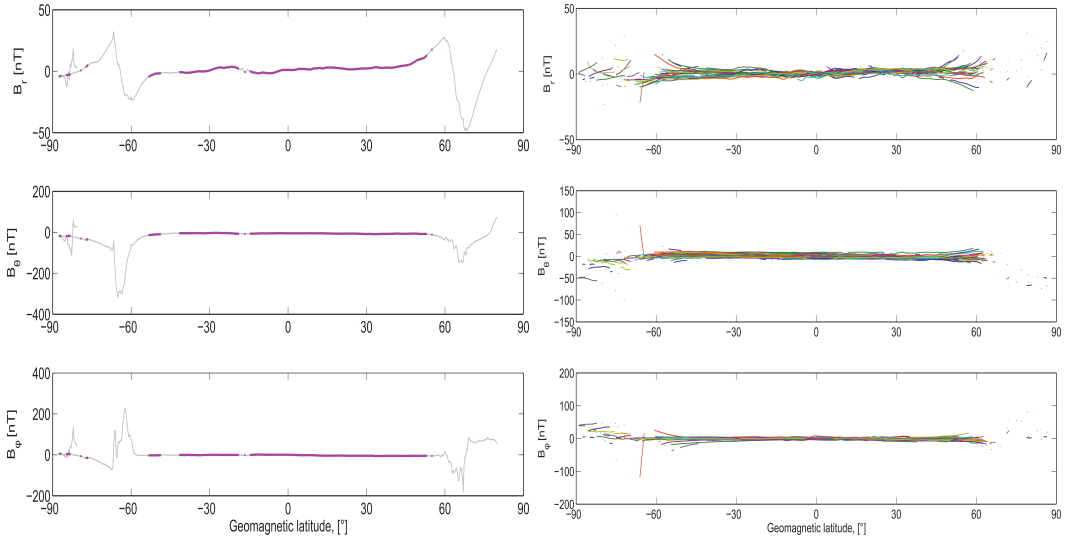

Figure 4.8: Selection using standard deviation (< 1.0nT) of residuals to IGRF for the same single orbit as figure 4.7 (left) and for all orbits on the 8th-9th September (right)

4.3 Removing the Need for an *a priori* Model

In the examples shown so far we have based the selection on the residuals to a pre-determined model. However, ideally we do not want to bias the data selection with the choice of an *a priori* model. Instead we seek a method to get the same information about the location of the oval using only the data.

We begin by subtracting a simple moving average of the original data, and then calculating the standard deviations of this new dataset. Based on a 5 second sampling rate of the data, the number of points in each bin needs to be kept relatively

small. If the bin size is too large then the data will span a large range of latitudes and the field will change more across the bin; then the trend can not be well explained by a linear best fit. The choice of bin size is therefore a trade off between having more points to average and the loss of linearity. We find that a bin size of 7 points works best for this data (equating to 35 seconds), with a standard deviation limit of 0.5nT, as for the residuals to CHAOS-2.

To test this method we again take the residuals between the newly selected data and the CHAOS-2 model. Figure 4.9 shows the data selected for the same orbit as in previous examples (left) and the selected data for the whole September dataset (right). This selection is similar to that based on the standard deviation of the residuals to CHAOS-2 (Figure 4.7), again excluding a section of data at low latitudes (at approximately $-15°$). However, this method also selects some data points at higher latitudes which have very small residuals, this suggests the potential for selecting additional quiet data at high latitudes which would normally be excluded.

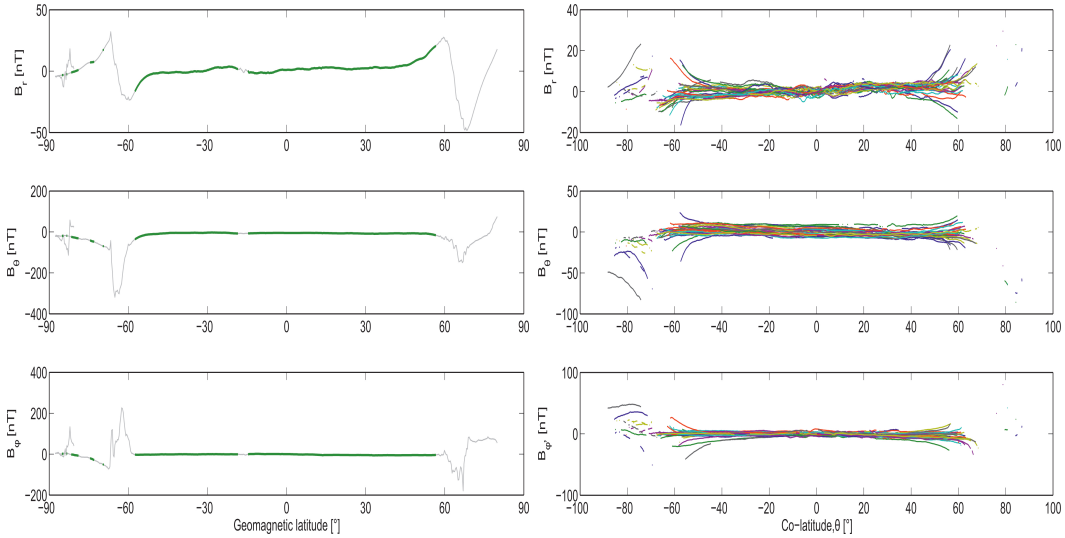

Figure 4.9: Selection based on residuals to a moving average for the same orbit as in Figure 4.7 (left) and all orbits on the 8th-9th September (right)

Unfortunately, this method fails when there are any data gaps, even if only one data point is missing, as it requires a small latitudinal spacing. This leads to large gaps even at low latitudes which are not actually related to the variation in the data. To address this we tried replacing the simple averaging technique with a full linear interpolation to estimate the data point at the centre of each bin in place of the simple average. However, although this does improve the situation, there are still large gaps in the selection even when only one value is missing from the original data.

To make a more complete estimation of the expected value at each point we employ a quadratic fit; the formulation of this fit is explained in full in Appendix B.

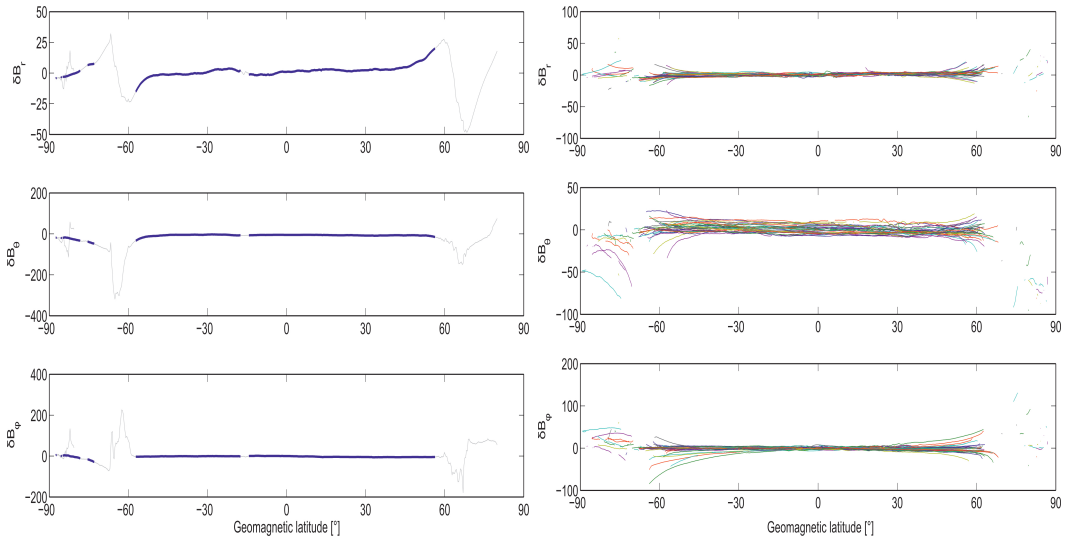

Figure 4.10: Selection using the standard deviation of residuals to a polynomial fit for standard deviation < 0.5 nT

By using a quadratic fit we get a much better estimation of the value of each data point, and the problems with missing data are alleviated. Figure 4.10 (left) shows the data selected for the same single orbit as the other examples. This method of selection does a good job at picking out the data which have small residuals to CHAOS-2. However, the plot including all the orbits for the September dataset (Figure 4.10 right) shows that at times some quite large residuals are included close to the poles, which is likely to not be ideal.

By using a higher degree fit the standard deviation will be smaller overall, so the limit used previously is now inadequate for selecting only quiet data. By reducing the standard deviation threshold to, for example, 0.2nT (Figure 4.11) a similar amount of data is selected as for the standard deviation of residuals to existing models (section 4.2.1). The inclusion of large residuals close to the poles is also reduced compared to the use of a threshold of 0.5nT and the noisier high latitude data seen in Figure 4.7 are no longer included.

It is also important to note that this method requires that the data are not spaced too far apart. As mentioned previously the field changes significantly with both time and location; this requires the bin size to be relatively small so that the method of fitting still holds true. Many existing models use a data sampling interval of 20 or more seconds, however, we find that for this method of selection to be successful the data require a smaller sampling interval of, for example, 5 seconds.

For the September dataset used in all the examples there are noticeably more data selected near the South pole than the North. Other examples show a variety of selections, with some of the example datasets providing very little data selected in either polar region, some showing an even selection in both poles and some selecting more data in one pole than the other.

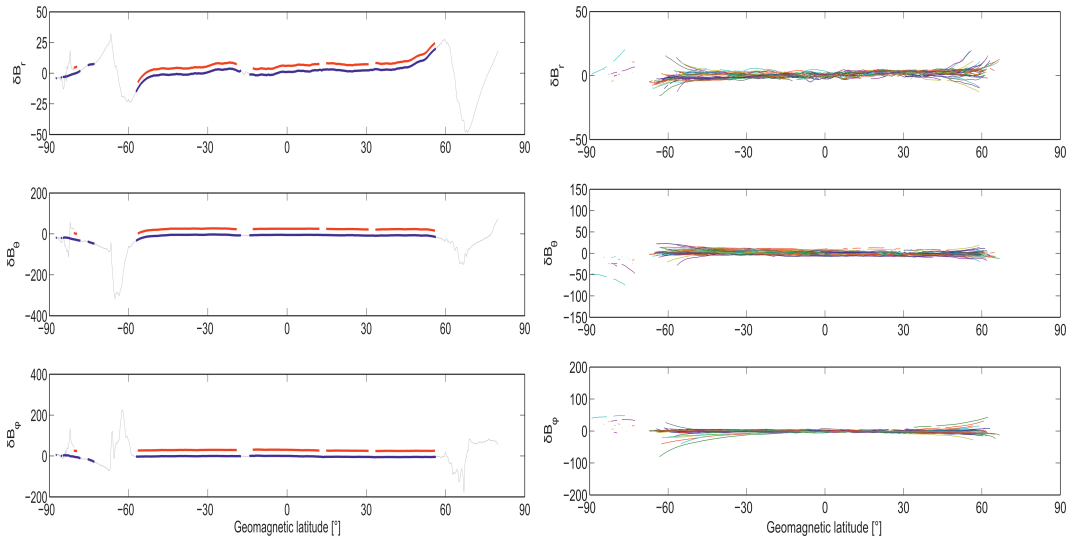

Figure 4.11: Selection using the standard deviation of residuals to a polynomial fit for standard deviation < 0.2 nT (in red, plotted with an offset) compared to the selection using standard deviation < 0.5 nT (blue). Plot on the right is the selection for all orbits in the September dataset for a standard deviation < 0.2 nT

4.4 Auroral Oval Summary

The auroral oval is clearly correlated with large satellite data residuals (Figure 4.1), and is the main source of noise in satellite data at high latitudes. In geomagnetic field modelling it is important that the data selection technique employed can identify, and therefore exclude data from this region. Currently, most modellers choose to avoid all vector data polewards of a fixed limit in geomagnetic latitude (either $\pm 50°$ or $\pm 60°$). We believe that more vector data could be used at high latitudes if the location of the oval is used to define the noisiest regions.

Models exist for identifying the location of the auroral oval (e.g., OVATION) which could be used to exclude data in this region (Figure 4.2). However, practical difficulties in using such models mean we need to look to other methods. Residuals with respect to *a priori* geomagnetic field models (Section 4.2.1) can also be used to provide information about the location of the oval. However, this leads to a circular argument where the initial choice of model will bias the data selected.

We have shown that it is possible to use the data alone to identify the noisiest parts of orbits which are related to external field sources. By estimating the expected value of a point, using a polynomial fit to nearby data points, we create a series of differences between the actual and expected values. Selections are then made based on the standard deviations of this de-trended dataset. Figure 4.11 shows that when we use this method we identify quiet data polewards of $\pm 60°$ geomagnetic latitude which have small residuals compared to existing models. When combined with the selection criteria in the following chapter (Chapter 5) this will enable an optimal

selection of quiet data at high latitudes.

Chapter 5

Identifying Low Activity Data in Satellite Magnetic Surveys

As discussed in section 2.6.2 there are many criteria which allow the selection of quiet (i.e. containing low magnetic activity of external origin) satellite data for use in internal models of the Earth's magnetic field. The data are generally selected to be night-side only and to fulfil criteria based on the K_p and D_{st} indices (see Section 2.4 for more on these indices). Furthermore, at high geomagnetic latitudes, vector data are typically discarded to limit the influence of field-aligned currents.

Here we investigate the possibility of identifying quiet vector data in the polar regions by examining indices that are better suited to the high latitude regions, and investigating new data selection techniques.

5.1 Using Magnetic Indices

Most models use magnetic indices as part of the data selection criteria (e.g., *Maus et al.*, 2008; *Thomson et al.*, 2010; *Olsen et al.*, 2010b). Most commonly used are the K_p and D_{st} indices. However, these indices have been found to be a poor indicator of activity at high latitudes (*Ritter et al.*, 2004b, and references therein). This is also evident from the plots in Chapter 3; all the data shown in Figure 4.4, for example, were selected with $K_p < 2o$ which is traditionally considered to be an upper bound on quiet conditions; however, near the poles there are clearly active regions which were not identified. Here we investigate the use of two regional indices for data selection: the Polar Cap (PC) and Auroral Electrojet (AE) indices. The PC index provides a measure of polar cap disturbance and the AE indices are a measure of activity in the auroral zone. For more information about these indices see section 2.4.

Figure 5.1 contains the Northern (PC_N, top plot) and Southern (PC_S, bottom plot) Polar Cap indices plotted against time. Also shown are the averages and standard deviations of the residuals (CHAMP minus CHAOS-2) for the ϕ (east)

component of data on 15th March 2001. The green and pink bands identify when the satellite is near the North (co-latitude $< 40°$) and South (co-latitude $> 140°$) geographic poles respectively. There is some indication that the residuals increase in size with PC, particularly their standard deviation, but it is far from conclusive at these low values of PC.

For more disturbed data (Figure 5.2), when the PC indices have more variation, there is better correlation between higher levels of PC and increased residuals, particularly for the South. In the North there are larger residuals when PC is higher, for example, after around 15:00 hours; however, there are also occasions when there are larger residuals seen even when PC is close to zero, for example, just after 10:00 hours. This would suggest that PC does quantify to some extent the size of the residuals but it does not provide the full picture.

Figures 5.3 and 5.4 contain plots of the AE index (top), with the averaged residuals and standard deviations also shown (as for PC above). The green and pink bands again indicate the northern and southern parts of the orbits, respectively. For 16th March (Figure 5.3) there is a clear increase in the magnitude of the residuals and standard deviations at approximately the same time as the AE index increases (>100nT increase at ∼1500 UT), although in the Southern Hemisphere this increase slightly precedes the AE index. This is probably due to the fact that the AE index uses only Northern Hemisphere observatories, and so will not capture all features of the southern auroral oval. On 15th March (Figure 5.4) the residuals are larger when the AE index increases (at ∼0700 UT); however, they do not decrease again when the AE index does; this suggests that the ionospheric currents remain energised and are slower to dissipate. The residuals shown are for the ϕ component, but we see the same pattern in all three components.

The examples for March show the most correlation of any of the datasets used in this study making it difficult to draw any firm conclusions. For the other days and months studied in this thesis (not shown here) the AE index is smaller overall, suggesting that the residuals may only be affected by AE when it reaches some threshold value.

Figure 5.5 contains scatter plots of the residuals with respect to CHAOS-2 against the indices. For PC North (South) only residuals for colatitudes $< 40°$ ($> 140°$) are plotted; for AE the residuals are plotted if they are within $40°$ colatitude of either pole. The left column shows the residuals for the quiet dataset in March, on the right is the disturbed dataset from September. Whilst there is no obvious linear correlation in these plots the disturbed plots in particular do show a general increase in the size of residuals with increasing indices. Although the relationship is not completely clear it suggests that it is still of value to set an upper limit for the indices, above which external field signal can be expected to be a significant component of the data.

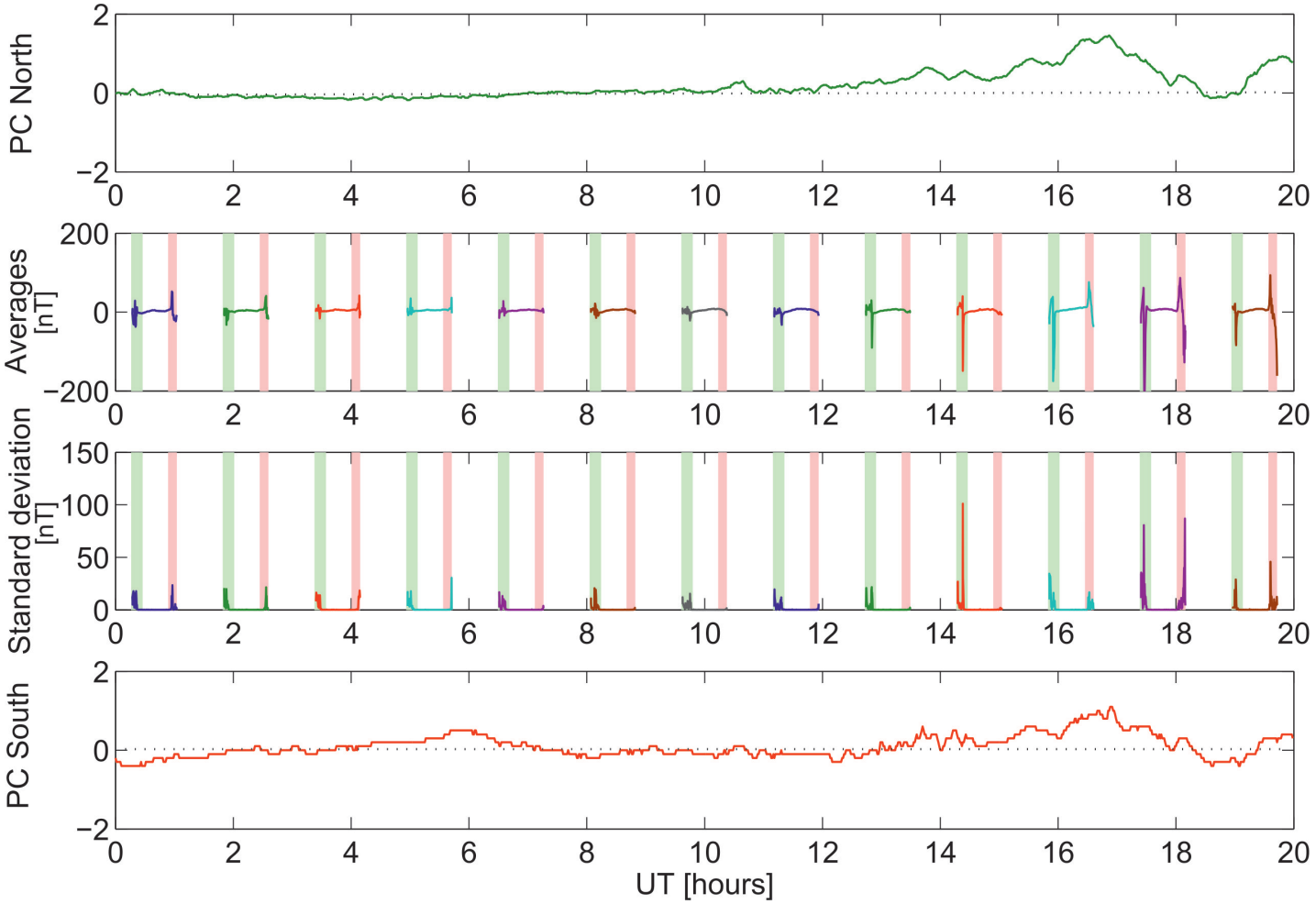

Figure 5.1: A comparison between the Polar Cap indices and the averages and standard deviations of the residuals. Top row, PC_N, second and third rows, averages and standard deviations of the residuals (CHAMP-CHAOS-2 in the ϕ component) in 1° bins of colatitude, bottom row, PC_S, for the 16th March 2001. Green and pink shading represents when the satellite is within 40° latitude of the North and South poles respectively.

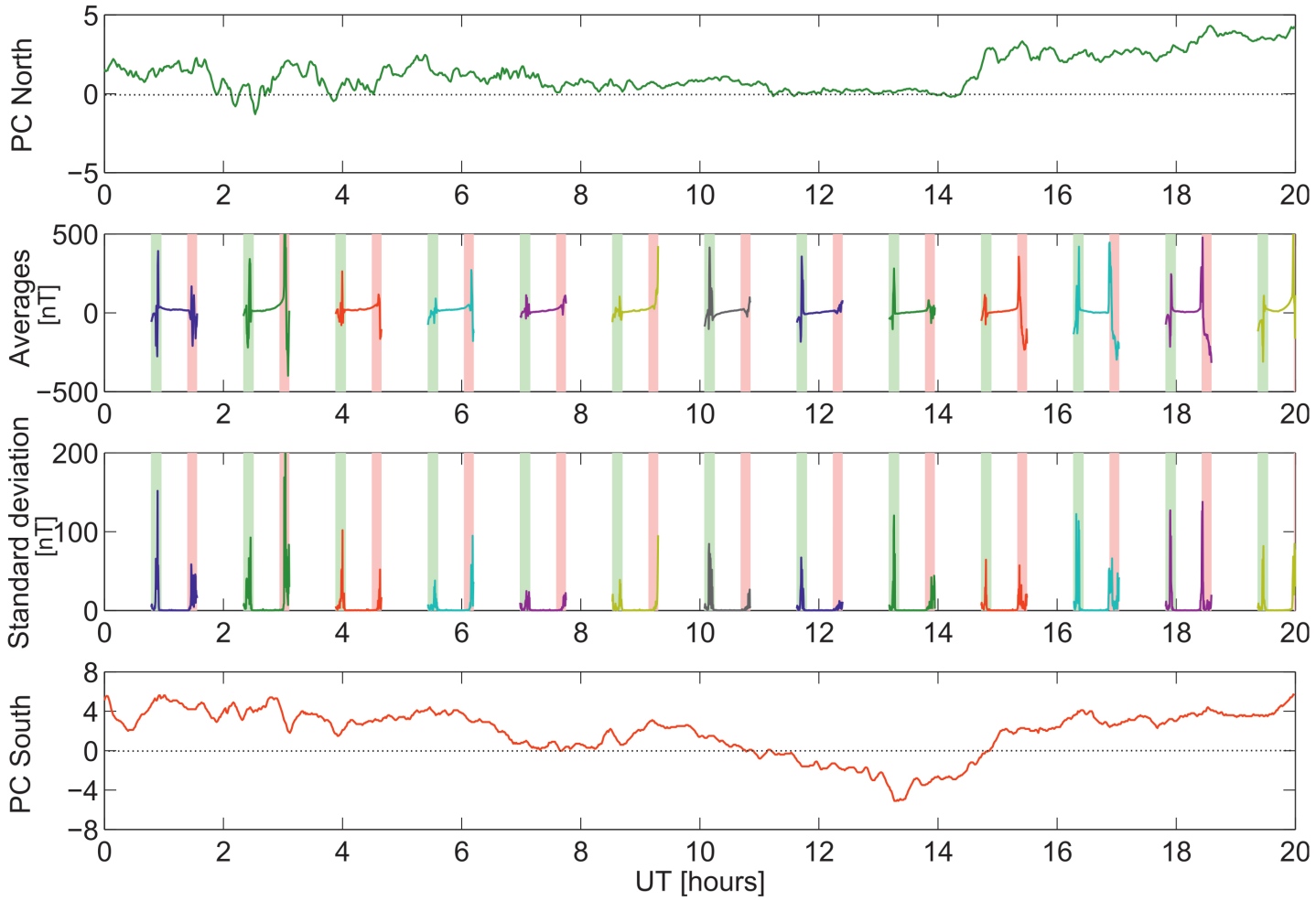

Figure 5.2: A comparison between the Polar Cap indices and the averages and standard deviations of the residuals. Top row, PC_N, second and third rows, averages and standard deviations of the residuals (CHAMP-CHAOS-2 in the ϕ component) in 1° bins of colatitude, bottom row, PC_S, for the 30th December 2001. Green and pink shading represents when the satellite is within 40° latitude of the North and South poles respectively.

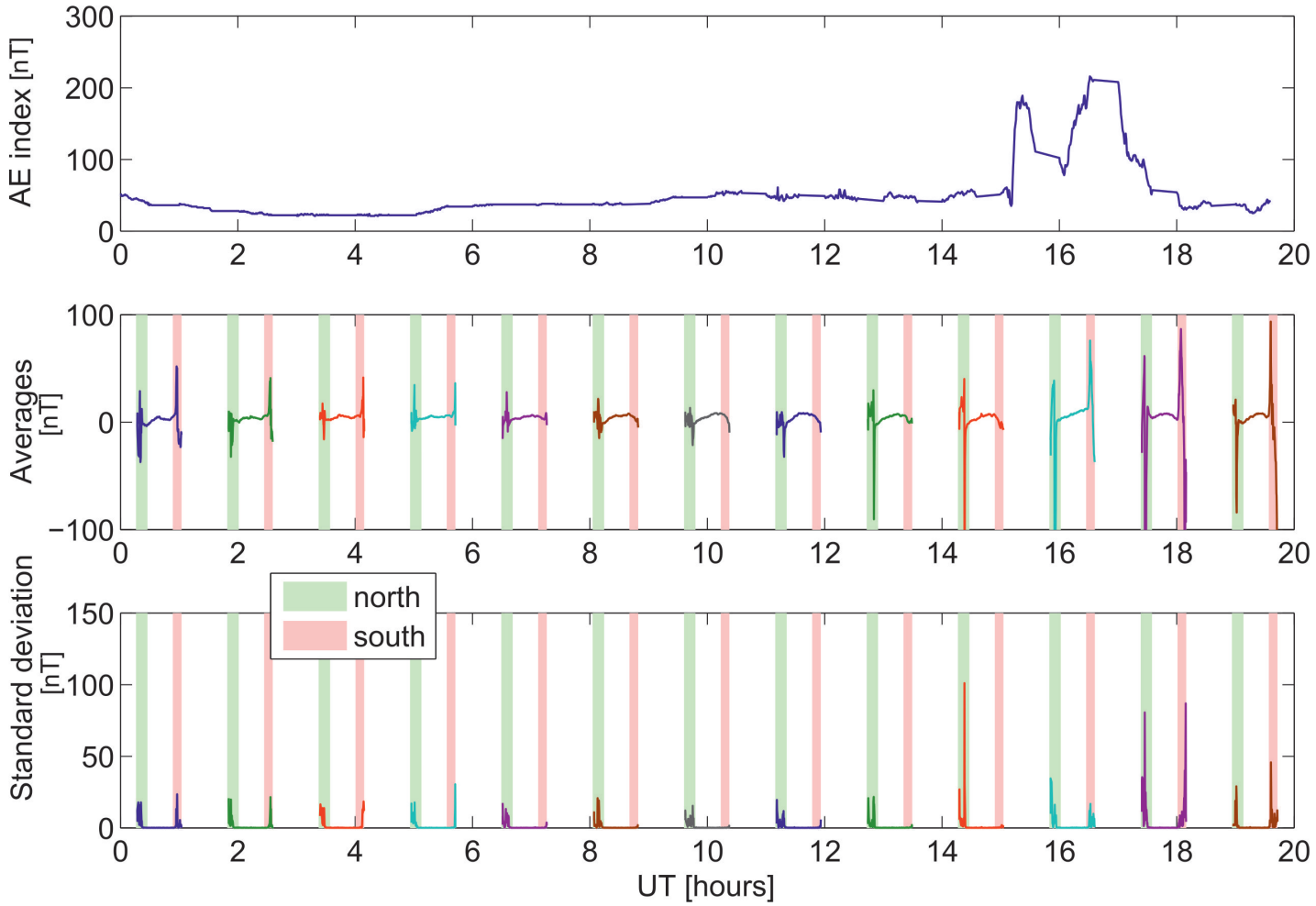

Figure 5.3: A comparison between the Auroral Electrojet index and the averages and standard deviations of the residuals. Top row, AE index, second and third rows, averages and standard deviations of the residuals (CHAMP-CHAOS-2 in the ϕ component) in 1° bins of colatitude, for the 16th March 2001. Green and pink shading represents when the satellite is within 40° latitude of the North and South poles respectively.

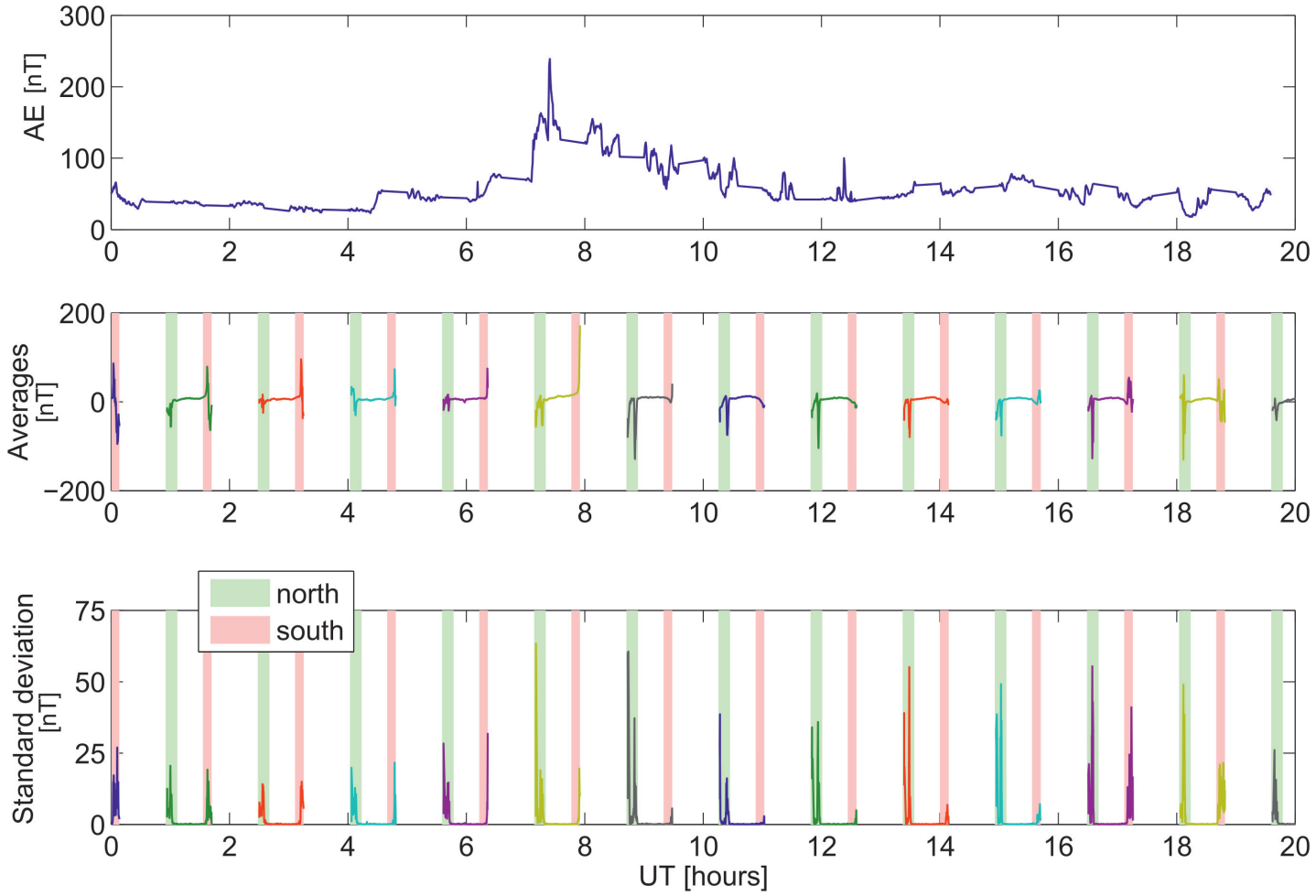

Figure 5.4: A comparison between the Auroral Electrojet index and the averages and standard deviations of the residuals. Top row, AE index, second and third rows, averages and standard deviations of the residuals (CHAMP-CHAOS-2 in the ϕ component) in 1° bins of colatitude, for the 15th March 2001. Green and pink shading represents when the satellite is within 40° latitude of the North and South poles respectively.

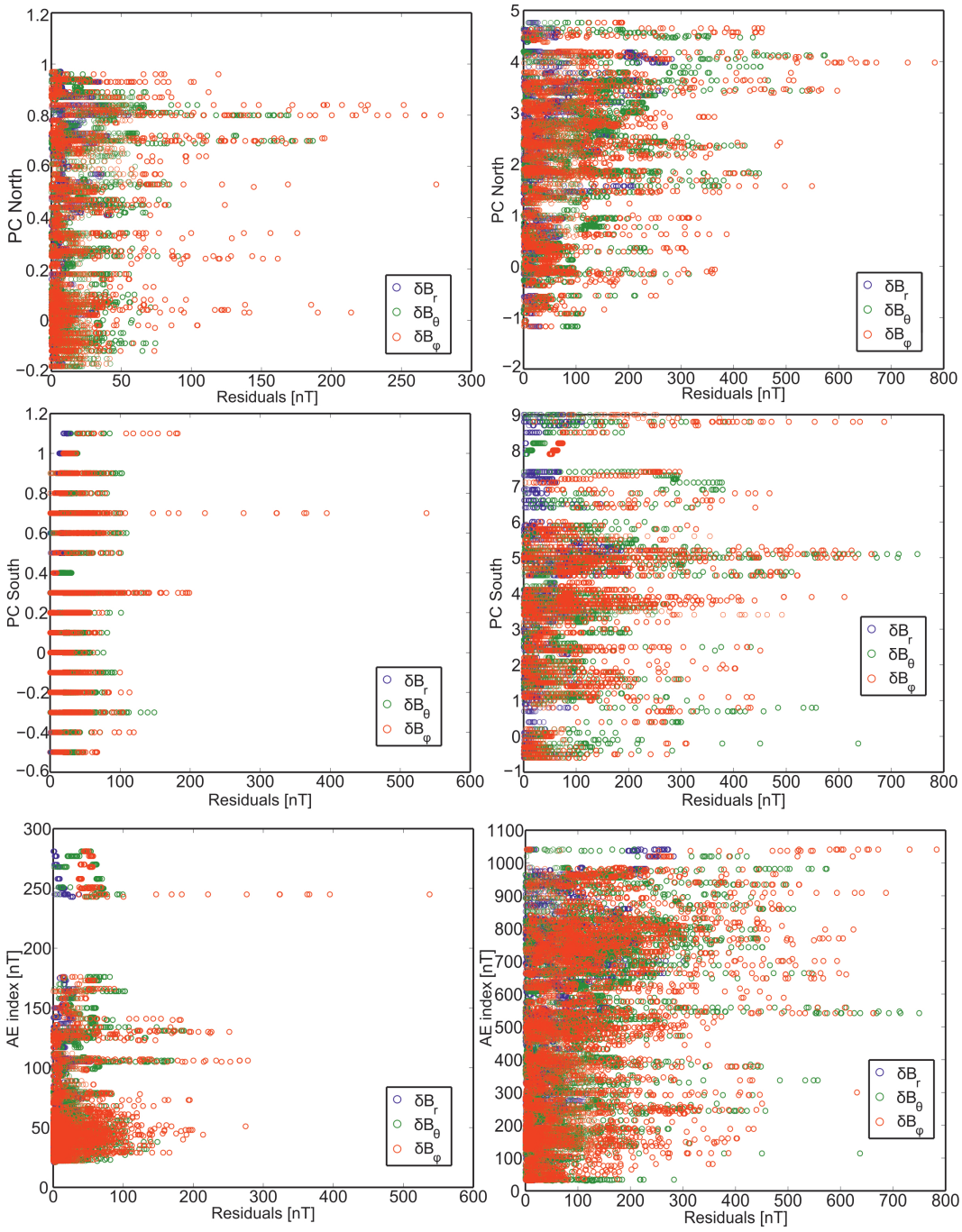

Figure 5.5: Plots of the magnitude of residuals (CHAMP-CHAOS-2) against size of indices for the ϕ component of the quiet March dataset (left) and the disturbed September dataset (right). For PC_N and PC_S only data within $40^circ\theta$ of the North and South poles respectively are plotted.

Kp	AE	PC	No. data selected	% data selected
2+	none	none	16135	48.1
none	100	2	13703	40.8
2+	100	2	13072	38.9
2+	50	2	11309	33.7

Table 5.1: Examples of the number of data selected for the September dataset. The PC and AE selections apply only to data within 40° geomagnetic latitude of the pole. The final column is the percentage of data selected using these indices from the original dataset.

Table 5.1 contains the number of data rejected for different selection criteria using the AE, PC and K_p indices for September 2001 dataset. As the AE and PC indices describe high latitude activity they are only used for the 40° of latitude nearest the geomagnetic poles. As might have been expected, using a selection based on the AE and PC indices at high latitudes rejects more data than a selection based on K_p alone in the polar regions.

Figure 5.6 (left column) shows the difference this selection makes to the two-day averages of the residuals (CHAMP-CHAOS-2). The selections that include AE and PC (bottom two rows) reduce the size of the averaged residuals close to the poles, particularly in the South. The effect of this additional selection is strongest in θ (co-latitude), which is probably due to the AE index. The AE index measures strength of the East-West auroral electrojets, which drive North-South magnetic variations; therefore the selection using AE will have most influence on the θ and r components.

Requiring AE to be less than 50 is probably too restrictive, as the averaged residuals are actually larger near both poles than for a limit of AE $\leq$ 100.

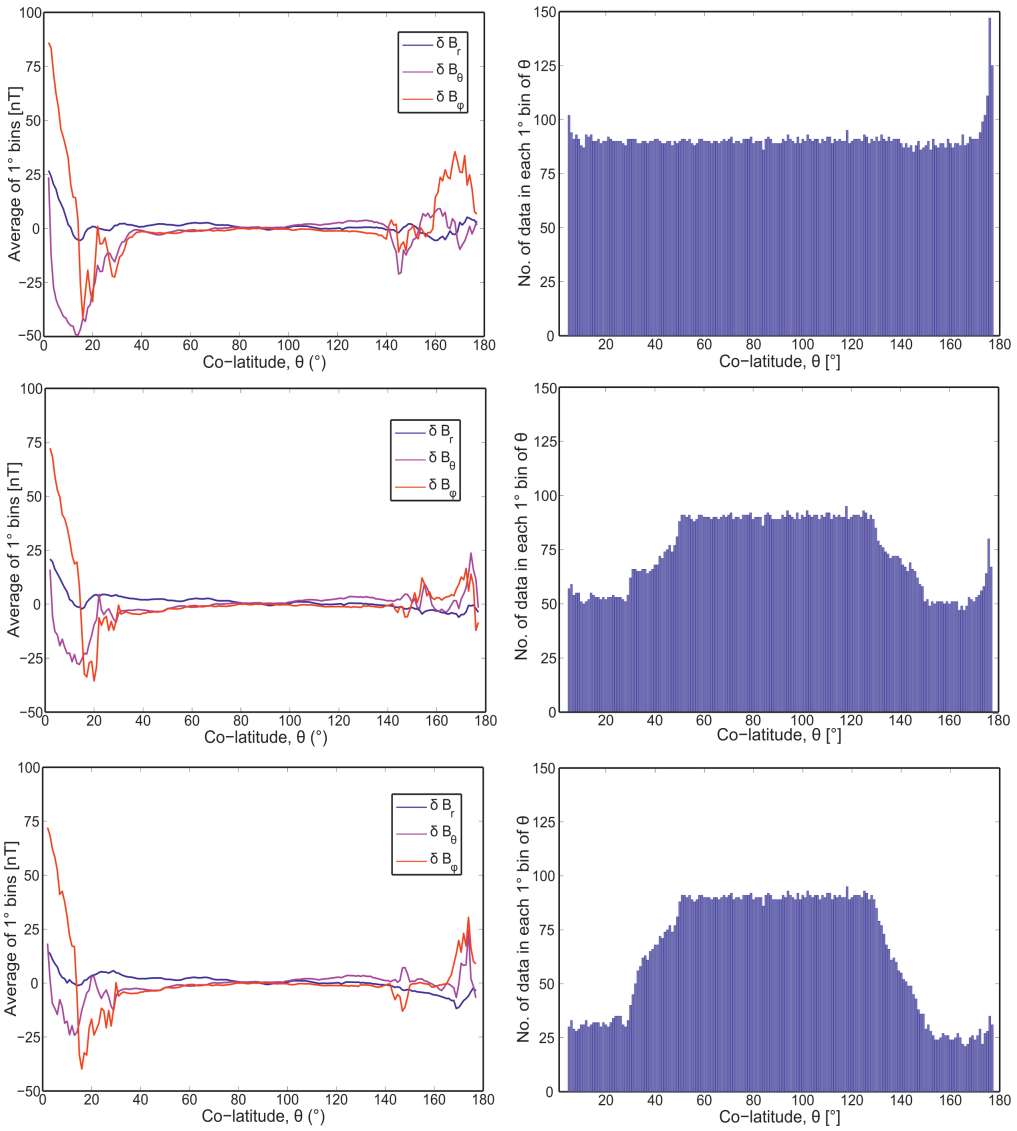

Figure 5.6: Averages of the residuals to CHAOS-2 in 1° bins of colatitude (left) and number of data selected for each degree of colatitude (right) for different data selection criteria. Top row, only K_p <2+, middle row, K_p < 2+, AE≤ 100, —PC—≤ 2, bottom row, K_p <2+, AE≤ 50 and —PC—≤ 2. The spike near the South pole is caused by the geometry of the orbit and the local time window used.

5.2 Estimating the Contribution From External Current Systems

Another possibility for aiding the selection of quiet data is to directly estimate the magnetic field variations associated with external current sources. This could be particularly useful if the means for doing so are independent from the satellite data, for example, by using data from observatories. Here we investigate the usefulness of this approach using the technique of Spherical Elementary Current Systems.

5.2.1 Spherical Elementary Current Systems

Spherical Elementary Current Systems (SECS) allow the estimation of ionospheric currents from magnetic measurements. This information can then be used to estimate the magnetic field due to ionospheric currents at any point on the Earth's surface.

Amm (1997) defined two types of spherical elementary (sheet) current systems, one divergence free ($\vec{J}_{el,df}$) and the other curl free ($\vec{J}_{el,cf}$) (depicted in Figure 5.7):

$$J_{el,df}\left(\theta'\phi'\right) = \frac{I_{0,df}}{4\pi R_I}\cot\left(\frac{\theta'}{2}\right)\hat{\mathbf{e}}_\phi \tag{5.1}$$

$$J_{el,cf}\left(\theta'\phi'\right) = \frac{I_{0,cf}}{4\pi R_I}\cot\left(\frac{\theta'}{2}\right)\hat{\mathbf{e}}_\theta \tag{5.2}$$

Their definition is in spherical coordinates (r', θ', ϕ') with unit vectors $(\hat{\mathbf{e}}_{\mathbf{r}'}, \hat{\mathbf{e}}_{\theta'}, \hat{\mathbf{e}}_{\phi'})$, with the pole of the elementary system at $\theta' = 0$. $I_{0,df}$ and $I_{0,cf}$ are the amplitudes of the scaling factors, and R_I is the radius of the ionosphere.

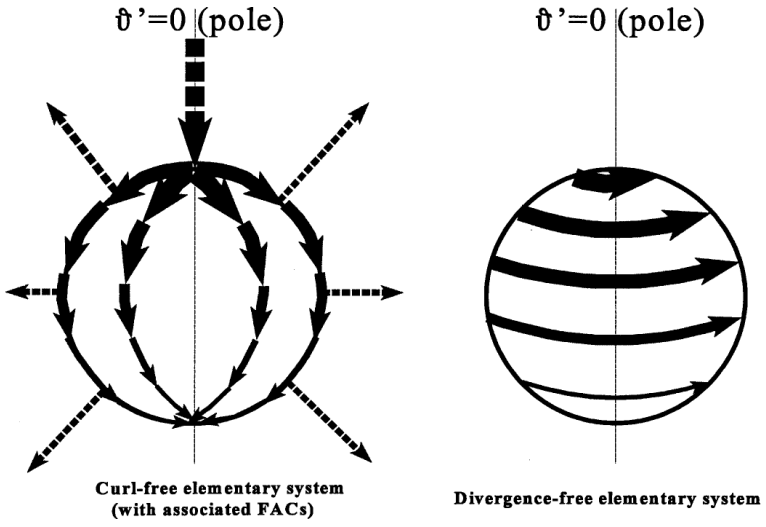

Figure 5.7: Sketch of the curl-free and divergence-free elementary systems from *Amm and Viljanen* (1999)

The curl free elementary system is associated with field aligned current at its

pole ($\theta' = 0$) and oppositely directed small FACs of constant latitude elsewhere (*Amm and Viljanen*, 1999). Below the ionosphere FACs and Pedersen currents have been shown to cancel each other out (*Fukushima*, 1976), so ground based data only contain a signature from Hall currents. This means that only the divergence free currents are required below the ionosphere.

For a point with radius $r < R_I$ the magnetic field effect of a divergence-free current system, flowing at $r = R_I$, is

$$B_{r'}\left(r,\theta'\right) = \frac{\mu_0 I_0}{4\pi r}\left(\frac{1}{\sqrt{1-\frac{2r\cos\theta'}{R_I}+\left(\frac{r}{R_I}\right)^2}}-1\right) \tag{5.3}$$

and

$$B_{\theta'}\left(r,\theta'\right) = -\frac{\mu_0 I_0}{4\pi r\sin\theta'}.\left(\frac{\frac{r}{R_I}-\cos\theta'}{\sqrt{1-\frac{2r\cos\theta'}{R_I}+\left(\frac{r}{R_I}\right)^2}}+\cos\theta'\right) \tag{5.4}$$

where θ' is the pole angle from the pole of the elementary current system. $B_{\phi'}$ is zero and there is no ϕ' dependence. For full details of the calculation of the magnetic field see *Amm and Viljanen* (1999).

Ground based observatory data are used here as they are independent of the magnetic satellite data we want to select. Because observatories are at fixed locations they only experience temporal variations of the magnetic field. This allows a quiet night-time value to be subtracted as an approximation of the internal field, leaving only the external variations.

As the component in the direction of the field ($\mathbf{B}$) is free from FACs (as discussed in Section 3.3.2) we compare this component to the divergence free SECS estimates. The SECS estimates require a good coverage of observatory data so we chose two orbits over Europe and two over North America to investigate. The locations of the European orbits and observatories are shown in Figure 5.8 and the N American locations are shown in Figure 5.9. The dashed lines mark the boundaries of the grids used; for Europe the same grid is used for both orbits. The yellow triangles mark the locations of the observatories that were used in the SECS estimates for all the orbits shown in each plot, the red and blue triangles indicate observatories that were only used for one orbit. The orbits used come from the September (blue) and March (red) datasets, with the numbers indicating the orbit number within the dataset.

Figure 5.10 contains the CHAOS-2 residuals and SECS estimates for two orbits over Europe. The SECS estimates are separated into the magnetic field contributions from external and internal (induced) currents. The SECS estimates are approximately the same order of magnitude as the CHAOS-2 residuals, although it is hard to identify any close correlation from these plots.

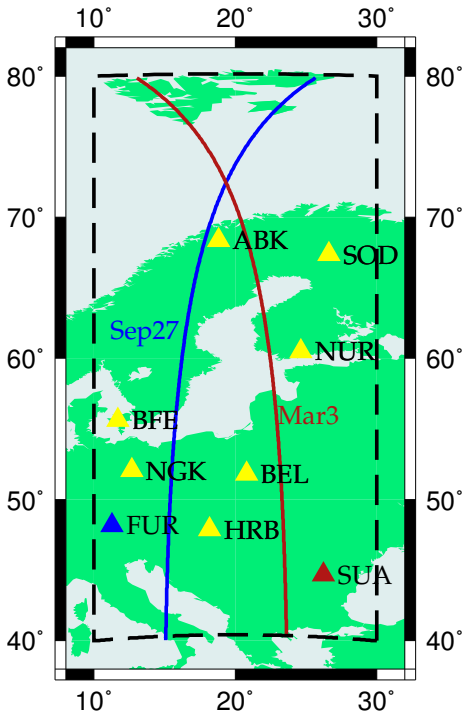

Figure 5.8: Locations of European observatories and orbits used to estimate SECS. The observatories shown in yellow were used for both orbits, SUA was only included in the estimation of orbit Mar3 and FUR was only used for orbit Sep27. The dashed line marks the boundary of the grid used.

Figure 5.11 contains plots of the CHAOS-2 residuals and SECS estimates for two orbits over N America. Again, for March orbit 8 (top) the SECS estimates are much more similar to the CHAOS-2 residuals than the European examples. September orbit 16 (bottom) shows the most similarity between the residuals and SECS estimates. It is maybe surprising that this last example appears to do the best, as the observatories have a larger longitudinal spread for this orbit. However, this orbit does have the widest latitudinal distribution of observatories suggesting that having data for all latitudes is more important than requiring observatories to be closely spaced in longitude.

We also investigated whether there are more similarities between the SECS estimates and the residuals if we take the difference between CHAMP and only the internal part of CHAOS-2, so that the residuals approximately represent the external field at the satellite. The example in Figure 5.12 shows that when we do this the CHAOS-2 residuals have a strong linear trend, increasing in magnitude towards the North pole; this suggests a long wavelength external field. The magneta line in the figures is a de-trended version of the residuals. Once de-trended the CHAOS residuals are much closer to the SECS estimates. Figure 5.13 is another example, this time for the N American observatories. In this example the CHAOS residuals do not show such a strong linear trend, however de-trending the residuals does still

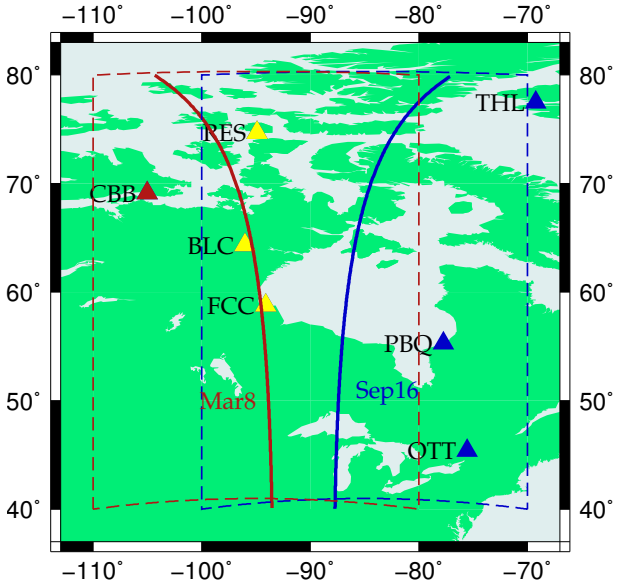

Figure 5.9: Locations of North American observatories and orbits used to estimate SECS. The observatories marked in yellow were used for both orbits, CBB was only included in the estimation of orbit Mar8 and the observatories shown in blue were only used for orbit Sep16. The dashed lines mark the boundary of the grids used for Mar8 in red and Sep16 in blue.

bring them closer to the SECS estimates.

It is not immediately obvious that there is a clear relation between the SCES estimates from observatory data and the satellite residuals that could be exploited for data selection. The main drawback of this method is the difference in altitude between the SECS estimates and the satellite residuals. However, to upward (or downward) continue the SECS estimates (satellite residuals) would require careful consideration of FACs and other ionospheric currents, and the problem is no longer purely divergence free. This is beyond the scope of this study. It is possible to use satellite data to calculate the SECS at satellite altitude. However in this study we were looking for an independent measure of the ionospheric currents to aid in the selection of satellite data.

The uneven global distribution of observatories is also a hindrance. In Europe and N America there is a relatively dense coverage of observatories, however, for much of the rest of the globe the satellite orbits would be too far from any observatories to be able to calculate meaningful SECS estimates.

We therefore conclude that although the SECS approach has merit, there are practical drawbacks (observatory distribution, satellite altitude and the presence of FACs) that mean it is not appropriate for our purpose: the rapid automated processing of large satellite magnetic survey datasets.

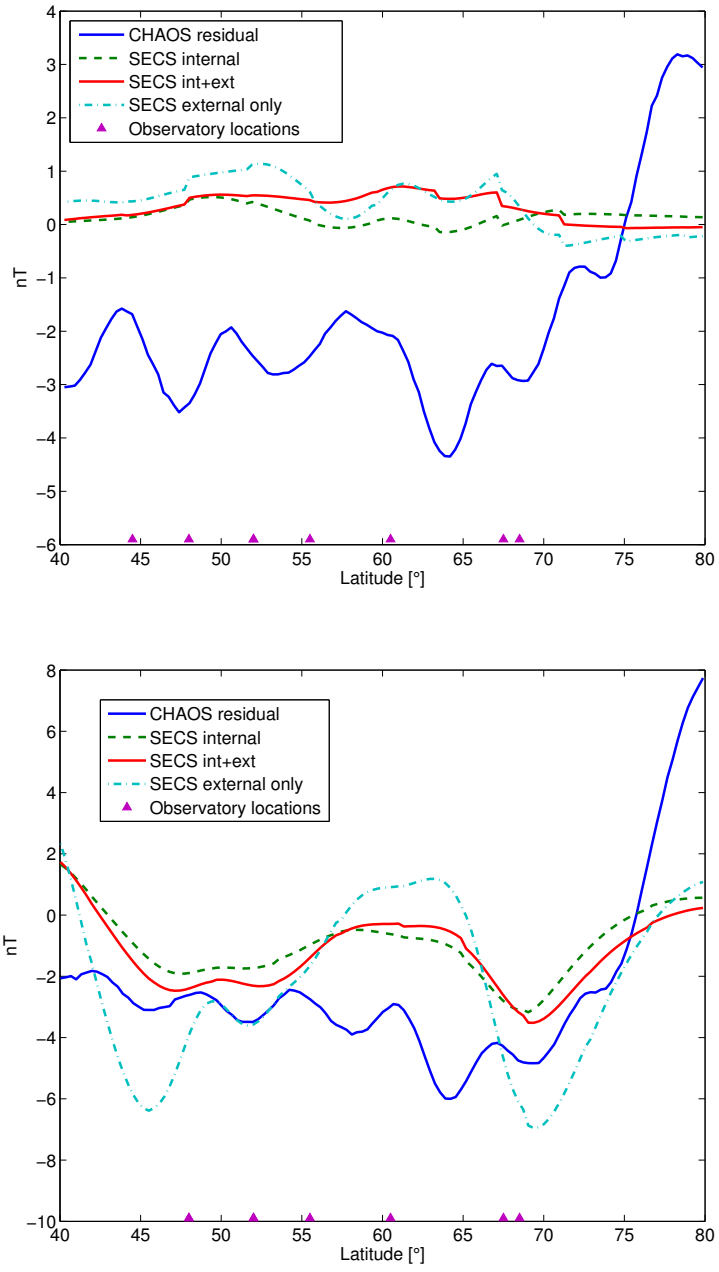

Figure 5.10: SECS estimates using European observatories for March orbit 3 (top) and September orbit 27 (bottom).

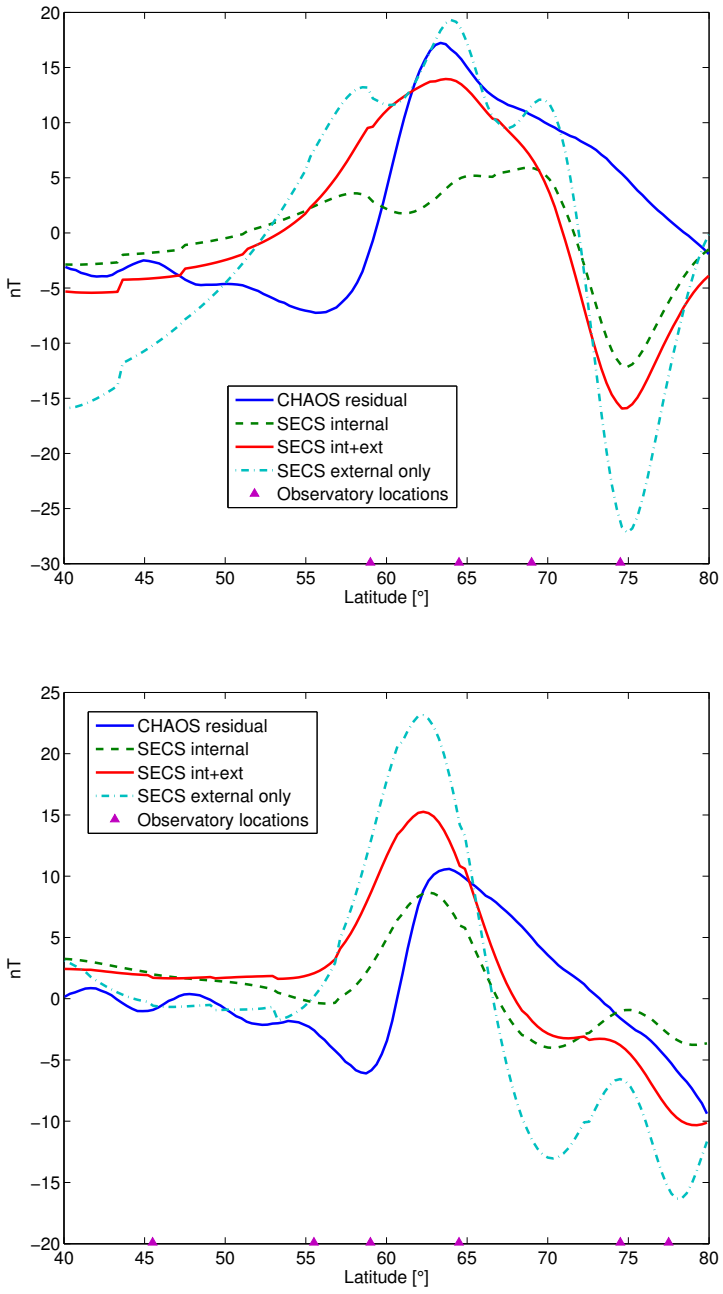

Figure 5.11: SECS estimates using N American observatories for March orbit 8 (top) and September orbit 16 (bottom).

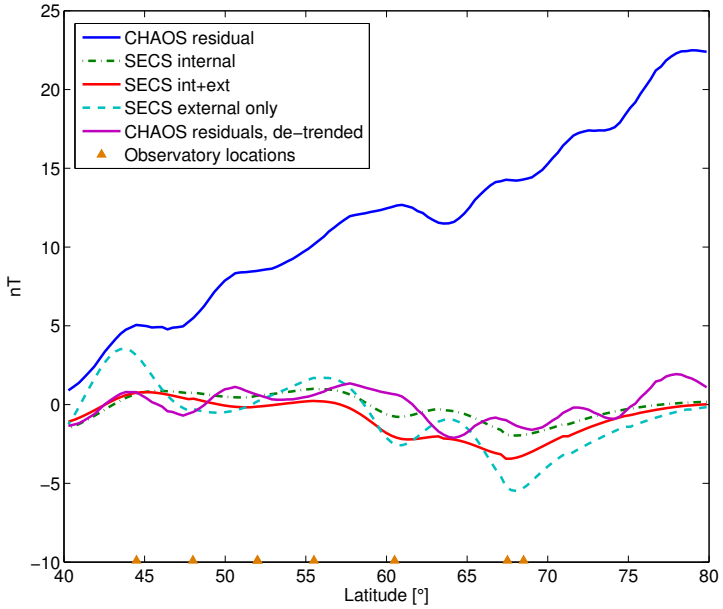

Figure 5.12: SECS estimates using European observatory data for March orbit 3 compared to residuals between CHAMP and the internal part of CHAOS-2.

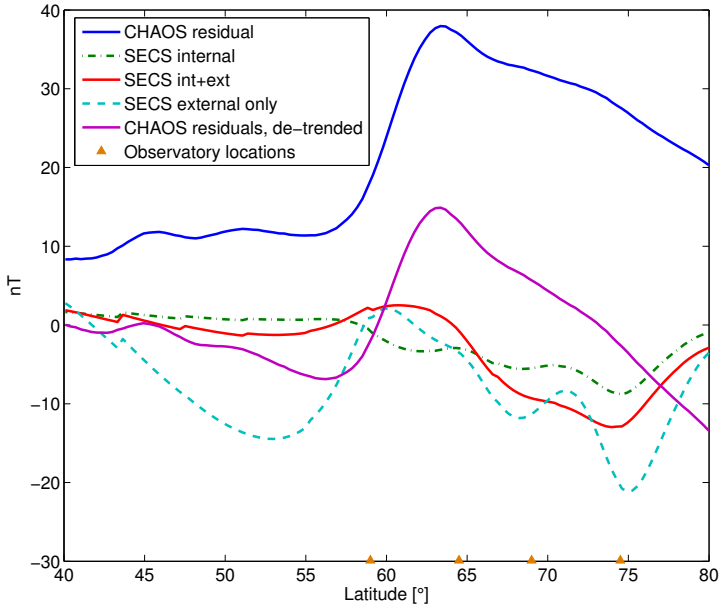

Figure 5.13: SECS estimates using N American observatory data for March orbit 8 compared to residuals between CHAMP and the internal part of CHAOS-2.

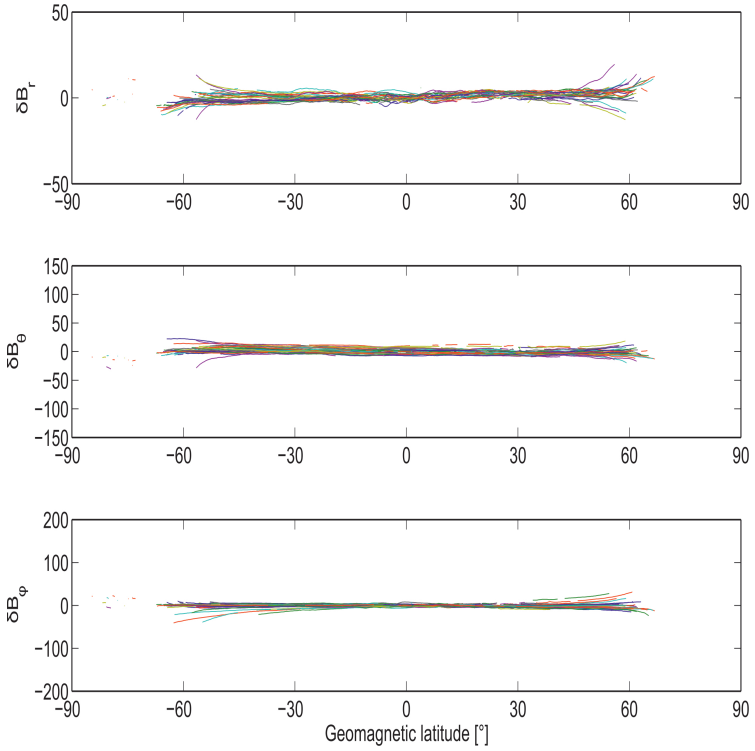

Figure 5.14: Final data selection criteria, $|PC| \leq 2$ and $AE \leq 100$ and standard deviation < 0.2nT of the residuals to a polynomial fit to the data for 8th-9th September 2001

5.3 Final Data Selection Criteria

The different selection criteria that we have examined can be combined by experimentation to determine an overall 'best' selection. Figure 5.14 shows the data selected for the two-day September dataset using just such a combination of criteria: $|PC| \leq 2$, $AE \leq 100$ and a standard deviation limit of 0.2nT after a polynomial fit to the data (outlined in the previous chapter 4). There is a clear reduction in signals related to field-aligned currents (compared to using indices alone) and the residuals are smaller in general than when only the oval selection is used. Figure 5.15 contains plots of the averaged residuals (CHAMP minus CHAOS-2) for this selection. The averages are noticeably reduced compared to using any single technique in isolation.

Table 5.2 shows the percentage of each selection which is vector, along with the percentage of all of the available data which were selected. Again the most data are excluded when all three indices are used, resulting in a higher percentage of vector data in the final selection. This is good as it means the final data selected are more uniform overall (provided a good global coverage is maintained).

Kp	AE	PC	% vector data in selection	% vector data selected
2+	none	none	64.5	31.0
none	100	2	71.5	29.2
2+	100	2	72.0	28.0
2+	50	2	79.0	26.6

Table 5.2: Example selections for the September dataset with four different combinations of indices, with the selection based on the standard deviation of the de-trended dataset added as a final stage of selection. The last two columns represent the percentage of the final selection which is vector data, and the number of vector data selected from the original dataset expressed as a percentage.

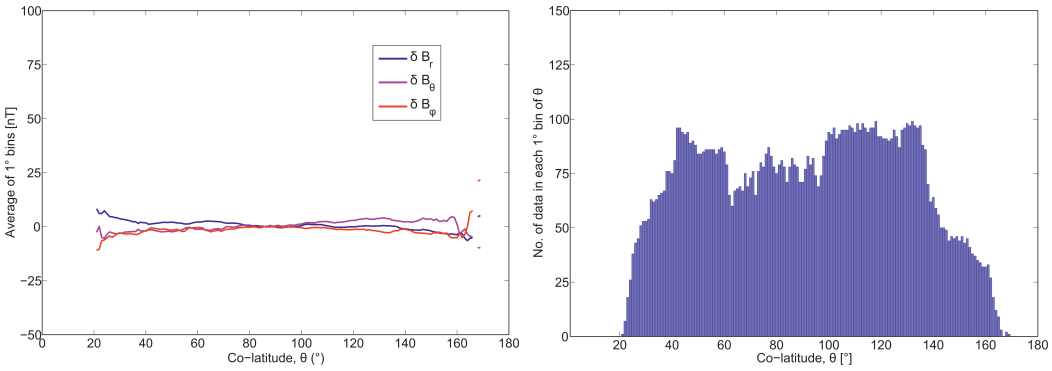

Figure 5.15: Averages of the residuals to CHAOS-2 in 1° bins of colatitude (left) and number of data selected for each degree of colatitude (right) for the data selection criteria: K_p <2+, AE$\leq$ 100 and |PC| $\leq$ 2 and a standard deviation $<$ 0.2nT after a polynomial fit to the data from 8th-9th September 2001.

5.4 Selection Summary

The AE and PC indices provide a measure of activity in the high latitude regions. There is some correlation between high values of these indices and large satellite data residuals. Unfortunately, there are some problems with these indices; the AE index is based on data from only the Northern hemisphere, and is not generally available for several years, which would hamper its use with Swarm, for example. There is also still much debate about whether the method for calculating the PC index is truly unified for the Southern and Northern versions of the index (e.g., *McCreadie and Menvielle*, 2010). In the example for the 15th March (Figure 5.4), the standard deviation values are much smaller in the Southern Hemisphere than the North, indicating that this event was localised in the North.

In spite of these difficulties we still believe it is valuable to use and set limits for PC and AE to exclude noisy data, i.e. data with substantial contribution from external fields. From extensive experimentation we choose a limit of AE $\leq$ 100 and |PC| $\leq$ 2. We come to these figures because they leave the smallest residuals to CHAOS whilst leaving an adequate coverage of data. This PC threshold is in agreement with *Lukianova et al.* (2002) who independently determined a range of 0 <PC< 2 as representing quiet in their work on the Northern and Southern PC indices.

The ionospheric currents, estimated using the Spherical Elementary Current System (SECS) method (*Amm and Viljanen*, 1999), are generally of a similar magnitude to the residuals to the satellite data. However, the latitude dependence of the signal from ionospheric currents does not match that of the residuals. Additional complications arising from upward (or downward) continuation of small amplitude, spatially localised ionospheric sources, and the uneven distribution of magnetic observatories means this method is not pursued further for the purpose of data selection.

In the previous chapter we found a method to identify the location of the auroral oval using standard deviation values for a de-trended data set. When this is combined with the selection using the PC and AE indices the residuals to CHAOS-2 are reduced (Figures 5.14 and 5.15) and the percentage of the selected data which is vector data is increased (Table 5.2). In the following chapter we investigate how these new combined selection criteria affect the modelling process. We also look at the effect on models from the indices selection and the auroral oval selection separately.

Chapter 6

Modelling the High Latitude Field

Our improved data selection criteria are tested by applying them to datasets to produce new models of the geomagnetic field. The new models are created within the framework of the BGS Global Geomagnetic Model (BGGM, *Hamilton et al.*, 2010), using data for the year 2007. To allow for comparisons between models we create two datasets, one using a 'typical' data selection (see Section 2.6.2) and the other using the criteria outlined in chapter 5. The typical selection uses the following criteria:

- $K_p < 2+$
- $|D_{st}| < 30nT$
- Local time 22:00-04:00
- 20 second sampling
- Scalar data only poleward of $\pm 50^\circ$ geomagnetic latitude

and is referred to as the 'traditional' dataset. The selection using the new criteria, outlined in Chapter 5, uses the following constraints:

- $K_p < 2+$
- $|D_{st}| < 30nT$
- Local time 18:00-06:00
- 5 second sampling
- |PC| $\leq$2
- AE $\leq$ 100

- Scalar data only when the standard deviation of the de-trended data is more than 0.2nT in any of the components (as described in Section 4.3).

and is called the 'vector' set. Five second sampling is necessary for the vector set to allow the standard deviation selection to be meaningful. With a slower sampling rate the satellite covers too great a distance between data points for the method of fitting to remain useful (as discussed in Section 4.3).

We also test two other datasets to assess the new selection criteria individually. One uses exactly the same selection criteria as the traditional set (although with 5 second sampling) but with an additional selection using $|PC| < 2$ and AE < 100 and is referred to as the 'PCAE' dataset. The final selection again uses the same criteria as the traditional dataset (with 5 second sampling), but replaces the $\pm 50^\circ$ geomagnetic latitude limit on vector data with the selection based on standard deviation; this dataset is referred to as the 'oval' selection (see section 6.2.2).

6.1 Distribution of the Selected Data

6.1.1 Distribution of data in time

The number of data selected with the traditional selection are shown in Figure 6.1, plotted against time. It is clear in this plot that there are large periods of time when only a very few data are included; this is due to the narrow local time window. Such variations in data density could produce spurious effects in the modelling process, particularly for any time-dependent parts of the model. Figure 6.2 shows the data density against time for the vector selection. With this selection the distribution of data is much more homogeneous over the whole year.

6.1.2 Global distribution of data

Figure 6.3 shows the vector data that are included in the traditional selection; the abrupt cut-off at 50° geomagnetic latitude is obvious. The vector selection in Figure 6.4 has a much less abrupt boundary to the vector data, with vector data at much higher latitudes and over the poles. The region for which there are only scalar data is much smaller than for the traditional selection. These plots also show the much wider spread of local times included in the vector selection.

6.1.3 Seasonal differences

To investigate any seasonal differences in the selections we plotted the vector data selected for the months around the equinoxes (March and Sepetember) and the solstices (June and December). The traditional selection is shown in Figure 6.5 and the vector selection in Figure 6.6. The traditional selection did not select any vector data (due to inadmissible local times) in March or December, so these plots are not

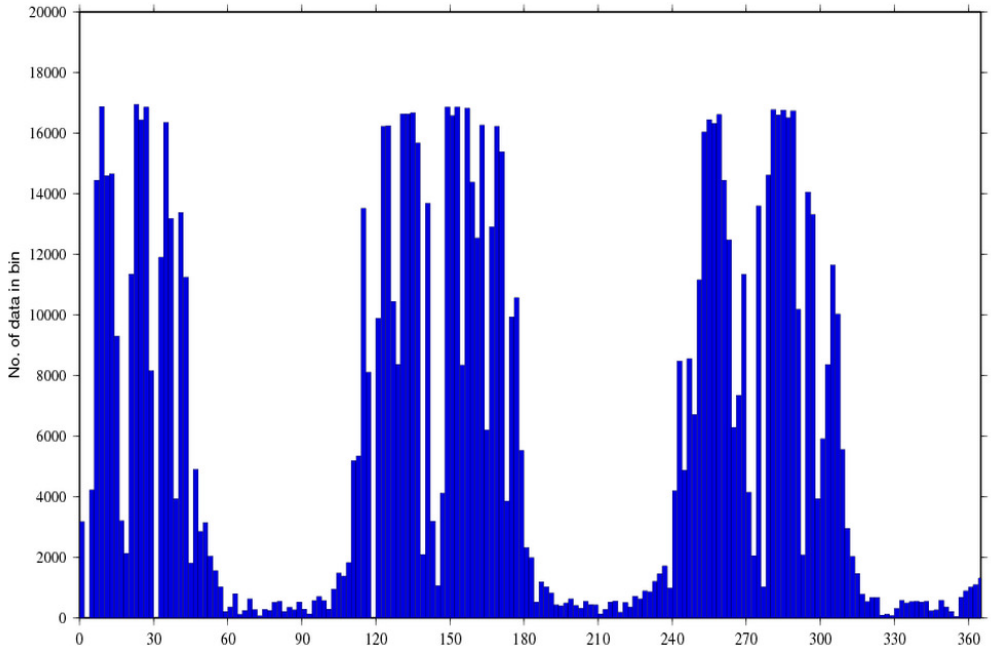

Figure 6.1: Number of data selected (in 2 day bins) for the 'traditional' dataset

shown. Clearly the vector selection has much more vector data than the traditional selection (i.e. March and December) which has far fewer data overall (including scalar) during times when the vector data are missing.

In September the vector selection has much more vector data, particularly at high latitudes. In June (December) we would expect that there would be fewer data selected near the North (South) pole as this pole is mostly sunlit, even during night-time hours. However, the selection is almost even between the two poles, and there appears to be fewer data selected overall than for the equinoxes. Despite this, in June there are still many occasions where there are additional vector data compared to the traditional data selection at high latitudes. However, there is also a less dense distribution of vector data at lower latitudes.

6.2 Global Magnetic Field Models

To test the performance of these selection criteria we use the BGGM modelling code (*Hamilton et al.*, 2010) to create models based on each of the selected datasets. The BGGM consists of a degree and order 60 spherical harmonic expansion with a degree 1 external field. The BGGM includes a degree 13 internal field and piecewise linear secular variation model. The degree 1 external field dependence includes periodic functions for the annual and semi-annual signals, and a dependence on the 20-minute Vector Magnetic Disturbance index (*Thomson and Lesur*, 2007). The data are weighted in according to data density in equal area tesserae (1° x 1° at the equator). The variance of the data is weighted by a weight factor calculated as the

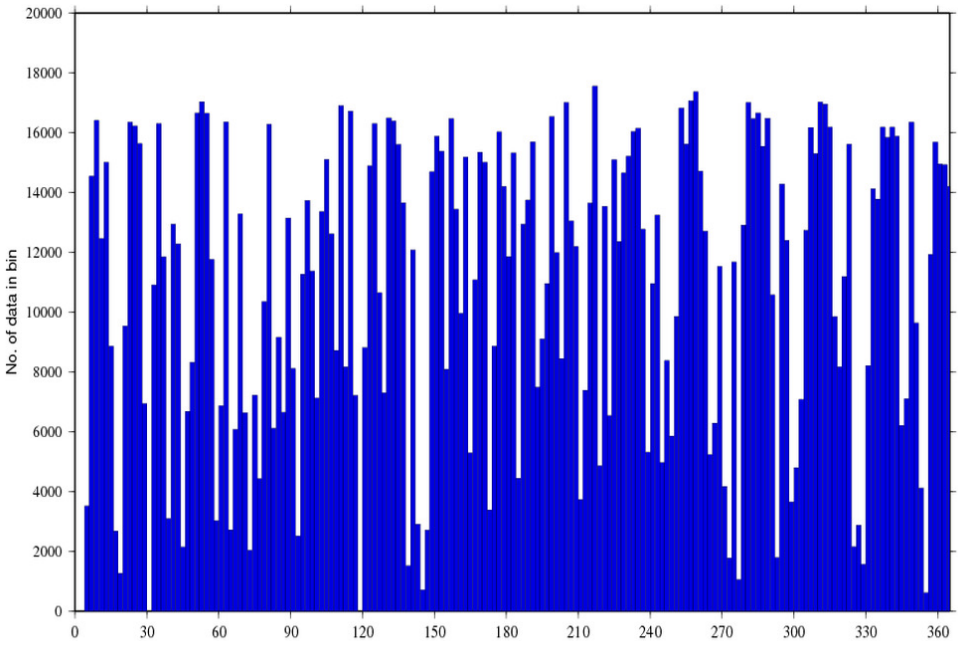

Figure 6.2: Number of data selected (in 2 day bins) for the 'vector' dataset

ratio of the average number of data in all (non-empty) cells to the number of data in the cell. The vector data are assumed to have a pre-weighted variance of 4nT^2; the scalar data variances are defined as

$$\sigma^2 = (\sigma_0 + d_z\,(1 + cos(za)))^2 \tag{6.1}$$

where za is the zenith angle of the sun, $d_z = 2nT$ and $\sigma_0 = 2nT$ for all data (after *Lesur et al.*, 2006). Here we discuss the similarities and differences between the models.

6.2.1 Comparing the 'Vector' and 'Traditional' selections

Models derived from the traditional and vector selections at the Earth's surface (not shown here), appear visually identical at full scale; this is encouraging as it shows that the additional vector data are not creating any spurious effects at high latitudes. For the purpose of brevity only the Z component is shown in the following plots; however, much of what is discussed is also evident in the X and Y components, unless otherwise mentioned. When the differences between the two models are taken, as shown in Figure 6.7, the biggest differences are at high latitudes. This is not surprising considering this is the area where the selections differ the most. The main discrepancies fall approximately within the auroral region, with the largest difference directly over the geographic poles, this is discussed in more detail below. There are also some smaller differences at low latitudes, for example, in the Pacific Ocean, at these latitudes the only difference in selection is in local time. This

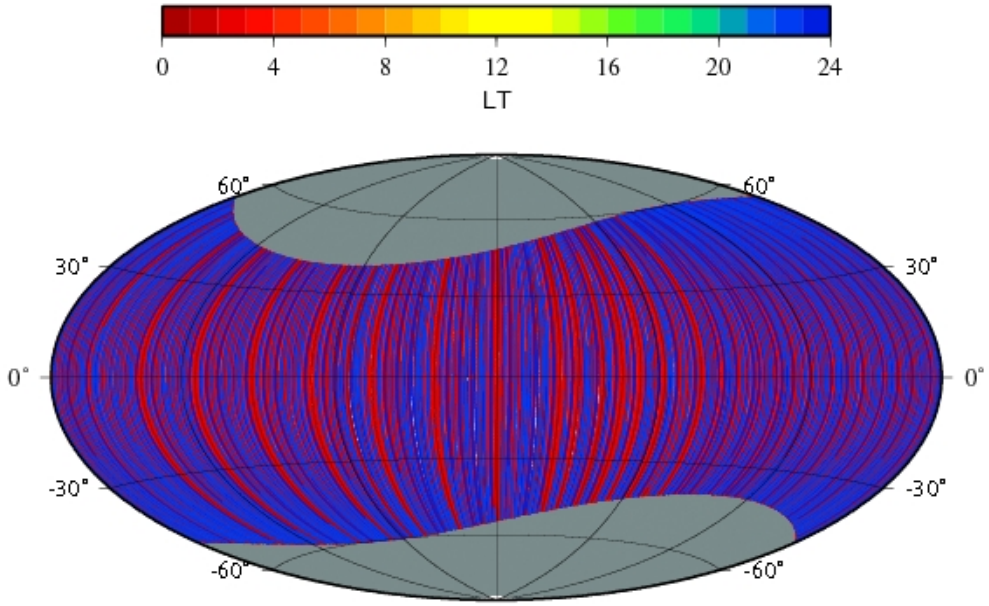

Figure 6.3: Vector data that are included in the 'traditional' selection. The white areas (close to the geographic poles) indicate regions where there are no data, grey indicates only scalar data and the colours represent the local time of the vector data.

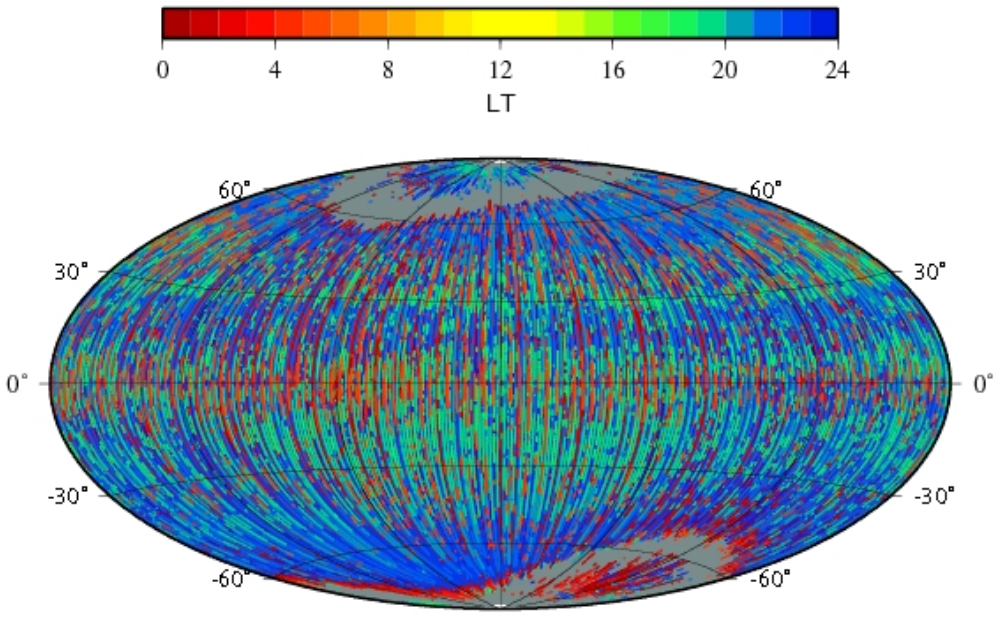

Figure 6.4: Vector data that are included in the 'vector' selection. The white areas (close to the geographic poles) indicate regions where there are no data, grey indicates only scalar data and the colours represent the local time of the vector data.

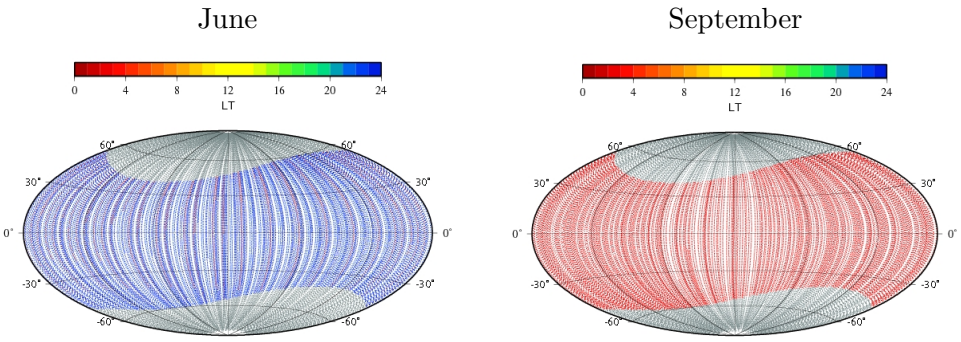

Figure 6.5: Distribution of the vector data selected using the 'traditional' criteria during specific months of the year. The white areas indicate regions where there are no data, grey indicates only scalar data and the colours represent the local time of the vector data.

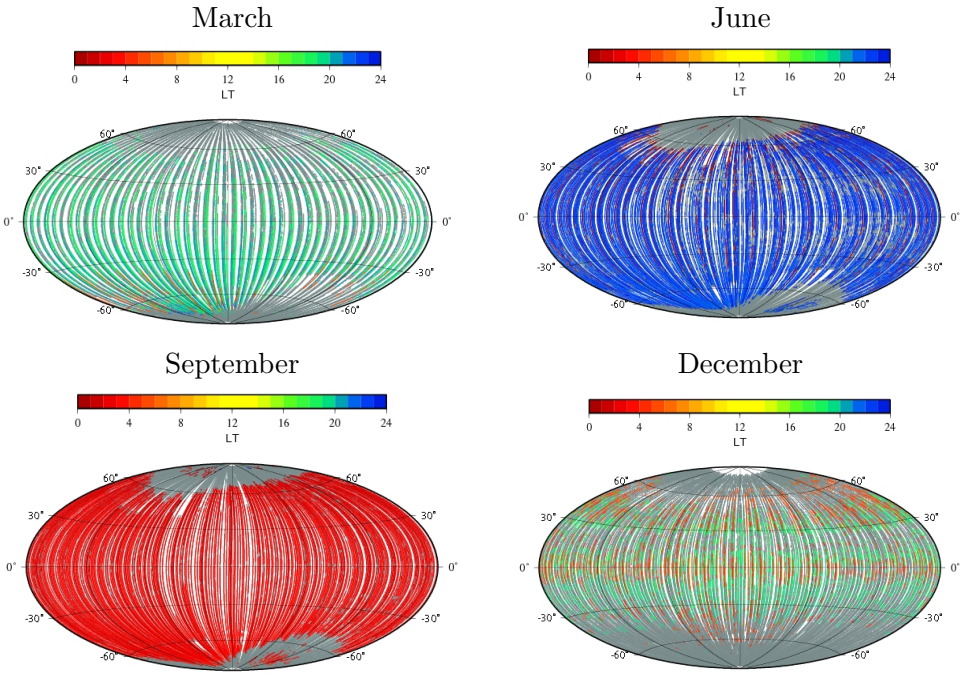

Figure 6.6: Distribution of the vector data selected using the 'vector' criteria during specific months of the year. The white areas indicate regions where there are no data, grey indicates only scalar data and the colours represent the local time of the vector data.

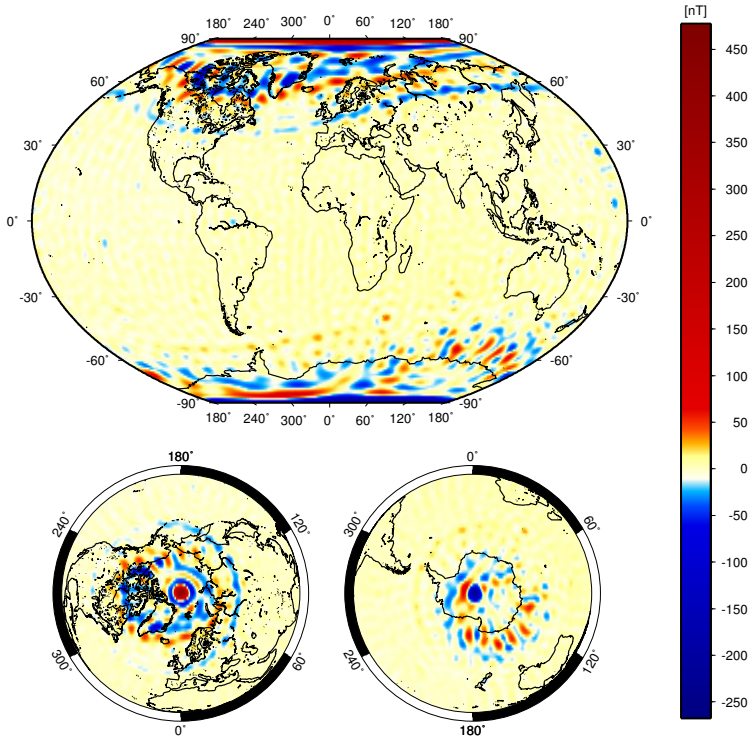

Figure 6.7: Difference between the models for the vector and traditional selections (Z component) at the Earth's surface.

indicates that the inclusion of additional vector data at high latitudes, along with more targeted selection criteria, does affect the whole model.

The core field (spherical harmonic degrees 1-15), at the core-mantle boundary (CMB), is plotted for both models in Figure 6.8. Again the models are very similar, although there are now a few more visible differences. For example, the negative region north of Canada does not extend as close to the pole in the vector selection and appears to have a sharper definition compared to the traditional selection. This indicates the vector selection may be better at characterising the field here. These high latitude differences are also clearly visible in the X and Y components (not shown here), particularly near the North pole. Again there are also some differences between the models at low latitudes, showing that any possible improvements to the model are not exclusively at high latitudes.

In the core field differences at the core mantle boundary, the highest degree included (n=15) dominates the downward continuation, and differences in the lower degree coefficients cannot be seen, so it is not included here. Figure 6.9 shows the core field differences at the Earth's surface; the high degree differences can still be seen to dominate the signal, however, the differences clearly become larger near the poles, with the largest occurring in the northern high latitude region.

The crustal field is shown in Figure 6.10; the two models are plotted on the same scale for comparison, as such the vector selection scale is saturated. The white area

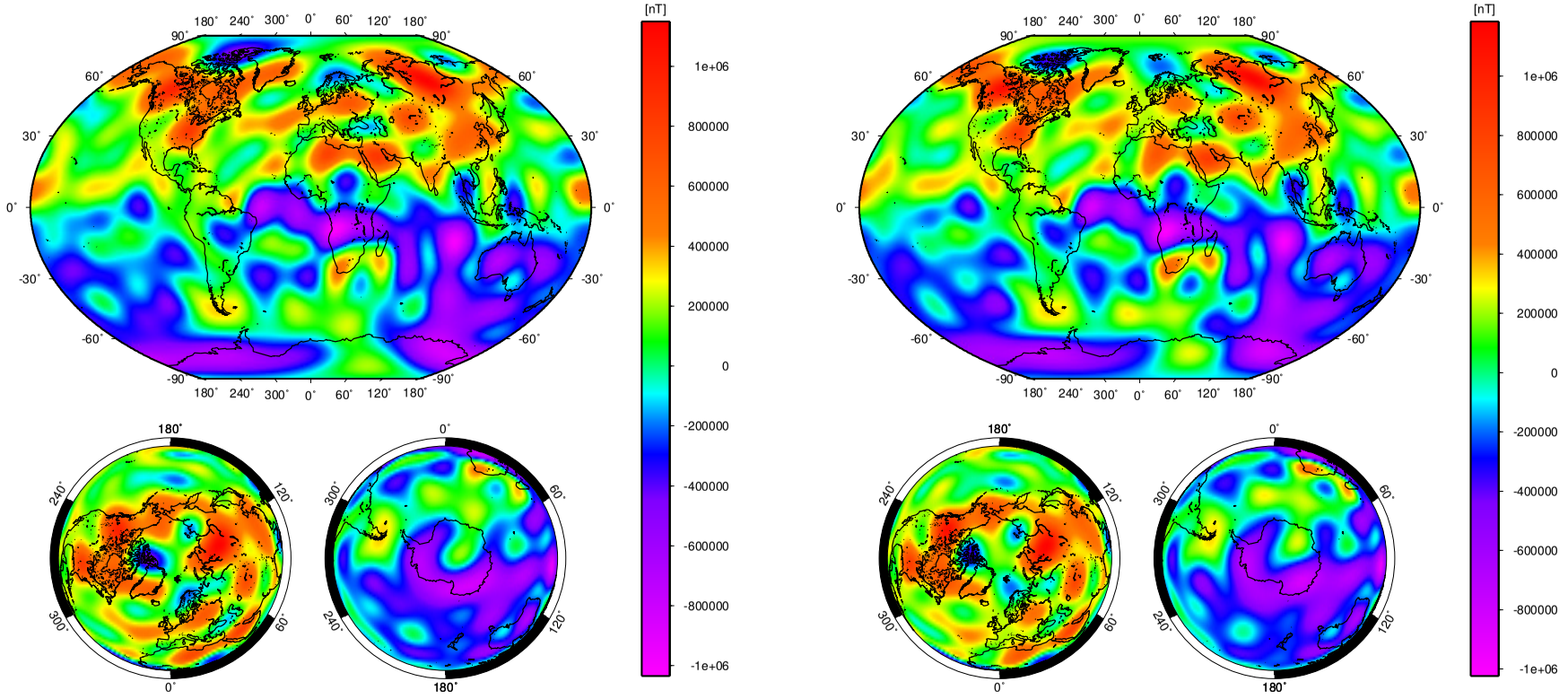

Figure 6.8: Plots of the Z component of the modelled geomagnetic core field (degrees n=1-15) at the core mantle boundary, using the traditional selection (left) and the vector selection (right).

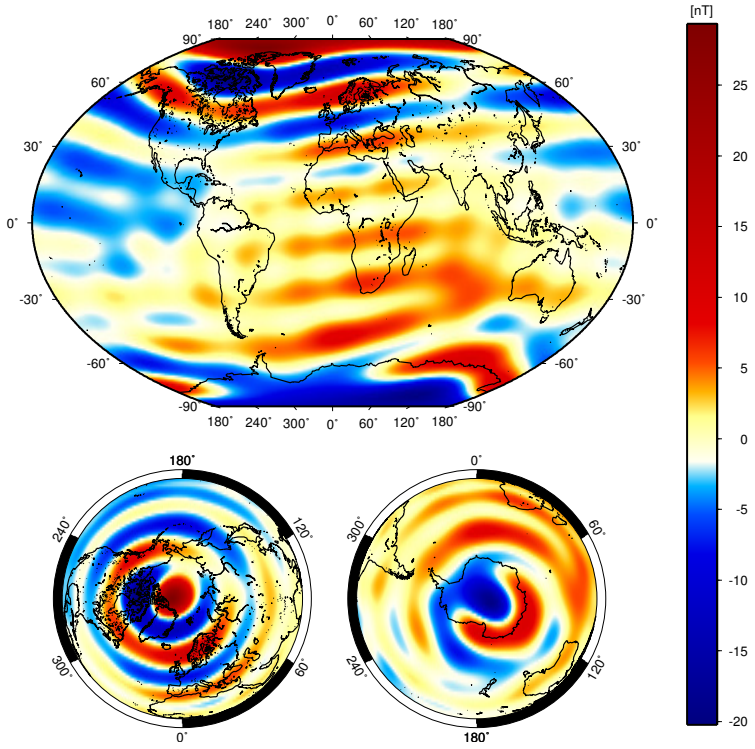

Figure 6.9: Difference between the core field models (n=1-15) for the vector and traditional selections (Z component) at the Earth's surface.

over the North pole is a large positive anomaly (reaching approximately 500nT at its centre). This large anomaly over the pole coincides with the satellite data gap and appears to be an instability in the model caused by missing data, rather than a real feature. However, the Y component (see Figure 6.12) does not show the large polar gap anomaly seen in the other components. It is unclear exactly what is causing this anomaly. It may be due to limiting the local time over the pole as this leads to asymmetric data distribution over the polar cap for each orbit.

Away from the pole, the two models again look similar with many of the well known crustal anomalies reproduced in both, for example, the Bangui anomaly in central Africa. The main differences are at high latitudes, although there are also differences in the magnitude and shape of anomalies at low latitudes.

In the traditional selection the anomalies near the South pole appear stronger and shorter wavelength than the vector selection, indicating that they may be affected by leakage of external fields in the auroral oval and polar cap into the model.

In Figure 6.11 it is clear that the major differences are again at high latitudes; their form appears to follow the auroral oval, showing that the two data selections deal with the external field sources quite differently. It is also important to note that the differences between the two models are of the same order of magnitude as the anomalies in the crustal model, so they are significant.

The power spectra for the two models are plotted in Figure 6.13. Up to degree

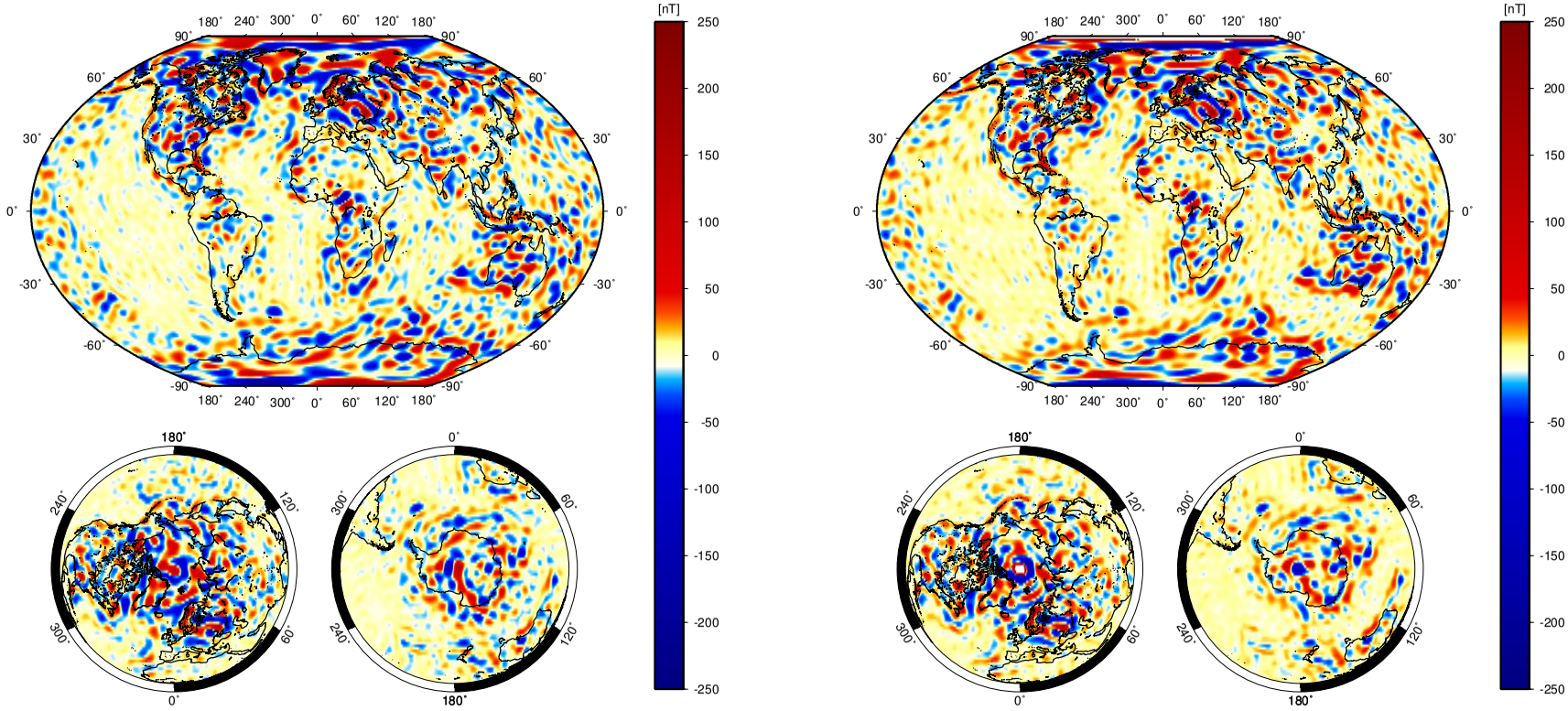

Figure 6.10: Plots of the Z component of the modelled crustal field (degrees n=16-60) at the Earth's surface, using the traditional selection (left) and the vector selection (right). The scale on the plot for the vector selection is saturated to allow direct comparison with the traditional plot. The white areas indicate where the plot goes off the scale, anomalies here reach up to 500nT.

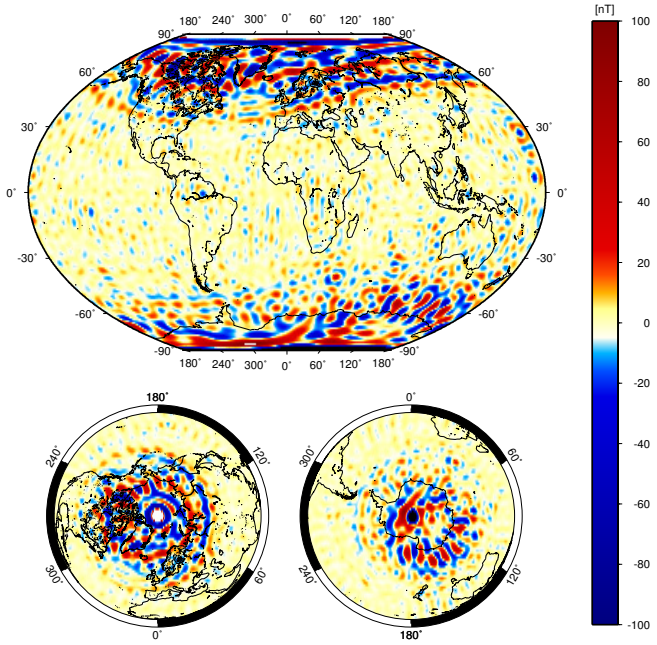

Figure 6.11: Difference between the crustal field models for the vector and traditional selections (Z component) at the Earth's surface. The scale is saturated to enable smaller scale differences to be seen, away from the anomaly over the geographic poles. White and black represent large positive (up to 250nT) and negative (reaching approximately -450nT) anomalies respectively.

14 the spectra (in the plot on the left) are essentially identical. This may explain why the highest degree in the core field model (up to 15) dominated the differences between the two models. Between degrees 14 and 25 the vector selection (red) has lower power, and therefore potentially less noise, than the traditional selection. However, this may be, at least in part, due to the larger number of data in the vector selection. After approximately degree 34 the vector selection becomes quite variable, suggesting more structure (including noise) in the vector model.

6.2.2 Comparing the PC/AE and Oval selections

To investigate which part of the selection has a bigger effect on the final model we look at the two further data selections mentioned earlier. The first, the 'PCAE' selection, uses the following criteria:

- $K_p < 2+$
- $|D_{st}| < 30nT$
- Local time 22:00-04:00
- 5 second sampling
- |PC| $\leq$2

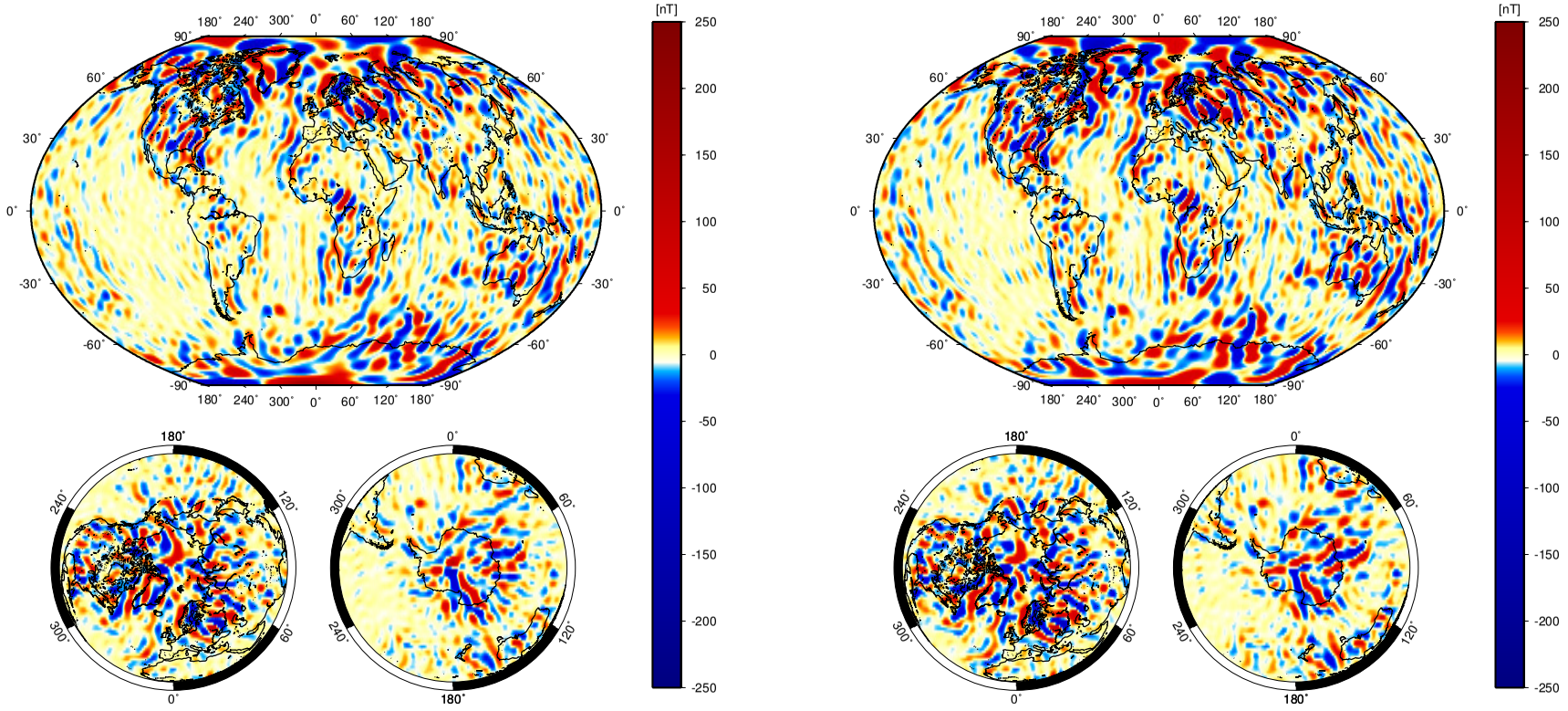

Figure 6.12: Plots of the Y component of the modelled crustal field (degrees n=16-60) at the Earth's surface, using the traditional selection (left) and the vector selection (right).

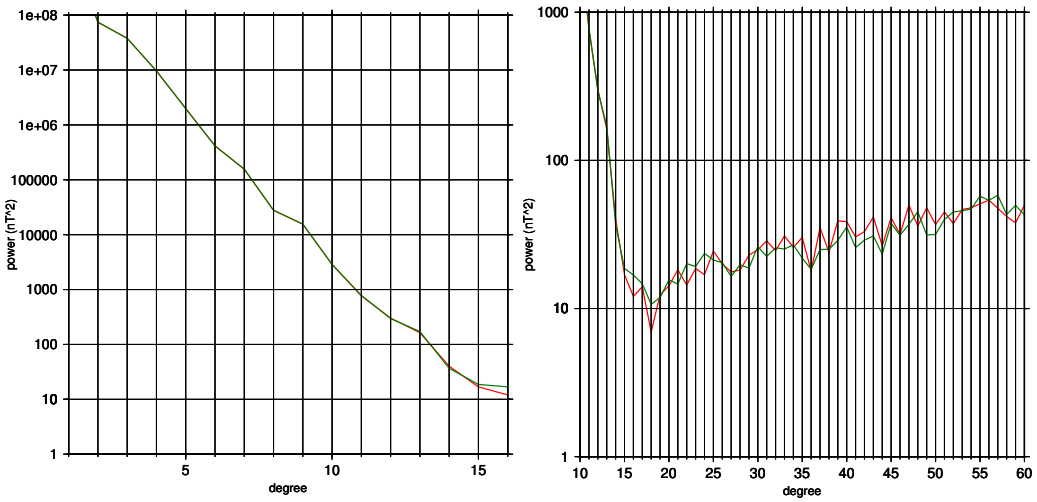

Figure 6.13: Power Spectra for the models made using the traditional (green) and vector (red) data selections

- AE ≤ 100
- Scalar data only, poleward of $\pm 50^\circ$ geomagnetic latitude

whilst the last, the 'oval' selection, uses:

- $K_p < 2+$
- $|D_{st}| < 30nT$
- Local time 22:00-04:00
- 5 second sampling
- Scalar data only, when the standard deviation of the de-trended data is more than 0.2nT in any of the components (as described in Section 4.3).

On initial inspection of the geographical maps for each model, for degrees 1-60, there is again very little difference between the plots at this scale. In a plot of the differences between the two selections (Figure 6.14) we can see that the main dissimilarities are at high latitudes. The biggest discrepancy occurs right over the poles, coinciding with the satellite polar data gap (as before).

For the core field at the CMB there are visible differences between the two models in Figure 6.15. For example, the negative anomalies near the North pole extend further poleward in the PCAE selection. The oval selection appears to show a sharper definition of features near the pole, perhaps suggesting the additional vector data is causing this selection to perform better near the poles.

In the crustal field (Figure 6.16) there are again some obvious differences, particularly at very high latitudes where the data in the oval selection model goes off scale. This confirms that the oval selection is responsible for the problem over the

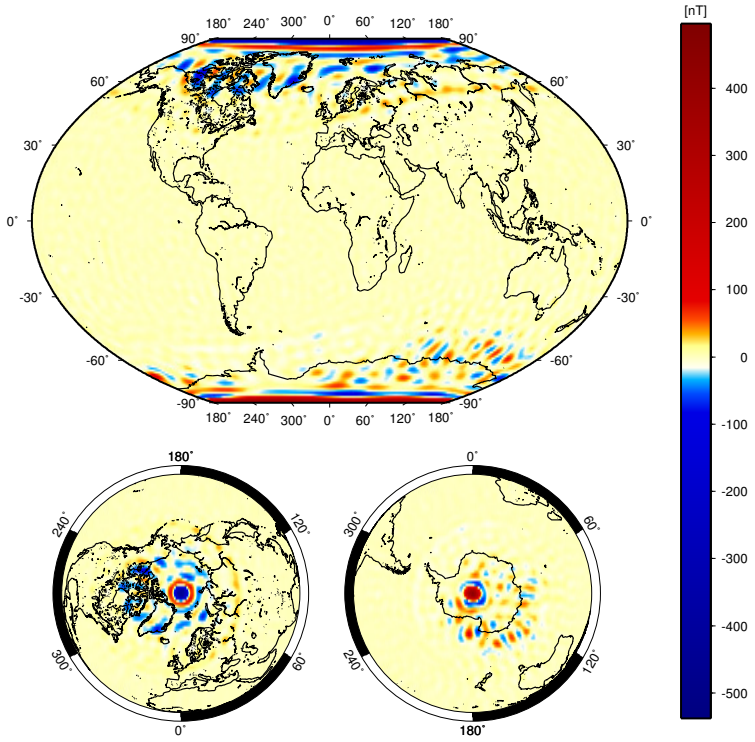

Figure 6.14: Difference between the geomagnetic field models (degree n=1-60) for the PCAE and oval selections (Z component) at the Earth's surface.

geographic poles. The main differences between the PCAE and oval selections are around the auroral oval, again showing that the external currents in this area have the most influence on the data.

In summary, the oval selection has a bigger effect overall, with sharper defined features at the CMB and more structure in the higher degrees. However, the power spectra, plotted in Figure 6.17, show that the oval selection (magenta line) is enhanced above approximately degree 28, suggesting either noise or external signals in the data. This selection method should probably not be used in isolation, the PCAE selection (blue line) clearly reduces the overall power of the vector selection (red), compared to using the oval selection alone.

6.3 Comparison with Existing Models

We can also compare the models produced using these selection criteria to some recent geomagnetic field models. This allows us to gauge how models generated from these relatively simple selection techniques compare to models with a more complex parametrisation, constructed over a much longer time period.

Although the models used are produced for different spherical harmonic degrees, any comparisons shown are like-for-like (i.e., the whole field is compared for degree n=1-60).

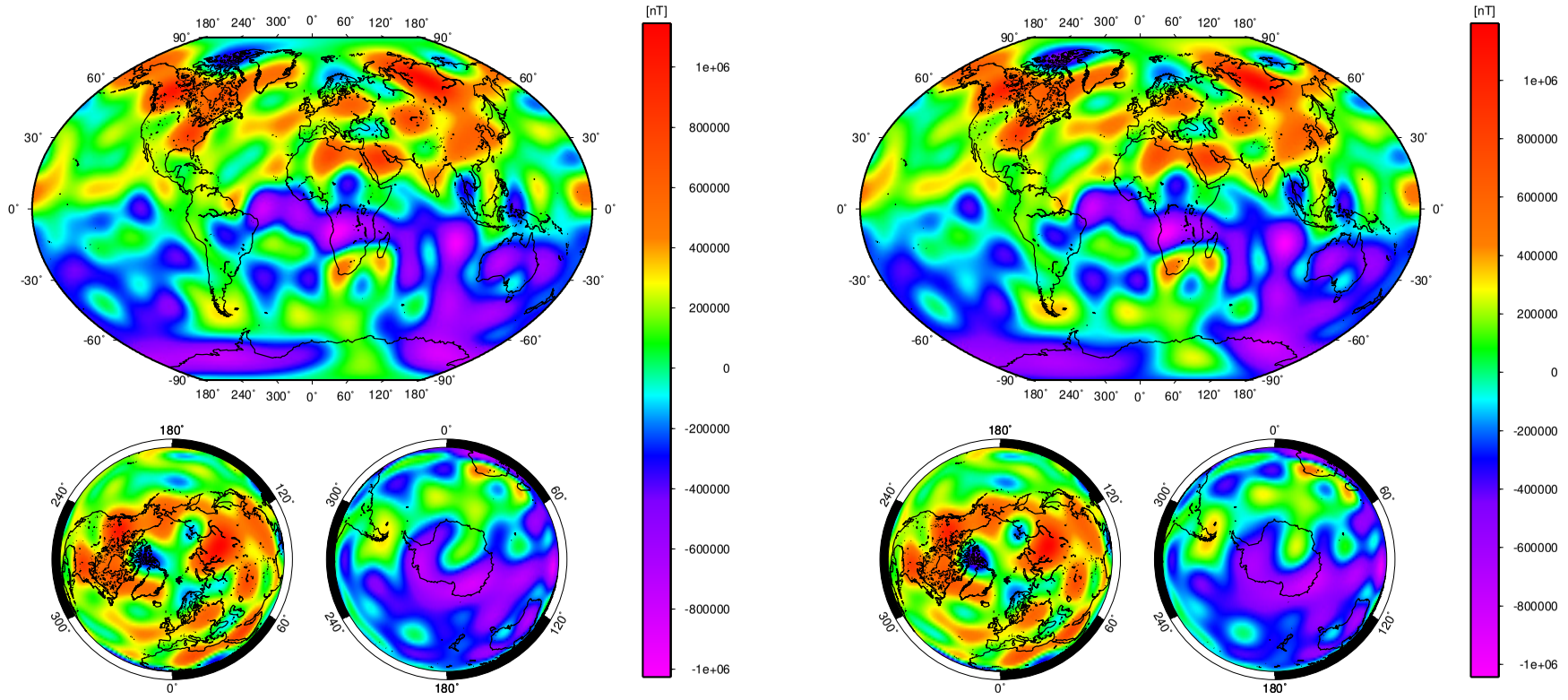

Figure 6.15: Plots of the Z component of the modelled core field (degrees n=1-15) at the core mantle boundary, using the PCAE selection (left) and the oval selection (right).

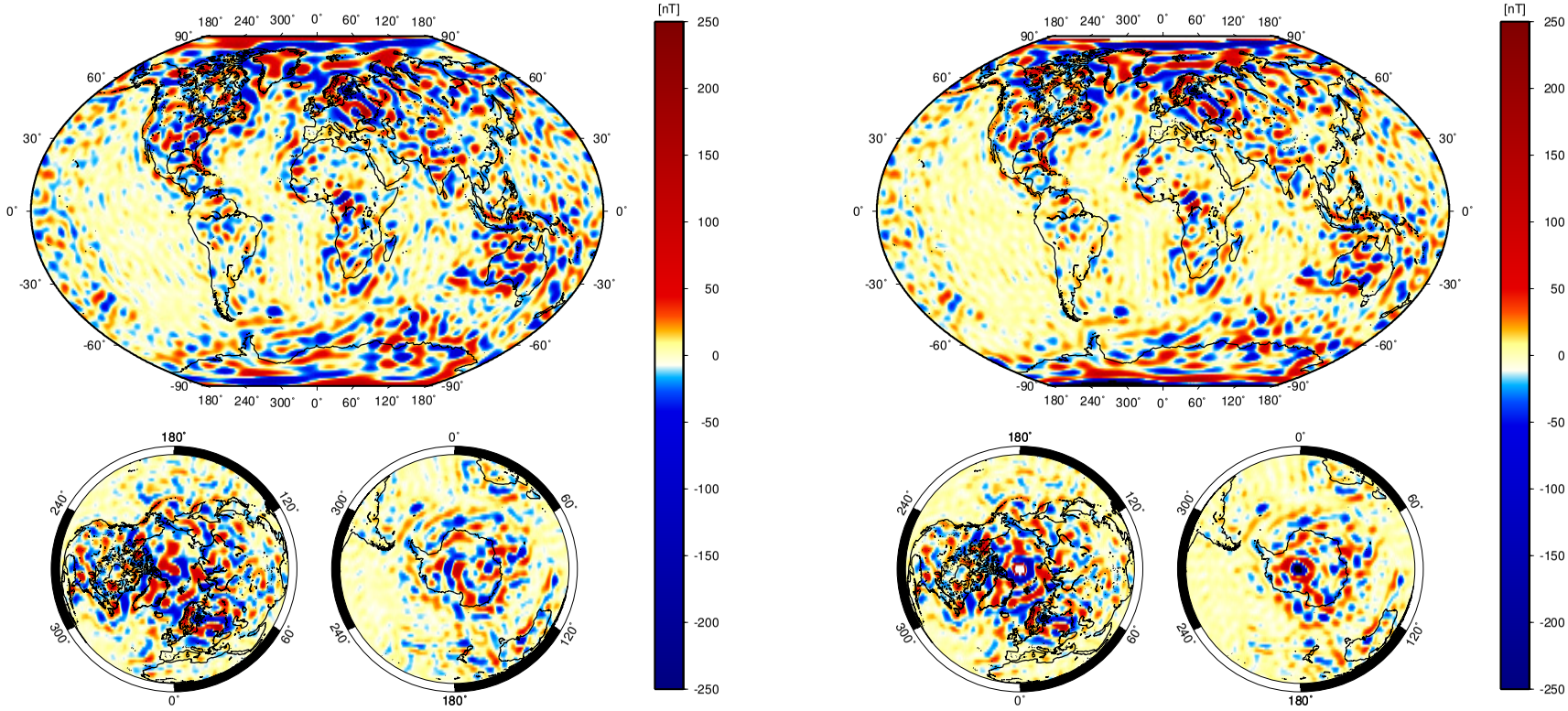

Figure 6.16: Plots of the Z component of the modelled crustal field (degrees n=16-60) at the Earth's surface, using the PCAE selection (left) and the oval selection (right). The oval selection is plotted on a saturated scale to allow a direct comparison. White and black represent large positive and negative anomalies respectively.

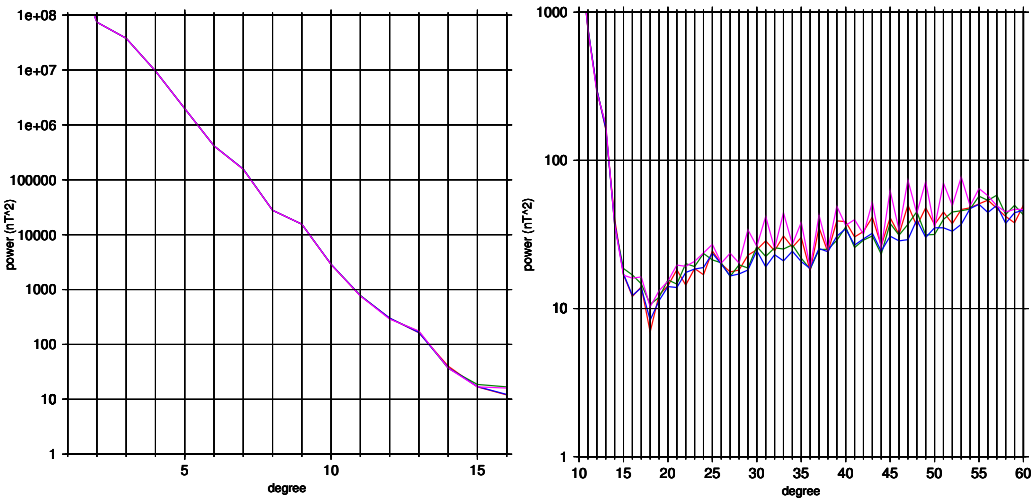

Figure 6.17: Power Spectra for the models made using the traditional (green), vector (red), PCAE (blue) and oval (magenta) data selections.

6.3.1 Comparison with CHAOS-4

We use CHAOS-4 (*Olsen et al.*, 2010b) as it is the newest version of the CHAOS model, derived in December 2010. CHAOS-4 is constructed from 11 years of geomagnetic data to define the field up to spherical harmonic degree n=100. CHAOS-4 also co-estimates a model of the large-scale magnetospheric field meaning that major external fields should produce less signal leakage into the internal field coefficients. Therefore if our vector selection produces similar results, but without this complicated treatment, and with far fewer data, then it would indicate that simple data selection techniques still have a useful role to play in geomagnetic modelling from satellite data.

The core field at the CMB (Figure 6.18) shows features near the North pole which do not extend as close to the pole as in the traditional selection (e.g., the negative anomaly over northern Canada). The negative (blue) anomaly near Svalbard, the positive region (red) south of the UK and the small positive anomaly over Antarctica look more similar to the vector selection than the traditional. This may suggest the vector selection is performing better than the traditional as it is closer to the CHAOS-4 prediction.

The differences between the vector selection and CHAOS-4 (Figure 6.19, right) are again dominated by the higher degree terms (i.e., n=15). The largest differences when either the traditional or vector models are compared to CHAOS-4, plotted at the Earth's surface, are clearly at high latitudes (Figure 6.19). At mid- to low-latitudes the differences between the vector model and CHAOS-4 appear reduced compared to the differences between the traditional selection and CHAOS-4.

The plot of the CHAOS-4 crustal field (Figure 6.20) looks very similar to the traditional and vector selections. In the difference plot (Figure 6.21) the major

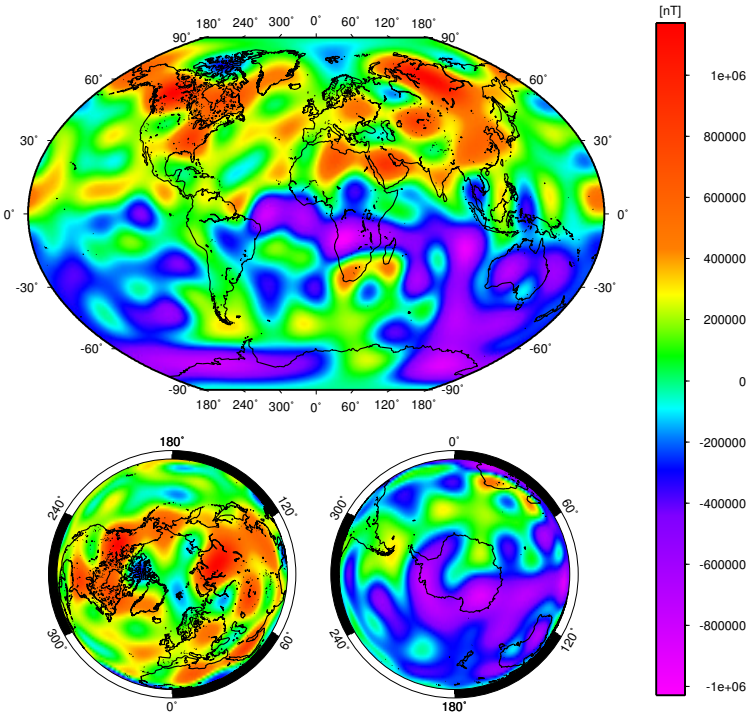

Figure 6.18: The Z component of the CHAOS-4 model of the core field (degrees n=1-15) at the core mantle boundary.

difference between the vector selection and CHAOS-4 again occurs directly over the geographic pole. The plot is saturated to make the smaller differences more visible. Away from the pole the largest differences are again at high latitudes. The largest differences between the traditional selection and CHAOS-4 also occur at high latitudes. In the Y component (Figure 6.22) the differences between the vector selection and CHAOS-4 are smaller at high latitudes than the difference between the traditional selection and CHAOS-4. This is the component for which there is no signature over the geographic poles. In the Z component the residuals between the vector selection and CHAOS-4 also seem to be smaller (away from the pole) than for the traditional selection. This suggests that if we can resolve this large anomaly the vector selection may be much closer to CHAOS-4 than the traditional selection. This is encouraging as it suggests the vector selection is performing almost as well as CHAOS-4 despite the much simpler modelling process and selection and the fact that we only use a single year's data.

6.3.2 Comparison with MF7

MF7 is the latest version of a series of models aimed at resolving the crustal magnetic field to high spherical harmonic degrees (e.g., *Maus et al.*, 2008). MF7 uses CHAMP measurements from May 2007 to April 2010 to model the field to degree 133.

Figure 6.23 shows comparisons of the MF7 and vector selection models, both

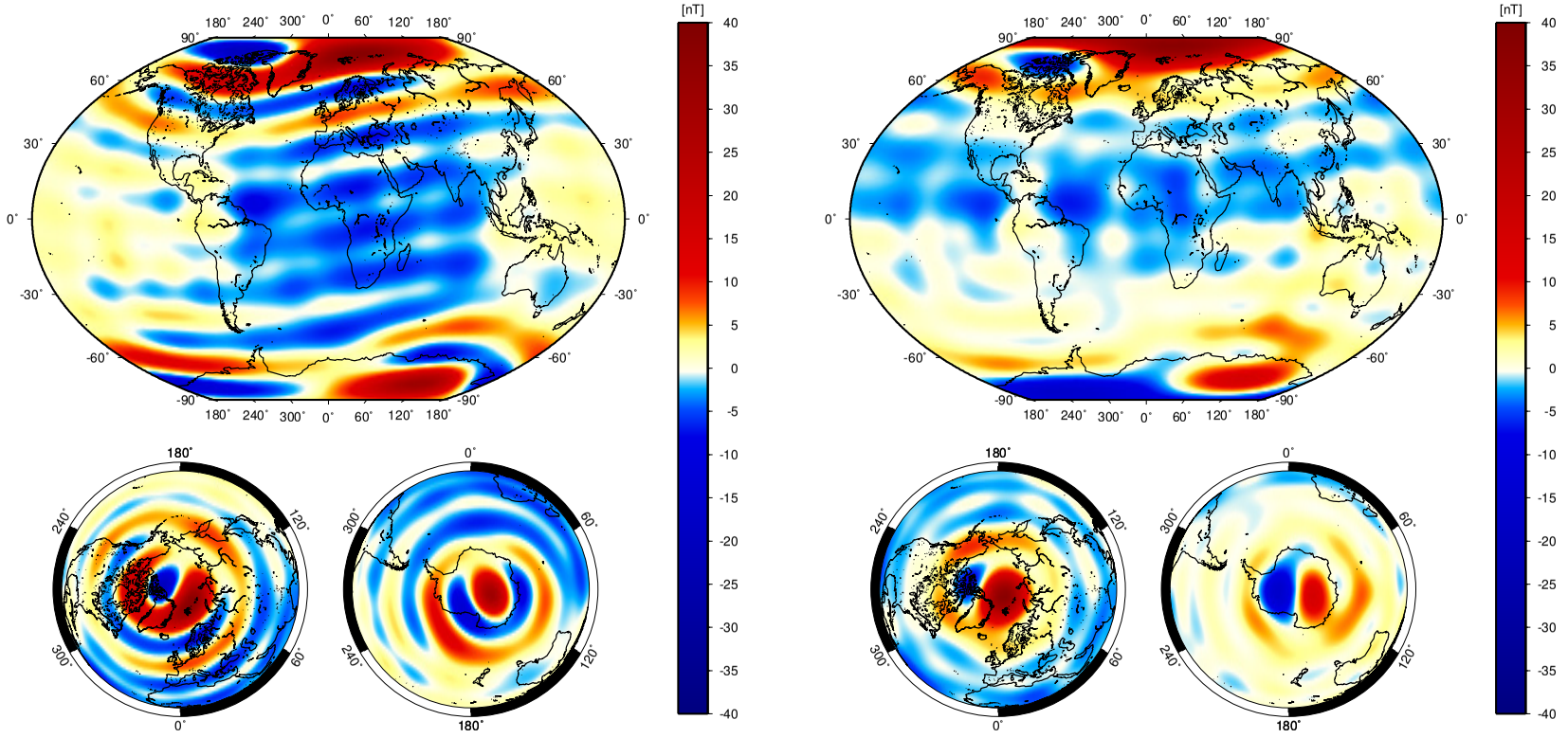

Figure 6.19: Differences between the core field models (degrees n=1-15) at the Earth's surface, traditional selection minus CHAOS-4 (left) and the vector selection minus CHAOS-4 (right).

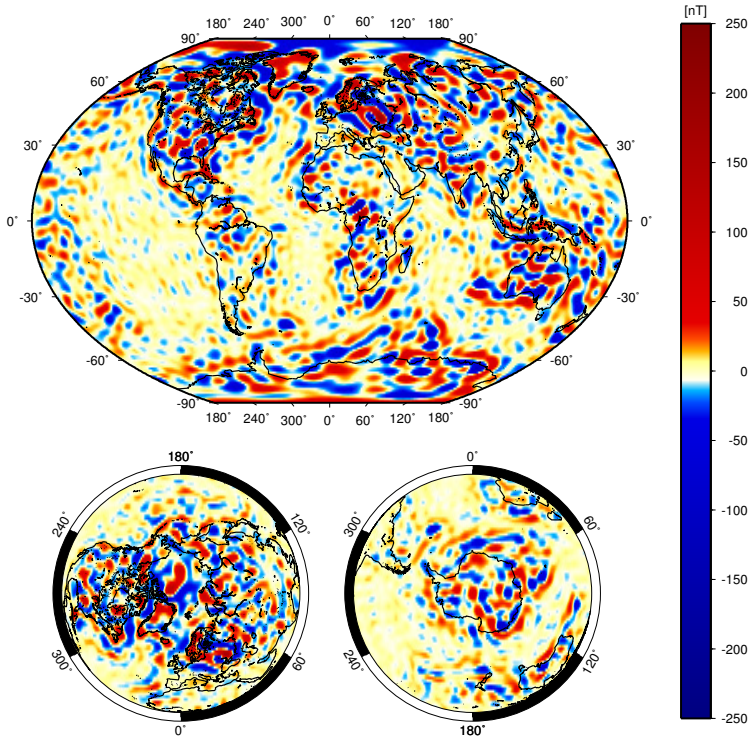

Figure 6.20: The Z component of the CHAOS-4 model of the crustal field (degrees n=16-60) at the core mantle boundary.

plotted for degrees n=15-60. Features in the ocean are stronger for MF7; however, many of the features seen in the MF7 model are reproduced in the vector plot, even at high latitudes, although they are often weaker. For example, in India and Australia, the shape and polarity of the anomalies seen here are the same in both plots, but are clearly stronger for MF7.

Figure 6.25 shows the differences between CHAOS-4 and MF7 in the crustal field. The largest differences are predominantly at high latitudes; This shows again that this is the most difficult region to model accurately.

6.3.3 Power Spectra comparisons

Up to approximately degree 28 the power spectrum for the vector selection is very similar to that of MF7 and CHAOS-4, whilst the model using the traditional selection has slightly more power between degrees 14-25 (Figure 6.26). At higher degrees (above n=28) both the traditional and vector selection models have higher power and perhaps therefore, contain more noise than the other models, although this is not particularly surprising as they are based on much fewer data than MF7 and CHAOS-4.

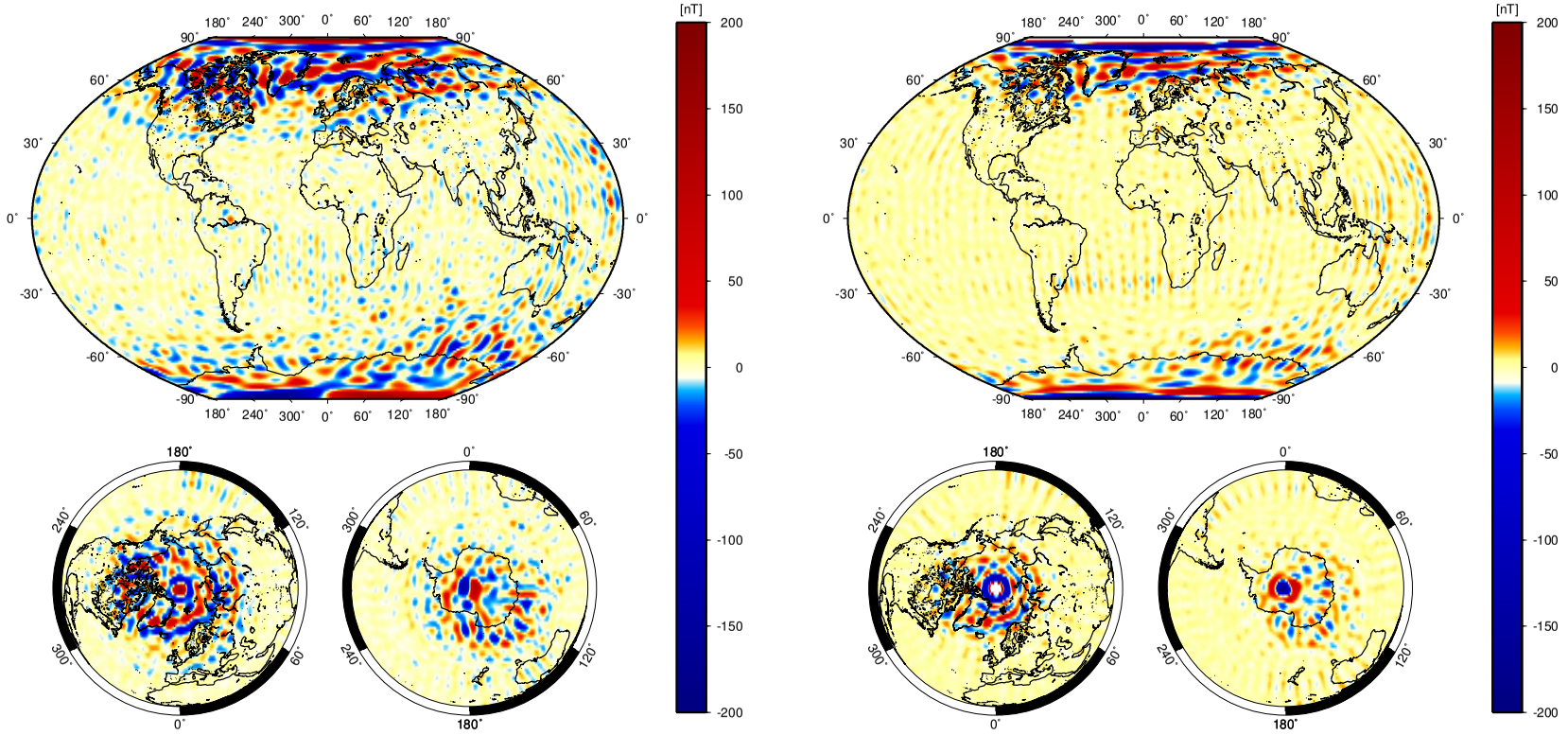

Figure 6.21: Differences between the Z component of the crustal field models (degrees n=16-60) at the Earth's surface, traditional selection minus CHAOS-4 (left) and the vector selection minus CHAOS-4 (right). The colour scale on the right hand plot is saturated to allow detail away from the pole to be shown; the white area over the north pole is a large positive anomaly.

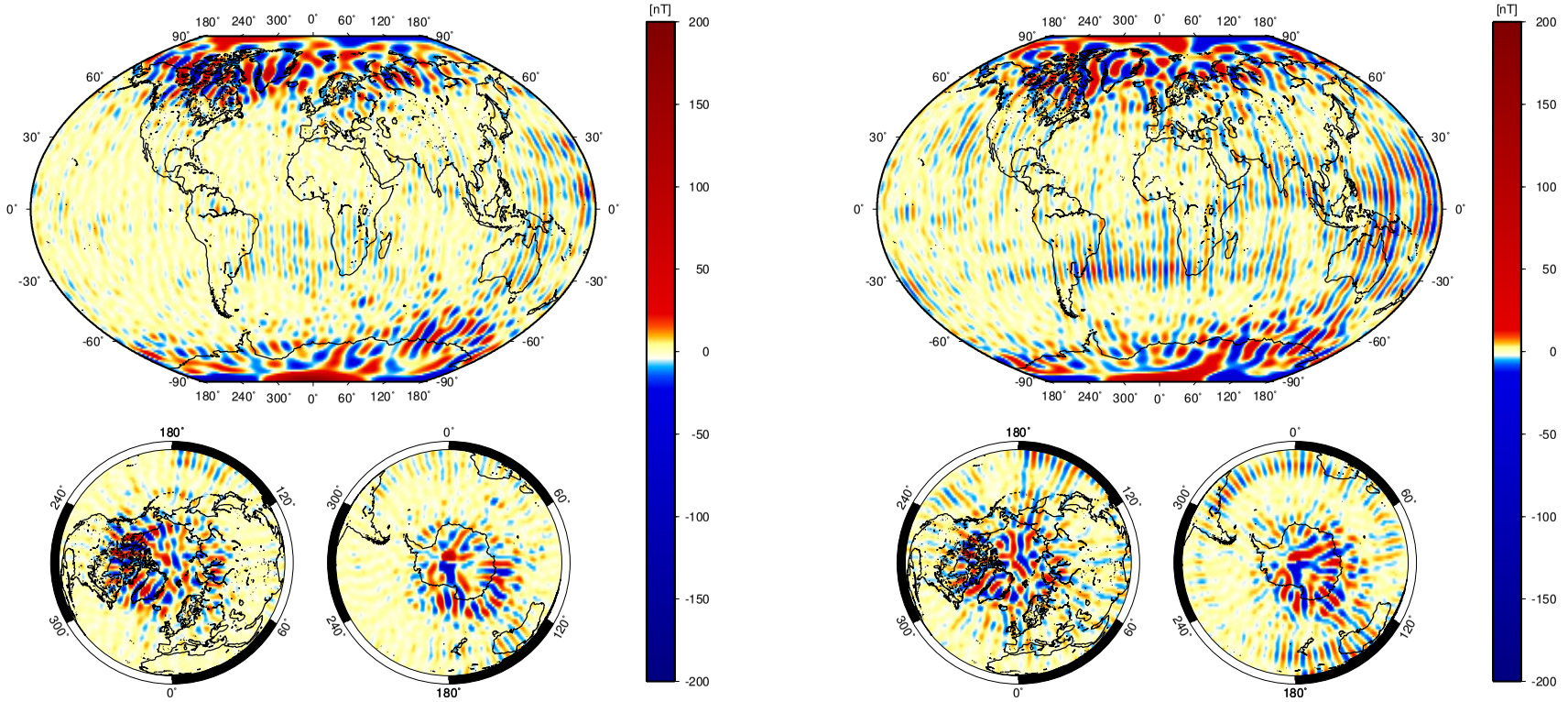

Figure 6.22: Differences between the crustal field models (degrees n=15-60) for the Y component, traditional selection minus CHAOS-4 (left) and the vector selection minus CHAOS-4 (right).

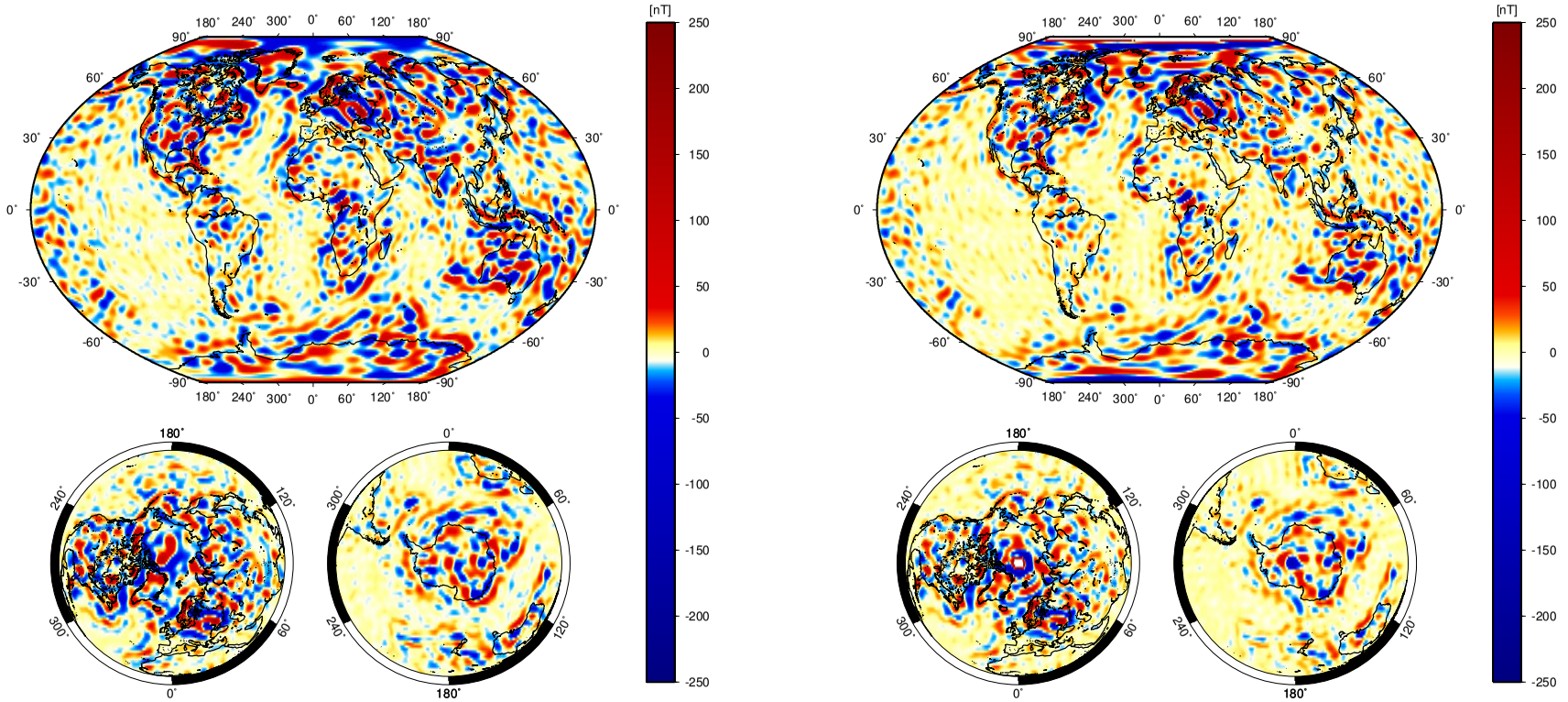

Figure 6.23: Z component of the MF7 (left) and the vector selection (right) models for spherical harmonic degrees n=15-60. The colour scale on the right hand plot is saturated to allow detail away from the pole to be shown; the white area over the north pole is a large positive anomaly.

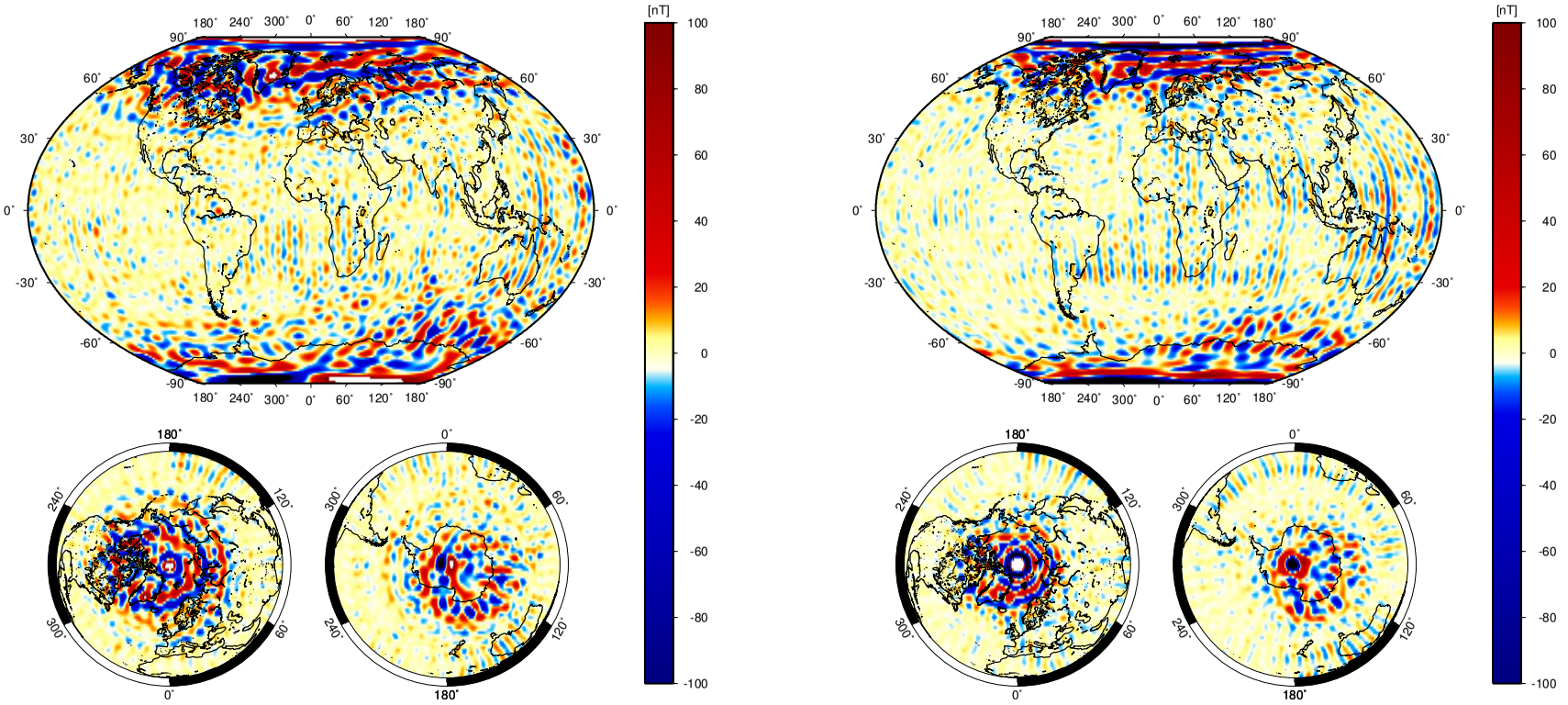

Figure 6.24: Differences between the traditional (left) and vector (right) crustal models and MF7 in the Z component.

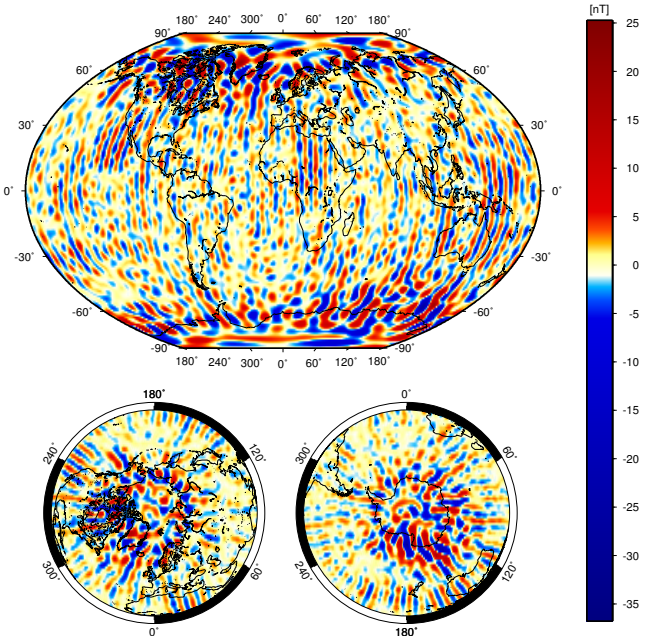

Figure 6.25: Differences between CHAOS-4 and MF7 in the crustal field (n=16-60)

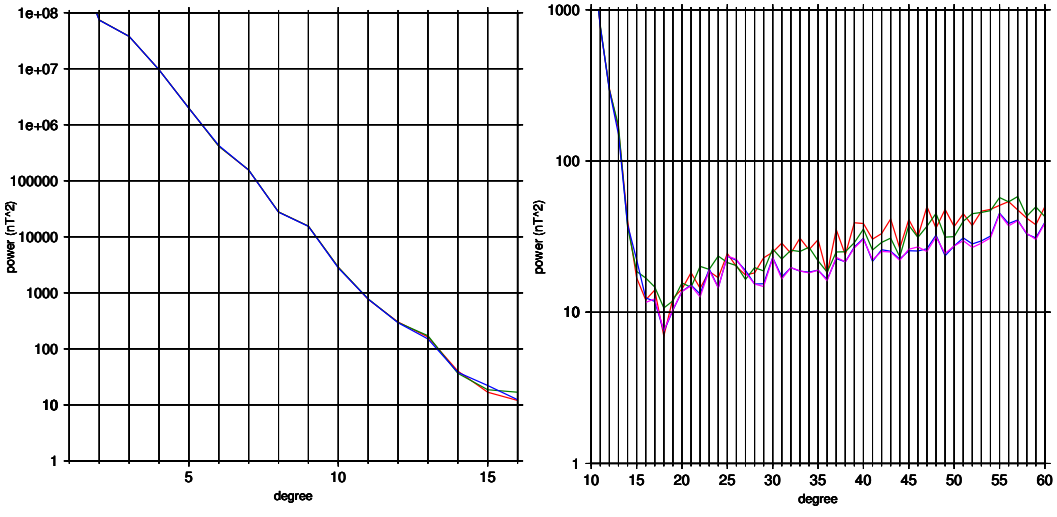

Figure 6.26: Power spectra for the vector selection (red), traditional selection (green), CHAOS-4 (blue) and MF7 (magenta).

6.4 Addition of Pseudo Data in the Polar Gap

The large anomaly over the geographic pole coincides with the polar data gap. This could be a result of having added more vector data close to this region. We investigate whether adding a small amount of pseudo data within the polar gap, as estimated by the CHAOS-4 model, will alleviate this problem.

The CHAOS-4 data added are spaced at 5° longitude for every 1° between 87° to 89.99° and −87° to −89.99° latitude. The data added can be seen in Figure 6.27 in red. The pseudo data are added for a 30 minute period immediately after midnight for the quietest day in each month, provided the Dst value is less than ±20nT at this time. The CHAOS-4 pseudo data account for approximately 8% of the final dataset. This selection is henceforth referred to as the pseudo selection.

In Figure 6.28 the core field for the pseudo selection model looks very similar to the vector selection; very close to the geographic poles the anomalies extend closer to the poles. In the plot of the crustal field (Figure 6.29) the anomalies over the geographic poles are much reduced, although still present, particularly over the North pole, compared to Figure 6.10. Whilst many of the low- and mid-latitude features remain unchanged, some of the high latitude features are smaller in magnitude and size.

In the differences between the pseudo and vector selections, shown in Figure 6.30 (right), the biggest effect of the addition of data in the polar gap occurs at the very high latitudes. This indicates that the additional pseudo data is having a positive impact on the anomaly in the satellite data gap. The differences between the pseudo selection model and CHAOS-4 are also smaller than the difference between the vector selection and CHAOS-4, again implying that adding CHAOS-4 values in the polar gap has helped to reduce the problem.

The power spectrum for the selection including CHAOS-4 pseudo data is shown in Figure 6.31 in black. This model has similar power to the vector model to approximately degree 25, then has lower power to approximately degree 43 and is closer to the power spectra for CHAOS-4 and MF7 here. Above degree 44 the pseudo selection has higher power than all the models, suggesting that this approach has perhaps added some additional noise in the highest degrees.

6.5 Model Residuals

The residuals between the models and the original data, for both the traditional and vector selections are shown in Figure 6.32. There are two clear times when there are large residuals, particularly in the X and Z components. These occur on day of year 36 and 243; there are no obvious anomalies in the data on these days, so the cause of these large residuals is, as yet, unknown.

Figures 6.33 and 6.34 show averages and rms values for bins of the residuals for

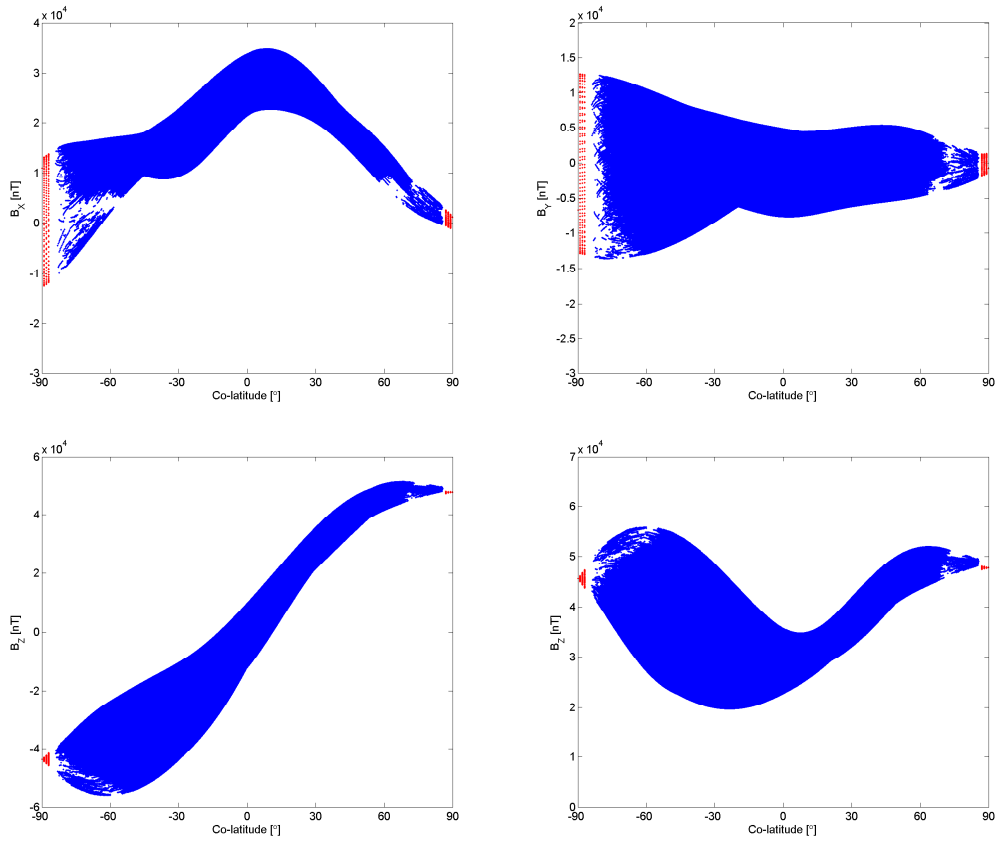

Figure 6.27: The additional CHAOS-4 pseudo data in red, the vector selection is shown in blue

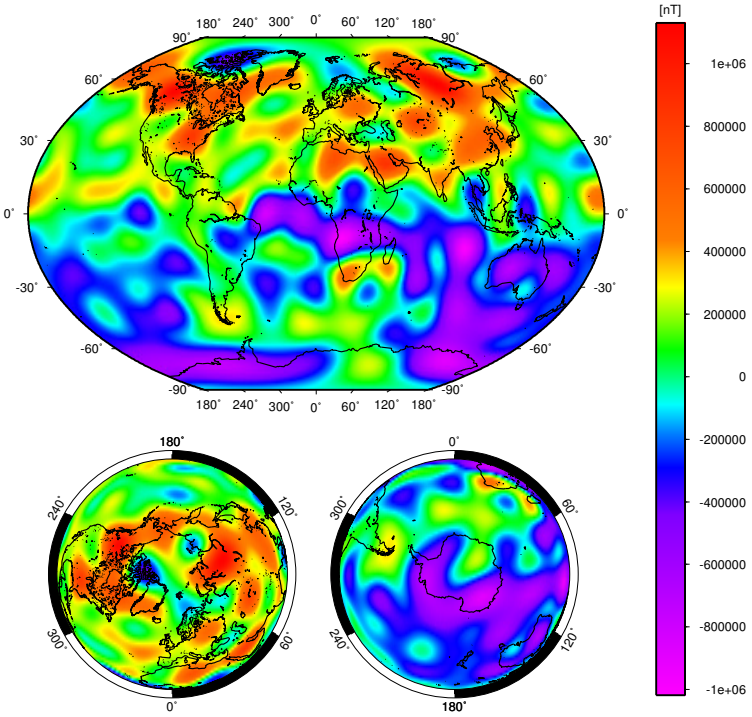

Figure 6.28: The core field model (n=1-15) for the Z component at the core-mantle boundary, generated using the vector selection with additional data calculated from the CHAOS-4 model in the satellite data gap.

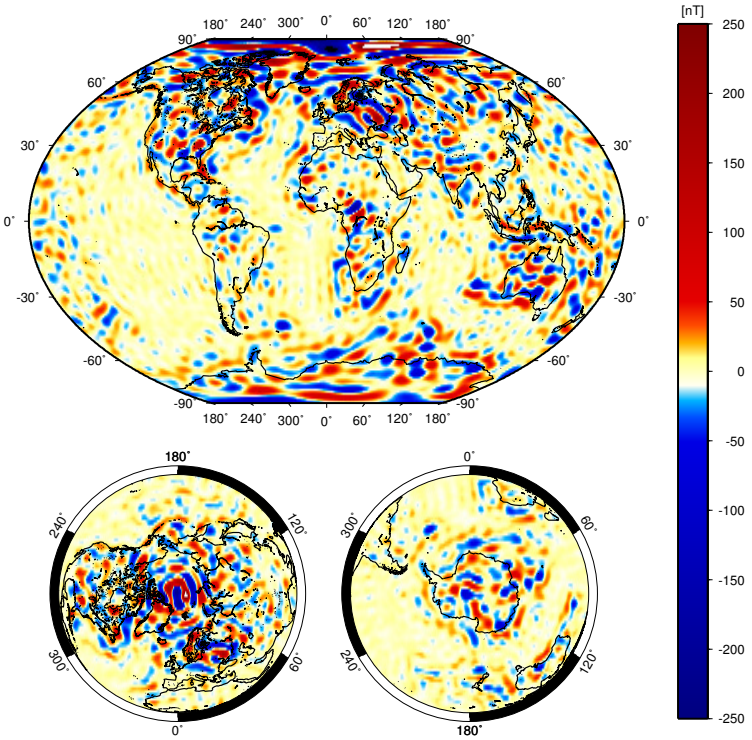

Figure 6.29: The crustal field model (n=16-60) for the Z component generated using the vector selection with additional data calculated from the CHAOS-4 model in the satellite data gap.

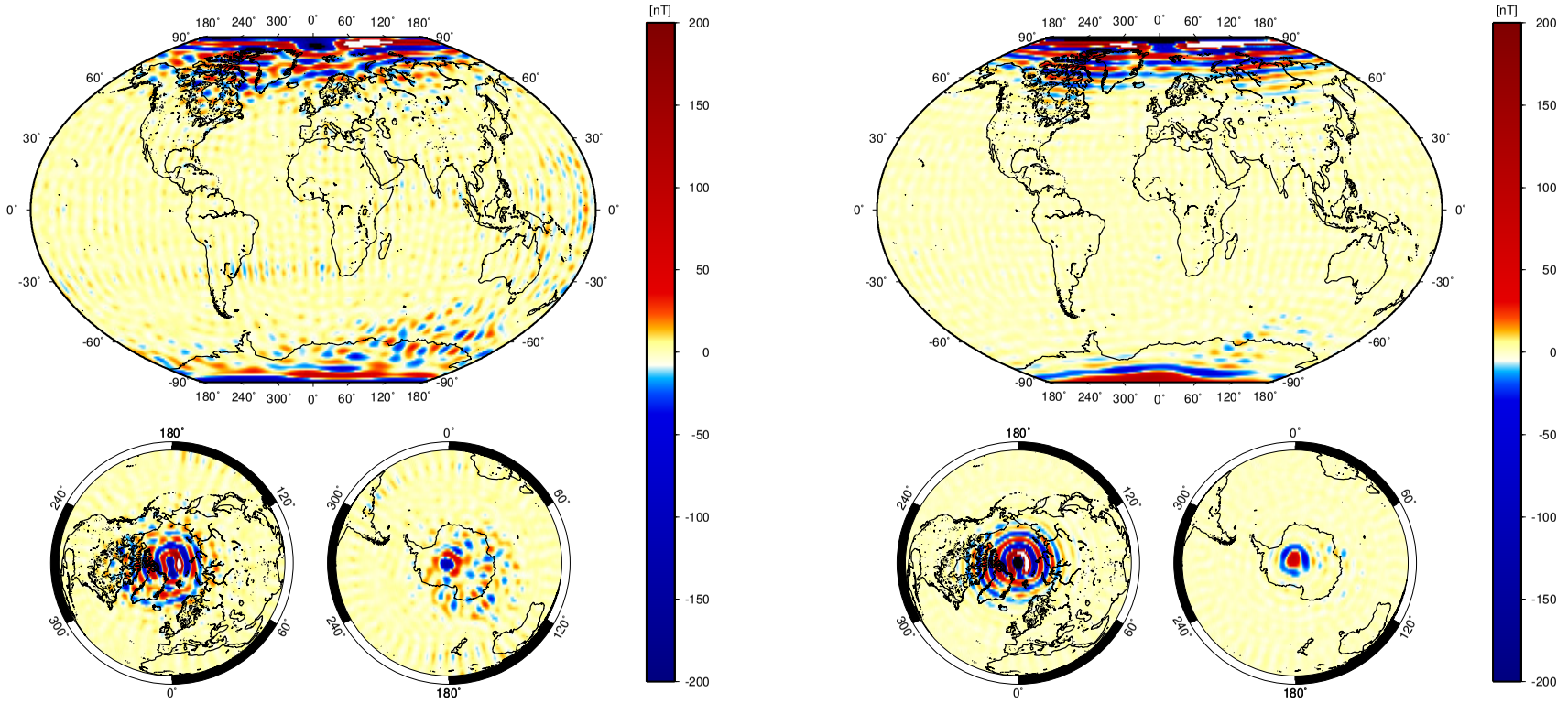

Figure 6.30: Differences between the pseudo data selection and the CHAOS-4 (left) and vector (right) crustal field models in the Z component.

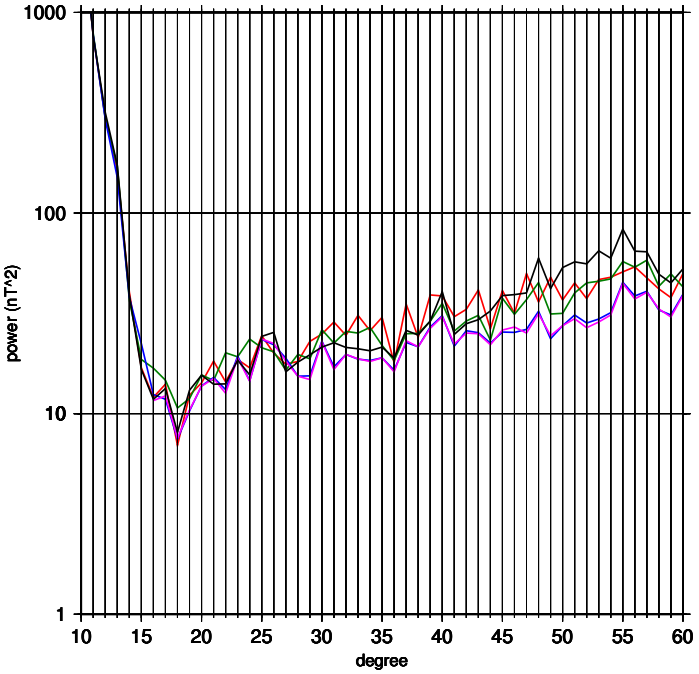

Figure 6.31: The power spectra for models created with the traditional selection (green), the vector selection (red), CHAOS-4 (blue), MF7 (magenta) and the selection with calculated CHAOS-4 values in the satellite data gap (black).

the traditional and vector selection models respectively. The anomalies at days 36 and 243 are again evident in both models, although the magnitude of the residuals on day 243 is much reduced in the vector selection model. Away from these anomalies the magnitudes of the residuals are similar between the two models.

The residual plots for the pseudo selection model are shown in Figures 6.35 and 6.36. There are clearly several occasions when the residuals are large. These large residuals appear to occur two days prior to each addition of synthetic data. It is not yet clear exactly what is causing these anomalies, although it undoubtedly is related to the CHAOS-4 synthetic data.

6.6 Preferred Model

Figures 6.37, 6.38 and 6.39 show all the components of our preferred model, using the vector selection. This model extends to spherical harmonic degree and order 60 and is based on CHAMP data for the year 2007. This model provides sharper features than the traditional selection at high latitudes, particularly at the CMB, and provides features which appear to be more like those of models such as CHAOS-4 and MF7. The relatively simple vector model produces a similar result to such complex and well established models, with far fewer data, which is encouraging.

There are still some obvious problems, for example, the anomaly produced by the polar gap. Although the addition of pseudo data in the polar satellite data gap

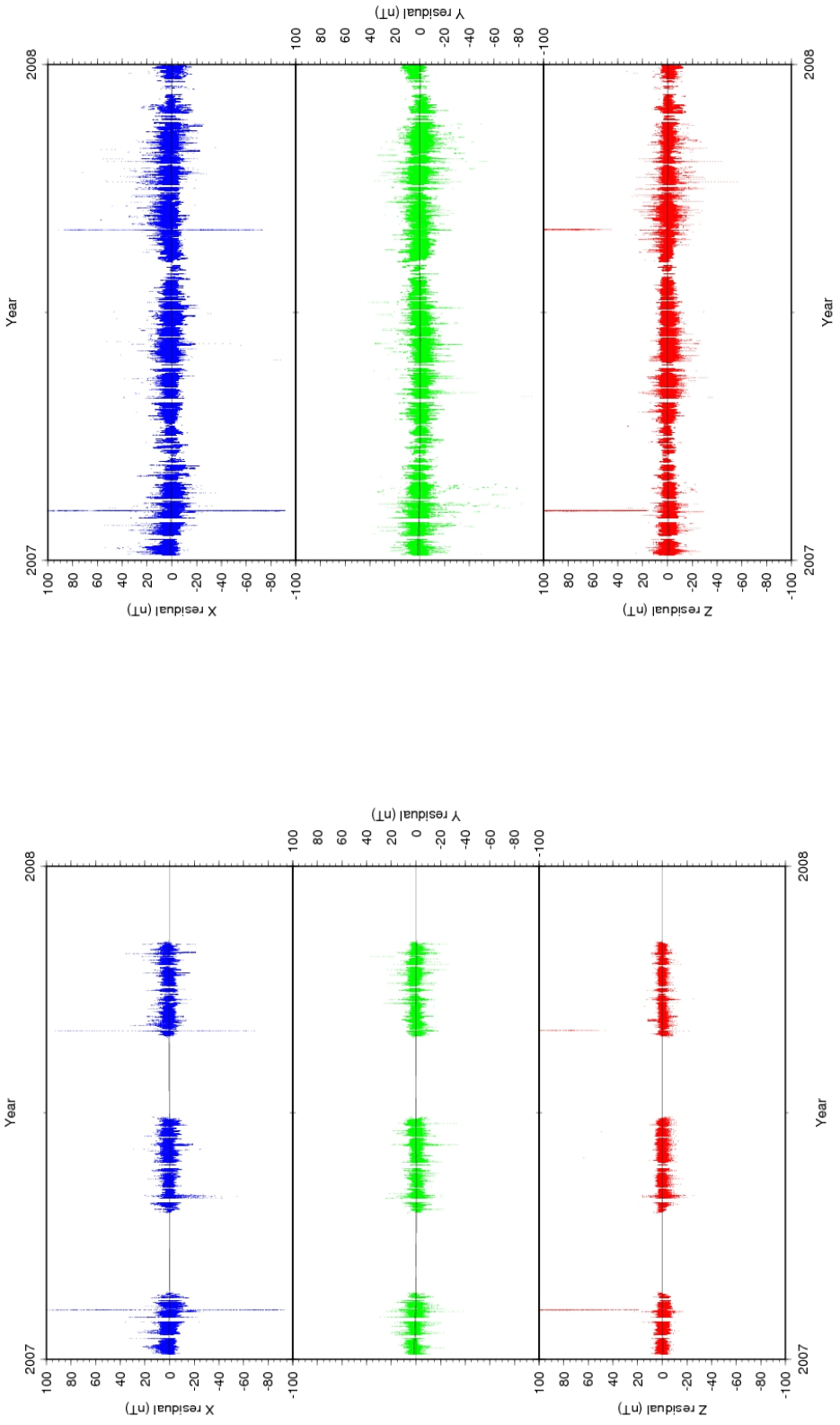

Figure 6.32: Residuals plotted against time for the traditional and vector selection models

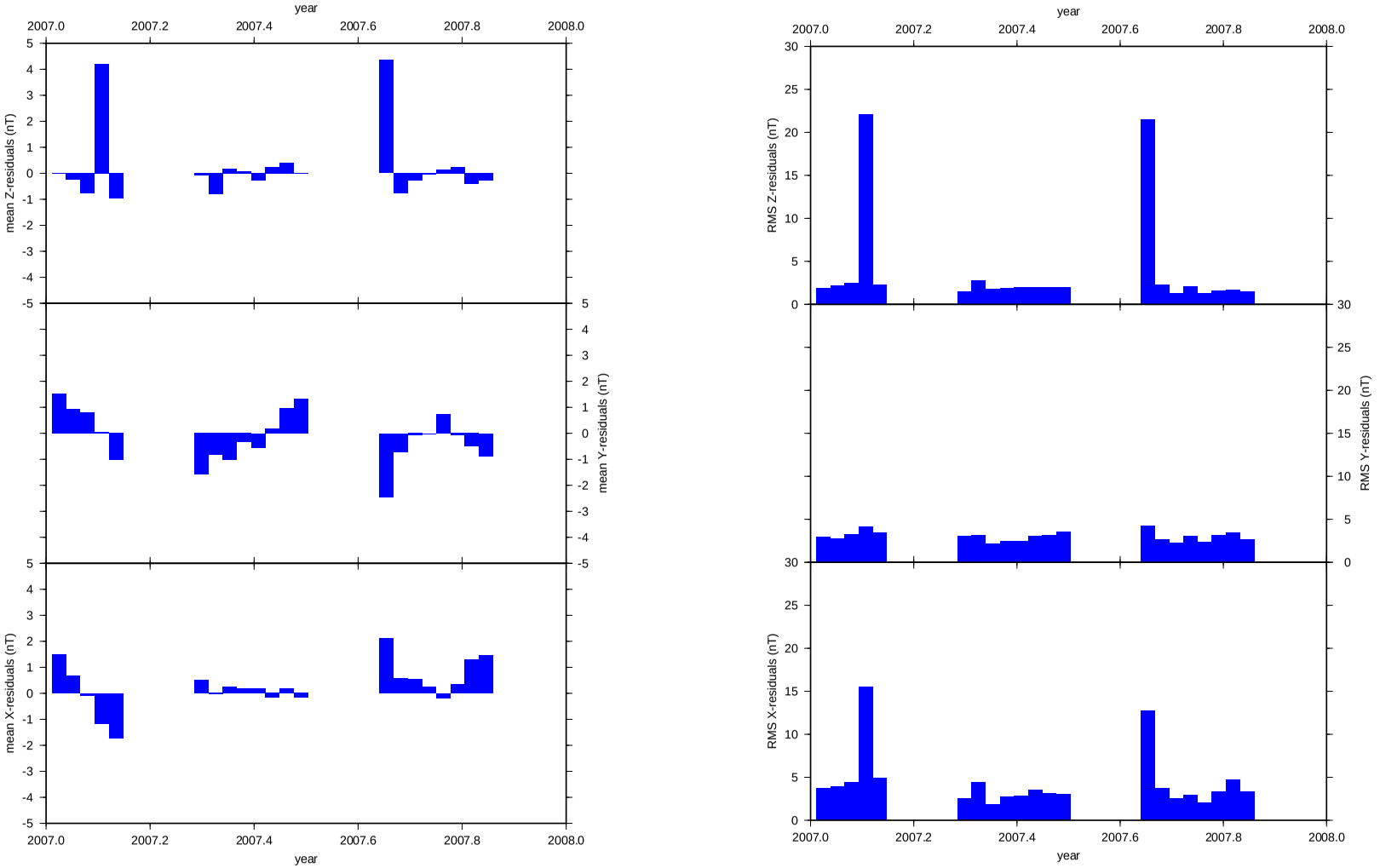

Figure 6.33: Residual averages and RMS values for the traditional model

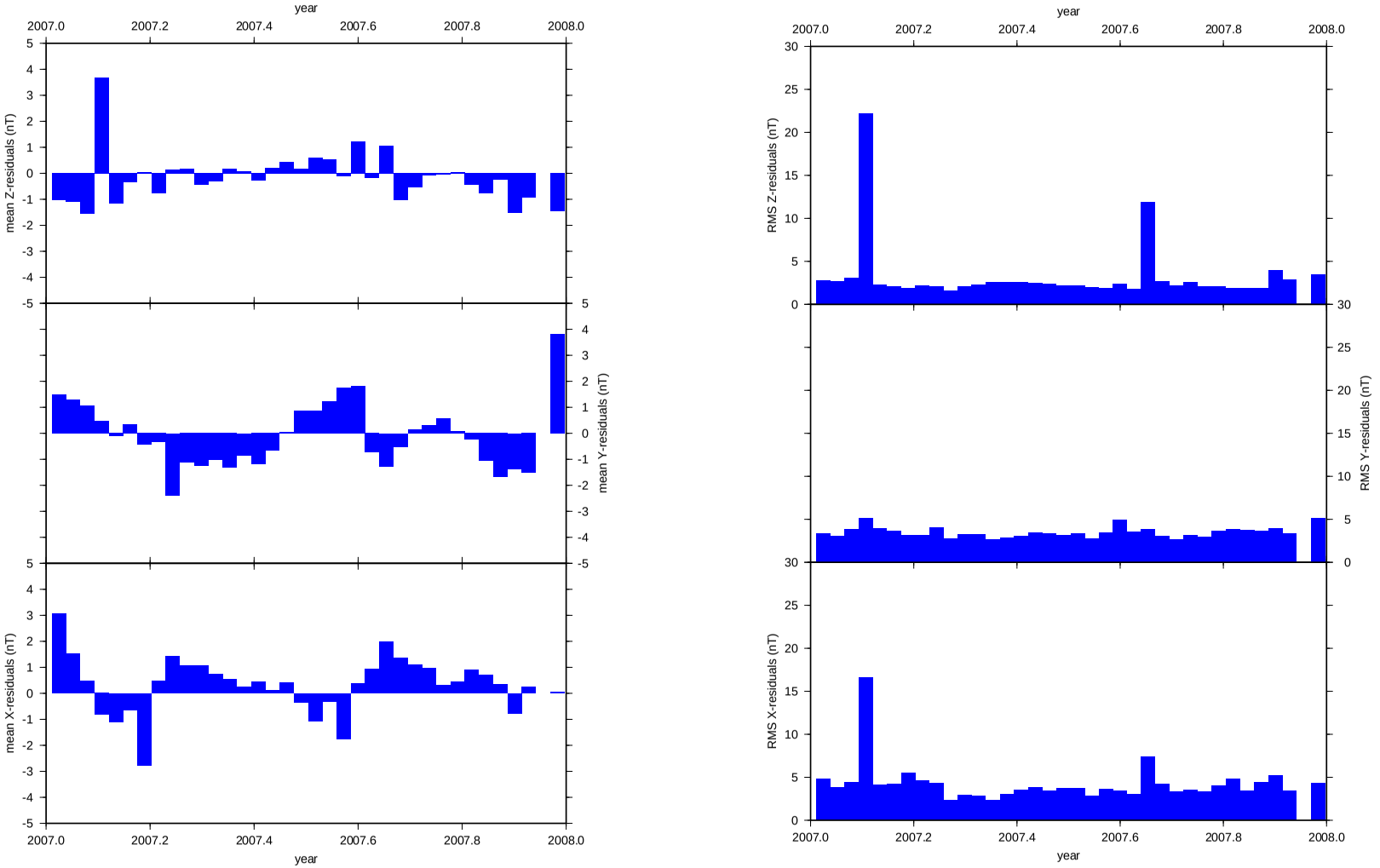

Figure 6.34: Residual averages and RMS values for the vector model

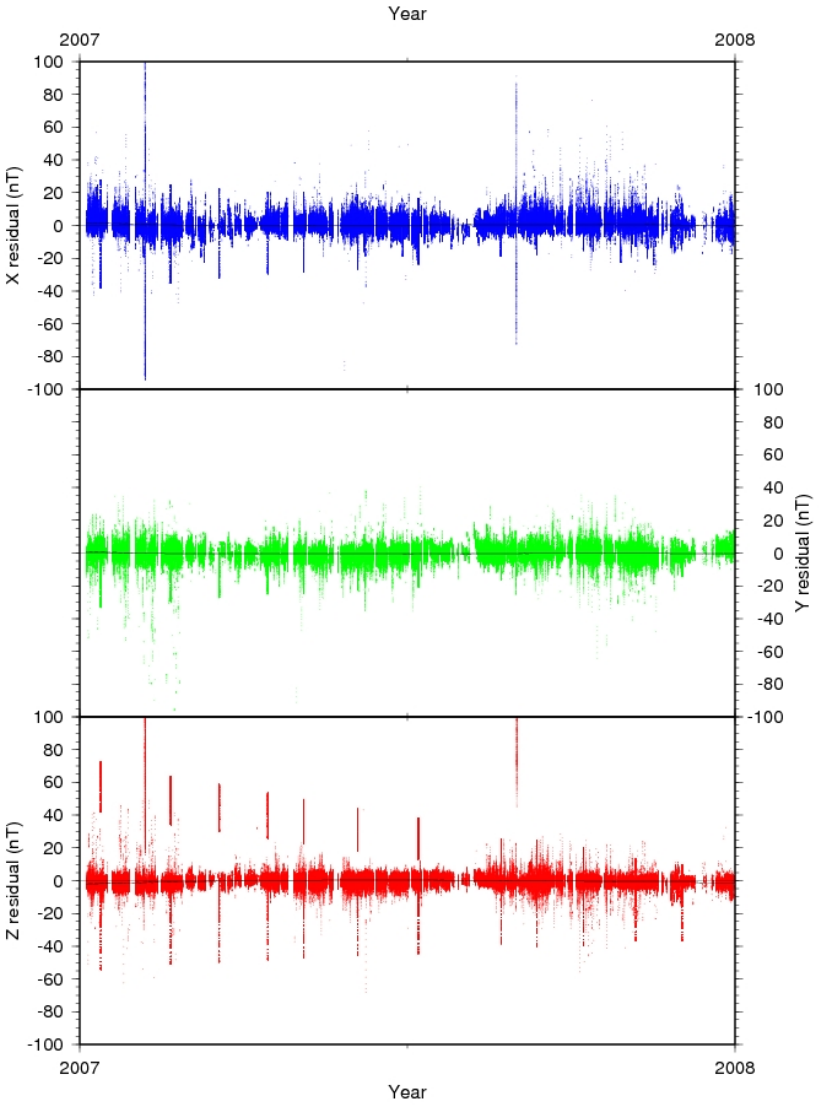

Figure 6.35: Residuals against time for the vector model, with additional synthetic data from CHAOS-4 in the satellite data gap.

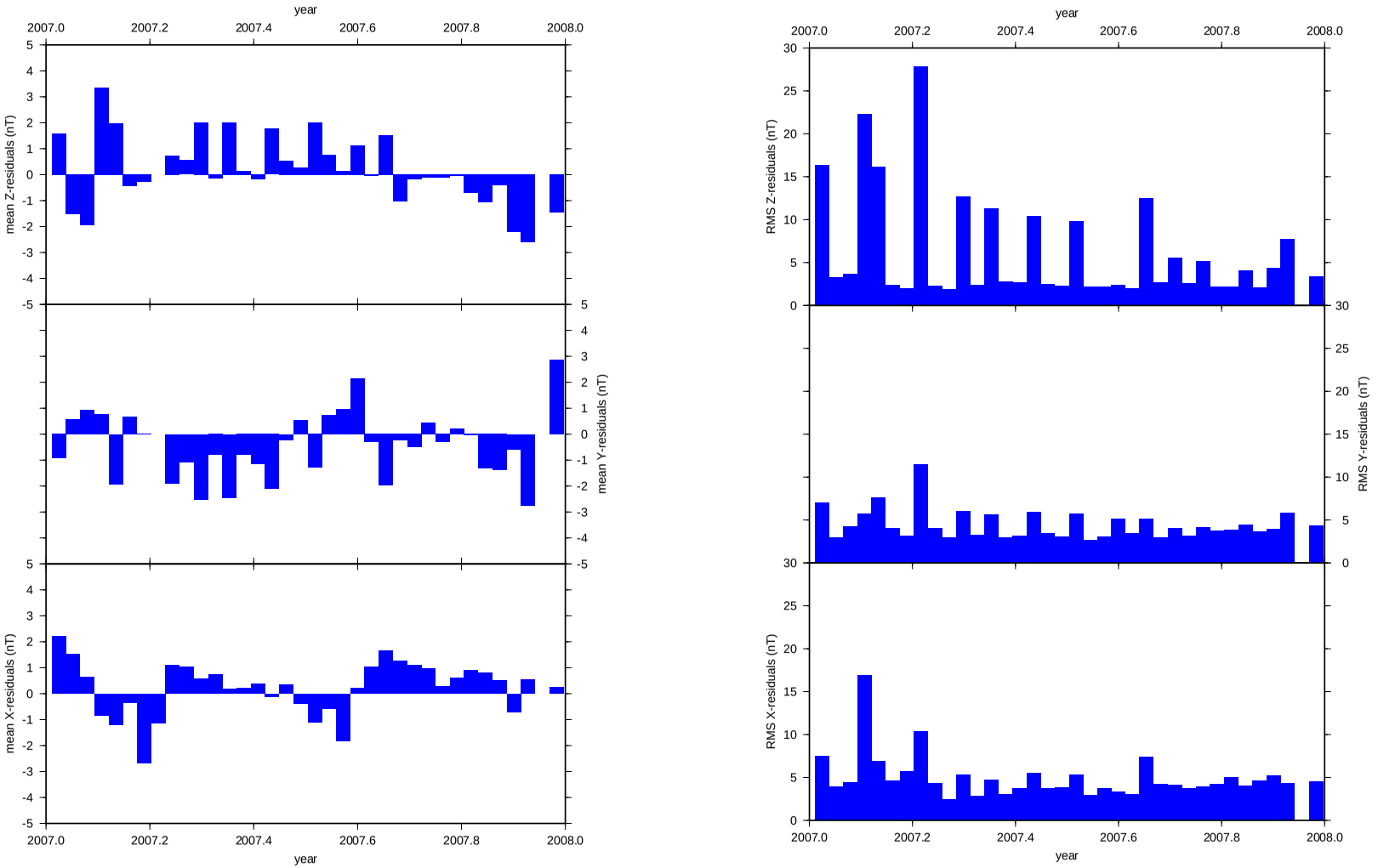

Figure 6.36: Residual averages and RMS values for the vector model with additional pseudo from CHAOS-4 in the satellite data gap.

did reduce the anomaly it did not fully resolve the problem, and introduced large residuals. In the power spectra the vector selection model is systematically higher in spectrum than CHAOS and MF7 after approximately degree 28 which may suggest a problem with the higher degree coefficients, or additional noise.

The PCAE spectrum maintains lower power than the vector selection for most spherical harmonic degrees, particularly the highest degrees, and arguably provides the better option for immediate use in a model, until the problems with the vector selection can be resolved. However, the dispute over the uniformity of the PC North and South indices, and the delay in obtaining the AE indices present practical problems for this selection too, particularly when Swarm data become available.

6.6.1 What have we learned about polar geomagnetism from field modelling?

In Figure 6.40 we compare our preferred model based on the pseudo selection with the full crustal field from CHAOS-4 (up to degree 100) and EMAG3 (*Maus et al.*, 2007b). EMAG3 is the NGDC candidate model for the World Digital Magnetic Anomaly Map (WDMAM). We use EMAG3 for comparison because it is a high resolution grid of the magnetic intensity compiled from satellite, marine, aeromagnetic and ground magnetic surveys. This means it provides a better representation of the crustal magnetic field than models made from satellite data alone. EMAG3 is provided on a 3 minute grid, however, to enable comparison of the large scale features in our vector model we have plotted all three models on a 1° grid.

The vector model clearly contains larger magnitude anomalies than EMAG3, as well as some large anomalies in regions which have only very small anomalies in EMAG3, for example, between Greenland and Norway. However, the large anomalies seen in EMAG3 are replicated in the vector model with a similar shape and extent (although they generally have a larger amplitude). In some cases the shapes of anomalies in EMAG3 are closer to the vector model than CHAOS-4. This shows that our models support observations and features from other, more complex, models, despite a different modelling approach. This ought to give the scientific community confidence that polar geomagnetism models have value and some accuracy, for science and for other applications.

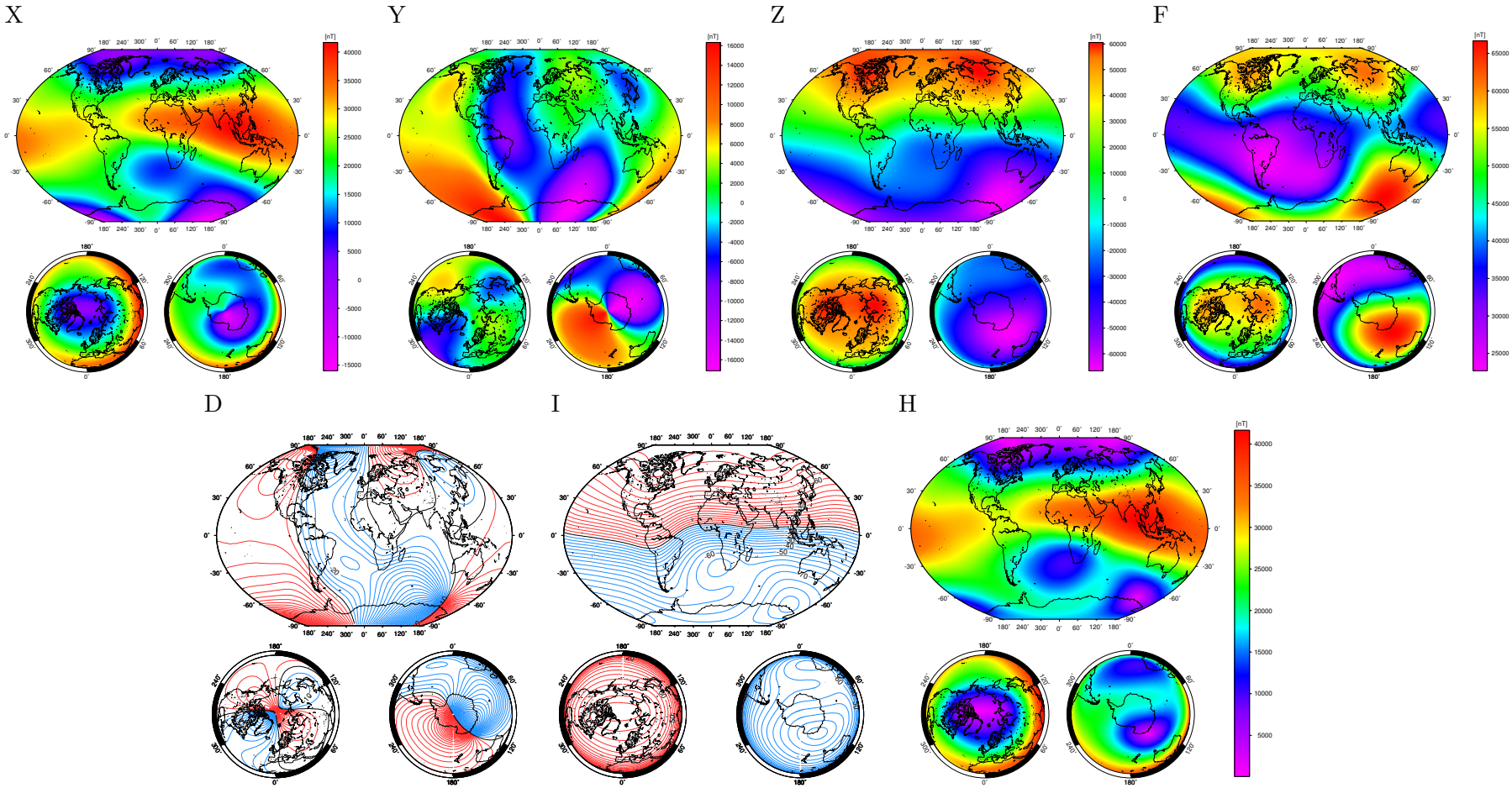

Figure 6.37: The magnetic components of our preferred model (for n=1-60) using the vector selection for 2007. The declination (D) and inclination (I) plots have contour intervals of 5°, blue and red represent negative and positive values respectively.

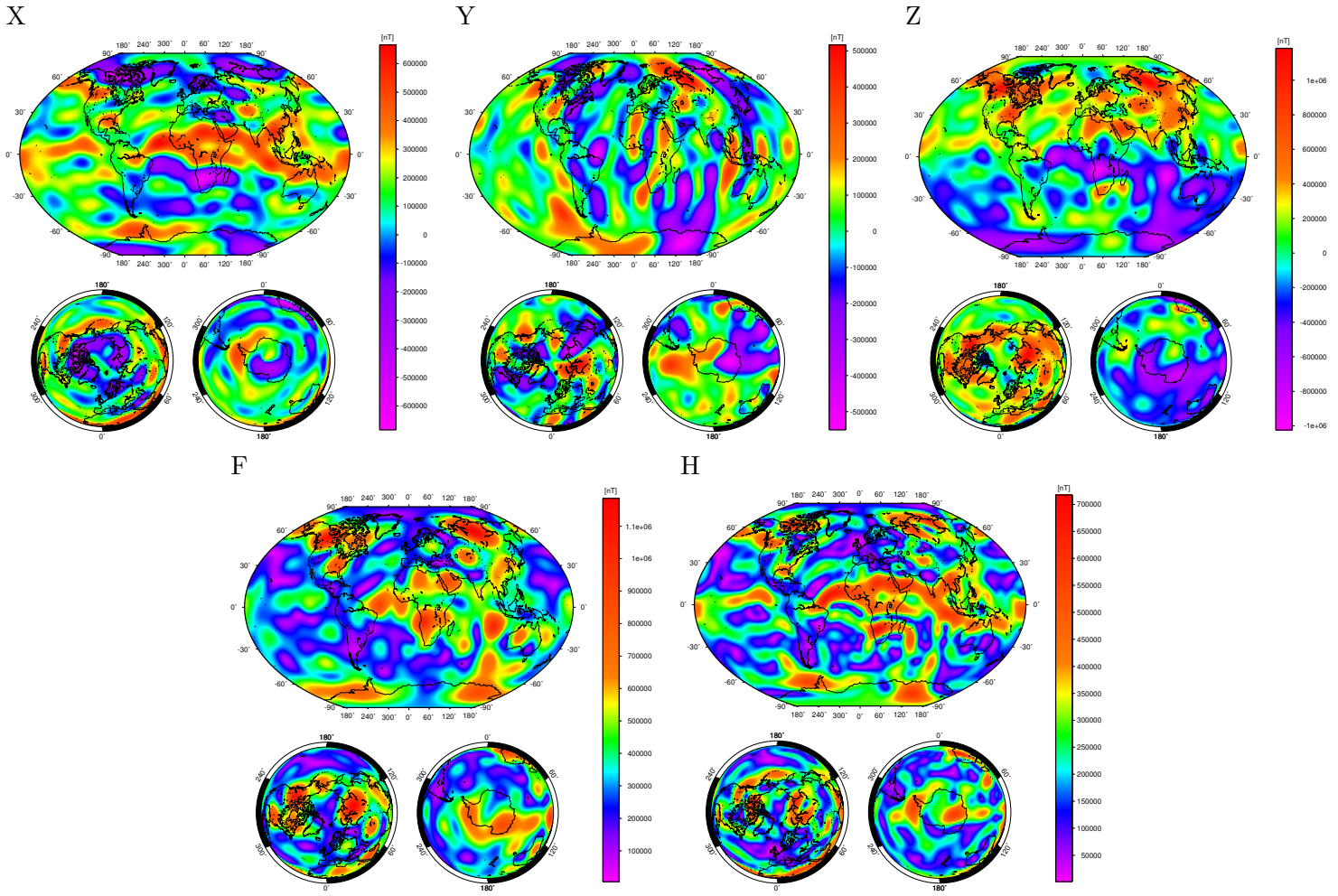

Figure 6.38: The magnetic components of the core field of our preferred model (for n=1-15) using the vector selection for 2007.

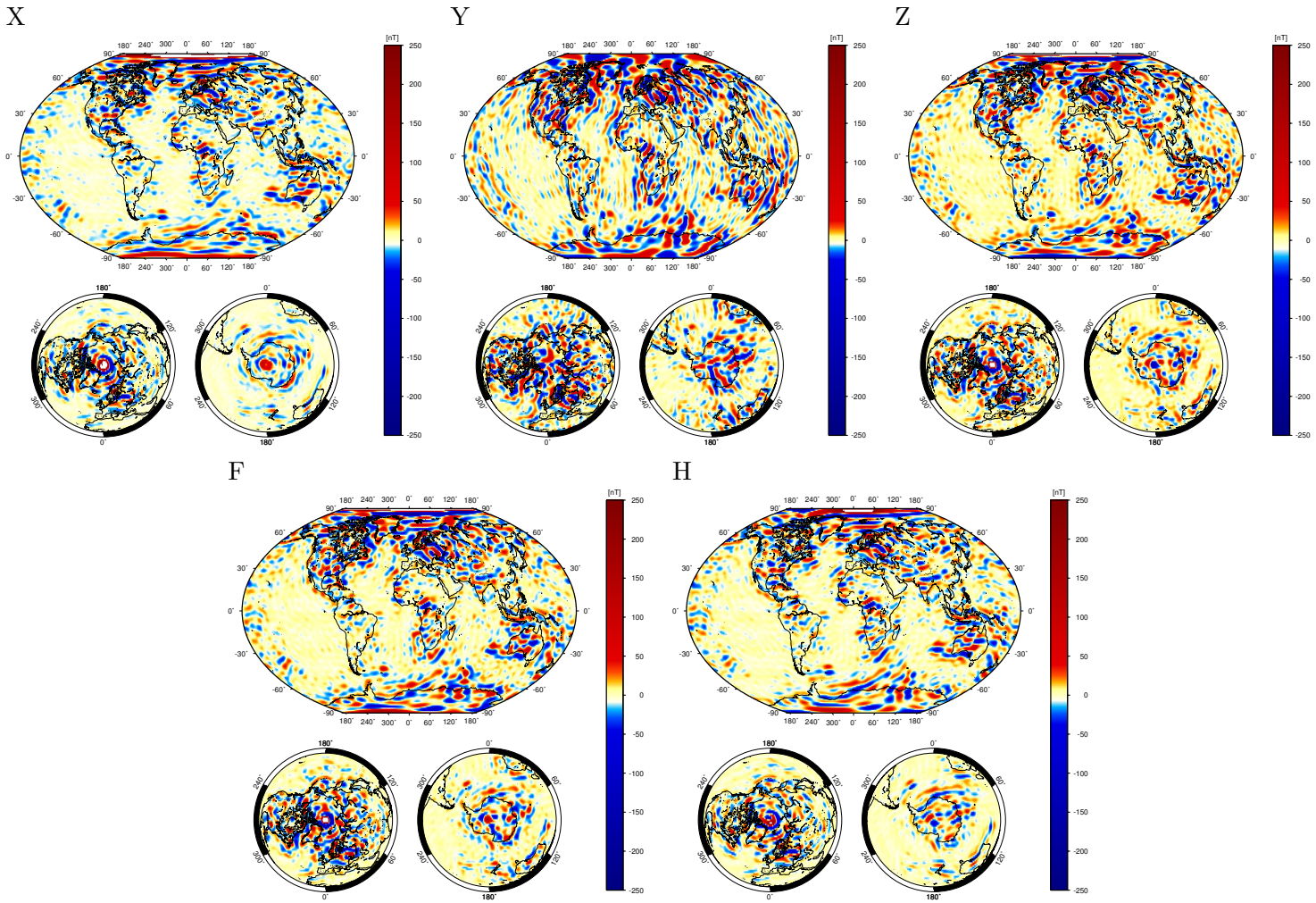

Figure 6.39: The magnetic components of the crustal field of our preferred model (for n=16-60) using the vector selection in 2007.

6.7 Modelling Summary

The vector selection, using our new criteria, selects more data (both scalar and vector) than the traditional selection. Many more vector data are included, especially at high latitudes, and the dataset is much more homogeneous throughout the year.

The addition of more high latitude vector data does not drastically alter the behaviour of the model. The largest differences between the vector selection and any of the other models are, unsurprisingly, at high latitudes, which is the focus of the differing selection criteria. However, we do also see differences at low latitudes.

Apart from the anomaly over the geographic pole, caused by the satellite data gap, the vector selection does have more similarity with the CHAOS-4 than the traditional selection. This is encouraging, as the CHAOS-4 model is based on data for a much longer timespan and a more complicated parameterisation. The same is true for MF7 which uses along track filtering, line levelling and corrections for the magnetosphere and ionospheric sources.

There is still some work required to resolve the problem with the satellite data gap, although the addition of some pseudo data from the CHAOS-4 model did go some way to alleviating this. However, the vector selection allows our relatively simple model, based on only one year's data, to approach much more complex models. Therefore in the future when we match this method of selection with a more complex modelling techniques we should get a better model of the geomagnetic field.

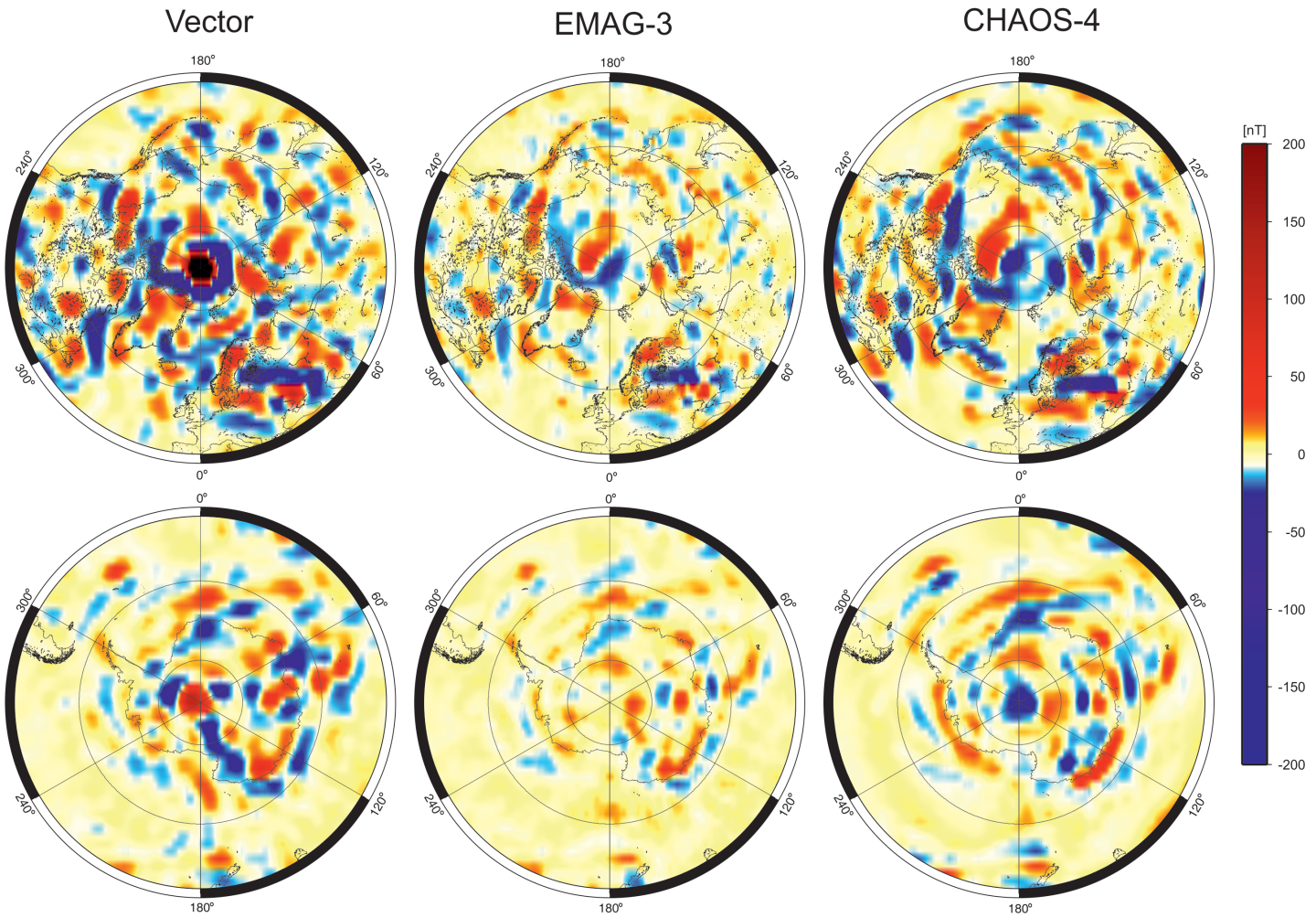

Figure 6.40: Comparison of crustal plots at the North and South poles for the vector selection model (n=16-60), CHAOS-4 (n=16-100) and EMAG3, the NGDC candidate model for the World Digital Magnetic Anomaly Map (compiled from satellite, marine, aeromagnetic and ground magnetic surveys). All maps are plotted on a 1° grid to allow for direct comparison of larger scale features.

Chapter 7

Synthesis and Discussion

Current published geomagnetic models perform well, with small residuals to magnetic field data over much of the globe. However, there are clear problems at high latitudes, where the field is highly complex. Currently most global magnetic field models exclude high latitude vector data completely in an effort to reduce the effect of highly time variable external magnetic field sources, particularly those associated with field-aligned currents. Here we have investigated the potential for using indices specific to the poles, alongside the global indices already used, and new selection techniques to better define 'quiet' data in the polar regions.

Through investigating existing models (Chapter 3) we find that the largest residuals to all three models we have studied (CHAOS-2, CM4 and T01) occur at high latitudes, particularly in the auroral oval. The largest residuals are related to FACs but auroral signatures are also evident (Section 3.3.2), identifiable in the residuals in the direction of the field. This means that using only scalar data at high latitudes will not totally remove the high latitude external signals. This is seen in plots of the scalar field (Section 3.4.3, Figure 3.9), where even in the scalar field there are some larger residuals near the pole.

The largest residuals we see are related to the most variable signals (i.e. highest standard deviation) as can be seen in Figure 3.11. Again this is consistent with signatures from the highly variable external fields in the auroral region.

The comparison between CHAMP and Ørsted (Section 3.7) shows that auroral signatures are consistent, in magnitude and location, with increasing altitude. This is important as it shows that steps need to be taken to reduce the influence of external magnetic fields for both satellites, as both show large residuals in the auroral regions. This will also be important for the upcoming Swarm mission, as we would expect to see these auroral signatures in all three satellites, one of which is at a higher altitude than the lower pair.

We also find that the auroral oval signature has some consistency with time. On timescales of approximately one month the location of the oval is relatively stable in time. In terms of data selection this implies that some oval signature will always be

present, even at quiet times. There may be a potential for using an average location of the oval in data selection, although this remains for future work.

Rather than simply discarding all vector data polewards of a fixed limit in geomagnetic latitude, we find that the location of the auroral oval itself can be used in the selection process (Chapter 4). This can be done using an existing model (for example OVATION, see Section 4.1), based on independent observations; however, gaps in the model and computational expense mean we instead found a data driven technique.

The variable nature of signals related to the auroral oval (as discussed in Section 3.5), allows the identification of the auroral oval using standard deviation values. One method for doing this is to take binned standard deviations of the residuals to an *a priori* model (e.g., CHAOS-2 or CM4) and then select data below a standard deviation threshold (see Section 4.2.1). This works well, but ideally we do not want to influence the selection of data with the choice of *a priori* model.

Taking the standard deviation (in bins) of a dataset which has been de-trended using a quadratic fit, works remarkably well at identifying the auroral oval (Section 4.3). This method allows the 'noisiest' data, i.e. that most affected by the highly variable external fields, to be identified and excluded from the data selection, without relying on a pre-existing model.

In addition to identifying the oval location, we also investigated using magnetic indices to improve the selection of high latitude data. In general, the K_p and D_{st} indices are used to select quiet data from the whole globe for use in geomagnetic field modelling. However, it has been shown, (*Ritter et al.*, 2004b, and references therein), that these indices are inadequate for describing activity at high latitudes. We found that the PC and AE indices are more successful criteria for data selection in the polar regions, particularly when used in combination with K_p and D_{st}. These indices also help reduce the influence of signatures from the auroral oval, which may remain in the scalar data, as mentioned above.

By employing the additional selection criteria we are also able to extend the local time window employed (18:00 to 06:00 LT). This makes the data density of the selection more homogeneous with time (Section 6.1). The narrower local time window (22:00 to 04:00 LT) led to large periods of time (approximately 50-60 days each) where there were very little scalar data and no vector data selected (Figure 6.1).

When comparing the model made with our new selection against a more traditional selection we find that the largest differences are at high latitudes. This is unsurprising as this is the region where the selections differ the most.

Aside from an anomalous region directly over the geographic poles (which is not a real feature of the field and is related to the polar gap in satellite data), the new selection appears to characterise the field better, with sharper defined features in

the core field, better identification of sea-floor stripes at divergent plate margins, and perhaps less visible leakage of external field noise into the crustal field. When we add pseudo data from CHAOS-4 to the selection, within the polar gap, we find that the anomaly over the geographic poles is reduced.

When comparing with other, more complex, field models our new selection performs well, reproducing many of the features, despite having far fewer data (one year compared to more than 11 years for CHAOS-4), and a simpler characterisation of the external fields.

7.1 Avenues For Further Research

In Section 4.1 we discussed the potential for using models of the auroral oval, such as OVATION, as an independent means for identifying the location of the highly variable external fields. This information can then be used to avoid selection of data which are affected by these fields. As models which provide the location of the auroral oval boundaries and field aligned currents improve, the use of such models could become a viable option for use in data selection. For example, the Active Magnetosphere and Planetary response Experiment (AMPERE)[1] allows radial current density to be estimated every 10minutes (as opposed to 2 hours for OVATION) from the Iridium® satellites.

The SECS method could also provide a means for reducing the influence of auroral currents on the high-latitude data, from both scalar and vector data. This could be through identifying the highly variable currents for data selection purposes from independent observatory data (as for the oval model), although observatory distribution and distance from ionospheric sources is a limiting factor. There is also a potential for using the SECS method as part of the modelling process, to aid in the parameterisation of external fields.

An obvious deficiency in our models is the limited time-span of our selection. Given more time we could extend the dataset up to the full CHAMP timespan (over a decade), and we could also introduce data from Ørsted and geomagnetic observatories. A longer time-span will also allow us to investigate the possible high latitude improvements to models of secular variation. In the future the Swarm mission will provide even better data, with three satellites measuring the geomagnetic field simultaneously.

[1] available from http://ampere.jhuapl.edu (website currently down for a rebuild), funded by the National Science Foundation.

Bibliography

Akasofu, S.-I., and S. Chapman (1961), The ring current, geomagnetic disturbance, and the Van Allen radiation belts, *J. Geophys. Res.*, *66*, 1321–1350.

Amm, O. (1997), Ionospheric elementary current systems in spherical coordinates and their application, *J. Geomag. Geoelectr.*, *49*, 947–955.

Amm, O., and A. Viljanen (1999), Ionospheric disturbance magnetic field continuation from the ground to the ionosphere using spherical elementary current systems, *Earth Planets Space*, *51*, 431–440.

Aurnou, J., S. Andreadis, L. Zhu, and P. Olson (2003), Experiments on convection in Earth's core tangent cylinder, *Earth Planet. Sci. Lett.*, *212*, 119–134.

Aurnou, J. M., J. L. Buttles, G. A. Neumann, and P. L. Olson (1996), Electromagnetic core-mantle coupling and paleomagnetic reversal paths, *J. Geophys. Res.*, *23*, 2705–2708.

Backus, G. E. (1970), Non-uniqueness of the external geomagnetic field determined by surface intensity measurements, *J. Geophys. Res.*, *75*, 6337–6341.

Barkhatov, N. A., L. I. Gromova, A. E. Levittin, and S. E. Revunov (2008), The relation between solar activity and orientation of the solar wind electric field relative to the Earth's magnetic moment, *Geomag. Aeron.*, *48*, 713–718.

Bartels, J. (1949), The standardised index, K_s, and the planetary index, K_p, in *IATME Bull.*, *Int. Union of Geod. and Geophys.*, vol. 12b, Publ. Off. Paris.

Bartels, J., N. H. Heck, and H. F. Johnston (1939), The three-hour range index measuring geomagnetic activity, *J. Geophys. Res.*, *44*.

Baumjohann, W., and R. Nakamura (2007), Magnetospheric contributions to the terrestrial magnetic field, in *Geomagnetism*, *Treatise on Geophysics*, vol. 5, chap. 3, pp. 77–92, Elsevier.

Baumjohann, W., and R. A. Treumann (1996), *Basic Space Plasma Physics*, Imperial College Press.

Bloxham, J., D. Gubbins, and A. Jackson (1989), Geomagnetic secular variation, *Philos. Trans. R. Soc. London A*, *329*, 415–502.

Bloxham, J., S. Zatman, and M. Dumberry (2002), The origin of geomagnetic jerks, *Nature*, *420*, 65–68.

Boakes, P. D., S. E. Milan, G. A. Abel, M. P. Freeman, G. Chisham, B. Hubert, and T. Sotirelis (2008), On the use of IMAGE FUV for estimating the latitude of the open/closed magnetic field line boundary in the ionosphere, *Ann. Geophys.*, *26*, 2759–27,969.

Buffett, B. A., and G. A. Glatzmaier (2000), Gravitational braking of inner-core rotation in geodynamo simulations, *Geophys. Res. Lett.*, *27*, 3125–3128.

Burton, R. K., R. L. McPherron, and C. T. Russel (1975), An empirical relationship between interplanetary conditions and Dst, *J. Geophys. Res.*, *80*, 4204–4214.

Campbell, W. H. (1996), Geomagnetic storms, the Dst ring-current myth and log-normal distributions, *J. Atmos. Sol.-Terr. Phys.*, *58*, 1171–1187.

Carbary, J. F. (2005), A K_p-based model of auroral boundaries, *Space weather*, *3*, S10,001.

Chapman, S. (1919), An outline of a theory of magnetic storms, *Proc. Roy. Soc. London*, *A-95*, 61–83.

Chen, G.-X., W.-Y. Xu, Z.-G. Wei, B.-H. Ahn, and Y. Kamide (2003), Auroral electrojet oval, *Earth Planets Space*, *55*, 255–261.

Constable, S. (1993), Constraints on mantle electrical conductivity from field and laboratory measurements, *J. Geomag. Geoelectr.*, *45*, 707–728.

Courtillot, V., and J.-L. Le Mouël (1984), Geomagnetic secular variation impulses, *Nature*, *311*, 709–716.

Courtillot, V., J. Ducruix, and J.-L. Le Mouël (1978), Sur une accélération récente de la variation séculaire du champ magnétique terrestre, *C. R. Acad. Sci. Paris. Ser. D*, *287*, 1095–1098.

Cowley, S. W. H., J. P. Morelli, and M. Lockwood (1991), Dependence of convective flows and particle precipitation in the high-latitude dayside ionosphere on the X and Y componenets of the Interplanetary Magnetic field, *J. Geophys. Res.*, *96*, 5557–5564.

Davis, T. N., and M. Sugiura (1966), Auroral electrojet activity index AE and its universal time variations, *J. Geophys. Res.*, *71*, 785–801.

De Michelis, P., R. Tozzi, and A. Meloni (2009), On the terms of geomagnetic daily variation in Antartica, *Ann. Geophys.*, *27*, 2483–2490.

Dormy, E., and J.-L. Le Mouël (2008), Geomagnetism and the dynamo: where do we stand?, *C. R. Physique*, *9*, 711–720.

Dormy, E., and M. Mandea (2005), Tracking geomagnetic impulses at the core-mantle boundary, *Earth Planet. Sci. Lett.*, *237*, 300–309.

Dungey, J. W. (1961), Interplanetary magnetic field and the auroral zones, *Phys. Rev. Lett.*, *6*, 47–48.

Feldstein, Y. I., and G. V. Starkov (1967), Dynamics of auroral belt and polar geomagnetic disturbances, *Planet. Space Sci.*, *15*, 209–229.

Finlay, C. C., et al. (2010), International Geomagnetic Reference Field: the eleventh generation, *Geophys. J. Int.*, *183*, 1216–1230.

Friis-Christensen, E., H. Lühr, D. Knudsen, and R. Haagmans (2008), Swarm – an Earth observation mission investigating Geospace, *Adv. Space. Res.*, *41*, 210–216.

Fukushima, N. (1976), Generalized theorem for no ground magnetic effect of vertical currents connected with Pedersen currents in uniform-conductivity ionosphere, *Rep. Ionos. Space Res. Japan*, *30*, 35–40.

Gjerloev, J. W. (2009), A global ground-based magnetometer initiative, *EOS*, *90*(27), 230–231.

Gjerloev, J. W., R. A. Hoffman, M. M. Friel, L. A. Frank, and J. B. Sigwarth (2004), Substorm behaviour of the auroral electrojet indices, *Ann. Geophys.*, *22*, 2135–2149.

Gubbins, D., and N. Roberts (1983), Use of the frozen flux approximation in the interpretation of archaemagnetic and palaeomagnetic data, *Geophys. J. R. Astron. Soc.*, *73*, 675–687.

Gussenhoven, M., D. A. Hardy, and W. J. Burke (1981), DMSP/F2 electron observations of equatorward auroral boundaries and their relationship to magnetospheric electric fields, *J. Geophys. Res.*, *86*, 768–778.

Gussenhoven, M. S., D. A. Hardy, and N. Heinemann (1983), Systematics of the equatorward diffuse auroral boundary, *J. Geophys. Res.*, *88*, 5692.

Halley, E. (1692), On the cause of the change in the variation of the magnetic needle; with an hypothesis of the structure of the internal parts of the earth, *Phil. Trans. Roy. Soc. Lond.*, *17*, 470–478.

Hamilton, B., S. Macmillan, and A. Thomson (2010), The BGS magnetic field candidate models for the 11th generation IGRF, *Earth Planets Space*, *62*, 737–743.

Hemant, K., E. Thébault, M. Mandea, D. Ravat, and S. Maus (2007), Magnetic anomaly map of the world: merging satellite, airborne, marine and ground-based magnetic data sets, *Earth and Plant. Sci. Lett.*, *260*, 56–71.

Holme, R. (2007), Large-scale flow in the core, in *Core Dynamics*, *Treatise on Geophysics*, vol. 8, edited by P. Olson, chap. 4, pp. 107–130, Elsevier.

Holme, R., and O. de Viron (2005), Geomagnetic jerks and a high-resolution length-of-day profile for core studies, *Geophys. J. Int.*, *160*, 435–439.

Holme, R., and N. Olsen (2006), Core surface flow modelling from high-resolution secular variation, *Geophys. J. Int.*, *166*, 518–528.

Holzworth, R. H., and C.-I. Meng (1975), Mathematical representation of the auroral oval, *Geophys. Res. Lett.*, *2*, 377380.

Holzworth, R. H., and C.-I. Meng (1984), Auroral boundary variation and the Interplanetary Magnetic Field, *Planet. Space Sci.*, *32*, 25–29.

Hulot, G., C. Eymin, B. Langlais, M. Mandea, and N. Olsen (2002), Small-scale structure of the geodynamo inferred from Oersted and MAGSAT satellite data, *Nature*, *416*, 620–623.

Iijima, T., and T. A. Potemra (1976a), The amplitude and distribution of field-aligned currents at northern high latitudes observed by Triad, *J. Geophys. Res*, *81*, 2165–2174.

Iijima, T., and T. A. Potemra (1976b), Field-aligned currents in the dayside cusp observed by Triad, *J. Geophys. Res.*, *81*, 5971–5979.

Iijima, T., and T. A. Potemra (1978), Large-scale characteristics of field-aligned currents associated with substorms, *J. Geophys. Res.*, *83*, 599–615.

Jackson, A., A. R. T. Jonkers, and M. R. Walker (2000), Four centuries of geomagnetic secular variation from historical records, *Phil. Trans. R. Soc. Lond. A*, *358*, 957–990.

Jonkers, A. R. T. (2007), Discrete scale invariance connects geodynamo timescales, *Geophys. J. Int.*, *171*, 581–593.

Kamide, Y., and S. Matsushita (1979a), Simulation studies of ionospheric electric fields and currents in relation to field-aligned currents 1. Quiet periods, *J. Geophys. Res.*, *84*, 4083–4098.

Kamide, Y., and S. Matsushita (1979b), Simulation studies of ionospheric electric fields and currents in relation to field-aligned currents 2. Substorms, *J. Geophys. Res.*, *84*, 4099–4115.

Kamide, Y., et al. (1998), Current understanding of magnetic storms: Storm-substorm relationships, *J. Geophys. Res.*, *103*, 17,705–17,728.

Karinen, A., and K. Mursula (2005), A new reconstruction of the D_{st} index for 1932–2002, *Ann. Geophys.*, *23*, 478–485.

Kerridge, D. (2001), INTERMAGNET: Wolrdwide near-real-time geomagnetic observatory data, in *Proc. Space Weather Workshop, ESTEC*.

Kim, H. R., L. R. Gaya-Piqué, R. R. B. von Frese, P. T. Taylor, and J. W. Kim (2005), CHAMP anomalies of the Antarctic crust, in *Earth observation with CHAMP: Results from three years orbit*, pp. 261–266, Springer-Verlag.

Kivelson, M. G., and C. T. Russel (1995), *Introduction to Space Physics*, Cambridge University Press.

Kono, M. (2007), Geomagnetism in perspective, in *Geomagnetism*, *Treatise on Geophysics*, vol. 5, edited by M. Kono, chap. 3, pp. 1–31, Elsevier.

Kullen, A., S. Ohtani, and T. Karlsson (2009), Geomagnetic signatures of auroral substorms preceded by pseudobreakups, *J. Geophys. Res.*, *114*, A04,201.

Kuvshinov, A. V. (2008), 3-D global induction in the oceans and solid Earth: recent progress in modeling magnetic and electric fields from sources of magnetospheric, ionospheric and oceanic origin, *Surv. Geophys.*, *29*, 139–186.

Langel, R. A., and R. H. Estes (1982), A geomagnetic field spectrum, *Geophys. Res. Lett.*, *9*, 250–253.

Langel, R. A., T. J. Sabaka, R. T. Baldwin, and J. A. Conrad (1996), The near-Earth magnetic field from magnetospheric and quiet-day ionospheric sources and how it is modeled, *Phys. Earth Planet. Int.*, *98*, 235–267.

Laundal, K. M., and N. Østgaard (2009), Asymmetric auroral intensities in the Earth's Northern and Southern hemispheres, *Nature*, *460*, 491–493.

Laundal, K. M., N. Østgaard, K. Snekvik, and H. U. Frey (2010), Interhemispheric observations of emerging polar cap asymmetries, *J. Geophys. Res.*, *115*, A07,230.

Le Huy, M., M. Alexandrescu, G. Hulot, and J.-L. Le Mouël (1998), On the characteristics of successive geomagnetic jerks, *Earth Planets Space*, *50*, 723–732.

Lester, M., S. E. Milan, G. Provan, and J. A. Wild (2006), Review of ionospheric effects of solar wind magnetopshere coupling in the context of the expanding contracting polar cap boundary model, *Space Sci. Rev.*, *124*, 117–130.

Lesur, V., S. Macmillan, and A. Thomson (2005), A magnetic field model with daily variations of the magnetospheric field and its induced counterpart in 2001, *Geophys. J. Int*, *160*, 79–88.

Lesur, V., S. Macmillan, and A. Thomson (2006), Deriving main field and secular variation models from synthetic Swarm satellite and observatory data, *Earth Planets Space*, *58*, 409–416.

Lesur, V., I. Wardinski, M. Rother, and M. Mandea (2008), GRIMM: The GFZ reference internal magnetic model based on vector satellite and observatory data, *Geophys. J. Int.*, *173*, 382–394.

Lesur, V., I. Wardinski, M. Hamoudi, and M. Rother (2010), The second generation of the GFZ Reference Internal Magnetic Model: GRIMM-2, *Earth Planets Space*, *62*, 765–773.

Longden, N., G. Chisham, M. P. Freeman, G. A. Abel, and T. Sotirelis (2010), Estimating the location of the open-closed magnetic field line boundary from auroral images, *Ann. Geophys.*, *28*, 1659–1678.

Love, J. J. (2008), Magnetic monitoring of Earth and space, *Physics Today*, *61*, 31–37.

Love, J. J., and K. J. Remick (2007), Magnetic indices, in *Encyclopedia of Geomagnetism and Paleomagnetism*, edited by D. Gubbins and E. Herrero-Bervera, pp. 509–512, Springer, Dordrecht, Neth.

Lowes, F. J. (1966), Mean-square values on sphere of spherical harmonic vector fields, *J. Geophys. Res.*, *71*, 2179.

Lukianova, R., O. Troshichev, and G. Lu (2002), The polar cap magnetic activity indices in the southern (PCS) and northern (PCN) polar caps: Consistency and discrepancy, *Geophys. Res. Lett.*, *29*, 26.

Lyons, L. R. (2000), Geomagnetic disturbances: characteristics of, distinction between types, and relations to interplanetary conditions, *J. Atmos. Solar-Terr. Phys.*, *62*, 1087–1114.

Macmillan, S. (2007a), Observatories, Overview, in *Encyclopedia of Geomagnetism and Paleomagnetism*, edited by D. Gubbins and E. Herrero-Bervera, pp. 708–711, Springer.

Macmillan, S. (2007b), Repeat stations, in *Encyclopedia of Geomagnetism and Paleomagnetism*, edited by D. Gubbins and E. Herrero-Bervera, pp. 858–859, Springer.

Macmillan, S., and C. Finlay (2011), *Geomagnetic Observations and Models*, chap. 10, The International Geomagnetic Reference Field, IAGA Special Book Series, Springer.

Malin, S. R. C., and B. M. Hodder (1982), Was the 1970 geomagnetic jerk of internal or external origin?, *Nature*, *296*, 726–728.

Mandea, M. (2006), Magnetic satellite missions: where have we been and where are we going?, *C. R. Geosci.*, *338*, 1002–1011.

Mandea, M., and M. Purucker (2005), Observing, modeling and interpreting magnetic fields of the solid Earth, *Surveys in Geophys.*, *26*, 415–459.

Mandea, M., E. Bellanger, and J. L. Le Mouël (2000), A geomagnetic jerk for the end of the 20th century?, *Earth Planet. Sci. Lett.*, *183*, 369–373.

Mandea Alexandrescu, M., D. Gilbert, J.-L. Le Mouël, G. Hulot, and G. Saracco (1999), An estimate of average lower mantle conductivity by wavelet analysis of geomagnetic jerks, *J. Geophys. Res.*, *104*, 17,735–17,745.

Matzka, J., A. Chulliat, M. Mandea, C. C. Finlay, and E. Qamili (2010), Geomagnetic observations for main field studies: From ground to space, *Space Sci. Rev.*, *155*, 29–64.

Mauersberger, P. (1956), Das Mittel der Energiedichte des geomagnetischen Hauptfeldes an der Erdoberfläche and seine säkulare Änderung, *Gerlands Beitr. Geophys.*, *65*, 207–215.

Maus, S. (2010), An ellipsoidal harmonic representation of Earth's lithospheric magnetic field to dergree and order 720, *Geochem. Geophys. Geosys.*, *11*, Q06,015.

Maus, S., and H. Lühr (2005), Signature of the quiet-time magnetospheric magnetic field and its electromagnetic induction in the rotating Earth, *Geophys. J. Int.*, *162*, 755–763.

Maus, S., and P. Weidelt (2004), Separating the magnetospheric disturbance magnetic field into external and transient internal contributions using a 1D conductivity model of the Earth, *Geophys. Res. Lett.*, *31*, L12,614.

Maus, S., M. Rother, R. Holme, H. Lühr, N. Olsen, and V. Haak (2002), First scalar magnetic anomaly map from CHAMP satellite data indicates weak lithospheric field, *Geophys. Res. Lett.*, *29*, 47.

Maus, S., S. Macmillan, F. Lowes, and T. Bondar (2005a), Evaluation of candidate geomagnetic field models for the 10th generation of IGRF, *Earth, Planets, Space*, *52*, 1173–1181.

Maus, S., H. Lühr, G. Balasis, M. Rother, and M. Mandea (2005b), Introducing POMME, Potsdam Magnetic Model of the Earth, in *Earth Observation with CHAMP: Results from three years in Orbit*, edited by C. R. et. al., pp. 293–298.

Maus, S., M. Rother, K. Hemant, C. Stolle, H. Lühr, A. Kuvshinov, and N. Olsen (2006a), Earth's lithospheric magnetic field determined to spherical harmonic degree 90 from CHAMP satellite measurements, *Geophys. J. Int.*, *164*, 319–330.

Maus, S., M. Rother, K. Hemant, C. Stolle, H. Lühr, and A. Kuvshinov (2006b), Earth's lithospheric magnetic field determined to spherical harmonic degree 90 from CHAMP satellite measurements, *Geophys. J. Int.*, *164*, 319–330.

Maus, S., M. Rother, C. Stolle, W. Mai, S. Choi, H. Lühr, D. Cooke, and C. Roth (2006c), Third generation of the Potsdam Magnetic Model of the Earth (POMME), *Geochem. Geophys. Geosys.*, *7*, Q07,008.

Maus, S., H. Lühr, M. Rother, G. Balasis, P. Ritter, and C. Stolle (2007a), Fifth-generation lithospheric magnetic field model from CHAMP satellite measurements, *Geochem. Geophys. Geosy.*, *8*(5).

Maus, S., T. Sazonova, K. Hemant, J. D. Fairhead, and D. Ravat (2007b), National Geophysical Data Center candidate for the World Digital Magnetic Anomaly Map, *Geochem. Geophys. Geosys*, *8*, Q06,017.

Maus, S., F. Yin, H. Lühr, C. Manoj, M. Rother, J. Rauberg, I. Michaelis, C. Stolle, and R. D. Müller (2008), Resolution of direction of oceanic magnetic lineations by the sixth-generation lithospheric magnetic field model from CHAMP satellite magnetic measurements, *Geochem. Geophys. Geosys.*, *9*, Q07,021.

Maus, S., C. Manoj, J. Rauberg, I. Michaelis, and H. Lühr (2010), NOAA/NGDC candidate models for the 11th generation International Geomagnetic Reference Field and the concurrent release of the 6th generation Pomme magnetic model, *Earth Planets Space*, *62*, 729–735.

Mayaud, P. N. (1980), *Derivation, meaning and use of geomagnetic indices*, Geophys. Monogr. Ser., AGU, Washington, D.C.

McCreadie, H., and M. Menvielle (2010), The PC index: review of methods, *Ann. Geophys.*, *28*, 1887–1903.

Mendes Jr., O., A. M. da Costa, and F. C. P. Bertoni (2006), Effects of the number of stations and time resolution on *Dst* derivation, *J. Atmos. Sol.-Terr. Phys.*, *68*, 2127–2137.

Menvielle, M., and A. Berthelier (1991), The K-derived planetary indices: description and availability, *Rev. Geophys.*, *29*, 415–432.

Menvielle, M., and A. Marchaudon (2007), Geomagnetic indices in solar-terrestrial physics and space weather, in *Space weather: Research towards applications in Europe*, *Astrophysics and space science library*, vol. 344, pp. 277–288, Springer, Dordrecht, Neth.

Milan, S. E. (2009), Both solar wind-magnetosphere coupling and ring current intensity control the size of the auroral oval, *Geophys. Res. Lett.*, *36*, L18,101.

Milan, S. E., T. A. Evans, and B. Hubert (2010), Average auroral configuration parameterized by geomagnetic activity and solar wind conditions, *Ann. Geophys.*, *28*, 1003–1012.

Moos, N. A. F. (1910), *Colaba Magnetic Data, 1846 to 1905. 2. The Phenomenon and its Discussion*, Bombay, India: Central Government Press.

Moretto, T., N. Olsen, P. Ritter, and G. Lu (2002), Investigating the auroral electrojets with low altitude polar orbiting satellites, *Ann. Geophys.*, *20*, 1049–1061.

Murayama, T. (1982), Coupling function between solar wind parameters and geomagnetic indices, *Rev. Geophys. Space Phys.*, *20*, 623–629.

Nagao, H., T. Iyemori, T. Higuchi, and T. Araki (2003), Lower mantle conductivity anomalies estimated from geomagnetic jerks, *J. Geophys. Res.*, *108*, 2254.

Newell, P. T., et al. (2002), OVATION: Oval variation, assessment, tracking, intensity, and online nowcasting, *Ann. Geophys.*, *20*, 1039–1047.

Nikolaeva, N. S., Y. I. Yermolaev, and I. G. Lodkina (2011), Dependence of geomagnetic activity during magnetic storms on the solar wind parameters for different types of streams, *Geomagn. and Aeronomy*, *51*, 49–65.

Olsen, N., and S. Kotsiaros (2011), Magnetic satellite missions and data, in *IAGA Special Sopron Book Series*, vol. 5, chap. 2, pp. 27–44, Springer.

Olsen, N., and M. Mandea (2008), Rapidly changing flows in the Earth's core, *Nature*, *1*, 390–394.

Olsen, N., et al. (2000), Ørsted initial field model, *Geophys. Res. Lett.*, *27*, 3607–3610.

Olsen, N., T. Moretto, and E. Friis-Chritensen (2002), New approaches to explore the Earth's magnetic field, *J. Geodynamics*, *33*, 29–41.

Olsen, N., H. Lühr, T. J. Sabaka, M. Mandea, M. Rother, L. Tøffner-Clausen, and S. Choi (2006), CHAOS – a model of the Earth's magnetic field derived from CHAMP, Ørsted, and SAC-C magnetic satellite data, *Geophys. J. Int.*, *166*, 67–75.

Olsen, N., G. Hulot, and T. J. Sabaka (2007), The present field, in *Geomagnetism, Treatise on Geophysics*, vol. 5, edited by M. Kono, chap. 2, pp. 33–75, Elsevier.

Olsen, N., M. Mandea, T. J. Sabaka, and L. T. Clausen (2009), CHAOS-2 a geomagnetic field model derived from one decade of continuous satellite data., *Geophys. J. Int.*, *179*.

Olsen, N., G. Hulot, and T. J. Sabaka (2010a), Measuring the Earth's magnetic field from space: Concept of past, present and future missions, *Space Sci. Rev.*, *155*, 65–93.

Olsen, N., H. Lühr, T. J. Sabaka, I. Michaelis, J. Rauberg, and L. Tøffner-Clausen (2010b), CHAOS-4 - a high-resolution geomagnetic field model derived from low-altitude CHAMP data, in *Abstract GP21A-0992,2010 Fall Meeting, AGU, San Francisco, CA*.

Olsen, N., G. Hulot, and T. J. Sabaka (2010c), *Handbook of Geomathematics*, vol. 2, chap. 5 Sources of the geomagnetic field and the modern data that enable their investigation, Springer.

Olson, P., U. Christensen, and G. A. Glatzmaier (1999), Numerical modeling of the geodynamo: Mechanisms of field generation and equilibration, *J. Geophys. Res.*, *104*, 10,383–10,404.

Østgaard, N., R. R. Vondrak, J. W. Gjerloev, and G. Germany (2002), A relation between the energy deposition by electron precipitation and geomagnetic indices during substorms, *J. Geophys. Res.*, *107*.

Park, J., C. Stolle, H. Lühr, M. Rother, S.-Y. Su, K. W. Min, and J.-J. Lee (2008), Magnetic signatures and conjugate features of low-latitude plasma blobs as observed by the CHAMP satellite, *J. Geophys. Res.*, *113*, A09,313.

Park, J., H. Lühr, C. Stolle, M. Rother, K. W. Min, and I. Michaelis (2010), Field-aligned current associated with low-latitude plasma blobs as observed by the CHAMP satellite, *Ann. Geophys.*, *28*, 697–703.

Pulkkinen, T. (2007), Space weather: Terrestrial perspective, *Living Rev. Solar Phys.*, *4*.

Purucker, M. E. (2007), Magsat, in *Encyclopedia of Geomagnetism and Paleomagnetism*, edited by D. Gubbins and E. Herrero-Bervera, pp. 673–674, Springer.

Rajaram, M. (1993), Magsat's contribution to geophysical surveys, *Advances in Space Research*, *13*, 33–42.

Rasson, J. L. (2007a), Observatories, Instrumentation, in *Encyclopedia of Geomagnetism and Paleomagnetism*, edited by D. Gubbins and E. Herrero-Bervera, pp. 711–713, Springer.

Rasson, J. L. (2007b), Observatories, INTERMAGNET, in *Encyclopedia of Geomagnetism and Paleomagnetism*, edited by D. Gubbins and E. Herrero-Bervera, pp. 715–716, Springer.

Reay, S. J., W. Allen, O. Baillie, J. Bowe, E. Clarke, V. Lesur, and S. Macmillan (2005), Space weather effects on drilling accuracy in the north sea, *Ann. Geophys.*, *23*, 3081–3088.

Ridley, A. J., and E. A. Kihn (2004), Polar cap index comparisons with AMIE cross polar cap potential, electric field, and polar cap area, *Geophys. Res. Lett.*, *31*, 13,429–13,435.

Ritter, P., and H. Lühr (2006), Search for magnetically quiet CHAMP polar passes and the characteristics of ionospheric currents during the dark season, *Ann. Geophys.*, *24*, 2997–3009.

Ritter, P., H. Lühr, A. Viljanen, O. Amm, A. Pulkkinen, and I. Sillanpää (2004a), Ionospheric currents estimated simultaneously from CHAMP satellite and IMAGE ground-based magnetic field measurements: a statistical study at auroral latitudes, *Ann. Geophys.*, *22*, 417–430.

Ritter, P., H. Lühr, S. Maus, and A. Viljanen (2004b), High-latitude ionospheric currents during very quiet times: their characteristics and predictability, *Ann. Geophys.*, *22*, 2001–2014.

Sabaka, T. J., R. A. Langel, R. T. Baldwin, and J. A. Conrad (1997), The geomagnetic field 1900-1995, including the large-scale field from magnetospheric sources, and the NASA candidate models for the 1995 revision of the IGRF, *J. Geomagn. Geoelectr.*, *49*, 157–206.

Sabaka, T. J., N. Olsen, and R. A. Langel (2002), A comprehensive model of the quiet-time, near-Earth magnetic field: phase 3, *Geophys. J. Int.*, *151*, 32–68.

Sabaka, T. J., N. Olsen, and R. A. Langel (2004), Extending comprehensive models of the Earth's magnetic field with ørsted and CHAMP data, *Geophys. J. Int.*, *159*, 521–547.

Schwenn, R. (2006), Space weather: The solar perspective, *Living Rev. Solar Phys.*, *3*.

Shue, J. H., et al. (1998), Magnetopause location under extreme solar wind conditions, *J. Geophys. Res.*, *103*, 17,691–17,700.

Sillanpää, I., H. Lühr, A. Viljanen, and P. Ritter (2004), Quiet-time magnetic variations at high latitude observatories, *Earth Planets Space*, *56*, 47–65.

Snyder, C. W., and M. Neugebauer (1963), Solar wind velocity and its correlation with cosmic-ray variations and with solar and geomagnetic activity, *J. Geophys. Res.*, *68*.

Sotirelis, T., P. T. Newell, and C.-I. Meng (1998), Shape of the open-closed boundary of the polar cap as determined from observations of precipitating particles by up to four DMSP satellites, *J. Geophys. Res.*, *103*, 399–406.

Spiro, R. W., P. H. Reiff, and M. L. J., Jr (1982), Precipitating electron energy flux and auroral zone conductances: An empirical model, *J. Geophys. Res.*, *87*, 8215–8227.

Sreenivasan, B., and C. A. Jones (2006), Azimuthal winds, convection and dynamo action in the polar regions of planetary cores, *Geophys. Astrophys. Fluid Dynamics*, *100*, 319–339.

Starkov, G. V. (1994), Mathematical model of the auroral boundaries, *Geomag. Aeron.*, *34*, 331–336.

Stauning, P., O. A. Troshichev, and A. S. Janzhura (2006), Polar cap (PC) index: Unified PC-N (North) index procedures and quality, *Scientific report 06-04*, Danish Meterological Institute, Copenhagen, Denmark.

Stening, R. J. (2003), Space weather in the equatorial ionosphere, *Space Sci. Rev.*, *107*, 263–271.

Stepanova, M. V., E. E. Antonova, and O. Troshichev (2005), Forecasting of Dst variations from polar cap indices using neural networks, *Adv. Space Res.*, *36*, 2451–2454.

Stolle, C., H. Lühr, M. Rother, and G. Balasis (2006), Magnetic signatures of equatorial spread F as observed by the CHAMP satellite, *J. Geophys. Res.*, *111*, A02,304.

Stubbs, T. J., R. R. Vondrak, N. Østgaard, J. B. Sigwarth, and L. A. Frank (2005), Simultaneous observations of the auroral ovals in both hemispheres under varying conditions, *Geophys. Res. Lett.*, *32*, L03,103.

Sugiura, M. (1964), Hourly values of equatorial Dst for IGY, *Ann. Int. Geophys. Year*.

Thomson, A. W. P. (2007), Geomagnetic hazards, in *Encyclopedia of Geomagnetism and Paleomagnetism*, edited by D. Gubbins and E. Herrero-Bervera, pp. 316–318, Springer.

Thomson, A. W. P., and V. Lesur (2007), An improved geomagnetic data selection algorithm for global geomagnetic field modelling, *Geophys. J. Int.*, *169*, 951–963.

Thomson, A. W. P., B. Hamilton, S. Macmillan, and S. J. Reay (2010), A novel weighting method for satellite magnetic data and a new global magnetic field model, *Geophys. J. Int.*, *181*, 250–260.

Tomita, S., et al. (2011), Magnetic local time dependence of geomagnetic disturbances contributing to the AU and AL indices, *Ann. Geophys.*, *29*, 673–678.

Troshichev, O., D. Sormakov, and A. Janzhura (2011), Relation of PC index to the geomagnetic storm Dst variation, *J. Atmos. Solar-Terr. Phys.*, *73*, 611–622.

Troshichev, O. A. (1982), Polar magnetic disturbances and field-aligned currents, *Space Sci. Rev.*, *32*, 275–360.

Troshichev, O. A., and V. G. Andrezen (1985), The relationship between interplanetary quantities and and magnetic activity in the southern polar cap, *Planet. Space Sci.*, *33*, 415–419.

Troshichev, O. A., N. P. Dmitreva, and B. M. Kuztnetsov (1979), Polar cap magnetic activity as a signature of substorm development, *Planet. Space Sci.*, *27*, 217–221.

Troshichev, O. A., V. G. Andrezen, S. Vennerstrøm, and E. Friis-Christensen (1988), Magnetic activity in the polar cap - a new index, *Planet. Space Sci.*, *36*, 1095–1102.

Troshichev, O. A., H. Hayakawa, A. Matsuoka, T. Mukai, and K. Tsuruda (1996), Cross polar cap diameter and voltage as a function of PC index and interplanetary quantities, *J. Geophys. Res.*, *101*, 13,429–13,435.

Troshichev, O. A., R. Y. Lukianova, V. O. Papitashvili, F. J. Rich, and O. Rassmussen (2000), Polar cap index (PC) as a proxy for ionospheric electric field in the near-pole region, *Geophys. Res. Lett.*, *27*, 3809–3812.

Troshichev, O. A., A. Janzhura, and P. Stauning (2006), Unified PCN and PCS indices: Method of calculation, physical sense, and dependence on the IMF azimuthal and northward components, *J. Geophys. Res.*, *111*.

Tsyganenko, N. A. (1989), A magnetospheric magnetic field model with a warped tail current sheet, *Planet. Space Sci.*, *37*, 5–20.

Tsyganenko, N. A. (1995), Modeling the Earth's magnetospheric magnetic field confined within a realistic magnetopause, *J. Geophys. Res.*, *100*, 5599–5612.

Tsyganenko, N. A. (1996), Effects of the solar wind conditions on the global magnetospheric configuration as deduced from data-based field models, *Eur. Space Agency Spec. Publ., ESA SP-389*, *181*.

Tsyganenko, N. A. (2002a), A model of the near magnetosphere with a dawn-dusk asymmetry - 1. Mathematical structure, *J. Geophys. Res.*, *107*.

Tsyganenko, N. A. (2002b), A model of the near magnetosphere with a dawn-dusk asymmetry - 2. Parameterization and fitting to observations, *J. Geophys. Res.*, *107*.

Vennerstrøm, S., E. Friis-Christensen, O. A. Troshichev, and V. G. Andrezen (1991), Comparison between the polar cap index PC and the auroral electrojet indices AE, AL and AU, *J. Geophys. Res.*, *96*, 101–113.

Verbanac, G., B. Vršnak, M. Temmer, M. Mandea, and M. Korte (2010), Four decades of geomagnetic and solar activity: 1960-2001, *J. Atmos. Solar-Terr. Phys.*, *72*, 607–616.

Viljanen, A., and L. Hakkinen (1997), IMAGE magnetometer network, in *Satellite-Ground based coordination sourcebook*, edited by M. Lockwood, M. N. Wild, and H. J. Opgenooth, p. 111, ESA publications, Noordwijk, SP-1198.

Vine, F. J., and D. H. Matthews (1963), Magnetic anomalies over oceanic ridges, *Nature*, *199*, 947–949.

Wardinski, I., and R. Holme (2006), A time-dependent model of the Earth's magnetic field and its secular variation for the period 1980-2000., *J. Geophys. Res.*, *111*, B12,101.

Weygand, J. M., and E. Zesta (2008), Comparison of auroral electrojet indices in the Northern and Southern hemispheres, *J. Geophys. Res.*, *113*.

Whaler, K. A. (2007), Geomagnetism in the satellite era, *Astron. & Geophys.*, *48*.

Winch, D. E. (1981), Spherical harmonic analysis of geomagnetic tides, *Phil. Trans. Royal Soc. London*, *303A*, 1–104.

Zhao, L., and C. Y. Tu (2005), A relation between the auroral X-ray total intensity and the substorms index-AE, *J. Geophys.*, *48*, 739–743.

Appendix A

Additional Information

A.1 Co-ordinate Systems

A description of co-ordinate systems mentioned in the text:

A.1.1 Geocentric Earth-Fixed coordinate system

The Geocentric Earth-Fixed (GEO) coordinate system is a Cartesian coordinate system which represents positions in X, Y and Z coordinates. This is the system used by some magnetic satellites, and is traditionally used for geomagnetic main field modelling (*Maus and Lühr*, 2005).

The Z-axis points North, parallel to the rotation axis, and the X-axis is in the equatorial plane and fixed with the rotation of the Earth through the Greenwich meridian (0° longitude); the Y-axis completes the orthogonal set. See figure A.1.

A.1.2 Spherical coordinates $\mathbf{r}, \theta, \phi$

Spherical coordinates are a system of curvilinear coordinates that are used to describe a position on a sphere (or spheroid). r is the radial distance from the origin to a point, θ (termed colatitude) is the angle from the positive Z-axis (and is equal to 90°− latitude), and ϕ is the azimuthal angle in the xy-plane from the X-axis and is the same as longitude. Also shown in Figure A.1.

A.1.3 Geocentric Solar Magnetospheric coordinates (GSM)

The Geocentric Solar Magnetospheric frame has its origin in the centre of the Earth. The x-axis always points towards the Sun, the y-axis is perpendicular to the geomagnetic dipole axis pointing eastward and z completes the right handed system. The magnetopause surface currents and the cross-tail current are thought to be organised in the GSM frame (*Maus and Lühr*, 2005).

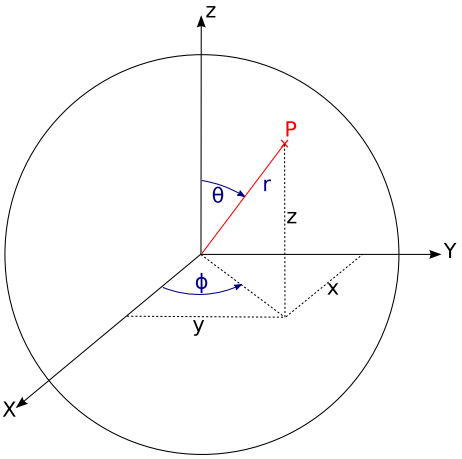

Figure A.1: GEO (black) and spherical (blue) coordinates for a point, P.

A.1.4 Solar Magnetic coordinates (SM)

The origin of the Solar-magnetic frame is also the centre of the Earth. The z-axis point northwards, parallel to the dipole axis, the x-axis points towards the Sun and the y-axis is orthogonal. The ring current is well described in SM coordinates (*Maus and Lühr*, 2005). The main difference between SM and GSM is that z is aligned with the dipole axis only in the SM frame.

A.2 Pole definitions

The geographic North and South poles are defined by the Earth's rotation axis and are centred at the Earth's centre.

The magnetic poles are the points on the Earth's surface where the magnetic field is vertical.

The geomagnetic poles are the antipodal points where the axis of the theoretical dipole intersects the Earth's surface. If the geomagnetic field were a perfect dipole the magnetic and geomagnetic poles would coincide. The geomagnetic poles are currently situated at:

- North: 80.1N, 72.4W
- South: 80.1S, 107.6E

as estimated by the IGRF-11 for 2012.

Appendix B

Parabolic fit to data

In Section 4.3 we require a method of de-trending the data to identify data which are least affected by the auroral oval, based on a standard deviation threshold. To de-trend the data we fit a polynomial through each bin of data. We aim to minimise $(y_i - y)$, where y_i is the data point and y is the predicted value

$$y = ax_i^2 + bx_i + c \tag{B.1}$$

So we minimise

$$\sum_i (y_i - ax_i - bx_i - c)^2 \tag{B.2}$$

$$\frac{\partial}{\partial a} \; : \; \sum_i x_i^2 \left(y_i - ax_i^2 - bx_i - c\right) = 0 \tag{B.3}$$

$$\frac{\partial}{\partial b} \; : \; \sum_i x_i \left(y_i - ax_i^2 - bx_i - c\right) = 0 \tag{B.4}$$

$$\frac{\partial}{\partial c} \; : \; \sum_i \left(y_i - ax_i^2 - bx_i - c\right) = 0 \tag{B.5}$$

We then have three equations:

$$\sum_i x_i^2 y_i = a\sum_i x_i^4 + b\sum_i x_i^3 + c\sum_i x_i^2 \tag{B.6}$$

$$\sum_i x_i y_i = a\sum_i x_i^3 + b\sum_i x_i^2 + c\sum_i x_i \tag{B.7}$$

$$\sum_i y_i = a\sum_i x_i^2 + b\sum_i x_i + nc \tag{B.8}$$

This set of simultaneous equations can then be solved to give the solutions:

$$
\begin{aligned}
a &= \left(-n\sum_i x_i^3\sum_i x_iy_i+\sum_i x^3\sum_i y_i\sum_i x_i+\sum_i x_i^2\sum_i x_i\sum_i x_iy_i+\right.\\
&\quad \left. n\sum_i x_i^2y_i\sum_i x_i^2-\sum_i x_i^2y_i\left(\sum_i x_i\right)^2-\sum_i y_i\left(\sum_i x_x^2\right)^2\right)\\
&\quad /D
\end{aligned}
\tag{B.9}
$$

$$
\begin{aligned}
b &= \left(-\sum_i x_iy_i\left(\sum_i x_i^2\right)^2+\sum_i x^2\sum_i x_i^2y_i\sum_i x_i+\sum_i x_i^3\sum_i x_i^2\sum_i y_i\right.\\
&\quad \left. -n\sum_i x_i^3\sum_i x_i^2y_i+n\sum_i x_i^4\sum_i x_iy_i-\sum_i x_i^4\sum_i x_i\sum_i y_i\right)\\
&\quad /D
\end{aligned}
\tag{B.10}
$$

$$
\begin{aligned}
c &= -\left(\sum_i x_i^4\sum_i x_iy_i\sum_i x_i-\sum_i x_i^4\sum_i x_i^2\sum_i y_i-\sum_i x_i^3\sum_i x_i^2\sum_i x_iy_i\right.\\
&\quad \left. +\sum_i x_i^2y_i\left(\sum_i x_i^2\right)^2-\sum_i x_i^3\sum_i x_i^2y_i\sum_i x_i+\left(\sum_i x_i^3\right)^2\sum_i y_i\right)\\
&\quad /D
\end{aligned}
\tag{B.11}
$$

where

$$
\begin{aligned}
D &= (n\sum_i x_i^4\sum_i x_i^2-\sum_i x_i^4\,(\sum_i x_i)^2-\left(\sum_i x_i^2\right)^3\\
&\quad -n\left(\sum_i x_i^3\right)^2+2\sum_i x_i^3\sum_i x_i^2\sum_i x_i\,)
\end{aligned}
\tag{B.12}
$$